Modelling the atmospheres of A-stars using ATLAS9 with OPAL EOS

060046537V

North-West University
Mafikeng Campus Library

NORTH-WEST UNIVERSITY
YUNIBESITI YA BOKONE-BOPHIRIMA
NOORDWES-UNIVERSITEIT

Author: Papi Lekwene

University Number: 18046312

Supervisor: Prof Thebe Medupe

A thesis presented to the department of physics and electronics in partial fulfilment of the degree of

Masters in Science

Department of Physics and Electronics

North-West University

South Africa

August 13, 2014

LIBRARY
MAFIKENG CAMPUS
Call No.:
2015 -01- 28
Acc. No.: 15/A022
NORTH-WEST UNIVERSITY

Declaration

I Papi Lekwene, declare that this thesis titled, 'Modelling the Atmospheres of A-Stars using ATLAS9 with OPAL EOS' and the work presented in it are my own. I confirm that:

- This work was done wholly or mainly while in candidature for a research degree at this University.
- Where I have consulted the published work of others, this is always clearly attributed.
- Where I have quoted from the work of others, the source is always given. With the exception of such quotations, this thesis is entirely my own work.
- I have acknowledged all main sources of help.
- Where the thesis is based on work done by myself jointly with others, I have made clear exactly what was done by others and what I have contributed myself.

Signed: P H LEKWENE

Date: 26/09/2014

Dedication

My Father **Olebogeng Job Lekwene**. I thank you papa for the son you have brought up in me, for the wisdom and support in my academics, you have truly inspired me and I have always endeavored to emulate you.

My mother **Gaboinewe Ruth Lekwene**. Thank you mama for the Love, the support and the encouragement in particular during the darker days we endured, you have been the rock and I heartily thank you.

To my Grandfather **Rabojale Hendrick Lekwene**. Ke a leboga go menagane Ntate ka kgodiso yame, kemonokeng e o mphileng le thotloetso ka dinako tsotlhe wena le **Mama Ndabula**.

To my late Grandmother **Gasebolelwe Lekwene**. ke a leboga mma, ka lerato, kgodiso le kemonokeng. ke tsaya gore koo robetseng teng, omo tlotlo ka 'Papso'.

To my late Grandmother **Bentlahatsi Mooketsi**. Ke a leboga Mma ka kgodiso, lerato le thotloetso.

To my sister **Malebo Lekwene**. Thank you ausi for the Love, the selfless nature within you, for backing our family during tough times and to see us leading a better life.

To my sister **Tsholofelo Lekwene**. thank you 'Monch' for the lively character you have displayed, thank you for the support and the Love.

To my nephew **Remoabetswe Lekwene**. By time you read this momo, you will feel very inspired to do even better than this.

To my best friend **Lerato Sebokolodi**. Thank you thando for the love, the constant support, your willpower to see me flourish has truly inspired me and I give much credit to you.

Acknowledgements

Foremost, I would like to express my sincere gratitude to my supervisor **Prof Thebe Medupe** for the constant support and advice on my Masters research. **Prof Medupe** has been patient, passionate and has exhibited a great deal of knowledge on the research topic. His guidance has been worthwhile for all the research I have done on this thesis. My hearty appreciation goes to him.

I would like to extend my thankfulness to the **Astrophysics research group members** for invaluable inputs, suggestions and advice on my thesis. The weekly meetings we held were particularly useful and played a significant role in putting up this thesis.

Thirdly, I would like to express my appreciation to my sponsor, the **National Astrophysics and Space Science Programme (NASSP)**. Without the sponsor's support and contribution it would have been a tough ask to complete this work.

I also thank heartily, the Science Centre Manager at North-West University (Mafikeng Campus), **Miss Lerato Molebatsi** for the support and understanding when I had to do my research during my stint at the Science Centre.

I would like to express my sincere appreciation to my **Family** and **Extended Family** for the constant support. A big thank you to my best friend **Lerato Sebokolodi** for the immense support she showed throughout.

Abbreviations

AAAS → American **A**ssociation for the **Advancement** of **Sc**ience.

AAS → American **A**stronomical **S**ociety.

AJP → American **J**ournal of **P**hysics.

ARA → Annual **R**eview of **A**stronomy.

ARA&A → Annual **R**eview of **A**stronomy and **A**strophysics.

A&A → **A**stronomy and **A**strophysics.

Ap.JS → **A**strophysical **J**ournal **S**upplement.

ASP Conf. Ser → **A**stronomical **S**ociety of the Pacific **Conf**erence **Ser**ies.

Astron.Astrophys.Suppl.Ser → **Astron**omy and **Astrophys**ics **Suppl**ement **Ser**ies.

Ap.J → **A**strophysical **J**ournal.

Ap.JS → **A**strophysical **J**ournal **S**upplementary series.

CP → **C**hemically **P**eculiar.

CPP → **C**ontributions to **P**lasma **P**hysics.

COROT → **CO**nvection **RO**tation and Planetary Transit.

EFF → **E**ggleton **F**aulkner **F**lannery.

EOS → **E**quation **O**f **S**tate.

HR → **H**ersprung **R**usssel.

HPR → **H**igh **P**ressure **R**esearch.

IAU → **I**nternational **A**stronomical **U**nion.

JQSRT → **J**ournal of **Q**uantitative **S**pectroscopy & **R**adiative **T**ransfer.

LTE → Local Thermodynamic Equilibrium.

Mem. Soc. Astron. Ital. → Memorie della Societa Astronomica Italiana.

MOST → Microvariability and Oscillation of Stars Telescope.

MHD → Mihalas Hummer Däppen.

MLT → Mixing Length Theory.

MNRAS → Monthly Notices of the Royal Astronomical Society.

MNASSA → Monthly Notes of the Astronomical Society of Southern Africa.

Nato SS → Nato Science Series.

ODF → Opacity Distribution Function.

OP → Opacity Project.

ppm → parts per minute.

PASP → Publications of the Astronomical Society of the Pacific.

Phys. Rep → Physics Reports.

roAp → rapidly Oscillating A peculiar.

RGB → Red Giant Branch.

RMAA→ Revista Mexicana de Astronomia y Astrofisica.

SAAO → South African Astronomical Observatory.

SAO → Smithsonian Astrophysical Observatory.

SIREFF → Swenson Irwin Rogers Eggleton Faulkner Flannery.

SSM → Standard Solar Model.

SSE → Stellar Structure Equation.

TOPPJ→ The Open Plasma Physics Journal.

ZAMS → Zero Age Main Sequence.

Physical Constants

$a \rightarrow$ The radiation constant $\approx 7.566 \times 10^{-15} erg.cm^{-3}.k^{-4}$.

$c \rightarrow$ The Speed of Light $\approx 2.997 \times 10^{10} cm.s^{-1}$.

$K \rightarrow$ The Boltzmann constant $\approx 1.380 \times erg.K^{-1}$.

$R \rightarrow$ The Universal Gas Constant $\approx 8.314 \times 10^{7} erg.K^{-1}.Mol^{-1}$.

$\sigma \rightarrow$ The Stefan-Boltzmann constant $\approx 5.6704 \times 10^{-5} erg.cm^{-2}.s^{-1}.K^{-4}$.

Symbols

$C_p \rightarrow$ Specific Heat Capacity.

$\Gamma_1 \rightarrow$ The First Adiabatic Exponent.

$\Gamma_3 - 1 \rightarrow$ The Third Adiabatic Exponent.

$\rho \rightarrow$ Density.

$\nabla_{ad} \rightarrow$ The Adiabatic Temperature Gradient.

$\nabla_{rad} \rightarrow$ The Radiative Temperature Gradient.

$Y_i \rightarrow$ Helium Mass fraction.

$X_i \rightarrow$ Hydrogen Mass fraction.

$Z_i \rightarrow$ Elements Heavier than Helium.

Contents

List of Figures

Abstract

ATLAS9 program is the standard tool for making model atmospheres of stars. It is used for producing synthetic spectra of stars that can be compared with observed spectra to determine the physics of the atmospheres of stars. It is valuable in determining effective temperature, surface gravity and composition of stars. Our project involved making improved stellar models of main sequence A-stars with the primary aim of replacing the Equation of State (EOS) used in ATLAS9 program with the OPAL Equation of State in order to determine the changes this will bring in the model atmosphere calculations. We changed the original ATLAS9 EOS by replacing ATLAS9 EOS routines with the OPAL EOS routines in the ATLAS9 program. On the broader context we wish to build good stellar models that will be used in stellar pulsation studies. With this, we want to produce good equilibrium models that can be used to calculate pulsation frequencies that can be matched accurately to the observed frequencies from the KEPLER and COROT missions.

In Chapter 2, we have compared the ATLAS9 EOS with the OPAL EOS to determine if the OPAL EOS works well in the atmosphere region. We find no significant difference in the calculation of density whether one uses ATLAS9 EOS or OPAL EOS except for hotter models (T_{eff}=9500 K). The calculations for thermodynamic variables such as the adiabatic exponent, temperature gradient, specific heat capacity and the third adiabatic exponent produced differences between the ATLAS9 program and the OPAL routines. This was due to the different thermodynamic states of the gas used by the two approaches. However, the profiles produce were essentially the same for all the models in the atmosphere and the upper layers of the envelope.

The OPAL EOS is state-of-the-art and includes more physical effects than the ATLAS9 EOS. Thus, the second aim of our project is to estimate the size of the error introduced when OPAL

EOS is not used in normal ATLAS9 model atmospheres The error introduced when calculating density (ρ), temperature, pressure, electron density and Rosseland mean opacity using ATLAS9 (with ATLAS9 EOS) ranges between 0.32 %–22 % for 7000 K $< T_{eff} <$ 9000 K. For thermodynamic variables the error introduced when calculating the first adiabatic exponent (Γ_1), adiabatic temperature gradient ($\bigtriangledown_{ad}$), radiative temperature gradient ($\bigtriangledown_{rad}$) and the specific heat capacity (C_P) using ATLAS9 (with ATLAS9 EOS) ranges between 2.8 %–90 % for 7000 K $< T_{eff} <$ 9000 K. The error introduced for the density derivatives was calculated to be in ranges 1.2 %–18 % for 7000 K $< T_{eff} <$ 9000 K. For the spectra calculated, the differences between the two methods were quite small and ranged between 0.13 %–0.6 % for both cooler and hotter models.

These error estimates must be quoted with the following in mind; One of the major challenges was that OPAL EOS does not work well for low temperature opacity. We believe that this challenge can be resolved by using an EOS that is easy to access and EOS tables that can be used for low temperature opacity. We have made tests to our models by revisiting the matching code by Mguda (2010) but the mismatch between the envelope and the atmosphere was still evident.

Chapter 1

Introduction

Stars have often been used as basis for understanding the realms of the universe. This is because the universe is chemically enriched with elements that were formed from the interior of stars. As a result, these round balls of gases have often been used to trace how the universe has evolved. They also continually ionise and re-ionise the intergalactic medium (Aerts et al. 2009). Therefore, our understanding of stellar structure, evolution and pulsations is fundamental to our understanding of the more distant universe by way of extrapolation. This means our knowledge of properties of stellar populations, calibration of distances to very remote galaxies using stars and even spectra of stars within these galaxies further enhances our understanding of the more distant universe (Maeder, 1995).

Our project aims to create equilibrium models of stars. The models we have endeavoured to build in our research work will be used in stellar pulsation studies. Modelling ionisation equilibrium model developed from the Saha equation, have over the years been at the fore front in enlightening us about the physics and dynamics of stars. Stellar models are essentially profiles of pressure, density, temperature and other stellar variables as a function of optical depth inside a star. These are some of the profiles we have calculated using the ATLAS9 program. Such profiles are calculated using the physics of gases. Such calculations are carried out by assuming that stars are large spherical gases. Stellar Pulsations in main sequence A-stars are due to p- and

g-modes that travel inside these stars. These seismic waves are sensitive to parts of a star they travel in, hence they are critical to our understanding of the physics and structure of the parts of a star where these waves travel. Comparison of the frequencies, amplitudes and phases of these waves with data is important in probing these different parts of a star. It has been an important challenge to have accurate models of pulsating stars that can be compared with highly accurate data obtained from Space-based Observatories such as KEPLER , COROT and MOST . For example, KEPLER can detect amplitudes of under 1 *ppm* (Kjeldsen & Bedding, 2011). In our attempt to produce accurate models of A-Stars, we match model atmospheres calculated using well tested ATLAS9 program (Kurucz, 1979) to envelope models that we calculate ourselves. Accurate stellar pulsation models are highly dependent on accurate equilibrium models. The work presented in this thesis is part of a project in our research group to produce highly accurate equilibrium models of atmospheres and envelope of A and B-Stars. The first attempt to do this by Mguda (2010) produced discontinuous matching between atmosphere and envelope models. My thesis attempts to remove these discontinuities by using the OPAL EOS in the calculations of model atmospheres. The atmosphere models were calculated using ATLAS9 program. We calculated envelope models from stellar structure equations. Furthermore, the envelope models were calculated using OPAL opacities and OPAL Equation of State. The ATLAS9 model atmosphere were calculated with Kurucz opacities and EOS. We therefore, thought that if we used the OPAL EOS in the ATLAS9 program, we will have improved model atmospheres and be able to produce continuous matching of atmosphere and envelope models.

The second aim of our project is to estimate the size of the error introduced when OPAL EOS is not used in normal ATLAS9 model atmospheres. Ultimately, we want to produce good equilibrium models that can be used to calculate pulsation frequencies that can be matched accurately to the observed frequencies from KEPLER and COROT missions. Linear stellar pulsations are generally regarded as linear perturbations to a star in equilibrium. Hence pulsation equations are linearly perturbed stellar structure equations with co-efficients that depend on equilibrium

models. Hence the accuracy of eigen frequencies will depend on how good the equilibrium model is. Thus, our project involved making improved stellar models of main sequence A-stars (reviewed in subsubsection 1.4.2.4). This has been done by using the OPAL EOS in the ATLAS9 model atmospheres. An attempt was made in this thesis to match these models smoothly.

From a theoretical point of view, the importance of modelling the atmosphere of a star lies in determining the stellar structure as well as the stellar evolution (Stutz, 2005). The role played by the EOS in stellar evolutionary models is that of providing variables such as pressure, density, adiabatic temperature gradient, specific heat at constant pressure as noted by Pols et al. (1995). Furthermore, if we are to successfully investigate the processes such as pulsation mode identification, then we ought to make accurate models of the structure of the atmosphere. Some examples in stellar astrophysics that need accurate modelling have been discussed by Saumon (1994) and includes solar oscillation spectrum, stellar pulsations, solar neutrino problems as well as the source of abundance for elements in the atmospheres of white dwarfs. There are challenges in stellar modelling and they include amongst others, inclusion of many of the spectral lines which need to be considered when one deals with the radiative transfer (Stutz, 2005). For our purpose, we modified an existing ATLAS9 code in order to obtain a more accurate model. The bigger picture for our research project lay in making good models of stars that will be used in modelling pulsations in A-stars. Pulsations are important because we can use them to constrain the theory of stellar evolution and study the stellar interiors.

Our long term goal involve modelling A-stars and making the smooth transition between the atmosphere and the envelope for stellar variables such as the first adiabatic exponent (Γ_1). This will be done using the matching code developed by Mguda (2010). The discontinuous matching reported by Mguda (2010) could be attributed to several unknown scientific causes, hence our research work was made to attempt to eliminate the discontinuities and further develop an understanding of any physics behind the previous discontinuities. However, with this in mind,

one could cite one aspect notable in Mguda (2010) and that is, the envelope was modelled with the OPAL approach while the atmosphere was determined using the ATLAS9 program. This primarily justified our call for uniformity in the EOS used having included the OPAL EOS in the ATLAS9 program. On the broader context, the primary task entailed modifying a pre-existing ATLAS9 program. This program as stated by Kurucz (1970), caters for temperatures and pressures that are not extremely high in the stellar atmosphere while the OPAL EOS according to our results has shortcomings in the stellar atmosphere region. This implies we have acquainted ourselves to a considerable degree on how the OPAL EOS are accessed and calculated. The knowledge thus obtained has been implemented when the ATLAS9 program was modified. Our models were applied to the matching code in order to achieve the smooth transition between the envelope and the atmosphere. The significance of this is that our research work has attempted to yield solutions of questions of several unmatched variables between the envelope and the atmosphere as well as contributing towards an equilibrium model that can be used in stellar pulsation equations.

This thesis is structured in the following manner. In §1 we give a background on key concepts that are essential for one to successfully carry out stellar modelling calculations. We further give a review on the EOS and the role it plays in stellar structure equations. We also discuss the seismology of stars, the stars to which we wish to apply our models and the role played by the Matching code in our models. We further give a thorough review of the stellar structure equations. In §2 the feasibility of the research question we have addressed is given by showing the comparison of the ATLAS9 EOS to the OPAL EOS method. In §3 we discuss the results obtained by including the OPAL EOS in the ATLAS9 program. We have also discussed the effect of the OPAL EOS on the ATLAS9 spectrum. Furthermore, we have also made comparisons of models to see if the new models are logical and consistent with those from the original ATLAS9 program and OPAL EOS. In §4 we bring the thesis to closure and make necessary recommendations.

1.1 The EOS in Stellar Astrophysics

To model a star one needs to divide the star into three major regions. From the center of the star extending to about 25 % of the radius is the core. This is the region where nuclear energy reactions produce the energy that we eventually see as light from the stellar surface. The region above the core is the stellar envelope through which the energy produced from the core travels mainly by radiation. For main sequence stars, this envelope occupies almost 70 % of the radius of a star. This is the region of a star that has been widely modelled using the OPAL Equation of State and opacities. We have used this approach for our research work and it is explained in the successive sections. The outer most region of a star is called the atmosphere, this is the part visible to us when we look at a star. This is the region in a star where our computer program of interest ATLAS9 calculates stellar models. The layers of a star below the atmosphere are completely opaque and invisible to us. Furthermore, one needs to specify the chemical composition of a star modelled since the opacity and nuclear reaction rate depend on the chemical composition. The chemical composition is usually given by indicating the mass fraction X_i of different elements that a star is composed of. The last step to complete a simple stellar model is that of determining the Equation Of State (EOS), opacity and the nuclear reaction rates as a function of temperature, density and chemical composition. The description of basic physical laws are essential to aid in our bid to understand the stellar interiors and eliminate any discrepancies that may be present. The laws in question include the EOS, opacities and thermal nuclear reactions as hinted before. The EOS includes the properties of matter together with the transport coefficients. It also relates stellar variables such as temperature, pressure and density thus making stellar structure equations solvable (Saumon, 1994). The pressure along with the entropy are not too hard to identify in these equations and they describe the mechanical and thermal equilibrium of a star as noted by Saumon (1994). However, there have been challenges related to the EOS that is used to describe the structure of stars and their evolution. The challenges include difficulties in describing the EOS for a plasma of a gas as well as the degree of scattering of atoms. However, one of the important contributors for any stellar model has been

the thermodynamics of the hot dense plasmas. This contribution has been in the form of the EOS. According to Haesel et al. (2007) the simple way of determining the EOS for densities in the intermediate regions is by way of interpolation between the low and high densities.

The EOS is our tool of interest and the discussion herein outlines how the EOS is used in Stellar Astrophysics. The EOS simply describes all possible values of pressure, density and temperature in a system, while ensuring that Local Thermodynamic Equilibrium (LTE) is retained. This implies for stellar systems we can use the EOS as a tool to study extreme conditions at the stellar core such as high density, energy and matter. To obtain all this we rely on advanced theoretical models as noted by Fotov & Lomonoso (2010). However, things get complex as far as the EOS is concerned, when non-ideal effects are introduced (Saumon, 1994). Furthermore, Saumon (1994) states that such calculations can only be done using numerical methods with results displayed in a form of a table, widely refered to as an EOS table.

A good EOS is not only a prime requirement for one to compare observations with theoretical models but also the accuracy of it has to be of the highest standard (Lin, 2010). In addition to determining the pressure, density and temperature the EOS also needs to determine the stellar composition. By composition we mean the mass fraction of hydrogen X_i, helium mass fraction Y_i and other elements heavier than helium Z_i (Christensen-Dalsgaard et al. 1996). In addition, the role played by the EOS in stellar matter is that of aiding in the determination of population levels. The levels provide absorption or scattering of radiation, stellar evolution and require one to use the simplest EOS available. Fundamentally, the plasma of a stellar interior consists of the mixture of perfect gases of all species (Charbonnel et al. 1999). With this in mind, an EOS is often deemed not to be of significant use if it cannot predict the properties of a plasma for an optical regime (Hummer & Mihalas, 1988). This according to Hummer & Mihalas (1988) is due to these properties being obtainable for experimental tests.

There are certain properties of stars, for which the EOS in applied on and these are discussed shortly. The range in temperature and density that is often found in stars is quite significant while the resulting Coulomb correlation is almost negligible (Rogers, 1994). In a similar way to the OPAL EOS we have used, the density-temperature profiles for main sequence stars is given by $R = \frac{\rho}{T_6^3}$. Where R is an iso-R track which brackets the path of stars, where ρ is the constant density in g.cm^{-3} and T_6 describes the ρ-T range for stars (Trampedach, 2006). For composition, there is a difference in composition for intermediate stars as far as stellar evolution is concerned. An example of these stars are those found on the main sequence band and more advanced stars in their evolution, such as white dwarfs and neutron stars. Any main sequence star is largely composed of hydrogen and helium This is different from the white dwarfs that are mainly composed of carbon and oxygen with a relatively large R (Rogers, 1994). The significance of this is that the conditions in main sequence stars generally limit Coulomb corrections to the EOS. The corrections are less than a few percent. The theoretical studies of the structure of neutron stars have been useful because the mass and the radius of the stars potentially helps in putting constraints on the EOS of dense matter (Lattimer & Prakash, 2001).

The EOS for liquids is difficult while that of a gas is relatively simple to handle. The EOS has been useful in Astrophysics by providing the thermodynamic properties needed for the description of stars and planets (Trampedach, 2006). Furthermore, the foundation of opacity calculations is the ionisation equilibrium and level populations of species provided by the EOS. The EOS for astrophysical applications is not always simple to calculate (Saumon, 1994). This is due to a number of questions that needs to be addressed and these include what EOS is most appropriate for a specific problem. With this in mind we have discussed in this thesis, how our choice of EOS (OPAL) approach compares with other EOS methods. Literature studies alone cannot aid in our quest to address questions concerning a particular choice of EOS made. Thus before we used the OPAL EOS tables, we have directly compared different methods, stating their shortcomings and poor approximations as noted by Saumon (1994). Our understanding of the role played by the EOS in astrophysics has emerged from studies of dense matter physics. This is partly due

to the contribution of computer technology in carrying out complex calculations associated with the studies of dense matter physics. Such calculations have been possible due to a number of approximations being used.

In looking at other properties of stars, we can have a system characterised by a great deal of compression in its atoms. This means it is a system with atoms closely packed and this leads to electrons that are likely to be in conducting states (Yildiz & Kiziloglu, 1997). This whole process leads to pressure ionisation. Pressure ionisation occurs when we have a system with many atoms that are compressed to such a level that some of the other atomic orbits overlap (Rogers et al. 1996). This implies the electrons which filled these levels are squeezed and become free. Thus, the pressure ionisation eventually becomes a complex problem to include in the EOS calculations. This problem has often been avoided by only interpolating for atomic and fully ionised limits (Saumon, 1994). The EOS for astrophysical plasmas is to a great deal nearly ideal and this EOS serves the purpose of determining the structure of the stellar interiors. A lot of stars have matter that is either in a state of a perfect gas or in a complete degenerate gas state. However, for either case the EOS is quite simple to understand. The EOS for an ideal gas is given by

$$P = nKT, \tag{1.1}$$

where n is the number of particles per unit volume, K is the Boltzmann constant and T is the temperature. When stellar matter is completely ionised at higher temperatures then equation (1.1) becomes

$$P = KT(n_e + n_I), \tag{1.2}$$

where n_e is the number of electrons particles and n_I is the number of ions that includes hydrogen, helium and all other elements heavier than helium (Fall, 2003). For sufficiently high temperatures we have a state of gas that is fully ionised. Under these conditions we assume stellar matter to be composed of hydrogen (H), helium (He) and other elements (Z) heavier than helium. This is because at high temperatures, H_2 dissociates into H. The significance of the specified composition

is that spectroscopic studies help us to determine the exact composition of a star. The dominance of H and He over other elements implies that, the rest of the elements are grouped as one entity. At the surface, the temperatures are not high enough for matter to be considered in a state of complete ionisation. However, the temperature may be high enough for the perfect gas law to hold (Kippenhahn & Weigert, 1994). This law is applicable for high temperatures and low pressures while for low temperatures and high pressures ionisation due to the pressure is likely to occur.

1.1.1 The Equation of State of stellar matter

The interior of a star is a mixture of ions, electrons and photons. With the exception of dense stars, most stars have ions and electrons which can be treated as an ideal gas with quantum effects neglected. Each of these particles contribute to the total pressure of a star as noted by Kippenhahn & Weigert (1994). Even though photons have zero mass, they do exert pressure since they have momentum. The sum of these pressures contribute to the equation of state. In simple terms the total pressure inside a star is given by

$$P = P_{ion} + P_e + P_{rad}, \tag{1.3}$$

where P_{ion} is the pressure due to the ions, P_e is the electron pressure and P_{rad} is the radiation pressure. The ion and the electron pressures added together results in the gas pressure. The Equation of State for an ideal gas is given by

$$P_{gas} = nkT, \tag{1.4}$$

where n is the number of particles per unit volume, k is the Boltzmann constant and T is the temperature. In a mathematical form $n = n_i + n_e$, where n_i and n_e are number densities of ions and electrons respectively. Furthermore, equation (1.4) can be expressed as

$$P_{gas} = \frac{R}{\mu}\rho T, \tag{1.5}$$

where R is the universal gas constant and μ is the average particle mass. The radiation pressure

is given by

$$P_{rad} = \frac{1}{3}aT^4, \tag{1.6}$$

where a is the radiation constant given by $\frac{4\sigma}{c}$, where σ is the Stefan-Boltzmann constant and c is the speed of light. Equation (1.5) and equation (1.6) imply that the dominating pressure between the gas and the radiation pressure at the core can be determined, by simply taking the ratio of the two in this region (Kippenhahn & Weigert, 1994). It has been determined that the radiation pressure is insignificant at the centre of stars with masses close to that of the Sun and less. However, this will not be true for more massive stars where the radiation pressure can be significant. Also, from equation (1.5) and equation (1.6) it can be easily deduced that, the radiation pressure will be equal to the gas pressure if

$$T^3 = \frac{3R}{a\mu}\rho, \tag{1.7}$$

Figure 1.1 shows regions in the log T and log ρ space, where the radiation pressure and gas

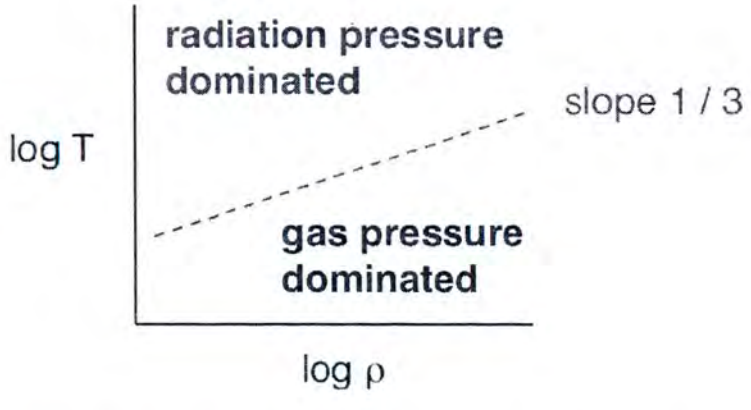

Figure 1.1: A sketch showing the regions in the log T–log ρ space, where the equation of state is dominated by radiation pressure above the dotted line and gas pressure below the dotted line. The dotted line is based on equation (1.7), taken from Fall (2003).

pressure are dominant. As shown in **Figure 1.1**, below the dashed line the EOS is dominated by the gas pressure while the radiation pressure dominates the EOS above the dashed line. Fall

(2003) has shown that the ratio of the radiation pressure to gas pressure in a star is proportional to M^2, in other words

$$\frac{P_{rad}}{P_{gas}} \propto M^2 \cdot \tag{1.8}$$

From equation (1.8) it is clear the gas pressure is significant in low mass stars while the radiation pressure is significant for high mass stars.

1.1.2 The EOS in Stellar Modelling

Stellar models of the EOS are currently used in models of the Sun and this was the case prior to the 1980s. The physics involved back then was two fold and it used the Saha equation to model the ionisation process and the other process modelled was the electron degeneracy (Gong et al. 2001). Stellar models are used for comparing with data and thus require codes used to be very accurate. The ionisation equilibrium model that was introduced by Saha (1920) led to changes in stellar modelling. This model has been useful for many purposes but had its fair share of shortcomings. For instance, Rogers et al. (1996) state that this model only uses ground state arrangements in the ionisation-balance equations. This is considered a shortcoming because a good model for a star is measured by its ability to include all excited states. Other stellar models that have been produced with success include that of Eddington (1929) which was more simple and analytic. However, while keeping the success of stellar models in mind, some credit is owed in part to the observational constraints such as Spectroscopy, Photometry, Astrometry and Interferometry of stars for putting constraints on theory (Aerts et al. 2009). These observations have succeeded partially in explaining the basic laws of physics under stellar conditions in spite of their poor precision as alluded to by Aerts et al. (2009). The observational techniques have over the years improved in quality and made new findings. The findings included identifying different stellar atmosphere layers for peculiar stars and horizontal branch stars (Stutz, 2005). Additionally, since the studies of Astereoseismology have been introduced, uninterrupted space photometry studies using the Kepler and the CoRot space telescopes have delivered accurate data for eclipsing binary research. The knock-on effect of these observations for Astereoseismology,

has been the development of eclipsing binary pulsating components as stated by Maceroni et al. (2009). These studies also probe other population of stars in the Milky Way Galaxy. These space missions have primary goals of searching for earth like planets in the habitable zones around their parent star.

Furthermore, studies of oscillations inside stars have aided in determining the properties of stars, their internal structure and dynamics. A case in point has been the studies of Helioseismology that is concerned with the oscillations within the Sun. This study has given us good insights about the internal structure of the Sun (Basu & Antia, 2008). In fundamental terms, this study uses the interior solar oscillations to study the interior properties of the Sun. In turn, stellar evolution codes have also proved useful in determining the properties of these oscillations as stated by Waelkens (1995). This has proved to be key on the observational front as well as theory. Furthermore, great strides have been made in explaining physical processes such as turbulent velocities in the stellar atmosphere and the existence of strong global magnetic fields (Stutz, 2005).

When one looks at evolution of stars, there is different time scale of stellar evolution and pulsations, hence it has been hard to do both these studies independently. According to Waelkens (1995), what has been revealed in stellar evolution and pulsations studies, is that pulsations lead to mass loss in hot massive stars as well as evolved low mass stars. Furthermore, according to Ciancio et al. (1997), the evolutionary computations of the Standard Solar Model (SSM) have played a key role in our understanding of the inner solar structure. This has consequently led to our understanding of the solar neutrino problems better than before. With all these good strides being made in stellar modelling, there are still discrepancies between theory and observations which have to do with the inadequate understanding of the EOS.

There are various research groups dedicated to calculating the EOS. The groups have managed

to link the astrophysical challenges connected to the EOS and any unclear physical theories. Furthermore, the groups have also managed to provide a good description for the large observational data that has been collected over the years. Additionally, what has been determined are the conditions in which the various EOS exists. The conditions include amongst others the regions where Coulomb interactions of stellar matter such as electrons and ions may occur moderately. By Coulomb interactions we mean that at extreme high densities the atoms tend to be closer to each other and according to Pols et al. (1995) these interactions can range from weak to strong interactions. Also, during this Coulomb interaction slight changes occur in the energy and the pressure. The influence of the resulting Coulomb potential is solely due to other charged particles in a plasma as alluded to by Bi et al. (2000). This may result in the bound electron not maintaining its original state. What we can deduce from these conditions is that the Coulomb interactions create a decreasing change in pressure and energy as noted by Yildiz & Kiziloglu (1997).

The EOS is usually provided in the form of tables and interpolation routines. The range these EOS calculations cover is from stellar scales to galactic scales. The high temperatures and densities in certain stellar regions make it hard for one to gain access to the quality of the EOS that is used (Gong et al. 2001). There are relations shared by the EOS calculations and those calculations needed to improve nuclear reaction rates at extremely high densities. The reviews of the groups dedicated to calculating the EOS will be discussed in subsection 1.1.4.

The type of EOS tables we have used has been provided by the widely known OPAL opacity approach. The opacity of stellar material controls the energy flow through a star and eventually the luminosity of a star (Christensen-Dalsgaard et al. 1996). A great excitement ensued when the OPAL opacity group at Lawrence Livermore National Laboratory released detailed associated EOS tables. This led to the resolution of several important problems in stellar astrophysics. For example, according to Van Horn (1992), at high densities the calculations of the

EOS for matter in regions of strong magnetic fields and radiative opacities have improved quite significantly. More over, the stellar models have been computed inconsistently since the EOS used to calculate the opacities has been different from the EOS used for calculating the rest of the model. Additionally, the OPAL EOS along with the Mihalas, Hummer and Däppen (MHD EOS) has been used for the calculations of the recent Standard Solar Model (SSM) as stated by Guenther et al. (1996). Furthermore, Christensen-Dalsgaard et al. (1996) have noted that the increased opacity results found by OPAL in the convection zone were mainly due to the effect of the improved EOS and the ion balance. This enhancement in opacities led to the substantial improvements in agreement between theory and the helioseismic data.

For opacities, Rogers et al. (1996) state that the role and the success enjoyed by the OPAL opacities has been that of providing the EOS data that is consistent with the already available opacity tables. Also, the opacities from the OPAL approach and the Opacity project (OP), agree quite well for a wide range of temperature values. For example, Alexander (1975) has calculated opacities for temperatures as low as 700 K and determined as well, the rough values for the opacities due to dust grains. The results thereof have been used to settle discrepancies between theoretical models and observations at lower temperatures (Ferguson et al. 2005). These OPAL opacity tables have also been used by Alexander & Ferguson (1994) at lower temperatures ($T_{eff} \approx 700K$).

1.1.3 Equation of state and Opacity

The opacity was recognised by Eddington as one of the two clouds that generally make stellar calculations obscured, while the other cloud produces the stellar energy (Däppen & Guzik, 2000). The atmosphere of a star generally has a very small part of its entire mass in it (Neuforge, 1993). Thus when the evolutionary tracks of stars have been made, the opacities in the atmosphere of a star have not played a significant role for this stellar evolution. The exception to this has been the extensively used low temperature opacity tables provided by Cox & Steward (1970)

and Alexandre (1975). On the other hand, the mean opacities have been useful in studying the interiors of cool stars, giant planets and the disk of material that usually forms stars and planets (Ferguson et al. 2005). For these low temperature opacities the type of stars that have been evaluated have been the population I stars with moderate values of metallicities (Z). Pre-calculated mean opacity tables have often been used for solving radiative transfer equations. This has been done for every part of the material that is optically thick (Ferguson et al. 2005).

The opacity tables have also been made available for protoplanetary disk models and these tables were computed by Semenov et al. (2003) for the gas and dust grains for temperatures between 10 K and 10000 K. When the pressure (P) and entropy (S) of stellar matter are related to the mass density (ρ) and temperature (T), the relation is widely refered to as the EOS. The EOS, opacity and nuclear reactions are very fundamental in stellar modelling (Däppen & Guzik, 2000). Furthermore, Däppen & Guzik (2000) highlight the importance of a smooth EOS, that is consistent and valid for a wide range in temperature and pressure. The first case of smoothness has been the motive for our research work as we have attempted to make the transition between the envelope and the stellar atmosphere as smooth as possible. For the Sun, the large solar convection zone makes it possible for the EOS to be determined with high accuracy. On the other hand there have been uncertainties in determining the opacity.

Inside the solar convection zone region the arrangement of layers is adiabatic and thus determined by thermodynamics (Christensen-Dalsgaard & Däppen, 1992). In case of stars more massive than the Sun, it is necessary to use an adequate EOS. For instance, Charbonnel et al. (1999) state that the OPAL EOS has been used because of the smooth thermodynamic quantities obtained. A good EOS has to be versatile; for instance, the OPAL EOS provides a strategic method for including the density effects (Däppen & Guzik, 2000).

Although the OPAL opacities have been used for temperatures greater than 6000 K, Ferguson

et al. (2005) used opacity tables at low temperatures as well. Furthermore, the OPAL opacities have a wide range in metallicity and composition. This consequently implies that one can include the composition profiles in the models constructed (Wood, 1994). Opacities in the atmospheric layers have been deemed to be important for computing the theoretical stellar evolutionary phases. This has been the case because the stellar atmosphere occupies only a small part of its mass (Neuforge, 1993). These evolutionary phases depend on the mass, chemical composition on the Zero Age Main Sequence (ZAMS), stellar age and the convection parameter. Other tables provided by Cox & Steward (1970) and Alexendra (1975) have also been used for low temperature opacities. Problems that have been encountered with these tables have been discrepancies for different temperature and density ranges (Neuforge, 1993). However, in the past decade there have been improvements in calculations of the radiative opacities, conductive opacities for mixed compositions and uniform compositions (Wood, 1994).

When we define opacity we look at the effect that photons have on atoms, free electrons and ions during their interactions. There are four processes that are widely known to contribute to the opacity and these are; the bound free transitions, free-free transition and the bound-bound transition. These processes primarily remove photons from the radiation. What is significant is that when opacity is evaluated for a model atmosphere, all opacity sources are considered. Also, for astronomers, when the opacity changes slowly with wavelength this results in the continuum spectrum being determined. These sources of opacity are discussed shortly.

- Bound Bound Transitions

This is the thermal process that occurs at temperatures as low as 1×10^7 K and it occurs when a photon is absorbed by an electron still bound inside an atom or ion and moves to a higher energy level. During this absorption process the photon immediately stops to exist resulting in the energy being released as photons. This is achieved because a photon collides with a bound

electron of a certain atom at a particular quantum level. This causes the electron to go to a higher energy level. If the electron makes the transition back to this energy level, it will not go back to the initial quantum level (Carol & Ostli, 1995). Instead it will release a photon with a different frequency and this explains the original photon being completely absorbed. If de-excitation is not to the original energy level, additional energy is released as thermal energy. This transition occurs along two states of energy and as such it is important for a small range of energies.

More importantly, this transition indicates changes in the specific intensity though for a short range. The bound bound transition produces the emission and absorption lines that are present in the stellar spectra. In this process the ability of stellar material to absorb radiation is explained. This effectively adds to the stellar opacity κ_λ of stellar material (Murdin, 2001).

- Free-free transitions

When a free electron passes close to an ion, it experiences an increase in speed, kinetic energy and consequently an increase in acceleration. This accelerated charge inevitably produces radiation. The significance of having an ion here is that energy has to be conserved. Also, when an electron passes closer to the ion, it tends to lose energy because it releases a photon. This causes the electron to decrease its speed and move to an unbound orbit of a higher energy. This free-emission simply limits radiation. This process also produces a continuum opacity at all wavelengths.

- Electron Scattering.

During this process a free photon is scattered and this scattering is caused by an electron.The photon changes direction but it does not lose its energy. The electron develops an oscillation phase and it is next to the photon's electromagnetic field. The scattering cross section is given

by

$$\sigma_T = \frac{1}{6\pi\epsilon_o^2}\left(\frac{e^2}{M_e c^2}\right)^2 \tag{1.9}$$

where e is the charge of an electron, M_e is the mass of an electron and c is the speed of light. Upon substituting the constants it can be shown that this cross section is significantly small. Equation (1.9) suggests that, a way to increase the cross section of this scattering area would be to increase the density of the electrons.

- Bound-Free absorption

During this process we have an incident photon with sufficient energy to ionise an atom as noted by Carol & Ostli (1995). The result of this process is a free electron. The cross section from this process in a quantum state n,m due to a photon is given by

$$\sigma_{bf} = 1.31 \times 10^{-19}\left(\frac{1}{n}\right)^5\left(\frac{\lambda}{500nm}\right)^3 m^2 \cdot \tag{1.10}$$

where λ is the wavelength. The bound free emission process occurs when an electron combines again with an ion (Kippenhahn & Weigert, 1994). This results in the photon being emitted in random directions. The energy of these photons gets reduced in the radiation field.

1.1.4 Methods for calculating the EOS

A stellar model requires an EOS that covers a wide range of temperature, density grid and composition. Such a model often makes use of online computed EOS tables. There have been various research groups dedicated to calculating the EOS. There are two widely used methods for computing the EOS, namely the chemical picture and the physical picture method. In the chemical picture the concept atoms, ions and molecules are separated from each other (Luo, 1994) and these sets of species reach a chemical equilibrium as stated by Trampedach (2006). An example of the EOS that uses the chemical picture is the Eggleton, Faulkner & Flannery (Eggleton et al. 1973), hereafter referred to as the EFF EOS. This method has been vastly used

in stellar modelling. In this method the non-ideal effects ensure that there is full ionisation at the stellar core. This ionisation is treated as a chemical reaction. Another example of the chemical picture method that has been in wide spread use is the Mihalas, Hummer & Däppen (MHD EOS), (Hummer & Mihalas (1988), Mihalas et al. 1988; Däppen et al. 1987, 1988).

An example of the physical picture method is the OPAL EOS that was developed by Rogers & Iglesias (1992) and Iglesias et al. (1992). This method treats a system using its basic constituents such as electrons and nuclei. The method adopted by the OPAL EOS is that of the expansion of pressure as a sum of two body or three body terms (Rogers et al. 1996). There is a thermodynamic consistency achieved in this physical picture method. This consistency is achieved by modelling a thermodynamic potential and thus calculating other thermodynamic quantities and derivatives from Maxwell relations (Trampedach, 2006). An advantage of the chemical picture method over the physical picture method is that the chemical picture method can model complicated plasmas and thus achieve numerically smooth thermodynamical properties. The chemical and the physical methods, along with improvements made on them, are discussed in detail in the following subsections including our justification for proposing to use the OPAL EOS over other methods.

There are criteria that a good EOS needs to meet and these include the following. The range of density and temperature grid for calculations to be carried out has to be large. A good EOS has to adapt to stellar composition that can be varied. This implies a good EOS has to cover all stellar regions, from the surface region to the core region. Also, if the EOS uses numerical methods then such methods have to be accurate (Saumon, 1994). This implies the EOS used has to converge with relatively good precision to ensure that all thermodynamic derivatives are calculated smoothly and accurately. Furthermore, when thermodynamic quantities are calculated, there has to be consistency between these quantities. By this we mean that other thermodynamic quantities can be calculated from one thermodynamic potential, which represents the thermo-

dynamic state of a system. Finally, a good EOS has to accommodate mixtures of elements that are deemed to be complex as noted by Saumon (1994). This is done with the inclusion of other chemical elements that are found to be in large abundance. This condition is important for opacity calculations because elements that are heavy are important for opacity calculations, which in turn relies on a good EOS.

1.1.4.1 The EFF EOS

The EFF EOS uses the so called chemical picture method. In this method it is assumed that atoms and ions are in their unperturbed ground states. Furthermore, the EFF EOS ignores the Coulomb interactions and treats heavy elements by assuming they are fully ionised. The advantage of this approach is that different composition for such elements can be easily accommodated (Eggleton et al. 1973). The disadvantage for this EOS is that when used outside its range of validity, it tends to give out unphysical phase transitions (Rogers, 1994). As noted by Lin & Däppen (2012), this EOS has been mainly used in codes used to calculate solar evolution and solar oscillations. This EOS further models processes such as Coulomb correction, pressure ionisation and classical ions. Coulomb correction results from the sum of interacting pairs of charged particles like electrons, nuclei and compound ions (Bi et al. 2000). The EFF method has been presented in an analytic form and thus has advantages over other tabulated EOS methods. Also, this method deals with varying composition and the new physics introduced with relative ease (Swenson & Rogers, 1992). The EFF EOS approach has been used as a simple ideal gas model of the plasma in the interior of the Sun (Bi et al. 2000).

An improved version of the EFF EOS was presented by Swenson, Irwin, Rogers, Eggleton, Faulkner & Flannery (Guzik & Swenson, 1997) and now it is called the SIREFF EOS. It is based on the EFF EOS and includes many changes to the physics used in the EFF EOS. The changes are those found in the OPAL and MHD EOS methods and include amongst others the pressure ionisation treatment. This pressure ionisation is still unusual but is a function of ion density and

electron density as stated by Däppen & Guzik (2000). Furthermore, Däppen & Guzik (2000) state that the parameters that can be adjusted from this pressure ionisation treatment have been determined and standardised. This has been done by comparing the SIREFF EOS to the OPAL EOS for stellar interior variables such as temperature and density. The SIREFF approach models processes such as Coulomb correction, electron exchange, partial ionisation, H_2 molecules, classical ions and does not model quantum diffraction. All the additional physics included are improvements to what EFF EOS was modelling before as noted by Däppen & Guzik (2000). The Coulomb correction mentioned before, comes from the sum of all charged particles such as electrons, nuclei and compound ions interacting. According to Saumon et al. (1999), there is a very strong link between these interactions and bound states. However, when the gas interior particles of the Sun for instance are not strongly coupled this causes the non-ideal effects such as coulomb corrections to change the structure of the Solar interior (Bi et al. 2000).

According to Eggleton (1973) the pressure ionisation does have an effect on this EOS. According to Rogers (1994), this pressure ionisation takes place when the distance between the particles is less than a Bohr distance, thus it is relevant only at high densities. We can also have the partial ionisation state and when this happens it implies that the thermodynamic properties depend on the ionisation state of that gas. For our purpose we have modelled the stellar atmospheres of main sequence A-stars with the OPAL EOS and this EOS includes the partial ionisation. The implication here is that the OPAL EOS may not work particularly well for low optical depths.

Another concept that is included in the EFF EOS is the classical ions. For this concept, we have stable electrons on the background and this is where the thermodynamic functions are calculated. The calculations are done by using a parameter as an independent variable (Bi et al. 2000). To better understand this we can write the following equation

$$\Gamma_j = \Gamma_e Z \tag{1.11}$$

where Γ_e is the classical coupling constant of electrons. This constant is a number that indicates the strength of the force applied during the interaction of electrons. Z is the nuclear charge and

indicates the total charge of all protons in the nucleus. Γ_j is the constant coupling parameter for that particular species j. Another concept included in the EFF EOS is the excitation states effect. This is a purely hydrogen effect and takes place in deeper layers of a star where 90 % of hydrogen is ionised. This is a region where the second ionisation zone of helium is located (Basu et al. 1999). What is important is that the excitation effect uses the most suitable helium abundance in the solar convection zone, so that helioseismic calculations can be done (Basu et al. 1999). Another important thing that is determined by the excitation state is the ionisation balance in star. The quantum diffraction is explained by the Heisenberg's uncertainty relation.

1.1.4.2 The MHD EOS

The MHD EOS was developed as part of the opacity project and has been widely used in stellar modelling. Its primary workings are also based on the chemical picture method. The free energy minimisation method of the MHD EOS is an algorithm that is based purely on the chemical picture method (Mihalas, Däppen & Hummer, 1988). The procedure in this method is to distinguish particle clusters such as atoms, ions and molecules in a plasma (Mihalas, Däppen & Hummer, 1988). Furthermore, solar models calculated using the MHD EOS have been found to match favourably with Helioseismology results (Yildiz & Kiziloglu, 1997). It was mainly developed to calculate the ionisation degrees of chemical elements. This is deemed to be important for the calculations of radiative opacity (Nayfonov et al. 1999). The physics of the MHD EOS is based on the occupation probability formalism. This formalism was derived by Hummer & Mihalas (1988) and has the internal free energy given by

$$F_{int} = -KTL_n \sum_{\sigma}^{2} N_\sigma \sum_{i} W_{\sigma i} g_{\sigma i} e^{\frac{\varepsilon_{\sigma i}}{KT}}, \tag{1.12}$$

Where F_{int} is the free configurational energy, i covers a wide range for all interior states of species σ_i, n is the total occupation number by a given species, $W_{\sigma i}$ is the occupational probability, $g_{\sigma i}$ is the multiplicity and $\varepsilon_{\sigma i}$ is the energy for a state i. The occupational probability is a measure of how much of the bound states of type i are available to be taken over. This occupational probability ($W_{\sigma i}$) is calculated by linearising $F_{conv}^{\bullet}$ in the free energy equation. This approach

is physically consistent and leads to unvarying free energies as stated by Trampedach et al. (2006). Also, the approach can aid in calculations of different arrangements of species (Nayfonov et al. 1999). For an interaction of neutral particles, the configuration that is used to calculate the occupation probability is that of a spherical gas (See Rogers 1994). Furthermore, Rogers (1994) states that for ion-ion interactions, the occupation probability is calculated by the electric microfield method. This method has been developed from the Stark-ionisation theory where energy levels in an atom split due to an applied electric field. The last configuration used is that of the ion-neutral, where the occupation probability is a combination of the neutral particle configuration and the ion-ion interaction configuration.

What is significant for our purpose is that the MHD EOS has been restricted to stellar envelopes where the densities are relatively moderate and not exceeding $\rho \sim 10^{-2}\ g.cm^{-3}$. The study of Helioseismology has put tight constraints on the EOS and the MHD EOS has fared well with slight discrepancies when compared to the inference from observations (Mihalas & Hummer, 1988). Some of these discrepancies were reduced by the OPAL EOS. However, it has been the better matching of MHD EOS to observational data for the outer parts of the Sun ($\frac{r}{R_\odot} \geq 0.97$) than OPAL EOS that has been striking. Furthermore, Nayfonov et al. (1999) compared the differences between squared sound speed determined from inversion of oscillation data and the Standard Solar Model computed using MHD and OPAL. From this, the OPAL EOS was found to be a better fit to data than the MHD for $0 \leq r \leq 0.97\ R_\odot$. One of the advantages of the MHD EOS over the OPAL EOS has been its inclusion of the hydrogen molecules (H_2, H_2^+ and H^-) which implies that the MHD EOS is valid for temperatures lower than the OPAL tables. Our calculations in Chapter 3 confirm this because we were unable to use the OPAL EOS for $T_{eff} < 6500$ K. The MHD EOS has also been valid for stars with mass as low as 0.4 $M_\odot$ whereas the OPAL EOS tables have been valid for stars with a minimum mass of 0.8 $M_\odot$ (Däppen & Guzik, 2000).

Furthermore, comparison of the MHD tables and OPAL tables shows that the tables used in the MHD EOS are based on Grevesse & Noels (1991) composition and contain elements such as He, C, N, O and Ne, where Ne represents all other elements. These elements are also used in OPAL EOS tables. One can thus compare the EOS used, based on these compositions. For example, the new solar abundance by Asplund et al. (2009) lowers the metallicity and halves the oxygen content, which is one of the most abundant in the Sun. The effect this has on the EOS is that γ_1 of the OPAL EOS is more sensitive to metal content than the MHD EOS.

The MHD EOS models include several effects in their calculations such as Coulomb correction, pressure ionisation, partial ionisation, classical ions, non-relativistic electron degeneracy, excited states, electron exchange and quantum diffraction. In addition, elements such as H_2, H_2^+ and elements in the excited states are included in the composition. The partial ionisation serves the purpose of measuring how energy flows along the layers of a star. This ionisation is also responsible for pulsations in a star. The non-relativistic electron degeneracy occurs at high densities with a temperature that is decreasing. This implies atoms or ions are close enough that quantum mechanical effects become important. This causes a complicated EOS that requires a simple form governed by several factors. The factors include amongst others the thermal energy that is smaller than electron rest energy and relativistic electrons that are degenerate completely. The Coulomb correction is mainly due to the sum of the all particles that interact, according to Bi et al. (2000) this is described by the Debye-Huckel approximations. According to Guenther et al. (1992), the MHD EOS has contributed to Astrophysics by giving a good description of the atomic physics.

1.1.4.3 The Activity Expansion Method that developed OPAL EOS

One of our interests lies in understanding the physical processes involved in the OPAL EOS hence we have outlined the physics involved in this method. This approach involves one viewing the system with respect to its fundamental constituents of electrons and nuclei as stated by Däppen & Guzik, 2000). As will be discussed shortly, such an arrangement in the OPAL EOS was de-

veloped on the basis of the grand canonical partition function. This function is a theoretical assembly of a system with a steady shape while the energy and the number of particles in such a system changes. Furthermore, according to Rogers et al. (1996) composite particles which includes ions, atoms and molecules also come into effect in this widely known 'physical picture' method of OPAL EOS.

Traditionally, a neutral gas in physics has pressure expanded as a sum of two-body and even three-body clusters of species. This extends to plasmas as well, in spite of the Coulomb potential introducing complications. An example of such complications is that the quantum nature of electrons results in the degeneracies and exchange corrections (Rogers et al. 1996). Fundamentally, this leads to atoms being stripped of electrons.

The electrons and the ions interact attractively and this results in divergence over a short distance. The electrons and ions then cluster in groupings. In analysing this system for electrons, the level population for electrons reached through OPAL EOS may be given in terms of the W_{ij} factors of the Opacity Project (OP), where W is the probability of an electron occupying a certain level, i is the number of electrons that are bound to that level and j is the energy level (Seaton & Badnel, 2004). In comparison with the Opacity Project the OPAL opacity project has a much bigger population of species in significantly high excited states (Seaton & Badnel, 2004). This strongly suggests that the use of OPAL EOS requires quantum mechanical methods (Däppen & Guzik, 2000). These are methods based on the calculations of chemical structure by using Schrodinger equations.

We can discuss the activity expansion method to see how the activity is used to set up the calculations of pressure and density for a hydrogen gas as discussed by Basu et al. (1999). The species interact in a medium that is limited to short distances. The pressure is that of an ideal

gas and it is calculated as follows

$$\frac{P}{K_B T} = \sum_{n=1}^{\infty} Z^n b_n, \tag{1.13}$$

where Z is the activity given by $Z = \lambda^{-3} e^{\frac{\mu}{K_B T}}$ and λ is the wavelength that can be expressed as $\lambda = \frac{h}{\sqrt{2\pi M_e K_B T}}$. Also, from equation (1.13) the symbol b_n indicates particle states with $n = 2$ representing two particle state and $n = 3$ representing three particle states. The physical picture is normally realised with the unmovable chemical potential acting as an independent variable. From this, the density and the number abundance follow as dependent quantities (Charbonnel et al. 1999) To calculate the density we start by differentiating equation (1.13) with respect to Z, in doing this we proceed as follows,

$$\frac{\partial P}{\partial Z} = K_B T \left(1 + 2Z b_2 + 3Z^2 b_3\right), \tag{1.14}$$

we then divide by $K_B T$ and multiply both sides of equation (1.14) by Z and consequently arrive at the following equation

$$\rho = \frac{Z}{K_B T}\left(\frac{\partial P}{\partial Z}\right) = Z + 2Z^2 b_2 + 3Z^3 b_3 \cdot \tag{1.15}$$

When we have an increase number of terms in the activity expansion, this consequently results in a orderly expansion in the density.

The activity expansion method further involves a numerical inversion before the thermodynamic quantities are expressed in their natural variables such as temperature, density and particle numbers. The limited number of OPAL EOS tables can be attributed to the computation time which is quite significant while modelling stars more massive than $0.8 M_{\odot}$. The review we have discussed here, is based on different components of plasmas such as the electrons and nuclei (Rogers, 1994). We can summarise the activity expansion method that sets up the OPAL EOS by mentioning the following key physical steps;

- The method begins from the standard multicomponent arrangement, this arrangement is a complete one with all possibilities of species (electrons and ions) arrangements.

- The terms can be collected again leading to screened cluster co-efficients as in equation (1.13).
- At this stage the classical Boltzmann factors can be restored in the standard multicomponent arrangement.

1.1.4.4 The OPAL EOS Tables

The OPAL EOS and OPAL opacities have been used to model stars. The first tables produced with a high quality grid were the 1996 OPAL EOS tables (see Rogers, Swenson & Iglesias, 1996). This is in comparison to the 1994 OPAL EOS tables by Rogers (1994). The OPAL EOS tables have primarily been used to model the envelope of stars. These are regions of stellar interiors in which we can still find atoms. The atoms are not disturbed by the sorrounding plasma (Seaton et al. 1994). The OPAL EOS tables cover a wide range in mass and include low mass stars. In spite of Charbonnel et al. (1999) having had challenges in using the OPAL EOS tables for less massive stars than 0.8 $M_{\odot}$, the tables have been made available for main sequence stars with mass greater than 0.1 $M_{\odot}$ (Rogers & Nayfonov, 2002). Also, the range in temperature-density is quite broad, thus aiding in studies of main sequence stars with masses greater than 0.8 $M_{\odot}$. In addition the same EOS data can be used for more massive stars. These massive stars are usually made up of significantly more non-ideal plasmas (Rogers & Nayfonov, 2002). The physics that drives this method is that of the interaction of nuclei and electrons due to a Coulomb potential. The interaction is widely known as the grand canonical ensemble of these species (Rogers, 1994). According to Seaton & Badnel (2004) this ensemble uses interpolation methods that can be explained by concepts of corresponding states. By corresponding states, we mean clusters of electrons and nuclei and electrons corresponding to ions, atoms and molecules (Trampedach et al. 2006). The OPAL opacities and the EOS were developed at the Lawrence Livermore National Laboratory by Iglesias & Rogers (1996), also see Rogers & Iglesias (1992) and Iglesias et al. (1992) for more insights. A detailed EOS has proved necessary for the evaluation of occupation numbers used in opacity calculations. These opacity calculations done with OPAL have aided

us in advancing the theoretical models of stars. This has been done by providing EOS data that is consistent with the already available opacity tables as hinted by Rogers et al. (1996). Furthermore, the role that has been played by OPAL EOS tables in helioseismology studies has been that of providing highly accurate thermodynamic derivatives (χ_T & χ_ρ) of the EOS. However, Lin & Däppen (2012) caution that the use of the pre-tabulated tables has disadvantages. Some of the disadvantages include the interpolations in the tables introducing errors and that the chemical compositions used have to be in line with the tables used at that time. For instance, according to Turcotte et al. (1998) the OPAL EOS could not be used to curb the shortcoming of the EFF EOS in handling the coulomb correction due to the fixed composition it has with the tables.

What is vital for this type of EOS as emphasised by Rogers et al. (1996) is that a large part of the stellar interior is largely made up of multicomponent plasmas. To evaluate such stellar regions one would expect the EOS to cover a significant range of temperature and density for different stellar compositions. The differences in composition includes elements that are heavier than Neon and are not dominant over the EOS results. The OPAL EOS tables cover the hydrogen mass fraction of typical range $0 \leq X \leq 0.8$ and the metallicity with ranges $0 \leq Z \leq 0.04$. In addition, the calculations of OPAL EOS include several quantum processes such as pressure ionisation, non relativistic Fermi-Dirac electrons, all stages of excitation and ionisation, degenerate Coulomb corrections, quantum electron diffraction, electron exchange and terms arising from ladder diagrams of quantum theory (Trampedach et al. 2006). When electrons interact with aligned and anti-aligned spins, this results in the energy difference hence we have the electron exchange energy (Guzik & Swenson, 1997). The results of the EOS calculations is a table which has temperature-density ranges of $3.7 \leq \log T \leq 8$ and $-14 \leq \log \rho \leq 4.9$. These ranges are shown in **Figure 1.2**.

When calculating the OPAL EOS we use an auxiliary code for interpolation in temperature (t_6),

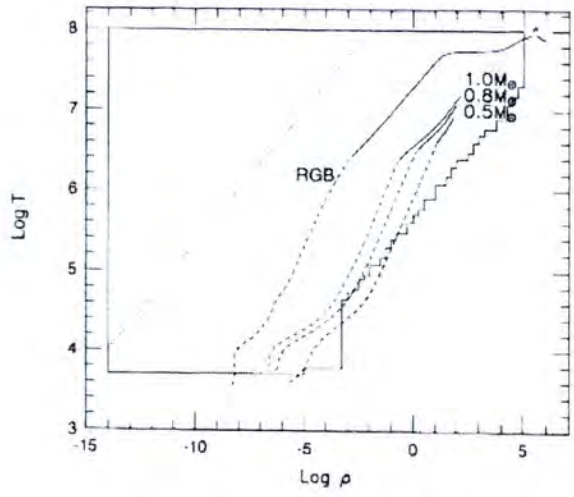

Figure 1.2: A plot showing the temperature-density range covered by the OPAL EOS tables. The model tracks for stars of mass 0.5 $M_{\odot}$, 0.8 $M_{\odot}$, 1.0 $M_{\odot}$ and a RGB star are also shown. The solid line is for purely radiative stars while the dashed lines indicate convective stars. Taken from Rogers et al. (1996)

density (ρ), composition (X) and the metallicity (Z). The interpolation used here does not often result in errors that are significant. Any error that may arise will be one closer to the edges of the range of tables that are being used. Another method that is used by the OPAL approach is that it makes use of a single configuration wavelengths functions. This means for example that a single electron has its orbital calculated using potentials that are arranged experimentally. This results in a good matching with energy level data (Seaton & Badnel, 2004). **Figure 1.2** shows the OPAL EOS data tables produced for astrophysical applications. The application shown is that of the stellar evolutionary tracks for three stars of masses 1.0 $M_{\odot}$, 0.8 $M_{\odot}$, 0.5 $M_{\odot}$ and a RGB star. More importantly, the tabulated data for temperature as a function of density can be used for calculating various second order quantities such as temperature exponent and the density exponent (Rogers et al. 1996). Furthermore, points to the left of the dotted line lying in the ranges -14 $\leq \log \rho \leq$ -2 and 4.0 $\leq \log T \leq 8$ may not be in local thermodynamic equilibrium As shown in **Figure 1.2**, stars with masses $\leqslant$ 0.8 $M_{\odot}$ fall outside the temperature and density

range over part of their tracks. The models presented are convective and radiative. The solid line indicates a star that is radiative and the dashed line indicates a star that is convective. By dividing the tracks into radiative and convective stars, it is shown that the OPAL opacity tables can extend to stars below $\leqslant 0.8$ $M_{\odot}$. The jagged edge towards the high densities and low temperatures has been attributed to an attempt that was made to limit the plasma conditions due to weak electron coupling, where Rogers et al. (1996) are confident that the physics used is well within the limits of validity.

Rogers (1981) states that the sequence that has been in use to evaluate the new EOS tables should be more accurate for stellar tracks with masses $M \geqslant 0.3$ $M_{\odot}$ while decreasing for less massive stars. There are errors accounted for in OPAL pressure calculations. The highest degree in error that can be reached by the OPAL method for non-ideal pressure calculations should be smaller than 5 % for parts that are non-ideal when one looks at the M=0.3 $M_{\odot}$ track (Rogers & Nayfonov, 2002).

According to the results of the evolutionary tracks models for low mass stars by Di Criscienzo et al. (2010), the OPAL EOS was found to be a good estimate in a wide temperature-density regions for low mass stars. However, Rogers et al. (1996) had difficulties in extending the tables to much higher temperatures of the order 10^9. This was due to pair production being a significant factor. OPAL interpolated data has been found not to be smooth and a need for tabulation of data on a more finely spaced temperature-density grid has been suggested. Also, the tables of Rogers et al. (1996) could not be extended to much lower temperatures below 5000 K due to numerical problems encountered when the electron density falls to very low values. The OPAL EOS tables provide the following outputs:

- Pressure
- Internal Energy
- Entropy

- Thermodynamic variable (temperature exponent), $\chi_T = (\frac{\partial \log P}{\partial \log T})_\rho$
- Thermodynamic variable (density exponent), $\chi_\rho = (\frac{\partial \log P}{\partial \log \rho})_T$
- The first adiabatic exponent, $\Gamma_1 = (\frac{\partial \log P}{\partial \log \rho})_S$
- The pressure derivative at constant entropy, $\frac{\Gamma_2}{\Gamma_2 - 1} = (\frac{\partial \log P}{\partial \log T})_S$
- The temperature derivative at constant entropy, $\Gamma_3 - 1 = (\frac{\partial \log T}{\partial \log \rho})_S$
- The specific heat capacity at constant volume, $C_V = (\frac{\partial E}{\partial T})_V$

From these outputs, the specific heat capacity at constant pressure can be calculated as.

$$C_P = \frac{P}{\rho T}\frac{{\chi_T}^2}{\chi\rho} + C_V, \tag{1.16}$$

and the adiabatic temperature gradient as

$$\nabla_{ad} = \frac{\Gamma_3 - 1}{\Gamma_1} = \frac{\Gamma_2 - 1}{\Gamma_2}. \tag{1.17}$$

The derivations in the following subsections, are for the OPAL EOS treatment.

1.1.4.5 Thermodynamical Properties of Matter

The laws of thermodynamics are fundamental in the work carried out in the stellar interiors, this is according to Cox & Giuli (1968). The assumption made in calculating the thermodynamic quantities is that there should be complete ionisation (Stoltmann & Blocker, 2000). Furthermore, thermodynamic variables are made available by a well defined system. This system includes the pressure, the internal energy, the density exponent and isocronic specific heat (Stoltmann & Blocker, 2000). The isocronic specific heat is evaluated with the volume kept constant. Other thermodynamic quantities such as the Isobaric specific heat and the adiabatic gradient can be determined from the temperature exponent and the density exponent. The isobaric process for a specific heat is determined in the pressure and volume range. This process connects the initial and final statistical states. When this happens there could be an expansion or compression, depending where the expansion mode goes to. The significance of determining all these thermodynamic quantities is that we will in all likelihood model a star accurately. The star modelled,

will have different physical conditions under different evolutionary stages. Stoltmann & Blocker (2000) have provided a base system which can be used to derive and determine other thermodynamical quantities. When modelling stars, it is a necessity to compute all thermodynamic quantities.

For our research work, the thermodynamics properties for the OPAL EOS are continuous functions of temperature and density. For our computational task we have used the OPAL EOS tables, the ATLAS9 programme and we relied as well on analytic formulae. For example the formulae of specific heat capacity (C_p) that will be derived shortly proved useful as it had the accuracy of producing similar profiles between OPAL EOS and ATLAS9 EOS. The importance of this thermodynamic variable (C_p) is that they aid our understanding of degree of ionisations for stellar matter (Stoltmann & Blocker, 2000). The specific heat of a system in general terms is the amount of heat (dQ) that must be included to a system in order to raise the temperature (T) of the system. In other words the specific heat is given by

$$C_\alpha = \left(\frac{dQ}{dT}\right)_\alpha , \tag{1.18}$$

where α is the constant of differentiation (Cox & Giuli, 1968). The small heat gain by dQ is given by

$$dQ = dE + PdV, \tag{1.19}$$

which is also called the first law of thermodynamics. The specific heats at constant pressure (C_p) and volume (C_v) have been the most widely used and they are both given by the following respective equations

$$C_p = \left(\frac{dQ}{dT}\right)_p , \tag{1.20}$$

$$C_v = \left(\frac{dQ}{dT}\right)_v . \tag{1.21}$$

When a system that is being described is complex, additional conditions must be included to make the specific heat meaningful (Cox & Giuli, 1968). For a system that is not complex, the

specific heat hold its meaning. This is done with a condition that all the numbers N_i for each particle are held constant. To carry out the derivations of thermodynamic variables we have assumed the system to be simple. Furthermore, the system has states that are evaluated by other state variables in P, V and T. Using equation (1.19) and the volume per unit mass given by $V = \frac{1}{\rho}$ we easily show that the first law of thermodynamic may be written as

$$dQ = dE + Pd\left(\frac{1}{\rho}\right). \tag{1.22}$$

now differentiating the second part of this equation, we can also show that

$$dQ = dE - \frac{P}{\rho^2}d\rho. \tag{1.23}$$

To give an expression for the specific heat at constant volume, we recall the form that is assumed by the internal energy per mole of a non degenerate gas, hence we can write the specific heat capacity given by equation (1.21) as follows,

$$C_v = \left(\frac{dQ}{dT}\right)_v = \left(\frac{\partial E}{\partial T}\right)_v = \frac{dE}{dT}. \tag{1.24}$$

This specific heat capacity according to Cox & Giuli (1968) does not usually change significantly for a gas that is non-relativistic and non-degenerate. The specific heat at constant pressure (C_p) can be determined as follows. We consider a gas with temperature and pressure to be independent variables. Differentiating the EOS for an ideal gas we deduce the following equation

$$d(PV) = PdV + VdP = RT, \tag{1.25}$$

where R is the universal gas constant. In re-arranging the above equation, we can equate the resulting equation to equation (1.19) as follows

$$d(PV) - VdP = PdV = dQ - dE, \tag{1.26}$$

but $dE = C_v dT$, this implies the above equation becomes

$$d(PV) - VdP = dQ - C_v dT. \tag{1.27}$$

Equation (1.27) can be re-arranged as follows

$$dQ = d(RT) - vdP + C_v dT, \tag{1.28}$$

and finally we arrive at

$$dQ = dT(R + C_v) - VdP, \tag{1.29}$$

dividing throughout by dT, we get

$$\frac{dQ}{dT} + V\frac{dP}{dT} = (C_v + R),$$

for constant pressure we have $\frac{dP}{dT}$ being zero. Also, recalling that $\frac{dQ}{dT}$ is the specific heat capacity at constant pressure. The above equation can finally be re-written as

$$C_p = C_v + R. \tag{1.30}$$

We can further express the specific heats with respect to the unit mass. To do this we proceed as follows, we recall equation (1.23) given by

$$dQ = dE - \frac{P}{\rho^2}d\rho,$$

The energy of the specific heats can be expressed as a function of pressure (P) and temperature (T) respectively. Therefore we can re-write the above equation as follows

$$dQ = \left(\frac{\partial E}{\partial P}\right)_T dP + \left(\frac{\partial E}{\partial T}\right)_P dT - \frac{P}{\rho^2}d\rho, \tag{1.31}$$

where $d\rho$ can be expressed as

$$d\rho = \left(\frac{\partial \rho}{\partial P}\right) dP + \left(\frac{\partial \rho}{\partial T}\right) dT,$$

substituting this in equation (1.31), we now have

$$dQ = \left[\left(\frac{\partial E}{\partial P}\right)_T dP + \left(\frac{\partial E}{\partial T}\right) dT\right] - \left[\frac{P}{\rho^2}\left(\frac{\partial \rho}{\partial P}\right)_T dP + \left(\frac{\partial \rho}{\partial T}\right)_P dT\right]. \tag{1.32}$$

opening the brackets and collecting like terms we can easily show that

$$dQ = \left[\left(\frac{\partial E}{\partial P}\right)_T - \frac{P}{\rho^2}\left(\frac{\partial \rho}{\partial P}\right)_T\right] dP + \left[\left(\frac{\partial E}{\partial T}\right)_P - \frac{P}{\rho^2}\frac{\partial \rho}{\partial T}\right] dT, \tag{1.33}$$

We can now divide throughout by dT to get the following equation

$$\frac{dQ}{dT} = \left[\left(\frac{\partial E}{\partial P}\right)_T - \frac{P}{\rho^2}\left(\frac{\partial \rho}{\partial P}\right)_T\right]\frac{dP}{dT} + \left[\left(\frac{\partial E}{\partial T}\right)_P - \frac{P}{\rho^2}\frac{\partial \rho}{\partial T}\right]\frac{dT}{dT},$$

It can be noted that $\frac{dP}{dT}$ is zero again at constant pressure and $\frac{dQ}{dT}$ is C_P, this means we finally end up with the following equation

$$C_P = \frac{dQ}{dT} = \left(\frac{\partial E}{\partial T}\right)_P - \frac{P}{\rho^2}\left(\frac{\partial \rho}{\partial T}\right)_P, \tag{1.34}$$

From the expression derived above for the specific heat at constant pressure, C_p, we can first express the derivatives $\left(\frac{\partial E}{\partial T}\right)_P$ and $\left(\frac{\partial \rho}{\partial T}\right)_P$ in another convenient form. This is done with a view to relate the specific heats C_P and C_V. Cox & Giuli (1968) writes latter expression on equation (1.34) as,

$$\frac{\partial \rho}{\partial T} = -\frac{\rho}{T}\frac{\chi_T}{\chi_\rho}, \tag{1.35}$$

with

$$\chi_T = \left(\frac{\partial \ln P}{\partial \ln T}\right)_v, \tag{1.36}$$

and

$$\chi_\rho = -\left(\frac{\partial \ln P}{\partial \ln V}\right)_T, \tag{1.37}$$

where equation (1.36) is the temperature exponent and equation (1.37) is the density exponent. and this is the pressure equation of state. The derivative $\left(\frac{\partial E}{\partial T}\right)_P$ in equation (1.34) can be changed into another form as follows. With the energy, $E(P(\rho, T), T)$ as a pure function of Pressure (P) as noted by Cox & Giuli (1968). We can then express the change in energy as

$$dE = \left(\frac{\partial E}{\partial P}\right)\left[\left(\frac{\partial P}{\partial \rho}\right)_\rho d\rho + \left(\frac{\partial P}{\partial T}\right)_\rho dT\right] + \left(\frac{\partial E}{\partial T}\right)_P dT, \tag{1.38}$$

dividing by dT and simplifying we can re-write this equation as

$$\left(\frac{\partial E}{\partial T}\right)_\rho = \left(\frac{\partial E}{\partial P}\right)_T \left(\frac{\partial P}{\partial T}\right)_\rho + \left(\frac{\partial E}{\partial T}\right)_P, \tag{1.39}$$

We can re-write equation (1.39) as follows

$$\left(\frac{\partial E}{\partial T}\right)_P = \left(\frac{\partial E}{\partial T}\right)_\rho - \left(\frac{\partial E}{\partial P}\right)_T \left(\frac{\partial P}{\partial T}\right)_\rho, \tag{1.40}$$

also, recalling equation (1.34) given by

$$C_P = \frac{dQ}{dT} = \left(\frac{\partial E}{\partial T}\right)_P - \frac{P}{\rho^2}\left(\frac{\partial \rho}{\partial T}\right)_P, \tag{1.41}$$

we can substitute equation (1.35) in equation (1.41), to get the following equation

$$C_P = \left(\frac{\partial E}{\partial T}\right)_P - \frac{P}{\rho^2} - \frac{\rho}{T}\left(\frac{\chi_T}{\chi_\rho}\right) \tag{1.42}$$

This equation then simplifies to

$$C_P = \left(\frac{\partial E}{\partial T}\right)_P + \frac{P}{\rho T}\left(\frac{\chi_T}{\chi_\rho}\right), \tag{1.43}$$

and using equation (1.40) in equation (1.43) we get the following equation

$$C_P = \left(\frac{\partial E}{\partial T}\right)_\rho - \left(\frac{\partial E}{\partial P}\right)_T \left(\frac{\partial P}{\partial T}\right)_\rho + \frac{P}{\rho T}\left(\frac{\chi_T}{\chi_\rho}\right), \tag{1.44}$$

recalling the specific heat at constant volume ($C_v = \left(\frac{\partial E}{\partial T}\right)$) and substituting in the above equation, we finally have

$$C_P = C_V - \left(\frac{\partial E}{\partial P}\right)_T \left(\frac{\partial P}{\partial T}\right)_\rho + \frac{P}{\rho T}\left(\frac{\chi_T}{\chi_\rho}\right), \tag{1.45}$$

from equation (1.45)

$$\left(\frac{\partial E}{\partial P}\right)_T \left(\frac{\partial P}{\partial T}\right)_\rho = -\frac{E}{T}\left(\frac{\partial \ln E}{\partial \ln \rho}\right)\frac{\chi_T}{\chi_\rho}, \tag{1.46}$$

as highlighted by Cox & Giuli (1968), we have

$$\frac{\partial \ln E}{\partial \ln \rho} = \frac{P}{\rho E}\left(\chi_T - 1\right) \tag{1.47}$$

this implies equation (1.46) becomes

$$\left(\frac{\partial E}{\partial P}\right)_T \left(\frac{\partial P}{\partial T}\right)_\rho = -\frac{E}{T}\left(-\frac{P}{\rho E}\right)\left(\chi_T - 1\right)\frac{\chi_T}{\chi_\rho} \tag{1.48}$$

Substituting equation (1.47) and (1.48) in (1.45), we then have

$$C_P = C_V - \left(\frac{-E}{T}\left(\frac{P}{\rho E}\left(\chi_T - 1\right)\frac{\chi_T}{\chi_\rho}\right)\right) + \frac{P}{\rho T}\frac{\chi_T}{\chi_\rho}$$

this equation reduces to

$$C_P = C_V + \left(\frac{P}{T\rho}\left(\chi_T - 1\right)\frac{\chi_T}{\chi_\rho}\right) + \frac{P}{\rho T}\frac{\chi_T}{\chi_\rho} \tag{1.49}$$

opening the brackets and simplifying the right hand side of equation (1.49) we can easily show that

$$C_P = C_V + \frac{P}{\rho T}\frac{\chi_T^2}{\chi_\rho} \tag{1.50}$$

The adiabatic exponents are important in our understanding of questions related to the stellar interiors. For example there are different roles played by Γ_1, Γ_2 and Γ_3, with Γ_1 aiding in our understanding of the dynamical instability concept. Γ_2 helps in studies of convective instability and Γ_3 helps in studies of pulsation instability. For the adiabatic exponents, we recall that from the first law of thermodynamics a relationship exists between differentials such as dP, dT and $d\rho$. The relation shared by these differentials for an adiabatic are explained by the adiabatic exponents.

$$\Gamma_1 = \left(\frac{d\ln P}{d\ln \rho}\right)_{ad}, \tag{1.51}$$

and the third adiabatic exponent is given by

$$\Gamma_3 - 1 = \left(\frac{d\ln T}{d\ln \rho}\right)_{ad}. \tag{1.52}$$

where the subscript *ad* indicates that the derivatives are calculated for the adiabatic case. There is a general relationship between all the gammas and this relation is given by

$$\frac{\Gamma_1}{\Gamma_3 - 1} \equiv \frac{\Gamma_2}{\Gamma_2 - 1} \tag{1.53}$$

This implies that when at least two of the gammas are known the other one may be determined. Furthermore, when the EOS is described, only one gamma from the three gammas may not depend on the other two. In this case, the EOS is specified when χ_ρ and χ_T are known. From this the known gamma may aid in determining the other unknown gammas.

1.1.4.6 How OPAL EOS are calculated

The OPAL group developed both the EOS tables and the opacity tables. The difference between the two is that the formats used are different because the data that is used in the OPAL method is usually tabulated in the temperature (T_6) and density (ρ). The EOS tables have been developed from the previously established updated EOS and EOS plus tables (Rogers et al. 1996). The data is tabulated for various stellar compositions. For instance the elements heavier than helium (Z) can take values Z=0.0, Z= 0.02 and Z=0.04 and those composed of hydrogen can take values X=0.0, X= 0.2 , X= 0.4, X= 0.6 and X= 0.8. The hydrogen table is available as well at X= 1.0 and Z=0.0. The interpolation is done as follows, we have a data file that could be represented by IEOS002Z08X.gz, where Z= 0.02 and X=0.8. Furthermore, there are codes used to interpolate the data and one of the codes is named Z-interp-IEOS.f that creates the file IEOSdata.gz. This data is subsequently interpolated in X, T_6 and ρ for a fixed value of Z. This is done by the code Z-interp-IEOS.f. Test calculations have been done to verify the validity of the interpolation. The derivatives of the EOS tables have often been calculated with a thin temperature and density grid (Rogers et al. 1996). The problem that arose before has been the large amount of time required to calculate the hydrogen and heavier elements mixtures.

1.2 ATLAS9 Program

ATLAS9 is a FORTRAN computer program that is used to calculate stellar model atmospheres or modify a pre-existing model. This program models stellar atmospheres in both the radiative and the convective equilibrium. These models are produced for a wide range of stellar effective temperatures and surface gravities. According to Kurucz (1970), the atmosphere modelled is subject to several approximations which include plane-parallel, steady state, horizontally homogeneous, non moving atmospheres with energy and the respective abundances not changing with respect to the depth inside a star. By plane parallel we mean that the thickness of the photosphere is much smaller than the radius of that star and the surface gravity is relatively

constant in the entire photosphere. By steady state we mean that the stellar properties remain constant with respect to time and the homogeneity implies physical quantities change with optical depth only. According to Kirby (2011) the ATLAS9 model atmosphere starts with Opacity Distribution Functions (ODFs). The importance of using the grids of stellar models is that we will determine the stellar observations and their basic parameters as stated by Trampedach et al. (2013). Furthermore, the atmosphere of the star, the evolutionary stage and the oscillation properties of a star are important for studying the complicated nature of stars (Cugier, 2012).

The approximations mentioned above mean that the atmosphere is relatively stable with no outburst activities like stellar winds on the stellar photosphere. Furthermore, the atmosphere can be used to computationally calculate synthetic spectra as it has been presented by Kurucz (1979) and Kirby (2011). However, we should be mindful as well that it is computationally expensive to generate a stellar spectrum. Researchers have instead adopted an approach of investing the computational resources upfront by generating a grid of synthetic spectra (Kirby, 2011). Additionally, in ATLAS9, the hydrostatic equation is determined using known tables of Rosseland mean opacity for a specific temperature, gas pressure and fixed abundances (Stutz, 2005). In order to carry out the calculations in our ATLAS9 models, we have used grids for models with 400 plane parallel layers. Our models were calculated with convection switched off.

Kurucz (1970) explains in detail the physics that has resulted in the FORTRAN source codes used in ATLAS9. Hence using ATLAS9 requires one to have a good understanding of the physics that forms the fundamental basis of the codes. The physics involved has remained unchanged for a number of years with the exception of more opacity lines added. The ATLAS9 program has over the years produced synthetic spectra that compare well with spectroscopic observations (see Kirby 2011). The ATLAS9 routines are often amended by the user and for our purposes, once modified successfully, ATLAS9 will aid in our quest for matching model atmosphere to those of the envelope. ATLAS9 has been deemed as the last version before ATLAS12 that solves models with the opacity distribution function (Castelli, 2005). The models are restricted to certain

abundances and micro-turbulent velocities. These are used in calculating the pre-tabulated line opacities (Castelli, 2005).

The ATLAS9 program has also played a role in calculating line by line (LL) models of stellar atmospheres. The role has been that of providing main program blocks that use direct treatment of the opacities (Stutz, 2005). This results in accurate description of the line absorption. Furthermore, such program blocks have been useful in the development of new software packages. This software determines atmospheres and Local Thermodynamic Equilibrium (LTE) models for young stars and intermediate types. The LTE models are often considered good estimates for photospheres of stars that do not have significantly high temperature or large dimensions. According to Shulyak et al. (2004) this was done with the LL method that computes opacity effects. Also, ATLAS9 calculates the line opacity using ODFs and this makes computation easier to handle as noted by Meszaros et al. (2012). The LL MODELS atmosphere code has routines developed to investigate and calculate opacity line by line. By line by line we mean calculating the line absorption using a very accurate wavelength grid. What we can get out of this method is a spectrum that is shown with finer details. Furthermore, the LL MODELS atmosphere code has routines developed to investigate the visible patterns in the stellar atmosphere for peculiar A-Stars (Stutz, 2005).

The models that will be implemented for our purpose will be radiative. The significance of this as Kurucz (1970) argues is that the radiative field may be determined. A benchmark that has been used for a good model is that the model has to converge to a constant smaller flux error and the conservation of the radiation equilibrium. For our purpose, we have tested convergence by doing 15 iterations and checking the difference in the flux and flux derivative for the last two iterations. We did more iterations when the criterion for convergence was not met. The first criterion has been deduced not to be sensitive to temperature variations for the optically thin layers (Stutz, 2005). The A-stars we have modelled seldom infringed the convergence criteria which means their atmospheric parameters agreed to an extend with ATLAS9's adoption of hy-

drostatic equilibrium (Kirby, 2011). The ATLAS9 programme can treat the convection process by using the Mixing Length Theory (MLT) with $\alpha = 1.25$. Castelli et al. (1997) calculated the other free parameters for the grids used for ATLAS9 models. These are other parameters which include the mixing length parameter l. The other parameters that are examined are those included when the convective flux, convective velocity and efficiency parameters are calculated. Another parameter that can be considered is that when the convective velocity is calculated. According to Castelli (1996) this convective velocity is derived by using the relation between the kinetic energy and work done on convective element. This convective velocity is given by

$$\overline{v} = \sqrt{\frac{k_1 g Q(\bigtriangledown' - \bigtriangledown)}{H_p}}\frac{l}{2} \tag{1.54}$$

from the equation above, k_1 is the free parameter, g is the gravity, $\bigtriangledown'$ is the temperature gradient with respect to the pressure of the convective elements, $\bigtriangledown$ is the temperature gradient with respect to the pressure of the sorrounding matter, H_p is the pressure scale height and Q is given by $\frac{-\delta \ln \rho}{\delta \ln T}$. This parameter regards any work that is separated by frictional forces. For instance the convective flux it is calculated as

$$4\pi H_{conv} = k\frac{L}{H_p}\rho C_p T \overline{v}(\bigtriangledown' - \bigtriangledown) \tag{1.55}$$

where k is the free parameter and it has a value of 0.5 if we look at motion of bubbles in the upward and downward direction. Furthermore, the code incorporates overshooting (Castelli, 2005). In addition, previous studies done by Lester & Neilson (2008) have changed the plane-parallel ATLAS9 routines. This has been done by adding for instance the spherical modification to the radiative transfer region as well as temperature correction. Also, there have been new Opacity Distribution Functions (ODFs) added for a few metallicities calculated. According to Castelli & Kurucz (2004) there have been small changes in a handful number of atomic and molecular data. In practise the model atmospheres are calculated using atlas9mem-newodf.for and the spectra are calculated using atlas9v.for. Therefore, in our modification we had to modify both programs.

1.2.1 ATLAS9 EOS

The equation of state described in this subsection is the type of EOS we have modified, hence we discuss the physics that developed the EOS and the algorithm of our interest. The pressure in the atmosphere is one of the requirements of the EOS. It is therefore fitting, to discuss how it is calculated in the stellar atmosphere as described by the ATLAS9 program.

1.2.1.1 Stellar Variables

A stellar mass element is subject to a particular motion described by the equation

$$\rho\frac{d^2x}{dt^2} = -\frac{dP_{total}}{dx} - \rho g, \tag{1.56}$$

where P_{total} is the total pressure in the atmosphere, ρ is the density, x is the radial distance within a star and g is the surface gravity given by $g = \frac{GM}{R^2}$. The surface gravity is constant since the atmosphere is assumed to be thin with an insignificant mass. With the acceleration on the LHS of equation (1.56) ignored, the hydrostatic equilibrium equation becomes.

$$\frac{dP_{total}}{dx} = -g\rho. \tag{1.57}$$

If the total mass of a star M is an independent variable, we can then multiply both sides of equation (1.57) by $\frac{dr}{dm}$ and re-write equation (1.57) as

$$\frac{dP_{total}}{dM} = g \tag{1.58}$$

The stellar surface region allows us to use the boundary condition, $P_{total} = P_{rad} = 0$ at $m = M$. Then we can easily show that

$$P_{total} = gM, \tag{1.59}$$

This total pressure is given by

$$P_{total} = P_{gas} + P_{turb} + P_{rad}. \tag{1.60}$$

where P_{gas} is the gas pressure, P_{turb} is the turbulent pressure and P_{rad} is the radiation pressure. According to Kurucz (1970), the turbulent effects due to gas motions often cause the turbulent

pressure and this pressure can be calculated as

$$P_{turb} = \frac{1}{2}\rho V_{turb}^2, \tag{1.61}$$

where V_{turb} is the turbulent velocity. The models we produced in this thesis use zero turbulent velocity.

1.2.1.2 Calculating Pressure for a Specific Temperature

In calculating the pressure for a specific temperature, we need an initial temperature estimate. This estimate is for a specific optical depth. After lengthy calculations the total pressure (P_{total}) can be computed as well. The question that may arise is how the initial temperature is estimated. This is done by using the Hofp function for temperature ($T(\tau)$) as done in the ATLAS9 code. In carrying out the derivation we start at the pressure balance equation given by equation (1.57) This equation can be re-written as

$$\frac{dP_{total}}{d\tau} = \frac{g}{\kappa}, \tag{1.62}$$

where τ is the optical depth, κ is the opacity and g is the gravitational acceleration. Before carrying out the integration of equation (1.62), the initial values of $T(\tau)$, $P_{turb}(\tau)$ and $P_{rad}(\tau)$ need to be known. The opacity and optical depths are inferred for regions closer to the surface (Kurucz, 1970). The integration is carried out while being mindful that the pressure and the optical depths change significantly from the top of the atmosphere to the bottom of the atmosphere (Kurucz, 1970). Hence this calls for equation (1.62) to change its form to a logarithm one. This is done by using the logarithm differentiation chain rule to arrive at.

$$\frac{dP_{total}}{d\tau} = \frac{P_{total}}{\tau}\frac{d\ln P_{total}}{d\ln \tau} = \frac{g}{\kappa}, \tag{1.63}$$

multiplying both sides of equation (1.63) by $\frac{\tau}{P_{total}}$, we now have

$$\frac{d\ln P_{total}}{d\ln \tau} = \frac{g\tau}{\kappa P_{total}}, \tag{1.64}$$

We can then use the integration for the stellar surface ($\tau = 0$) to the first τ in the atmosphere layers. In this case κ is assumed to be constant (Kurucz, 1970). The iteration in the opacity

factor (κ) carries on until the difference between new total pressure (P_{total}^{new}) and the old pressure (P_{total}^{old}) is sufficiently small. The mathematical description of this is in the following equation.

$$\left|\ln P_{total}^{new} - \ln P_{total}^{old}\right| \leqslant 0.00005 \tag{1.65}$$

The mass density is calculated by appreciating that the mass density comes from the atomic number density and the mass of each atom. Therefore recalling that by definition the average atomic weight is

$$\mu = \sum X_i M_i \tag{1.66}$$

where X_i is the hydrogen fraction by number and M_i is the mass of each Hydrogen atom. This implies the mass density becomes

$$\rho = N_A \mu M_A \tag{1.67}$$

where N_A is the Avogadro's number, μ is the average atomic weight and M_A is the atomic mass unit.

ATLAS9 also calculates the specific heats at either constant pressure or volume. These specific heats are given by the following equations

$$C_v = \left(\frac{\partial E}{\partial T}\right) \tag{1.68}$$

where E is the energy per unit mass and T is the temperature. The energy is calculated as follows, for a particle of mass m, at a position $x.y$ and z. These are three (3) components and they each contribute $\frac{1}{2}K_B T$. This implies the total energy for the components is given by $\frac{3}{2}K_B T$. The energy due to the radiation pressure is given by $\frac{3}{2}P_{rad}$. The total energy for a given mass is then given by the energy due to the ideal gas, radiation pressure, ground energy and the internal energy (Kurucz, 1970). In an equation form this can be writen as

$$E = \frac{3}{2}\frac{n_{total} KT}{\rho} + \frac{3}{2}P_{rad} + \sum n_i \left[E_i + \left(\frac{d\ln u_i}{d\ln T}\right) kT\right] \tag{1.69}$$

The temperature from ATLAS9 is calculated as follows. We use the Hopf function as an initial estimate to the temperature $T(\tau)$. This initial estimate of temperature is given by

$$T^4 = \frac{3}{4} T_{eff}^4 \left(\tau + q(\tau)\right) \tag{1.70}$$

where T is the temperature, T_{eff} is the effective temperature, τ is the Rosseland optical depth and $q(\tau) = \frac{2}{3}$ for the Eddington law. As stated by Audard et al. (1998) the temperature $(T(\tau))$ relation does not include convection while the radiation factor depends on frequency. The specific heat at constant pressure is given by

$$C_p = \left(\frac{\partial E}{\partial T}\right)_{P_{total}} + \left[\frac{\partial}{\partial T}\left(\frac{P_{total}}{\rho}\right)\right]_{P_{total}} \tag{1.71}$$

where P_{total} is the total pressure and ρ is the density. This equation can then be reduced to

$$C_p = \left(\frac{\partial E}{\partial T}\right)_{P_{total}} - \frac{P_{total}}{\rho^2}\left(\frac{\partial \rho}{\partial T}\right)_{P_{total}} \tag{1.72}$$

These specific heat equations can be further expressed in much convenient way for calculations. For this to be possible we use a mathematical identity which is usually expressed as follows. For variables u, v and y, that identity may be expressed as

$$\left(\frac{\partial f}{\partial u}\right)_v = \left(\frac{\partial f}{\partial u}\right)_y - \frac{\left(\frac{\partial f}{\partial y}\right)_u \left(\frac{\partial v}{\partial u}\right)_y}{\left(\frac{\partial v}{\partial y}\right)_u} \tag{1.73}$$

Now using this identity we can write the specific heat capacity at constant volume as follows

$$\left(\frac{\partial E}{\partial T}\right)_\rho = \left(\frac{\partial E}{\partial T}\right)_P - \frac{\left(\frac{\partial E}{\partial P}\right)_T \left(\frac{\partial \rho}{\partial T}\right)_P}{\left(\frac{\partial \rho}{\partial P}\right)_T} \tag{1.74}$$

Also using the same identity, the specific heat capacity at constant pressure can be calculated as follows

$$C_P = \left(\frac{\partial E}{\partial T}\right)_P - \frac{\left(\frac{\partial E}{\partial P}\right)_T \left(\frac{\partial P_{total}}{\partial T}\right)_P}{\left(\frac{\partial P_{total}}{\partial P}\right)_T} - \frac{P_{total}}{\rho^2}\left[\left(\frac{\partial \rho}{\partial T}\right)_P - \frac{\left(\frac{\partial P}{\partial \rho}\right)_T \left(\frac{\partial P_{total}}{\partial T}\right)_P}{\left(\frac{\partial P_{total}}{\partial P}\right)_T}\right] \tag{1.75}$$

Now when the turbulent pressure is ignored with radiation pressure changing as T^4, this means then

$$\left(\frac{\partial P_{total}}{\partial P}\right)_T = 1 \tag{1.76}$$

The adiabatic temperature gradient is given by

$$\nabla_{ad} = \left(\frac{\partial \ln T}{\partial \ln P}\right)_s = \frac{P_{total}}{T\rho C_p}\left(\frac{\partial \ln \rho}{\partial \ln T}\right)_{P_{total}} \tag{1.77}$$

Density Derivatives are calculated from opacity tables. These tables are pre-tabulated and are included in the Rosseland mean opacity tables.

1.2.2 Limits of ATLAS9 EOS

The modified ATLAS9 version differs with the original ATLAS9 code with respect to the treatment of the physics in both the old ATLAS9 and new ATLAS9. In this section we outline some of the shortcomings endured by the ATLAS9 EOS. These are the limits of the ATLAS9 code for the model atmosphere. According to Kurucz (2005) the code was written by assuming that a star has no waves and no magnetic pressure, to mention just two limitations. Also, the EOS for ATLAS9 does not exist for population I abundances at low temperatures (Kurucz, 2005). Furthermore, the EOS does not consider high ionisation stages for the iron group at extremely high temperatures. Also, the temperature at the bottom of the model is twice or more than the effective temperature with problems encountered for $T_{eff} \geqslant 60\ 000$ K. Unlike the ATLAS9 EOS, the OPAL approach to the EOS is that of using statistical mechanism of relatively ionised plasmas (Cugier, 2012). Also, the OPAL EOS now includes the relativistic degenerate electrons and for our purpose this is vital for the stellar models we have calculated. The previously neglected relativistic corrections in the OPAL 1996 EOS tables have for instance resulted in the over estimation of the Γ_1 variable for stellar central regions (Baturin, 2010). ATLAS9 codes ware primarily created to do near exact physics for near exact observations.

1.3 Stellar Structure Equations

In the subsections that follows we discuss the key role that is played by the EOS in stellar structure equations. We also discuss how other stellar structure equations are derived and how they link to our research work.

1.3.1 Role of the EOS in Stellar Structure Equations

One of the important factors that determine the structure of stars is the balance between the energy that is lost at the surface and the energy produced at the core by nuclear reactions. The balance of the gravitational force and the pressure force is usually referred to as the hydrostatic equilibrium. This balance of forces gives a relation between the pressure gradient and the acceleration due to gravity. Furthermore, there are other important factors that are essential for stellar structure and evolution such as basic physics coupled with equations to explain the dynamics within stars. Consequently, this aids us in our quest of understanding the structure of stars.

The stellar structure is determined by four basic first order differential equations, hereafter referred to as Stellar Structure Equations (SSE). For such equations to be useful for modelling stars, they need to be supplemented by the EOS, knowledge of stellar opacity and the stellar boundary conditions. Theoretical models generally begin by assuming a star to be in a state of hydrostatic equilibrium. Using the basic law of gravity and Newton's second law, we can derive the following SSE as follows. At the centre the temperatures are extremely high and the pressure will inevitably be high. This is illustrated in the following equation as follows.

$$\frac{dP}{dr} = -g\rho, \tag{1.78}$$

where P is the pressure, g is the gravitational acceleration and ρ is the density with the gravitational acceleration given by $g = \frac{Gm}{r^2}$, we can re-write equation (1.78) as

$$\frac{dp}{dr} = -G\frac{M(r)\rho}{r^2}, \tag{1.79}$$

If we assume that $M(r)$ is the independent variable, this implies that the hydrostatic equilibrium condition can be deduced by multiplying equation (1.79) by $\frac{\partial r}{\partial m} = \frac{1}{4\pi r^2 \rho}$. This equation reduces to ;

$$\frac{\partial P}{\partial m} = -\frac{GM}{4\pi r^4}. \tag{1.80}$$

The second SSE is the mass conservation equation and describes how mass varies with the radius

within a star. This equation is given by ;

$$\frac{dM_r}{dr} = 4\pi r^2 \rho. \tag{1.81}$$

From equation (1.81), we can deduce that, the mass contained within the radius r increases from the stellar core to the surface.

The third SSE that will be described is the energy conservation equation. Taking into consideration the energy flow across the sphere with radius r and the total energy generated in the shell, one can then deduce that for the gas to be in thermal equilibrium the radiation loss must be equal to the energy gain generated by nuclear reactions. This leads to the following equation ;

$$\frac{dL_r}{dr} = 4\pi r^2 \epsilon(r)\rho(r), \tag{1.82}$$

where ϵ is the energy generation rate and L_r is the stellar luminosity. What should be noted is that $\epsilon(r)$ applies necessarily only to main sequence stars. When we have a shell burning, $\epsilon(r)$ is non-zero in shells away from the core. From equation (1.82) we can deduce that the energy flow rate L_r increases outwards.

The fourth and final SSE is the energy transport equation which describes how heat naturally flows by radiation and convection from the core to the surface. The equation is given by ;

$$\frac{dT_r}{dr} = -\frac{3}{4ac}\frac{\kappa(r)\rho(r)L_r}{T_r^3 4\pi r^2} + F_C, \tag{1.83}$$

Where T_r describes how the temperature varies as a function of radius in a star, $\kappa(r)$ is the stellar opacity, L_r is the stellar luminosity, a is the radiation constant and F_c is the convective flux. All four SSEs above have four primary variables M_r, P, L_r and T_r. These variables are all functions of r. The variables P and ϵ are functions of density, temperature and composition. We can then

express the SSEs in terms of a single independent mass variable M_r as follows ;

$$\frac{dr}{dM_r} = \frac{1}{4\pi r^2 \rho}, \tag{1.84}$$

$$\frac{dp}{dM_r} = -\frac{GM_r}{4\pi r^4}, \tag{1.85}$$

$$\frac{dL_r}{dM_r} = \epsilon(T, \rho, X_i), \tag{1.86}$$

$$\frac{dT_r}{dM_r} = -\frac{3}{4ac}\frac{\kappa L_r}{T_r^3 16\pi^2 r^4} + \frac{F_c}{4\pi r^2 \rho}, \tag{1.87}$$

we now have four differential equations with five variables, r, P, L_r, T and ρ. Thus the system of equations is unclosed and depends on ϵ and κ. To close the system one needs to relate at least two of the variables. This then calls for the EOS as it relates P, ρ and T. For our purpose, we make use of OPAL project for tables of EOS.

1.3.2 Physics of the Stellar Pulsations

The radial and non radial oscillations of a star that pulsates are due to the sound waves that resound within a star. Using the diameter of a star we can easily deduce the pulsation period by observing how long it would take a sound wave to go accross this diameter (Carol & Ostli, 1995). The adiabatic sound speed is written as

$$v_s = \sqrt{\frac{\gamma P}{\rho}}. \tag{1.88}$$

where P is the pressure, ρ is the density and γ_1 is the adiabatic exponent. Now recalling that the hydrostatic equilibrium is given by,

$$\frac{dP}{dr} = -\frac{GM_r}{\rho} r^2, \tag{1.89}$$

we can then use this equation to deduce the pressure by assuming the density to be a constant. In equation (1.89) M_r is the stellar mass with radius r, ρ being the density and P is the pressure. Substituting the mass $M{=}\frac{4}{3}\,\pi r^3 \rho$ in equation (1.89), we now have

$$\frac{dP}{dr} = -\frac{(\frac{4}{3}\pi r^3 \rho)\rho}{r^2} = -\frac{4}{3}\pi G \rho^2 r, \tag{1.90}$$

It is now a trivial matter to integrate equation (1.90) by using the boundary condition $P = 0$ at the surface to arrive at the following equation.

$$P(r) = \frac{2}{3}\pi G\rho^2(R^2 - r^2), \tag{1.91}$$

The pulsation period is then given by

$$\Pi \approx 2\int_0^R \frac{dr}{v_s} \approx 2\int_0^R \frac{dr}{\frac{2}{3}\gamma\pi G\rho(R^2 - r^2)}. \tag{1.92}$$

What we can deduce from equation (1.92) is that the pulsation period of a star is inversely proportional to the square root of its mean density (Carol & Ostli, 1995).

1.3.3 Theory of Stellar Oscillations

Stellar oscillations are generally thought of as a perturbation in a fluid. The gas in propagation is considered to be a continuum with its properties being a function of displacement ($\mathbf{r}$) and time ($\mathbf{t}$). When we assume that stellar gas is treated as a continuum, then its properties can be thought of as functions of position $\mathbf{r}$ and time $\mathbf{t}$. The properties include the local density $\rho(\mathbf{r}, \mathbf{t})$, local pressure $P(\mathbf{r}, \mathbf{t})$, other thermodynamic quantities and the local instantaneous velocity $v(\mathbf{r}, \mathbf{t})$, where $\mathbf{r}$ signifies the position vector to an assigned position in space and this representation is what is seen by a stable observer (Aerts et al. 2009). We will use the basic hydrodynamics equations in the following subsections and apply some perturbations.

1.3.3.1 The equation of continuity

The SSE are 1-D version of fluid dynamics equations. Given that the mass is conserved, we can express the continuity equation as

$$\frac{\partial\rho}{\partial t} + div\,(\rho\mathbf{v}) = 0, \tag{1.93}$$

where ρ is the density, $\mathbf{v}$ is the velocity of the fluid and t is the time. The conservation in the equation is seen with the right hand side of the equation having no mass sources. This is the

standard conservation equation where there is an equal rate of change of a quantity in a volume with the flux of the quantity into the volume. Using the time derivative, we can express the continuity equation as

$$\frac{d\rho}{dt} + \rho \, div \, \mathbf{v} = 0 \tag{1.94}$$

Where $\frac{d}{dt}$ is material time derivative. We now consider the time derivative of a quantity ϕ that is expressed when following the motion. We can then write the following equation

$$\frac{d\phi}{dt} = \left(\frac{\partial \phi}{\partial t}\right)_r + \frac{dr}{dt} \cdot \nabla\phi = \frac{\partial \phi}{\partial t} + \mathbf{v}.\nabla\phi, \tag{1.95}$$

1.3.3.2 Equation of Motion

The conditions in the Sun or any other star are governed by a few factors. The factors include the internal friction or viscosity and can be ignored for a real gas. For a given volume of gas we have the surface forces and the body forces that are present. This implies that the equations of motion can be expressed as follows

$$\rho \frac{d\mathbf{v}}{dt} = -\nabla P + \rho \mathbf{f}, \tag{1.96}$$

where $\mathbf{f}$ is the force due to the body forces, P is the gas pressure, ρ is the density and $\mathbf{v}$ is the velocity of the fluid. Using the form taken by equation (1.95), we can then express the equation of motion as

$$\rho \frac{\partial \mathbf{v}}{\partial t} + \rho \mathbf{v}.\nabla \mathbf{v} = -\nabla p + \rho \mathbf{f}. \tag{1.97}$$

In considering Poisson's equation, Christensen-Dalsgaard (2003) examines only the effect of gravity. This implies the role played by the magnetic fields may be ignored with a view of eliminating body forces on the gas. Newton's law expresses the gravity as the force per unit mass. This gravity g can be expressed as the gradient of the gravitational potential (Φ) as seen in the following equation.

$$g = -\nabla\Phi, \tag{1.98}$$

where Φ ensures that Poisson's equation can be expressed as

$$\nabla^2\Phi = 4\pi G\rho. \tag{1.99}$$

1.3.3.3 Energy equations

The first law of thermodynamics is given by

$$\frac{\partial q}{\partial t} = \frac{\partial E}{\partial t} + P\frac{\partial V}{\partial t}, \tag{1.100}$$

where q is the heat gain or loss, E is the internal energy and V is the volume of the gas. We can work our way towards finding the relation between pressure (P) and the density (ρ). As we have done previously, the volume for a unit mass can be expressed as $V = \frac{1}{\rho}$. What equation (1.100) emphasises is that, the heat gained or lost changes the internal energy. Another way of expressing this equation is by using the form of the continuity equation, thus we can re-write it as follows

$$\frac{\partial q}{\partial t} = \frac{\partial E}{\partial t} - \frac{P}{\rho^2}\frac{\partial \rho}{\partial t}, \tag{1.101}$$

and by using the form taken by the continuity equation, equation (1.101) can be further expressed as

$$\frac{\partial q}{\partial t} = \frac{\partial E}{\partial t} + \frac{P}{\rho}\left(\nabla \cdot \mathbf{v}\right). \tag{1.102}$$

By using the thermodynamic formulas, the energy equation can be further expressed as follows

$$\frac{\partial q}{\partial t} = C_v\left[\frac{\partial T}{\partial t} - (\Gamma_3 - 1)\frac{T}{\rho}\frac{\partial \rho}{\partial t}\right], \tag{1.103}$$

$$\frac{\partial q}{\partial T} = C_p\left[\frac{\partial T}{\partial t} - \left(\frac{\Gamma_2 - 1}{\Gamma_2}\right)\frac{T}{P}\frac{\partial P}{\partial t}\right], \tag{1.104}$$

$$\frac{\partial q}{\partial T} = \frac{1}{\rho\left(\Gamma_3 - 1\right]}\left[\frac{\partial P}{\partial T} - \frac{\Gamma_1 P}{\rho}\frac{\partial \rho}{\partial t}\right], \tag{1.105}$$

where C_v and C_p are the specific heat capacities at constant volume and pressure respectively. The first, second and third adiabatic indices are given by

$$\Gamma_1 = \left(\frac{\partial \ln P}{\partial \ln \rho}\right)_{ad}, \frac{\Gamma_2 - 1}{\Gamma_2} = \left(\frac{\partial \ln T}{\partial \ln P}\right)_{ad}, \Gamma_3 - 1 = \left(\frac{\partial \ln T}{\partial \ln \rho}\right)_{ad}. \tag{1.106}$$

1.3.4 3-Dimensional Oscillations in Stars

Part of the following argument is taken from Aerts et al. (2009). Stars have 3 dimensions and this implies their characteristic oscillation modes are described by nodes in 3 perpendicular directions. The directions include the distance r to the centre , the co-latitude θ and the longitude ϕ. The co-latitude θ is measured with respect to the pulsation pole and this pole is the axis of symmetry. For a star that is symmetric, the solutions to the equations of motions with displacements along the (r, θ, ϕ) directions are expressed as

$$\xi_r(r, \theta, \phi) = a(r)\Upsilon_l^m(\theta, \phi)\exp(-i2\pi\nu t), \tag{1.107}$$

$$\xi_\theta(r, \theta, \phi, t) = b(r)\left(\frac{\partial\Upsilon_l^m(\theta, \phi)}{\partial\theta}\right)\exp(-i2\pi\nu t)\partial\theta, \tag{1.108}$$

$$\xi_\phi(r, \theta, \phi, t) = \frac{b(r)}{\sin\theta}\left(\frac{\partial\Upsilon_l^m(\theta, \phi)}{\partial\varphi}\right)\exp(-i2\pi\nu t)\partial\phi, \tag{1.109}$$

Where the displacements are given by ξ_r, ξ_θ, ξ_ϕ and a_r, b_r are the amplitudes and ν is the oscillation frequency. The symbol $Y_l^m(\theta, \phi)$ is the spherical harmonics and it is expressed as.

$$Y_l^m = (-1)^m\sqrt{\frac{(2l+1)(l-m)!}{4\pi(l+m)!}}P_l^m(\cos\theta)\exp(im\phi), \tag{1.110}$$

where $P_l^m(cos\theta)$ is the Legendre polynomial given by the following equation.

$$P_l^m(\cos\theta) = \left(1-\cos^2\theta\right)^{\frac{m}{2}}\frac{d^m P_l(\cos\theta)}{d\cos\theta^m}. \tag{1.111}$$

1.3.5 Radiative Stellar Envelope

High mass stars generally have a convective envelope at the core, followed by a radiative envelope that usually extends to the surface. The significance of this envelope is that many observed properties such as T_r and L_r have been determined by the nature or the state the radiative envelope assumes. The mass (M) and the Luminosity (L) are treated as constants in the radiative envelope since most of the mass and the luminosity are contributed by the interior regions of a

star. The optical depth increases towards the inner core region and virtually becomes zero at the surface. A similar argument can be put forward for the variation of temperature with the optical depth. This is with the exception that the temperature does not fall to zero at the surface. The flux radiation that causes the temperature gradient is expressed as follows

$$F_\nu = -\frac{4\pi}{3}\frac{1}{\kappa_\nu \rho}\frac{\partial B_\nu}{\partial r} = \frac{L_\nu}{4\pi r^2}, \tag{1.112}$$

where ρ is the density, κ_ν is the opacity over frequency and B_ν is the Planck function. The radiation pressure is given by

$$P_{rad_\nu} = \frac{4\pi}{3}B_\nu. \tag{1.113}$$

Equation (1.112) and equation (1.113) can be integrated over the frequency as follows. From equation (1.113) by adding $\frac{d}{dr}$ on both sides we have

$$\frac{dP_{rad}}{dr} = \frac{d}{dr}\left(\frac{4\pi}{3c}B_\nu\right), \tag{1.114}$$

this equation can simply be arranged as

$$\frac{dP_{rad}}{dr} = \frac{dB_\nu}{dr}\left(\frac{4\pi}{3c}\right). \tag{1.115}$$

Going a step back we realise that equation (1.112) can be re-writen as

$$-\frac{4\pi}{3}\frac{1}{\kappa_\nu \rho}\left(\frac{\partial B_\nu}{\partial r}\right) = \frac{L_\nu}{4\pi r^2}, \tag{1.116}$$

and multiplying by $\frac{3}{4\pi}$ throughout we obtain

$$\frac{\partial B_\nu}{\partial r} = \frac{-3}{16\pi^2 r^2}L_\nu \kappa_\nu \rho, \tag{1.117}$$

finally we sub equation (1.117) in equation (1.115) to arrive at the following equation.

$$\frac{dP_{rad}}{dr} = -\frac{\kappa \rho L_\nu}{4\pi r^2 c}. \tag{1.118}$$

The symbol κ is defined by the relation

$$\kappa = \frac{1}{L}\int_0^\infty \kappa_\nu L_\nu d_\nu, \tag{1.119}$$

where L is the frequency integrated luminosity. To obtain an expression for the radiation pressure we can integrate equation (1.118) from the centre of a star to the surface as follows. If we consider some point near the core to be a radius r and the full stellar radius to be R. Then the radiation pressure is equivalent to

$$P_{rad} \approx -\int_R^r \frac{\kappa_\nu \rho L_\nu}{4\pi r^2 c} dr \approx \int_0^\tau \frac{L}{4\pi R^2 c} d\tau, \tag{1.120}$$

upon integrating this equation we have

$$P_{rad} = \frac{L}{4\pi R^2 c}\tau + P_{rad}(\tau = 0), \tag{1.121}$$

recalling that the flux is given by $F = \frac{L}{4\pi R^2 c} = \sigma T_{eff}^4$, equation (1.120) can be reduced to

$$P_{rad} = \frac{\sigma T_{eff}^4}{c}\tau + P_{rad}(\tau = 0), \tag{1.122}$$

we can evaluate the radiation pressure at the optical depth of zero as follows. The relation between the radiation pressure and the density can be described by the following equation.

$$P_{rad} = \frac{2\pi}{c}\int_0^\pi I(\theta)\cos^2\theta \sin\theta \, d\theta. \tag{1.123}$$

What we can deduce from equation (1.123) above is that $I(\theta) = \frac{\sigma}{\pi}T^4$ in the radiative equilibrium. Where the symbol σ is the Stefan Boltzmann constant. For isotropic intensity we have

$$P_{rad} = \frac{4\sigma T^4}{3C}, \tag{1.124}$$

for all outgoing angles it is reasonable to assume that $I(\theta)$ is isotropic for angle θ in ranges $0 < \theta < \frac{\pi}{2}$. However, $I(\theta)$ is zero for angles $\frac{\pi}{2} \leqslant \theta \leqslant \pi$. This prompts us to conclude that our star does not allow any radiation from the outside to go through. This implies that equation (1.123) can be reduced to

$$P_{rad}(\tau = 0) = \frac{2\pi}{3C} I(\tau = 0), \tag{1.125}$$

and this is at the surface where $\tau = 0$. The intensity can be computed by evaluating the net flux at the surface. We then determine the net flux at the surface in our bid to evaluate the intensity at this region. This is determined as follows.

$$L = 4\pi R^2 2\pi \int_0^{\frac{\pi}{2}} I(\tau = 0)\cos\theta \sin\theta \, d\theta, \tag{1.126}$$

we then use the u substitution method to evaluate the integral. With $\sin\theta = u \Rightarrow du = \cos\theta\, d\theta$. The integral then becomes

$$I = \int_0^{\frac{\pi}{2}} I(\tau = 0) u\, du = I(\tau = 0)\pi, \tag{1.127}$$

therefore equation (1.126) becomes

$$L = 4\pi R^2 2\pi I(\tau, 0) \tag{1.128}$$

from equation (1.127) $\Rightarrow I(\tau = 0) = \frac{L}{4\pi R^2}$ and incorporating the condition $I(\tau = 0)$ in it, we can easily show that equation (1.125) becomes

$$P_{rad}(\tau = 0) = \frac{2\pi}{3C}\frac{L}{4\pi R^2} = \frac{2}{3C}\sigma T_{eff}^4, \tag{1.129}$$

and recalling that

$$P_{rad} \approx \frac{\sigma T_{eff}^4}{C}\tau + P_{rad}(\tau = 0), \tag{1.130}$$

we can substitute equation (1.129) in (1.130) to arrive at the following equation

$$P_{rad} \approx \frac{\sigma T_{eff}^4}{C}\tau + \frac{2}{3C}\sigma T_{eff}^4, \tag{1.131}$$

taking out the common factor $\frac{\sigma T_{eff}^4}{C}$, we then have

$$P_{rad} = \frac{\sigma}{C} T_{eff}\left(\tau + \frac{2}{3}\right), \tag{1.132}$$

recalling that $P_{rad} = \frac{4}{3}(\frac{\sigma T^4}{C})$, we can then equate this radiation pressure to equation (1.132). Now solving for the temperature (T), we arrive at the following equation

$$T^4(\tau) = \frac{1}{2} T_{eff}^4\left(\frac{3}{2}\tau + 1\right) \tag{1.133}$$

1.3.6 Radiative Transfer Equations

Part of the following discussion is taken from Kippenhahn (1994). The specific intensity is given by $I = I(r, \theta, \phi)$. On the other hand, the mean intensity is given by

$$J_\lambda = \frac{1}{4\pi}\int_{\omega} I_\lambda d\omega, \tag{1.134}$$

where I_λ is the specific intensity and ω is the solid angle. For a spherical body with area $A = 4\pi r^2$, the luminosity is given by

$$L = \sigma T_{eff}^4 4\pi r^2, \tag{1.135}$$

The Eddington flux H is given by

$$H = \int_\omega \mu I \frac{d\omega}{4\pi} = \frac{F}{4\pi}. \tag{1.136}$$

From equation (1.135) and (1.136), we can easily show that

$$L = 16\pi r^2 H \tag{1.137}$$

and using the product rule to differentiate, we can derive

$$\frac{dL}{d\tau} = 32\pi^2 RH + 16\pi^2 R^2 \frac{DH}{d\tau}. \tag{1.138}$$

Also, recalling that $H = \frac{\partial}{\partial\tau} \int \mu I \frac{d\omega}{d\pi}$ and using our knowledge of planar geometry with

$$\mu \frac{\partial I}{\partial \tau} = (I - S). \tag{1.139}$$

We will arrive at the following equation. Where equation (1.139) is the radiative transfer equation in the plane-parallel atmosphere.

$$\frac{dH}{d\tau} = \int \mu \frac{\partial I}{\partial \tau} d\omega, \tag{1.140}$$

1.3.7 Diffusion Approximation

A spherical star has its luminosity given by

$$L = 4\pi r^2 F, \tag{1.141}$$

where F is the flux and $4\pi r^2$ is the area. The photons moving out along the stellar envelope are somewhat obstructed by opacity. The radiative transfer is diffusive in nature and the following reasons account for this assertion. To start with, the temperature gradient is the driving mechanism for the transfer of energy. This is primarily the reason we have the radiative energy

transfer showing a diffusive nature. The Fick's law is deployed to fully describe how photons diffuse through the stellar material. The diffusion of particles is given by j= $-\nabla n D$, where D is the diffusion co-efficient and n is the particle density. This diffusion co-efficient D is given by

$$D = \frac{1}{3} v l_p,$$

where v denotes the velocity and l_p is the mean free path. If we consider the transfer of energy inside a star, we have the proton flux F, the velocity of the particle increased to the speed of light c. The mean free path now takes the form $\frac{1}{k\rho}$, where k is the collisional cross section for the photon path and ρ is the density of the material. The proton flux is therefore given by

$$F = c\nabla n \frac{1}{3}\frac{1}{k_p}, \tag{1.142}$$

The local thermal equilibrium is assumed for the stellar envelope structure and this implies the star radiates perfectly as a blackbody. We then represent the number density of photons by the integrated Planck function given by

$$B(T) = \frac{4acT^3}{\pi}, \tag{1.143}$$

where a is the radiation constant, c is the speed of light and T is the temperature. Now differentiating the above equation leads to

$$\frac{dB}{dT} = \frac{\partial T}{\partial r} 4acT^3, \tag{1.144}$$

where $aT^3 \approx n$. The radiation density constant has a numerical value of $a = 7.566\times10^{-15} erg.cm^{-3}.k^{-4}$

$$\nabla n = \frac{\partial u}{\partial r} = 4aT^3 \frac{\partial T}{\partial r}, \tag{1.145}$$

now recalling that the luminosity is given by $L = 4\pi r^2 F$, we then substitute equation (1.142) in this equation to arrive at the following equation.

$$L(r) = 4\pi r^2 \left(c\nabla n \frac{1}{3}\frac{1}{k_p} \right), \tag{1.146}$$

and now using equation (1.145) we have

$$L(r) = 4\pi r^2 \left(-\frac{1}{3} c \frac{1}{K_p} 4aT^3 \frac{\partial T}{\partial r} \right), \tag{1.147}$$

and finally this equation can be re-written as

$$\frac{\partial T}{\partial r} = \frac{3L(r)k_p}{16\pi r^2 acT^3}. \tag{1.148}$$

1.3.8 Radial Pulsation Equations

The radial pulsation equations can be derived by using the Lagrangian perturbations to the equilibrium equations. We can also take the horizontal perturbations to be zero. For the reader's purpose, the derivations are extended fully by Christensen-Dalsgaard & Frandsen (1983). The following equations show the significance of the equilibrium models in stellar pulsations.

$$\frac{d\delta r}{dr} = -\frac{\delta\rho}{\rho}, \tag{1.149}$$

$$\frac{d}{dr}\left(\frac{\delta P}{P}\right) = \frac{\rho}{P}\left[g\frac{\delta P}{P} + \left(\omega^2 - \frac{dg}{dr} - 4\pi G\rho\right)\delta r\right], \tag{1.150}$$

$$\frac{d\delta H}{dr} = \rho B\kappa_a\left[\left(\frac{4i\omega\,\nabla_{ad} - \omega_R\,\triangle_c\,(\kappa_a P + \rho_p)}{i\omega - \omega_R(4 - \triangle_c(\kappa_a T + \rho_T))}\frac{\delta P}{P}\right) - \frac{i\omega + \omega_R\,\triangle_c\,(\kappa_a T + \rho_T)}{i\omega - \omega_R(4 - \triangle_c(\kappa_a T + \rho_T))}\frac{\delta T}{B} - \frac{\triangle_c\delta\kappa_R}{\kappa_R}\right] \tag{1.151}$$

$$\frac{d\delta\kappa}{dr} = -\rho\kappa_R\left[\frac{\delta\kappa_R H}{\kappa_R} + \delta H\right]. \tag{1.152}$$

Where δ indicates the Lagrangian-Perturbation. The symbols used in the above equations can be defined as follows; B is the Planck function, C_P is the specific heat at constant pressure, δ is the Lagrangian perturbations, $\triangle_c = (\frac{J}{B}) - 1$ and $\omega_R = \frac{4\pi\kappa_R}{C_P T}$, where ω is the angular pulsation frequency. Equation (1.149) is perturbation of equation (1.96). Equation (1.150) is perturbation of equation (1.96) while equation (1.151) and (1.152) result from perturbation to radiative transfer equation. Where $\frac{\delta\rho}{\rho}$ is the perturbation in density and $\frac{\delta\kappa_R}{\kappa_R}$ is the perturbation in opacity, These expressions are given by

$$\frac{\delta\rho}{\rho} = \rho_T\frac{\delta T}{T} + \rho_P\frac{\delta P}{P} \tag{1.153}$$

$$\frac{\delta\kappa_R}{\kappa_R} = \chi_{aT}\frac{\delta T}{T} + \chi_{aP}\frac{\delta P}{P} \tag{1.154}$$

From equation (1.154), the opacity derivatives can be expressed as follows $\chi_{aP} = \left(\frac{\partial \ln P}{\partial \ln \kappa_R}\right)_T$ and $\chi_{aT} = \left(\frac{\partial \ln T}{\partial \ln \kappa_R}\right)_\rho$. The Density Derivatives at constant pressure and temperature can be obtained from the EOS.

1.4 The Matching Code

This code models stellar envelopes from the bottom of atmosphere to the stellar envelope and has been described in Mguda (2010). More importantly though, it will be used to match model atmospheres based on our modified ATLAS9 program to the envelope models calculated using OPAL opacity and EOS tables. It uses several inputs and they include the effective temperature and gravity as is the case in ATLAS9. The code uses Clayton's model (see Clayton 1986) to calculate the envelope models by using the ATLAS9 inputs. It then calculates the temperature using $T(\tau)$ for all the layers starting from the bottom of the atmosphere. The code further calculates the opacity (κ) and density (ρ) using OPAL opacity and OPAL EOS. In addition, the optical depth and the radial distance for the envelope can be calculated.

The code is useful in determining the structure of the envelope and it needs a starting density value for one to produce a model. The derivative of the Planck function with respect to the optical depth can then be calculated and the stellar structure equations for the envelope solved. This can be readily achieved as follows, for a given metallicity the OPAL EOS tables require the temperature and pressure to calculate density. The OPAL opacity tables require metallicity, temperature and density in order to calculate opacity and opacity derivatives. This implies the opacity and the density structure throughout the star can be derived. This will in turn be useful in solving the equations of the stellar envelope.

1.4.1 Helioseismology

The high temperatures and densities at the stellar core imply that the EOS for high temperatures can be solved theoretically. The theoretical calculations have been improved by Helioseismology studies which test the EOS for such extreme conditions (Lin & Däppen, 2005). For our purpose, when modelling stars using Helioseismology we need a smooth, consistent and valid EOS. Similarly, accurate thermodynamic quantities are required for an extended range in temperature and density (Trampedach et al. 2006).

Helioseismology is a study concerned with oscillations of waves inside the Sun and it also allows researchers to calculate parameters that determine the solar interior structure as noted by Christensen-Dalsgaard et al. (2005). This according to Basu & Antia (2008) enables good tests for solar model calculations. The parameters include the temperature, composition, mass, angular momentum and motions in much deeper layers of the Sun and these parameters do have an effect on the oscillations periods. Solar oscillations detected have been particularly useful by providing the frequencies of the Sun and consequently determining the properties of the Sun. Furthermore, the Solar Oscillations frequencies can be inverted to establish the inner structure of the Sun (Basu & Christensen-Dalsgaard, 1997). The properties include different evolutionary stages, metal abundances, effective temperatures and gravities (Samadi et al. 2003). Solar like oscillations have also been found in other stars, although having a different evolutionary phase and metallicities (Samadi et al. 2003). These are oscillations that are small with finite lifetimes. This study does not only put constraints on the thermodynamic quantities but it also checks how accurate theoretical models are in hot dense plasmas (Gong et al. 2001).

The oscillations are generated by processes in the main convective regions and they get excited in the inner layers of the Sun while moving through the plasma medium. On the surface things are slightly different as these waves appear as oscillations that are either up or down. Such oscillations are observed by the phenomenon of Doppler shift of spectrum lines (*Astro.phys.au.dk*)

Solar oscillations were discovered by Leighton et al. (1962) in the 1960s. The observations carried out resulted in analysis of the dopplergrams and the findings highlighted oscillations which could determine certain properties in the atmosphere. Furthermore, Leighton et al. (1962) emphasised that the oscillations could be excited in the granulation layer of the Sun thus explaining the energy transported from the convection zone to the chromosphere (Kosovichev, 2005). Further findings from these observations were that the Sun mainly had oscillations in the Doppler velocity with periods of about 5 minutes.

The question that often arises is, why do we have interest in the Sun as a case study? To date, the Sun has been well studied due to its close proximity and consequently we receive far more light from the Sun, than other distant stars. Furthermore, the Sun is one of the very few stars whose dynamics and magnetism can be studied in great detail (Rozelot & Neiner, 2011). The justification put forward makes the Sun a far more reliable star to collect data from and instantly use the results thereof in other studies such as Astereoseismology.

On the more scientific observation front, the Sun has been well observed by various telescopes around the world. There have been several findings from these observations which include the Sun pulsating simultaneously with about a million different tones. The tones are determined at very high accuracy and the significance of many of these tones is that we can determine the internal properties of the sun, which can in turn be compared with the computer models for the structure of the Sun (*Astro.phys.au.dk/*). According to Bachall et al. (1995), for one to have results in agreement with observational evidence provided by helioseismology studies, it is fundamental not only to have accurate input physics but also accurate treatment of element diffusion along with the solar structure. What is significant for our purpose is that, the unknown uncertainties in the structure of the outer layers of the Sun along with the opacities and the EOS do account for the observed p-modes and the frequencies of these modes (Guenther et al. 1996). Also according to Guenther et al. (1992), the physical location of the surface convection zone has been computed with the aid of Helioseismology studies.

1.4.2 Astereoseismology

This study is concerned with probing the interior of other stars aside from our parent star, as it was the case with the Helioseismology studies. The study primarily uses oscillations in these stars as well. By applying data on these stellar oscillations we can advance our knowledge of

stellar structure and evolution as noted by Aerts et al. (2009). Thus, this study is one of the foundation for our understanding of the nature of the universe. The structure and evolution of stars can be determined by using the light given off at the stellar surface to map the nature of the internal structure as well as any physical changes that a star may undergo. Furthermore, astereoseismic research studies present the likelihood of examining the physical properties of matter in stars. The properties that have been tested in detail include the opacity and the EOS (Christensen-Dalsgaard & Däppen, 1992). Also, it may be possible as well to evaluate properties of the inner stellar rotation and further discover proof for large scale internal magnetic fields.

The foundation of Astereoseismology has been the asymptotic theory of stellar oscillations because the properties of modes of oscillations can be better understood by this theory. The theory also aids in our understanding of the relation between the structure of a star and its oscillation frequency. The inner stellar structure is accountable for the deviations from this asymptotic theory.

A part of the following case study is courtesy of Astro.phys.au.dk/KASC/seismology/seism.html. In our bid to fully examine the internal structure of stars we use the pulsating stars as a means to study the internal properties of stars. Pulsating stars have been studied to establish the reasons and the manner in which other types of stars pulsate. Additionally, the pulsations are mainly used to find the basic meaning of the general properties of these stars. These stars have their brightness, size and temperature changing in a periodic manner with time. They are often divided into classes that correspond to the manner in which they oscillate. For instance, those that fall under the same class of pulsating stars resemble each other physically. In further categorising these stars, it has been noted that different groups of pulsating stars are found across the Hertzsprung Russel diagram (HR diagram). On the observational front, the pulsations for distant stars have been modelled with space missions such as the MOST and COROT in 2003 and 2006 respectively. Another useful mission deployed is the Kepler satellite, which allows us to

probe even deeper layers. This is done in our bid to study pulsations as well as determine stellar matter properties that govern the internal structure of other stars. What we hope to achieve in the future for Astereoseismology studies is improved understanding of our knowledge of stellar structure and evolution (Soriano & Vauclair, 2010).

1.4.2.1 roAp Stars

The equilibrium models that we seek to calculate will be used to model pulsations in A-stars. In this section we give an outline of the properties of pulsating stars that can be modelled by our models. Model atmospheres are important in explaining the observations of real stars. The acronym roAp stands for rapidly oscillating 'A peculiar' stars. They are termed 'peculiar' because their composition on the surface is due to atomic diffusion (Aerts et al. 2009). They burn hydrogen in the core and have a mass of ≈ 2 $M_{\odot}$. These stars were discovered by Kurtz (1982) who established that these stars have amplitudes of up to 0.01 mag peak to peak in the blue wavelength region for five of their class members. These are stars found in the upper main sequence region and they are known to pulsate in non-radial p-modes of high overtone (Martines & Kurtz, 1995). The roAp stars can be characterised by being magnetic and chemically peculiar main sequence stars. The number of known roAp stars is known to be at around 40 and all these stars have many periodic variations that agree with high order and low degree p modes (Aerts et al. 2009). The κ excitation mechanism has been shown to have limits when exciting high frequency modes of these stars (Di Mauro, 2012).

Their temperatures ranges from the bottom of the cooler instability strip up to and even beyond the hot temperature region (Wolff, 1983). The roAp stars produce magnetic, spectrum, photometric and radial velocity variability with similar time period in a given star. These velocity variations are explained by the model known as the oblique rotator. This model assumes that the spectral peculiarities began in spots of irregular abundance of the stars' surface as noted by Martines & Kurtz (1995). The pulsations and magnetic axis are aligned and inclined with respect

to the axis of rotation as hinted by Di Mauro (2012). The importance of studying pulsations for these stars is that we can determine amongst others, the stellar rotation periods, magnetic geometries, luminosities, masses, radii and magnetic fields as stated by Kurtz (1990).

1.4.2.2 δ Scuti Stars

These are stars with a spectral type of A0 to F5 and they typically have masses in ranges $1.5M_{\odot}$ to 2.0 $M_{\odot}$. The δ Scuti stars are best know for showing very strong rich spectra of oscillations. These stars have a short pulsating period, typically with ranges from one and half to 8 hours. They pulsate in p-modes thus enabling us to probe the stellar envelope (Grigahcence et al. 2010). The short pulsation periods account for their small radii but there are many of these pulsating variables in the Milky Way Galaxy, second only to white dwarfs. For stars of population I, the amplitudes of pulsations are known to be small with visual amplitudes found to be a few m mag. However, this can reach a maximum of about 800 m mag (Breger, 1995). The Sun has quite a number (1000) of pulsation modes occurring at the same time for a good number of pop I δ Scuti stars. This makes them particularly good nodes compared to the δ Scuti stars at only 15. They have a mass of about $2M_{\odot}$ and their location on the HR diagram is along the main sequence or just after this band (Dziembowski & Pamjatnykh, 1991). Like the roAp stars these stars are also driven by the κ mechanism which occurs in the He II ionisation zone as noted by Grigahcence et al. (2010)

Their evolution spans from pre-main sequence, to the hydrogen burning on the main sequence and finally to the giant stage (Breger, 1995). These stars have been known to be the best targets for Astereoseismology. The primary classification that has been adopted for these stars often stems from two factors which are Pulsation amplitudes and metal abundances. The effect of pulsation amplitudes is that large amplitude stars are subject to radial pulsations. They also oscillate in one strong mode at a given time (Breger, 1995). Their low amplitude counterparts are main or post main sequence stars with significantly larger periods. These stars are specifically useful for Astereoseismology studies, as they have abundant mixtures of radial and non-radial p-mode

candidates, which can be used for carrying out studies of Astereoseismology. The significance of studying such stars is that the results of parameters such as temperature, luminosity, mass and composition can be applied on evolutionary theories or used on other stars.

1.4.2.3 γ Doradus Stars

The γ Dor type of star has been well studied from its member class. They were discovered to be changing in luminosity by Cousins & Waren (1963) and Cousins (1966) because of their non radial pulsations at the surface. These stars are found to be in the range F0 and their luminosities ranges from V, VI to IV. According to Kaye et al. (1999) their absolute magnitude is the same as that of δ Scuti stars although with a cooler surface temperature. They also have similar masses in ranges 1.25 $M_{\odot}$–2.5 $M_{\odot}$. When one looks at their location on the HR diagram, they extend with δ Scuti stars on the H-R diagram but have much higher pulsation periods in comparison to the δ Scuti stars. The γ Doradus stars also have convective cores, lower depth in their envelopes and they spin quite fast as highlighted by Grigahcence et al. (2010). Progressively, this star according to Eyer et al. (2001) emerged as the prototype of a new-class of stars that pulsate. The light curve of a γ Doradus and its dual periodicity is conducive for some pulsations that have a period greater than the anticipated one for a δ Scuti star (Kaye et al. 1999). In the last ten years or so, there have been 40 variable stars that show similar spectral types and Luminosity classes to δ Doradus. Furthermore, the variability they produce is for time ranges of an order of magnitude slower. They are the type of stars that show changes in luminosity because of the radial and non radial pulsations they have at the surface.

In the last two decades, the existence of a fairly new class of variables has been found in main sequence early type F-stars (Balona et al. 1994). These stars have periods that vary for a handful of hours. What we can conclude from this is that these periods are significantly larger than can be considered belonging to P-mode pulsation characteristic of δ Scuti stars. The g-modes similar to those in the Sun have been found on the γ Doradus variables though on the back of challenges such as these modes reaching the stellar surface with lower amplitudes (Grigahcence

et al. 2010). The significance of this is that the g-modes detection allows us to study the stellar core. According to Balona et al. (1994) most of these stars are not well understood as their nature remains a mystery. Balona et al. (1996) made good photometric and spectroscopic studies of δ Doradus and their findings were one additional frequency domain for these stars. These findings were preceded by the proposal made by Balona et al. (1994) of γ Dor being an associate of a new class of non-radial gravity- mode pulsators. Cousins (1992) alludes to a lot of variations being explained by making some assumptions. The assumptions are sinusoidal variations having periods of $P = 0.7570$ and $P = 0.7334$. These periods according to Balona et al. (1994) do not signify any data and there is a large uncontrolled variability.

1.4.2.4 Normal Main Sequence A-stars

These are the type of stars we seek to model. The main sequence stars are the type of stars undergoing fusion of hydrogen into helium. Our Sun is an example of a main sequence star. Stars are classified into groups according to their spectra. The classification that has been adopted is that of using the letters O, B, A, F, G, K and M, this sequence is easily remembered by astronomers as "Oh Be A Fine Girl Kiss Me". The O stars being the hottest stars and other successive letters being progressively cooler stars towards M type stars. The group of stars we define here are called A stars. These are stars with spectra defined by strong hydrogen balmer absorption lines. As mentioned in the preceding section, the ATLAS9 programme has been widely used to model the atmospheres of main sequence A stars. Some of these stars have waves inside and detecting these waves allows us to determine the properties of the interior of stars (Aerts et al. 2009). This is due to these waves being sensitive to regions of stars they travel through. Furthermore, the waves travel through the different parts of the star. Hence we model these stars, attempting to build an equilibrium model which can be used in studies of oscillations in A stars. The mass ranges for A-stars is widely known to be $1.4\ M_{\odot} \leq M \leq 2\ M_{\odot}$ and they have effective temperatures of $6500\ K \leq T_{eff} \leq 10\ 000\ K$.

The hotter main sequence A-stars have been known to have a radiative atmosphere as one moves from the mid A-stars towards the cooler F stars (Adelman, 2004). It is further stated in Adelman (2004) that convection begins to play a role in the energy transport in the atmosphere at effective temperatures below 7500 K. The main sequence A-stars falling within the instability strip on the HR diagram will have pulsations and thus be used for studying stellar pulsations and equilibrium models. About 30 % of A-stars in the instability strip are known to pulsate. Some of the A-stars may be pulsating in amplitudes that are below the detection threshold and as a result they are not yet detectable as pulsators.

However, in the temperature ranges of 7000 K$\leq$ T_{eff} $\leq$ 30 000 K we find the families of chemically peculiar (CP) stars. According to Preston (1974) there are four distinct groups based primarily on their abundance anomalies amongst other criteria. The CP1 class has non-magnetic and slow rotating metallic line (am) stars having temperature ranges of 7400 K $\leq$ T_{eff} $\leq$ 10200 K. The CP2 have temperature ranges of 7400 K $\leq$ T_{eff} $\leq$ 23000 K. Hence we can see that A-stars can fall in the CP1 and CP2 classes. The CP1 stars are often called the Ap stars. The CP2 generally have a flux depression around 5200 $\AA$. For observation purposes this feature can be detected photometrically (Stutz, 2005).

Recent studies have tackled shortcomings that have to do with model atmosphere with specific abundances to individual elements. This has particularly occurred in these chemically peculiar stars where stratification of elements needs to be taken into account. This is due to the spectra of these stars having a distribution of abundance that is vertical (Shulyak et al. 2004). The CP1 stars span a wide range in temperatures covered in ATLAS9 atmosphere model hence we have modelled this type of A-stars.

Chapter 2

A Comparison of OPAL EOS and ATLAS9 EOS

In this Chapter we compared thermodynamic variables calculated using OPAL EOS with the ATLAS9 EOS with a view of probing the feasibility of our research work. Comparing the two EOSs is an important part in our attempt to develop accurate stellar equilibrium models we plan to use in calculating pulsation frequencies. The comparison has been done by first producing an ATLAS9 model atmosphere for a certain range of temperature and surface gravities. The temperature and pressure used are taken from ATLAS9 model atmosphere. We also specified the composition by using a fixed mass content of hydrogen, helium and all other elements heavier than helium to be solar. All the calculations were carried out for the hydrogen mass fraction, $X = 0.7381$, Helium mass fraction, $Y = 0.2485$ and the heavy metals, $Z = 0.0134$ for the solar composition (Asplund et al. 2009). The temperature ranges used were 7000 K $\leqslant T_{eff} \leqslant$ 9500 K. The surface gravities ranges were $3.5 \leqslant \log g \leqslant 4.5$. This covers essentially the Normal Main sequence A-Stars.

For a given composition ($Z = 0.0134$) corresponding to solar composition, we used ATLAS9 to calculate model atmospheres for T_{eff} and log g described above. This gave us $T(\tau)$ and $P(\tau)$

which we used as input to the OPAL interpolation routines to obtain the following variables;

- density (ρ).
- The first adiabatic exponent (Γ_1).
- The third adiabatic exponent ($\Gamma_3 - 1$).
- Adiabatic temperature gradient ($\bigtriangledown_{ad}$).
- The specific heat capacity (C_P) at constant pressure.

These were then compared with similar variables from the ATLAS9 program itself. Comparisons of these quantities are presented in the following sections. ATLAS9 program gives output of the following thermodynamic variables;

- Γ_1
- Specific Heat Capacity (C_P) at constant pressure.
- $\bigtriangledown_{ad}$
- Radiative temperature Gradient ($\bigtriangledown_{rad}$).
- The density derivative at constant pressure $(\frac{d\log\rho}{d\log T})|_P$
- The density derivative at constant temperature $(\frac{d\log\rho}{d\log P0})|_T$

To make relevant comparisons, we had to convert the specific heat capacity at constant volume (C_v) to C_p using the formula

$$C_p = C_V + \frac{P}{\rho T}\frac{\chi_T^2}{\chi_\rho}, \tag{2.1}$$

where χ_T is the temperature exponent in the pressure equation of state and it is given by;

$$\chi_T = (\frac{\partial \ln P}{\partial \ln T})\,|_\rho, \tag{2.2}$$

and χ_ρ is the density exponent in the pressure equation of state and it is given by;

$$\chi_\rho = (\frac{\partial \ln P}{\partial \ln \rho}) \mid_T \cdot \tag{2.3}$$

The $\Gamma_3 - 1$ function is not calculated in ATLAS9 and for good comparisons, we had to convert $\Gamma_3 - 1$ using the formula

$$\Gamma_3 - 1 = \Gamma_1 \ \nabla_{ad} \cdot \tag{2.4}$$

2.1 Density

In **Figures 2.1–2.4**, we present plots of density for the ATLAS9 model atmosphere and the OPAL EOS routines. The density was calculated using ATLAS9 for a certain temperature range and optical depths starting from the surface of a star at τ=0.0001 up to τ = 70 000 as shown in **Figure 2.1**. This density profile is consistent with our knowledge of how the gas density varies as a function of optical depth from the stellar core to the surface. As seen in **Figure 2.1** (a) the density increases from the outer layers of the stellar atmosphere towards the inner layers in the atmosphere. This is seen for optical depths of $0.0001 \leqslant \tau \leqslant 1$. From τ =1 there is a significant decline in density because of the hydrogen ionisation zone. To further explain this dip near τ =10, we recall the hydrostatic equilibrium equation that is given by

$$\frac{dP}{d\tau_R} = \frac{g}{\kappa_R}, \tag{2.5}$$

where κ_R is the Rosseland mean opacity, g is the gravitational acceleration and τ_R is the Rosseland optical depth. In the hydrogen ionisation zone, the opacity is high (it has a big peak) due to a large number of free electrons. Therefore, according to equation (2.5), the pressure gradient should decrease. Also, if we assume that in this part of a star, the gas behaves like an ideal gas then

$$P = \frac{\rho K_B T}{\mu m} \tag{2.6}$$

hence the density gradient would also decrease. The usefulness of the hydrogen ionisation zone is that these are regions in the stellar interior where increasing opacity can provide the kappa

(κ) mechanism for pulsations to be driven. At first glance, there appears to be a good matching between the density calculated using the ATLAS9 model atmosphere and the one from OPAL EOS tables for the stellar atmosphere region at lower and high optical depths. However, if one closely looks at the two approaches by taking the ratio for the density between the ATLAS9 model atmosphere and the OPAL EOS, there are small differences between the two approaches. Furthermore, since OPAL routines require metallicity (Z), hydrogen mass fraction (X_h) and helium mass fraction (Y), we wrote a program for converting ATLAS9 individual composition to Z, X_h and Y. A consistent comparison of OPAL EOS on model atmosphere calculation must involve completely replacing the ATLAS9 EOS routines with OPAL EOS interpolation routines. This is presented in Chapter 3. In addition, one would have had to replace the opacity calculation routines as well. This is a big undertaking which was not done due to time constraints. This could be done as a part of a PhD thesis, for instance. We took the ratio of the ATLAS9 model atmospheres to the calculated OPAL EOS models. This was done to help us quantify the percentage difference between ATLAS9 EOS and the OPAL EOS in the atmosphere region. For our analysis we have taken the ratios for low effective temperatures (T_{eff} = 7000 K), high effective temperatures ($T_{eff} \geq$ 9000 K) and the surface gravities (log g=3.5 and log g=4.5) with a view to see the trend of the ratio as a function of optical depth. As seen in **Figure 2.2**, at low effective temperatures the calculated OPAL density (ρ) matches with the ATLAS9 density for low optical depths. This is evident with the ratio between the two models being ≈ 1. The percentage difference between the two models ranges between 1.5%–5.5%. For high effective temperatures the percentage difference ranges between 18.3%–110%.

Figure 2.2, shows ratios of density calculated using ATLAS9 program and that using OPAL routines. We see differences of up to 6 % for cooler models in the surface layers. Models as hot as T_{eff} =9500 K show very large differences of up to 100 %. This implies that for these models using the current ATLAS9 program introduces large errors in calculation of densities in the atmospheres of A-stars. **Figures 2.3–2.4** show the differences indicated by arrows between the two models at low optical depths.

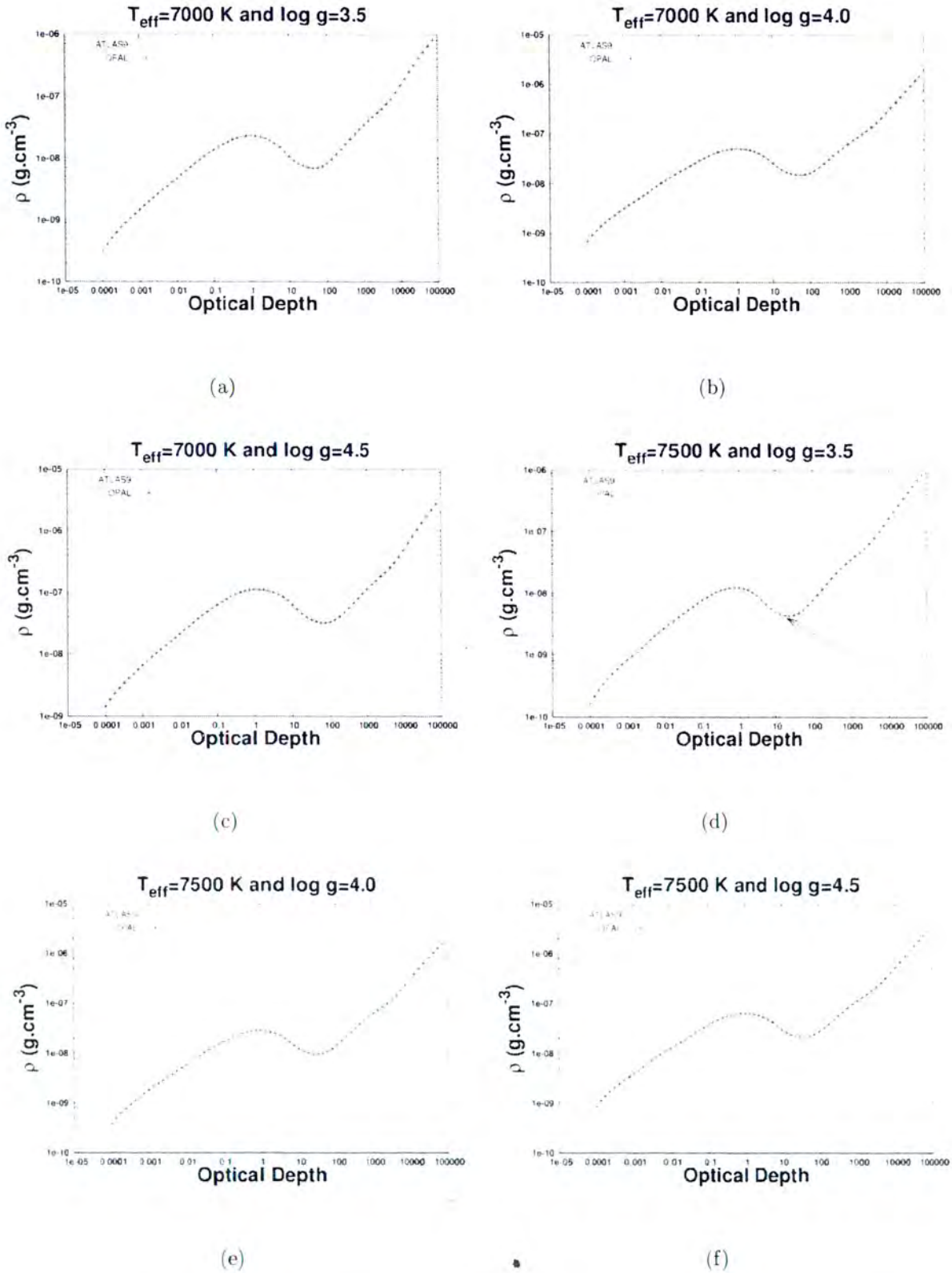

Figure 2.1: Plots of density (ρ) as a function of optical depth for various effective temperatures (T_{eff} =7000 K–7500 K) and surface gravities ($\log g$ =3.5–4.5). The solid line was calculated using normal ATLAS9 EOS. The crossed line was calculated using the OPAL EOS. The arrow indicates the hydrogen ionisation zone. These are models of the atmosphere and upper layers of the envelope.

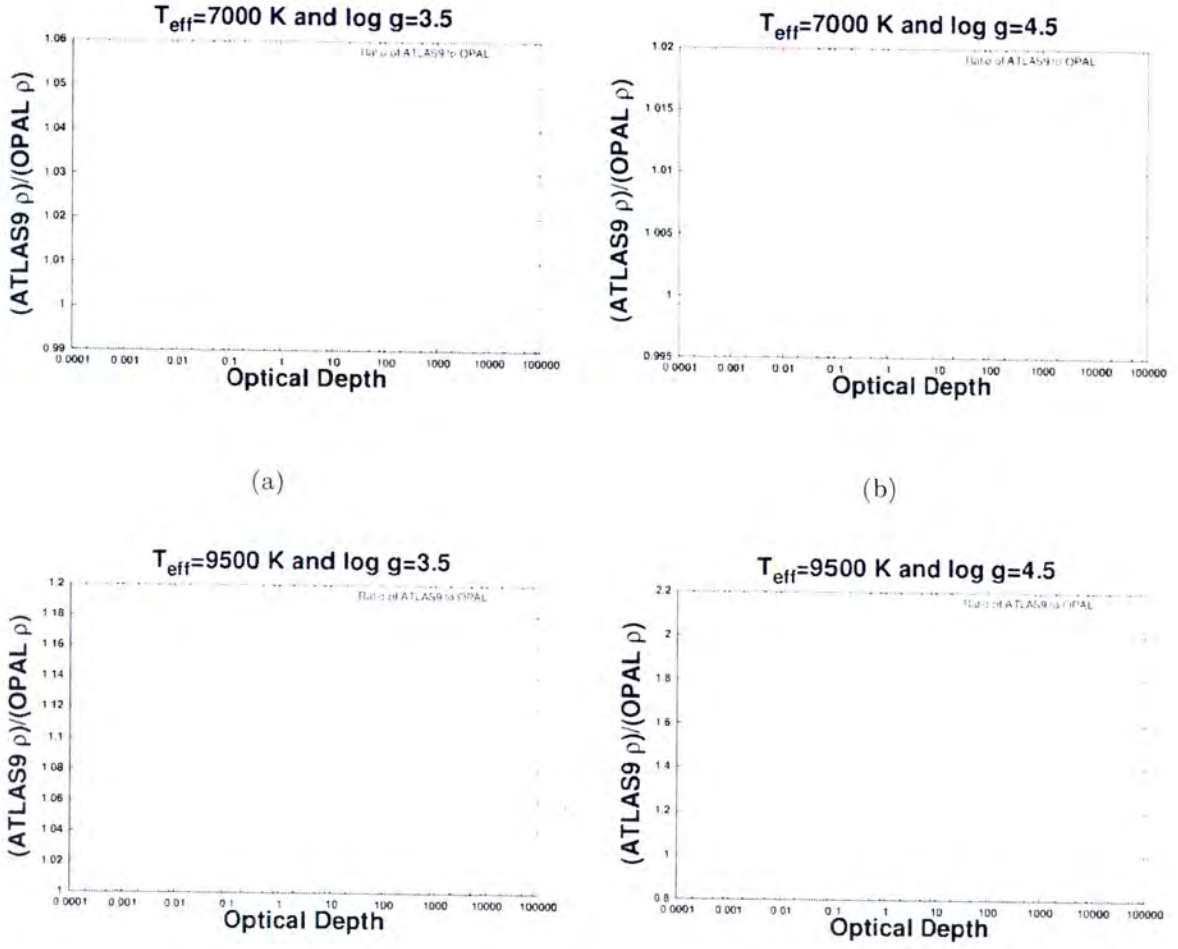

Figure 2.2: Plots of ratio of ATLAS9 density to OPAL density as a function of optical depth. The ratio was taken for the atmosphere region and upper layers of the envelope region.

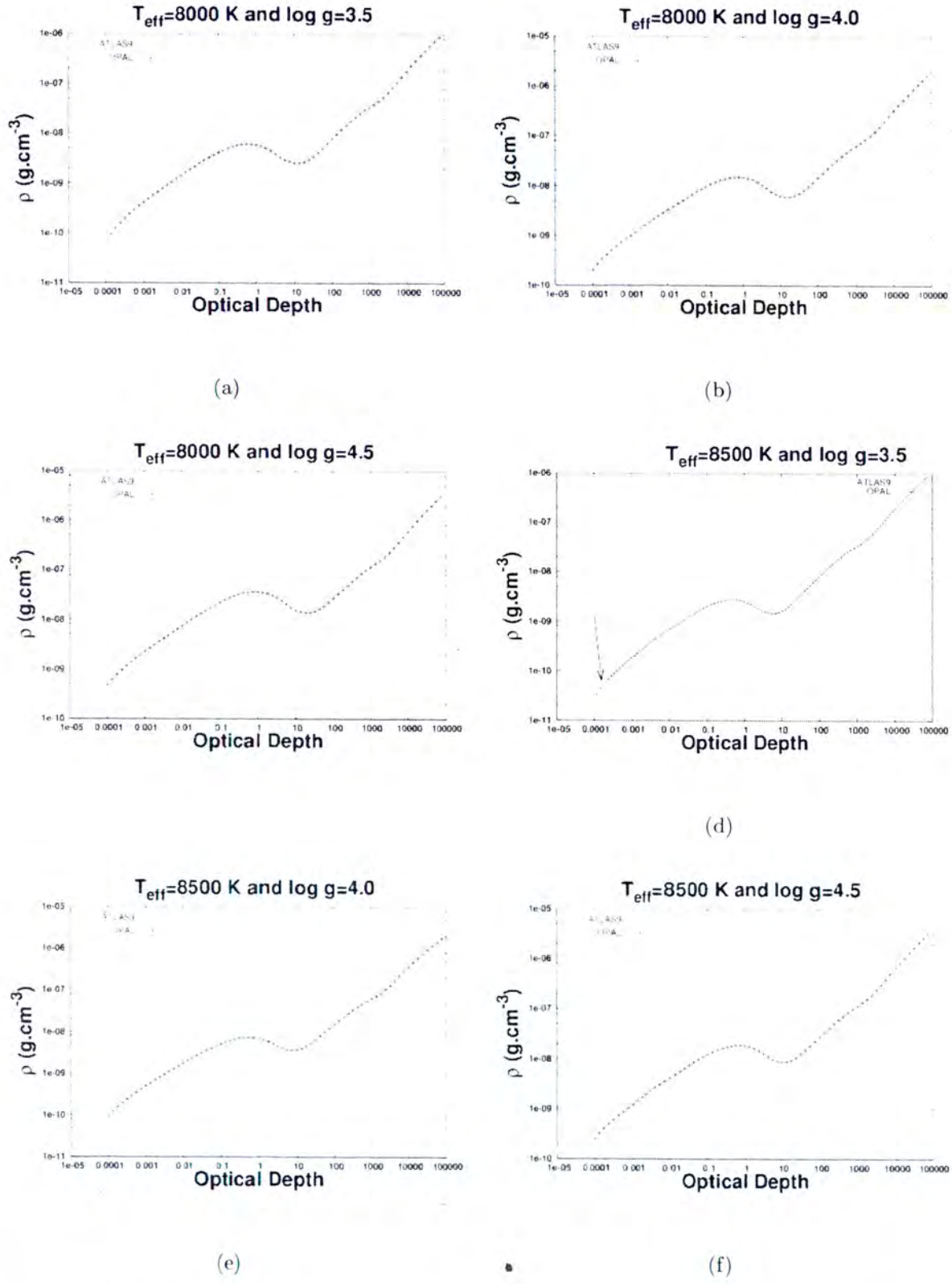

(a) (b)

(d)

(e) (f)

Figure 2.3: Plots of density (ρ) as a function of optical depth for various effective temperatures (T_{eff} =8000 K–8500 K) and surface gravities ($\log g$ =3.5–4.5). The solid line was calculated using normal ATLAS9 EOS. The crossed line and the dotted line was calculated using the OPAL EOS. The arrow indicates the differences between the two models. These are models of the atmosphere and upper layers of the envelope

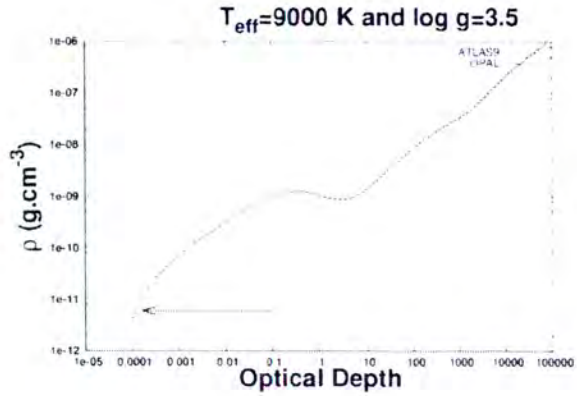

(a)

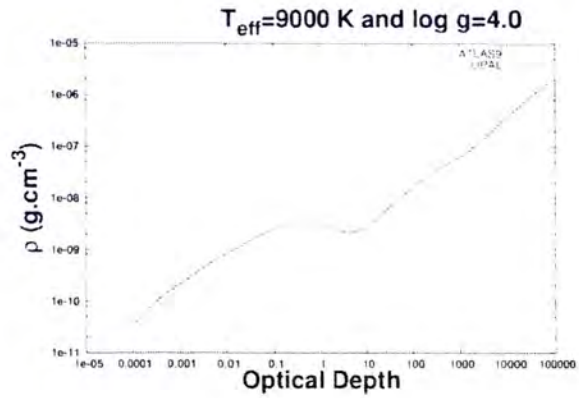

(b)

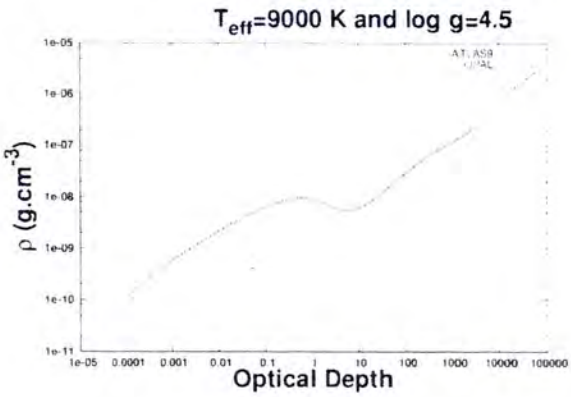

(c)

Figure 2.4: Plots of density as a function of optical depth for effective temperature T_{eff}=9000 K and various surface gravities ($\log g$ =3.5–4.5). The solid line was calculated using normal ATLAS9 EOS. The dotted line was calculated using the OPAL EOS. The arrow at low optical depths, indicate the major differences between the density calculated using ATLAS9 model atmosphere and OPAL EOS routines. These are models of the atmosphere and upper layers of the envelope.

2.2 The first Adiabatic Exponent (Γ_1)

The first adiabatic exponent (Γ_1) is important because it can be used to study the adiabatic processes in an ionising gas. Other adiabatic exponents are also important in stellar interior studies as noted by Lobel et al. (1992). This adiabatic exponent varies quite significantly between $\frac{4}{3}$ and $\frac{5}{3}$. An example of a gas that has $\Gamma_1 = \frac{4}{3}$ is H_2O in its gaseous state and that of a gas with $\Gamma_1 = \frac{5}{3}$ is Argon (Ar).

This thermodynamic variable also gives us a good indication about the location of the ionisation zones. We observe effects of first hydrogen ionisation zone on Γ_1 near optical depths of around $\tau \approx 10$. There are two regions were Γ_1 has dips in the curve, as seen in **Figure 2.5**. These regions are the hydrogen ionisation zone and the first helium ionisation zone. In the hydrogen ionisation zone, at about temperatures of 10^4 K the opacity is known to be higher as stated by Christy (1962). This is the region where the ionisation of hydrogen (HI) along with the single ionisation of helium (HeI−HeII) takes place. The second dip, is where the helium ionisation (HeII) takes place at temperatures of about $4 \times 10^4 K$. The actual location of these zones depends on the effective temperature of a star. For instance, at high effective temperatures, the ionisation zones will be shifted to the surface. This is seen if one compares **Figures 2.5** (a)–(c) for plots with low effective temperatures to **Figure 2.6**–**2.8** with plots for high effective temperatures
What can be observed here is that the first helium ionisation zone and the second helium ionisation zone, do not go as low as the first hydrogen ionisation zone. The Γ_1 decreases in the ionisation region and this is due to the low pressure gradient. We have also observed that as hydrogen starts to ionise, Γ_1 drops below the value of ≈ 1.67 and it can only reach this value when the ionisation is fully complete. In our analysis we have investigated how the surface gravity affects the matching of the two models, the same way we did for the adiabatic temperature gradient. Inspection of **Figure 2.5** seems to suggest that Γ_1 is the most affected by the equation of state. It is in this variable that the differences in the two EOS are most prominent both in the surface layers as well.

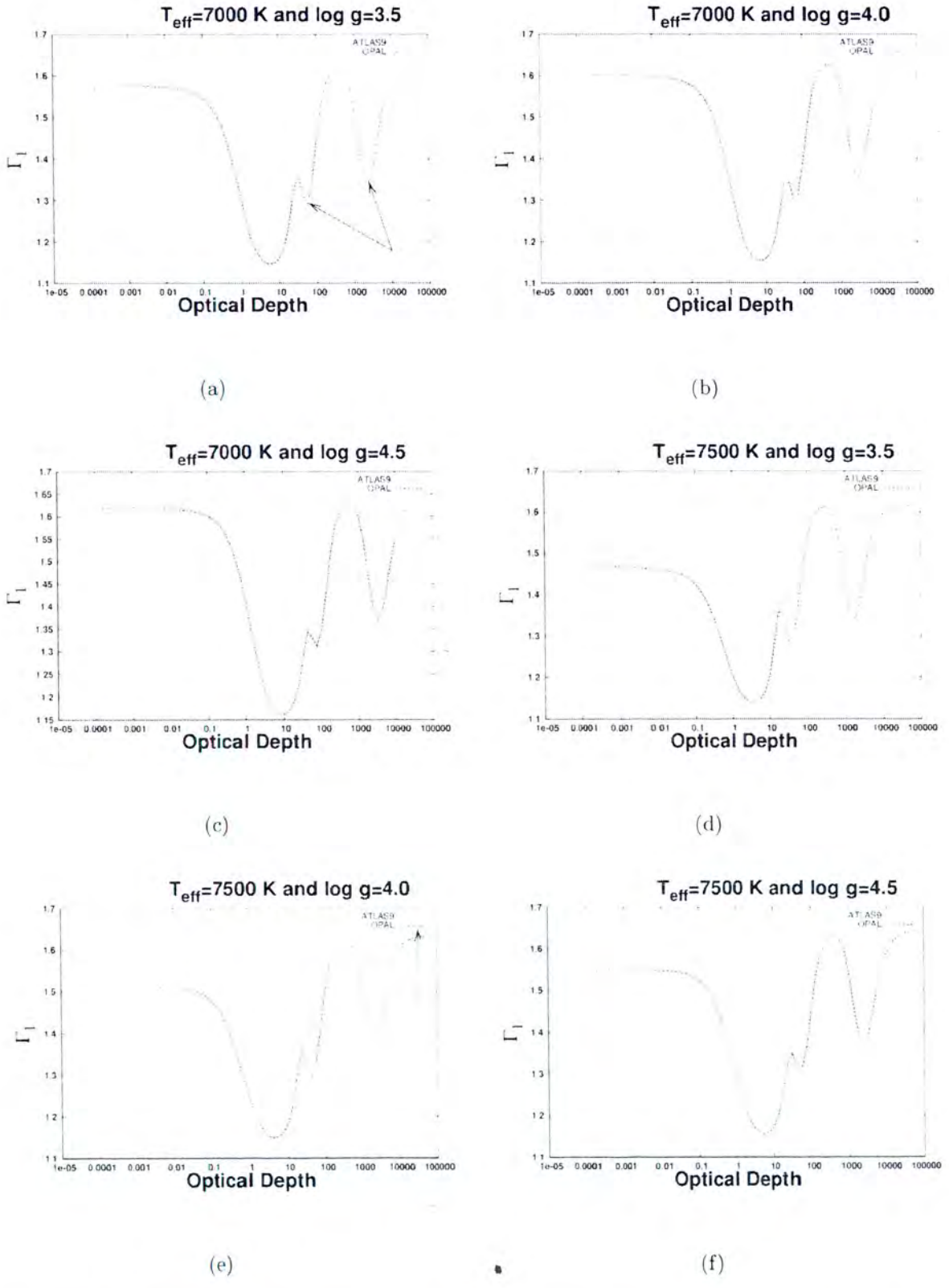

(a) (b)

(c) (d)

(e) (f)

Figure 2.5: Plots of the first adiabatic exponent (Γ_1) as a function of optical depth for various effective temperatures and surface gravities. The solid line was calculated using normal ATLAS9 EOS. The dotted line was calculated using the OPAL EOS. The arrows in subfigure (a) indicate the first and second helium ionisation zones respectively. The arrow in subfigure (e) indicates a slight discontinuity of ATLAS9 at high optical depths

After the hydrogen ionisation zone dip, we see a dip due to the first helium ionisation zone occurring at $\tau \approx 70$. Furthermore, a visible dip which signifies the second helium ionisation zone occurs at around $\tau \approx 5000$. The Γ_1 calculated from OPAL EOS routines and that from ATLAS9 show similar trends and features but their differences are generally pronounced near the surface layers (τ <0.1) and deeper layers (τ >50). Interestingly the dip due to the hydrogen ionisation zone is well matched by the two approaches. The dips due to the first and second helium ionisation zones are in general not well matched. The differences are up to 70 % for surface layers and up to 3.5 % for sub-photosphere regions. Some of the hotter models (such as T_{eff} =8000 K, log g=3.5, T_{eff} =9000 K, log g=3.5.) show dramatic differences between the Γ_1 calculated using ATLAS9 and OPAL EOS. The ATLAS9 generally shows a decrease of Γ_1 with increasing τ, whereas OPAL EOS shows an increase followed by a decrease closer to the hydrogen ionisation zone. We did not observe any discontinuities in these Figures because OPAL calculations were consistent throughout for calculations in this chapter.

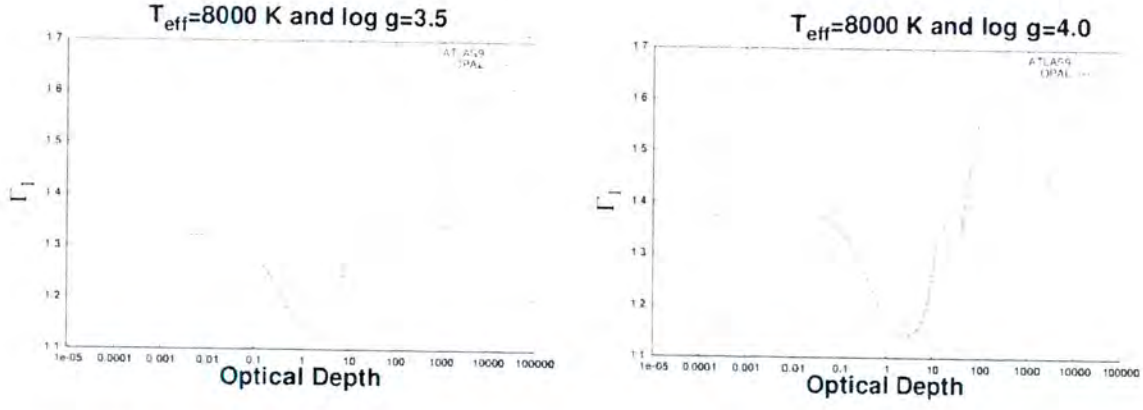

Figure 2.6: Plots of the first adiabatic exponent (Γ_1) as a function of optical depth effective temperature T_{eff}=8000 K and surface gravities (log g=3.5–4.0). The solid line was calculated using normal ATLAS9 EOS. The dotted line was calculated using the OPAL EOS. These are models of the atmosphere and upper layers of the envelope.

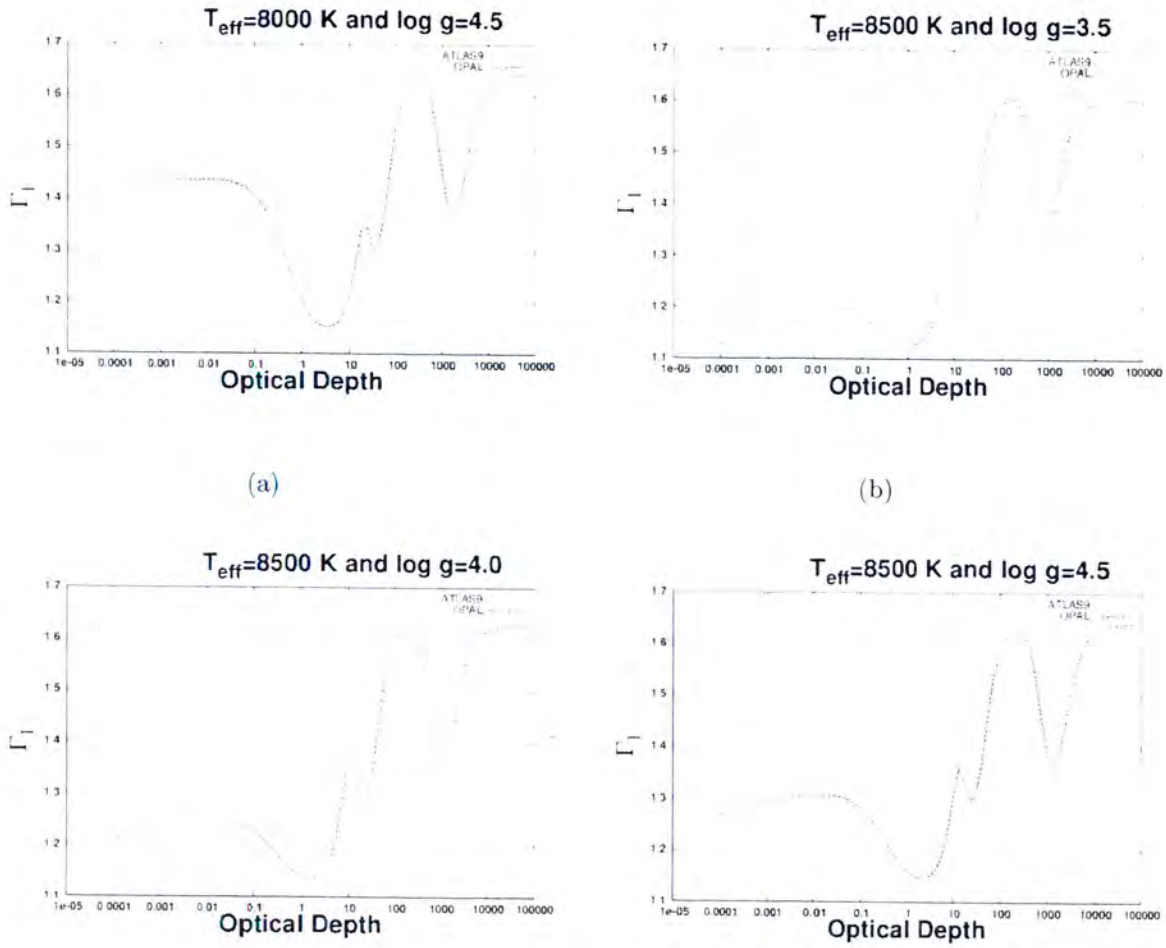

(a) (b)

(c) (d)

Figure 2.7: Plots of the first adiabatic exponent (Γ_1) as a function of optical depth for various effective temperatures (T_{eff}=8000 K–8500 K) and surface gravities ($\log g$=3.5–4.5). The solid line was calculated using normal ATLAS9 EOS. The dotted line was calculated using the OPAL EOS. These are models of the atmosphere and upper layers of the envelope.

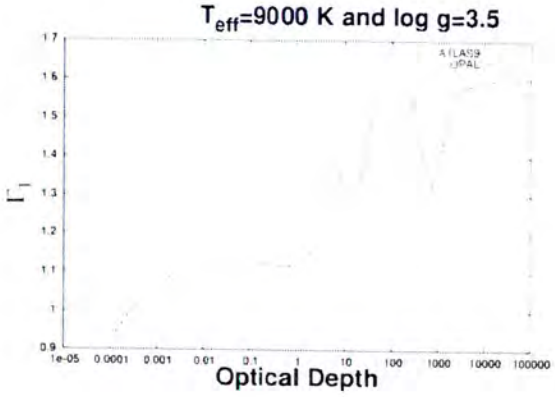

(a)

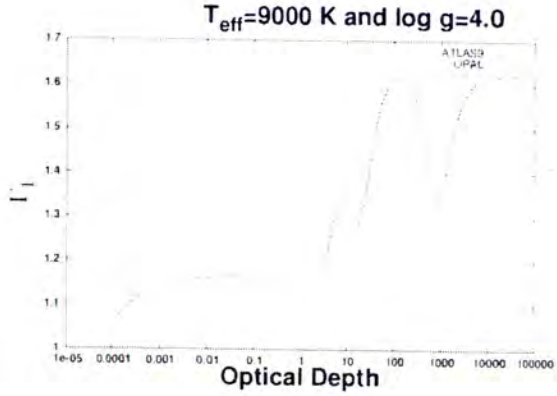

(b)

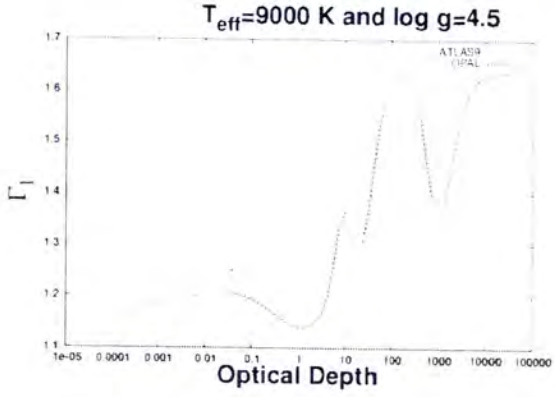

(c)

Figure 2.8: Plots of the first adiabatic exponent (Γ_1) as a function of optical depth for effective temperature T_{eff}=9000 K and surface gravities (log g=3.5–4.5). The solid line was calculated using normal ATLAS9 EOS. The dotted line was calculated using the OPAL EOS. These are models of the atmosphere and upper layers of the envelope.

The Γ_1 plot shown in **Figure 2.8** (a), also shows differences between the two EOS.

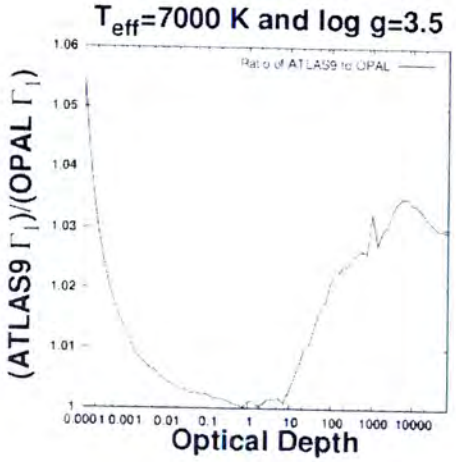

(a)

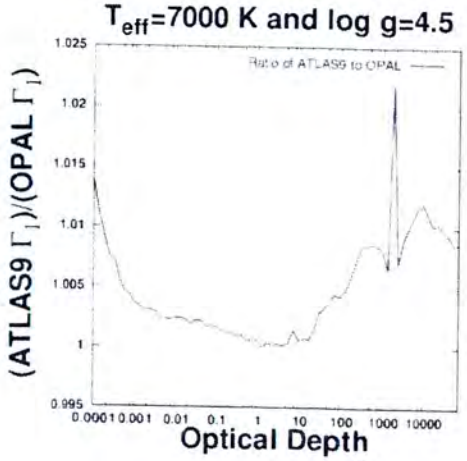

(b)

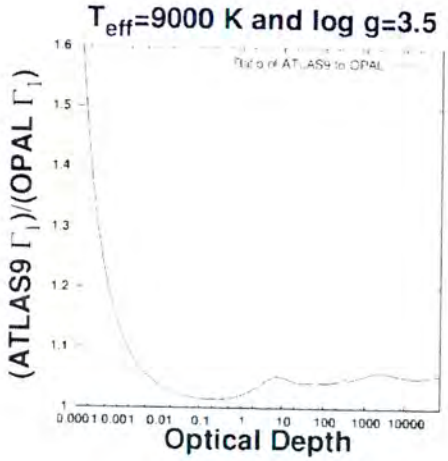

(c)

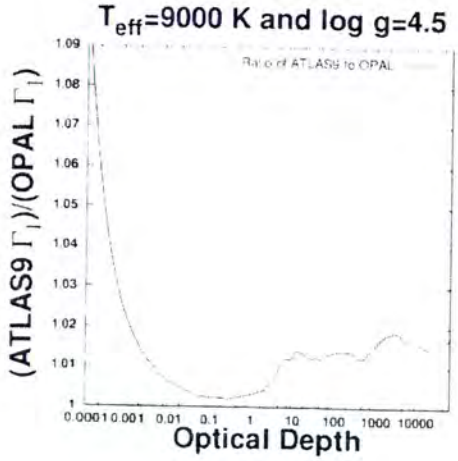

(d)

Figure 2.9: Plots of ratio of ATLAS9 Γ_1 to OPAL Γ_1 as a function of optical depth. The ratio was taken for the atmosphere region and upper layers of the envelope region. The spikes that we see at T_{eff} =7000 K cannot be explained yet.

2.3 Helium Dips

We have also investigated the HeII dip by changing the helium (Y) composition for both cooler and hotter models. This was done for the OPAL routines because Γ_1 in ATLAS9 is independent of the individual mass fractions. The results are show in **Figures 2.10–2.12** for Γ_1 as a function of optical depth (τ). We observed that in all models the 'bump' due to Helium II ionisation zone is more pronounced than in Model S (Christensen-Dalsgaard et al. 1996). This suggests that ATLAS9 exaggerates the Helium abundance in the second Helium ionisation zone. Thus, this 'bump' gets reduced when Helium abundance is increased.

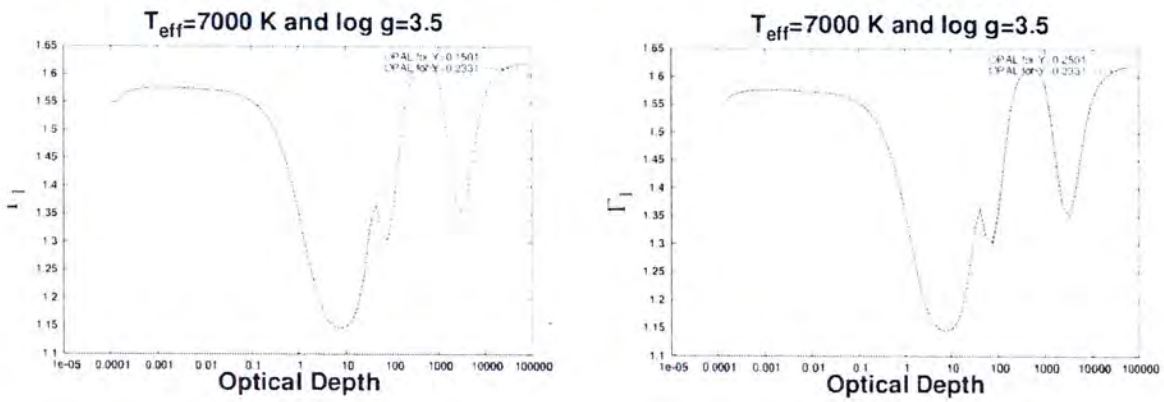

(a) (b)

Figure 2.10: Plots of the first adiabatic exponent (Γ_1) as a function of optical depth for effective temperature T_{eff} =7000 K and surface gravity log g=3.5 for helium dips. The solid and the dotted line were calculated using the OPAL routines. The HeII dips are at optical depths $\approx$ 50 and 1000. These are models of the atmosphere and upper layers of the envelope.

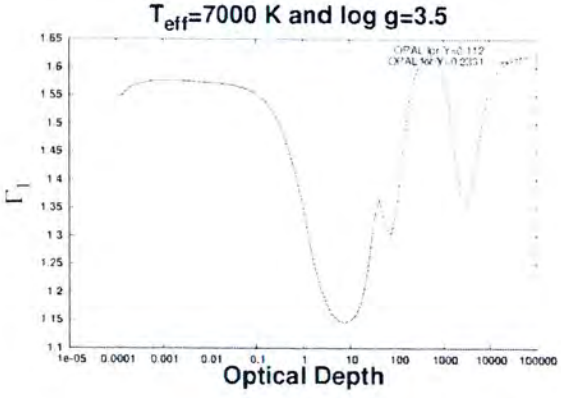

(a)

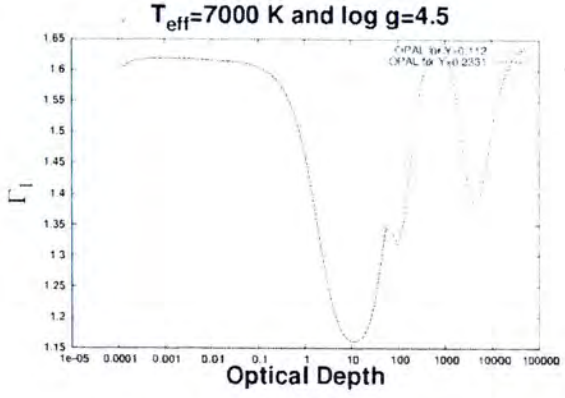

(b)

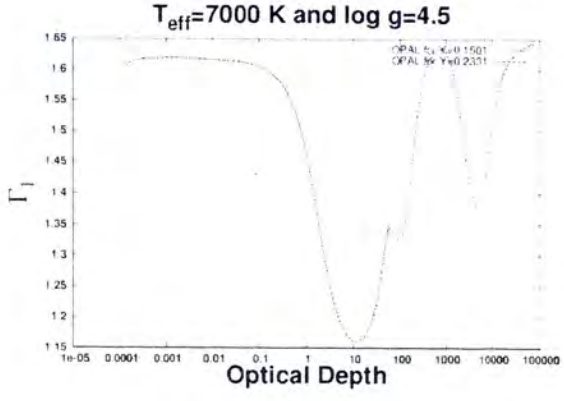

(c)

Figure 2.11: Plots of the first adiabatic exponent (Γ_1) as a function of optical depth for effective temperature T_{eff} =7000 K and surface gravities (log g=3.5 & log g=4.5) for helium dips. The solid and the dotted line were calculated using the OPAL routines. The HeII dips are at optical depths $\approx$ 50 and 1000. These are models of the atmosphere and upper layers of the envelope.

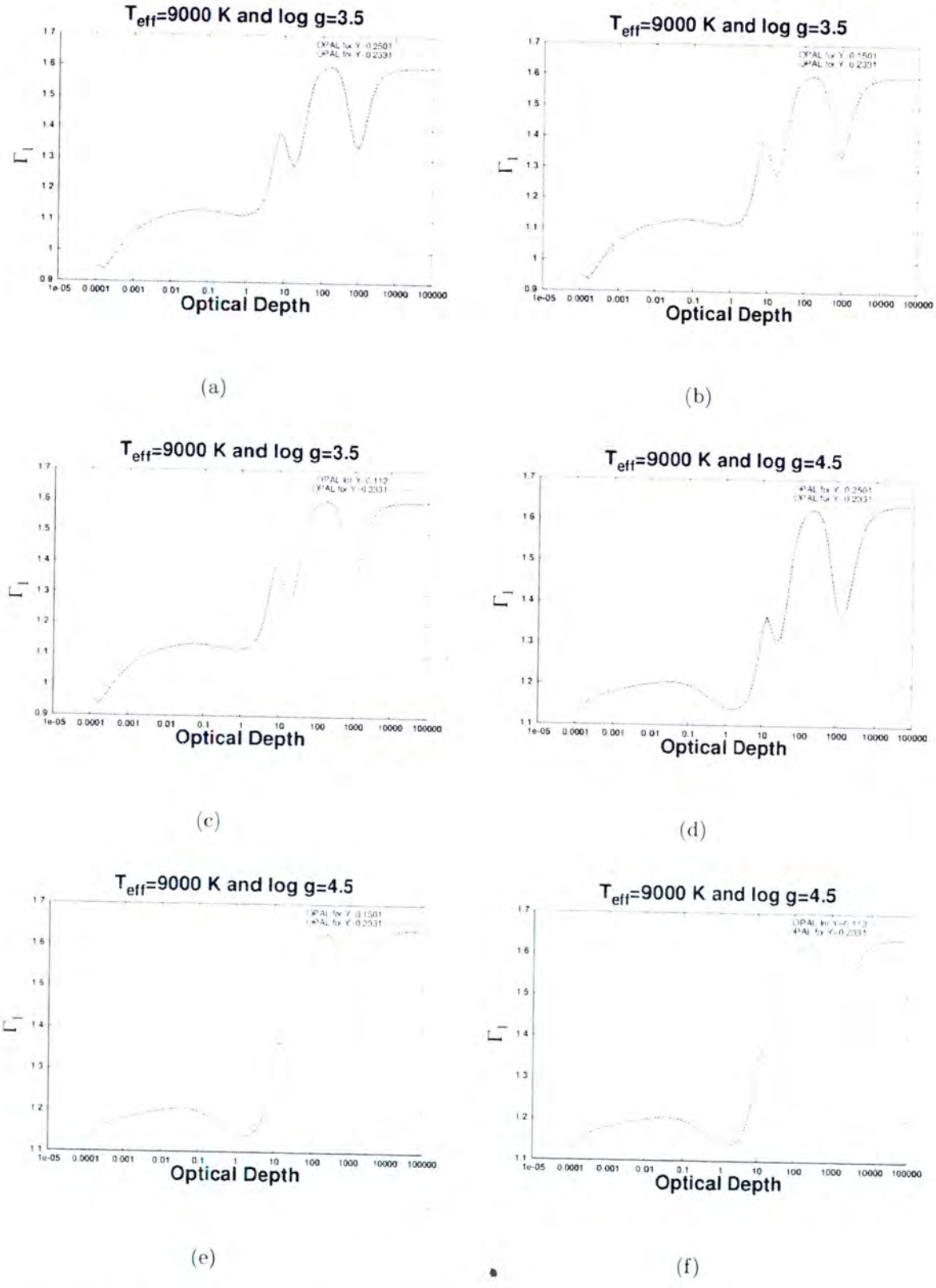

Figure 2.12: Plots of the first adiabatic exponent (Γ_1) as a function of optical depth for effective temperature T_{eff}=9000 K and surface gravities (log g=3.5 & log g=4.5). The solid and the dotted line were calculated using the OPAL routines. The HeII dips are at optical depths $\approx$ 50 and 1000. These are models of the atmosphere and upper layers of the envelope.

2.4 The Third Adiabatic Exponent (Γ_3-1)

The significance of calculating the third adiabatic exponent ($\Gamma_3 - 1$) is that this variable helps us to understand the pulsational instability as noted by Lobel et al. (1992). As was the case with the first adiabatic exponent, it has all the ionisation zones discussed previously.

As seen in **Figure 2.13**, at lower surface gravities there is a mismatch for high optical depths and lower optical depths where the OPAL method has a steeper slope than ATLAS9. However, the high surface gravity (log g=4.5) at relatively low effective temperatures (T_{eff} = 7500 K) yields good matching for the two models. From **Figure 2.14**, we see that good matching is observed for T_{eff} = 8500 K and log g=4.5. A mismatch is observed at lower optical depths, at the highest peak in **Figure 2.14** at $\tau = 500$ and high optical depths. For this thermodynamic property ($\Gamma_3 - 1$), we have also observed a slight dip in of the ATLAS9 model for T_{eff} = 7500 K. This is seen in **Figure 2.13** (d)–(f) at $\tau \approx 50\ 000$.

We have further looked at the Γ_3-1 ratios for both low effective temperatures and surface gravities. As seen in **Figure 2.15**, the percentage difference between the old ATLAS9 and the new ATLAS9 has been calculated to be ranging between (5 %–50 %).

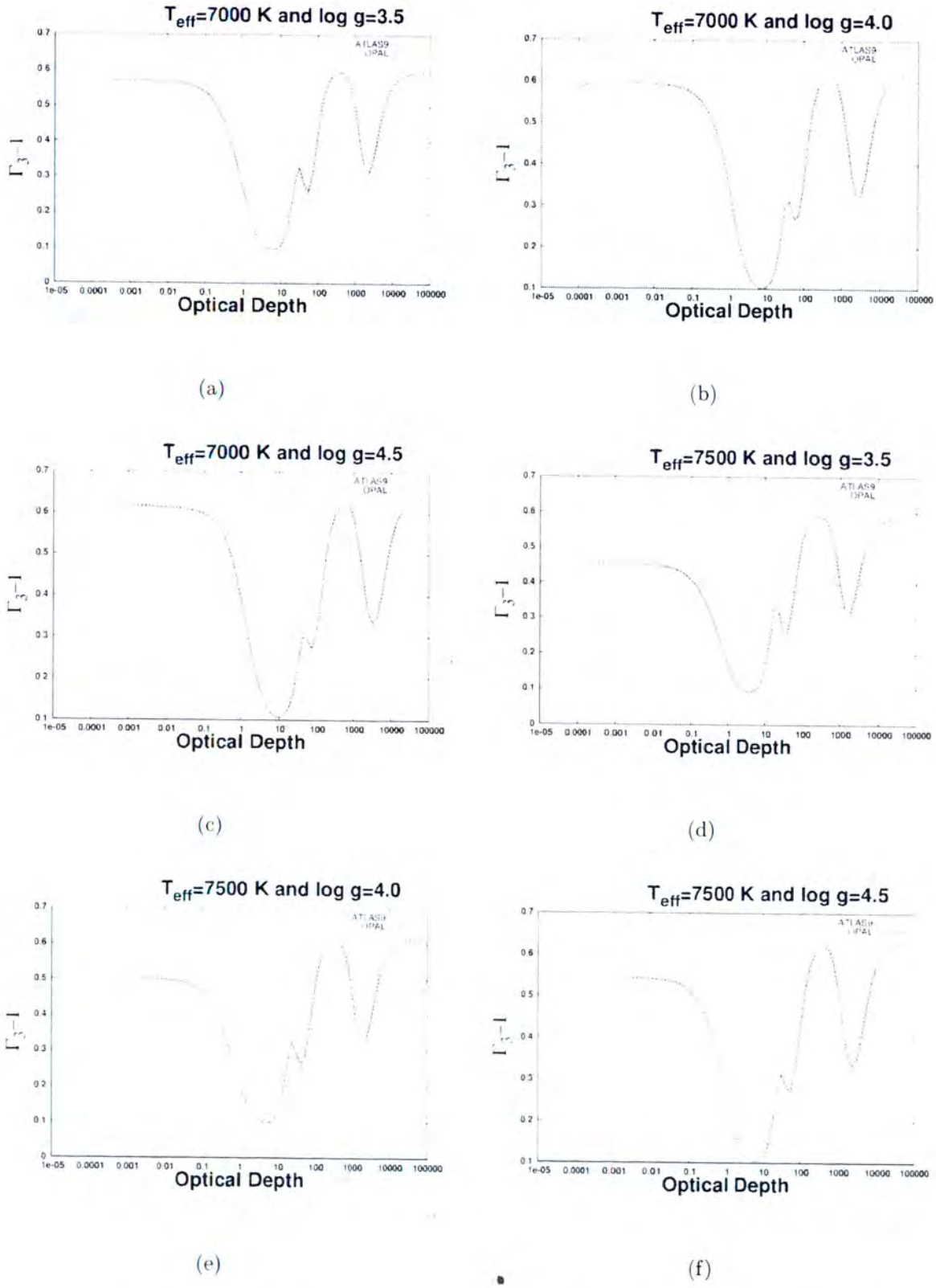

Figure 2.13: Plots of the third adiabatic exponent (Γ_3-1) as a function of optical depth for various effective temperatures (T_{eff}=7000 K–7500 K) and surface gravities (log g=3.5–4.5). The solid line was calculated using normal ATLAS9 EOS. The dotted line was calculated using the OPAL EOS. These are models of the atmosphere and upper layers of the envelope.

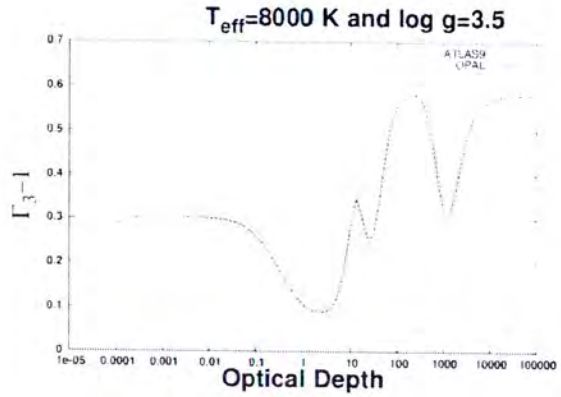

(a)

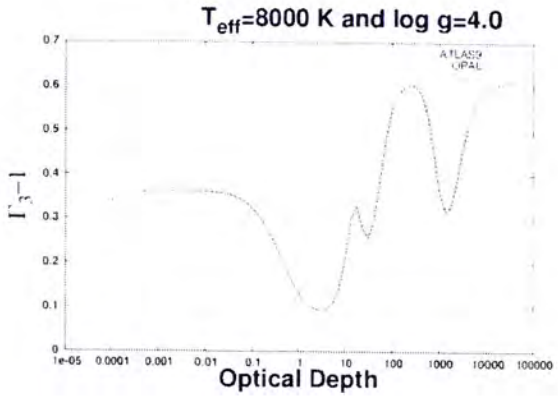

(b)

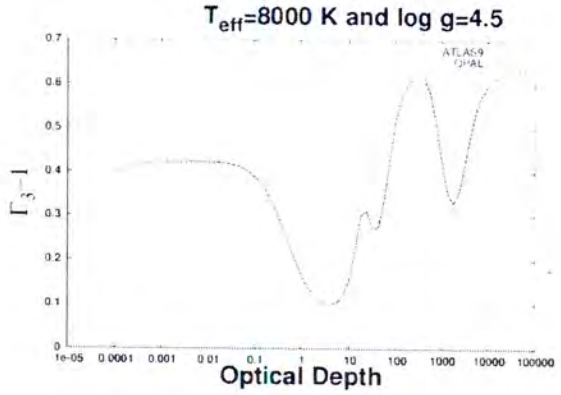

(c)

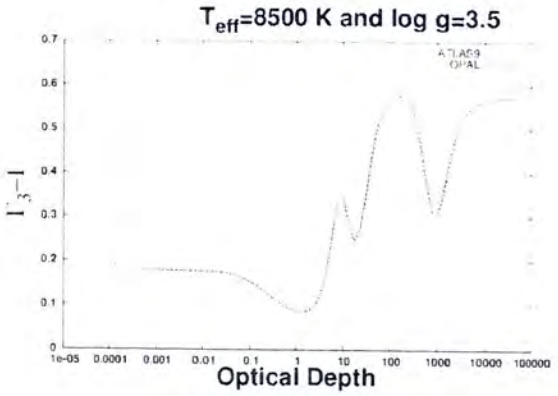

(d)

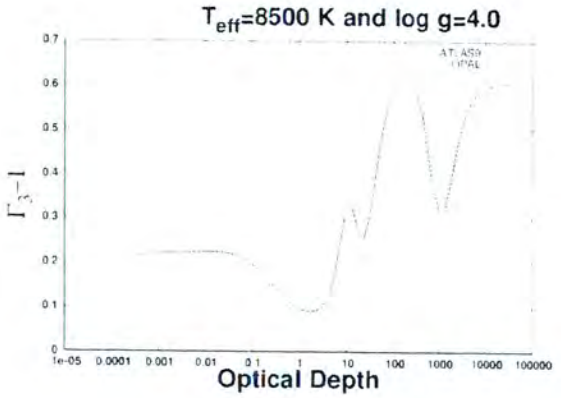

(e)

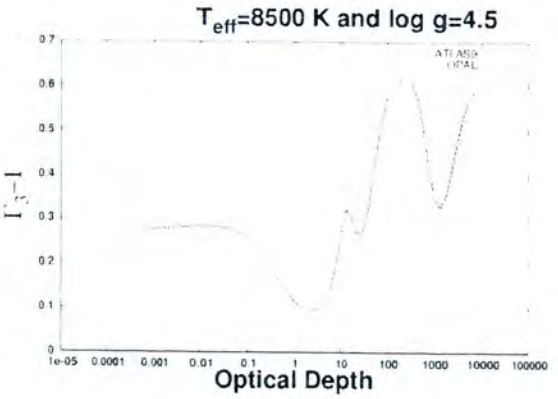

(f)

Figure 2.14: Plots of the third adiabatic exponent (Γ_3-1) as a function of optical depth for various effective temperatures (T_{eff}=8000 K–8500 K) and surface gravities (log g=3.5–4.5). The solid line was calculated using normal ATLAS9 EOS. The dotted line was calculated using the OPAL EOS. These are models of the atmosphere and upper layers of the envelope.

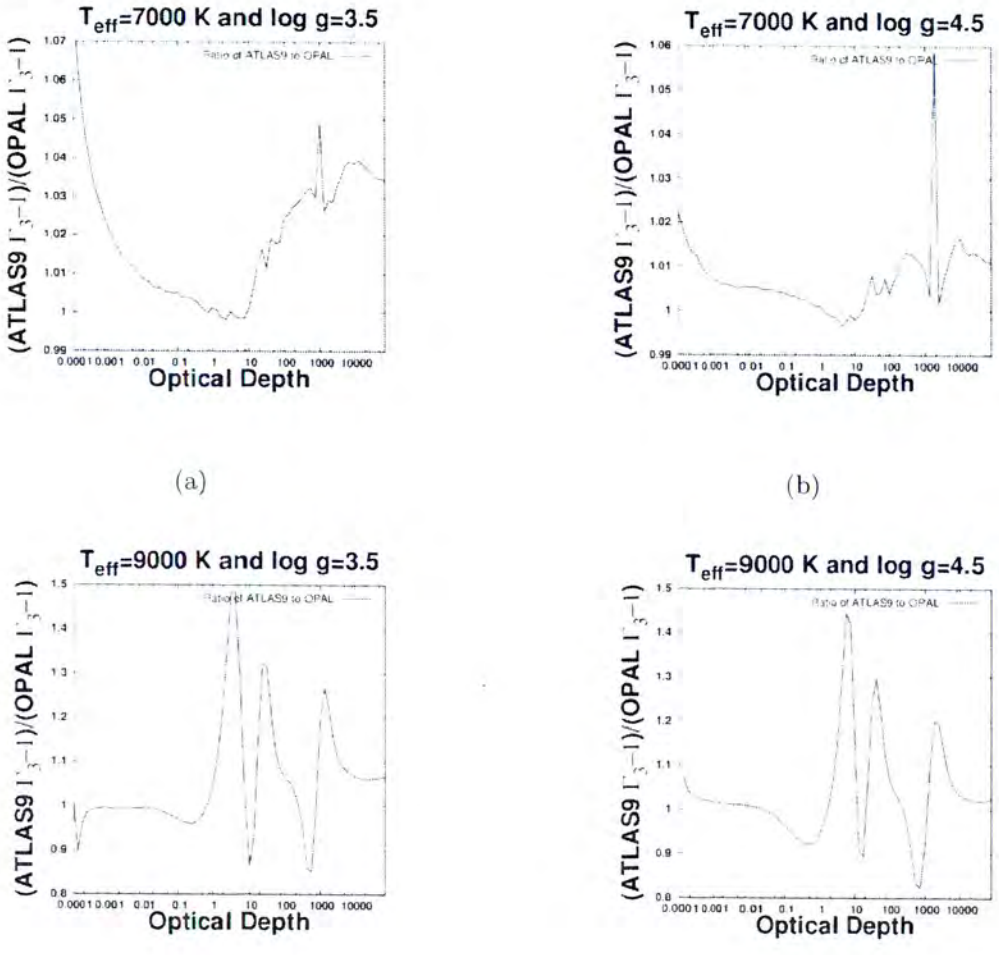

Figure 2.15: Plots of ratio of ATLAS9 Γ_3-1 to the OPAL Γ_3-1 as a function of optical depth. The ratio was taken for the atmosphere region and upper layers of the envelope region.

2.5 The Adiabatic Temperature Gradient (∇_{ad})

As we have seen from some of the derivation of the OPAL EOS, the adiabatic temperature gradient is calculated using the equation

$$\nabla_{ad} = \left(\frac{\Gamma_2}{\Gamma_2 - 1}\right). \tag{2.7}$$

In a nutshell we used the temperature and pressure that were obtained from the ATLAS9 model to calculate the adiabatic temperature gradient. For the results obtained, we see good agreement between the OPAL EOS tables and the ATLAS9 program. The region where a mismatch is seen is for lower temperatures at around T_{eff} = 7000K, this is seen in optical depths less than 0.01 ($\tau \leq 0.01$). This occurrence of a mismatch is seen in the first three plots of **Figure 2.16**. For the surface gravity good matching is seen for regions with a high surface gravity at log g= 4.5 while for low surface gravities at log g=3.5 we see a mismatch. Based on this analysis we can conclude that good models for the adiabatic temperature gradient at lower temperatures were obtained for high surface gravities.

The profile obtained for both the ATLAS9 and the OPAL EOS tables is quite similar to that of the adiabatic temperature gradient (∇_{ad}). There is a persistent mismatch between the OPAL EOS and ATLAS9 observed for high effective temperatures, this will be discussed shortly.
At first glimpse we see the occurrence of the ionisation of hydrogen, first and second ionisation of helium. The two models in ATLAS9 and OPAL EOS match quite well for high temperatures (T_{eff} =8500 K) and surface gravities (log g= 4.5). This good matching is observed in Subfigure (f) of **Figure 2.17**. At low surface gravity (log g= 3.5) and high temperatures there is a slight mismatch for lower optical depths (see subfigure (e)). This mismatch causes a a steep decline in gradient for the ATLAS9 model at low optical depth as. A great deal of a mismatch is seen quite clearly in subfigure (d) of **Figure 2.17**.

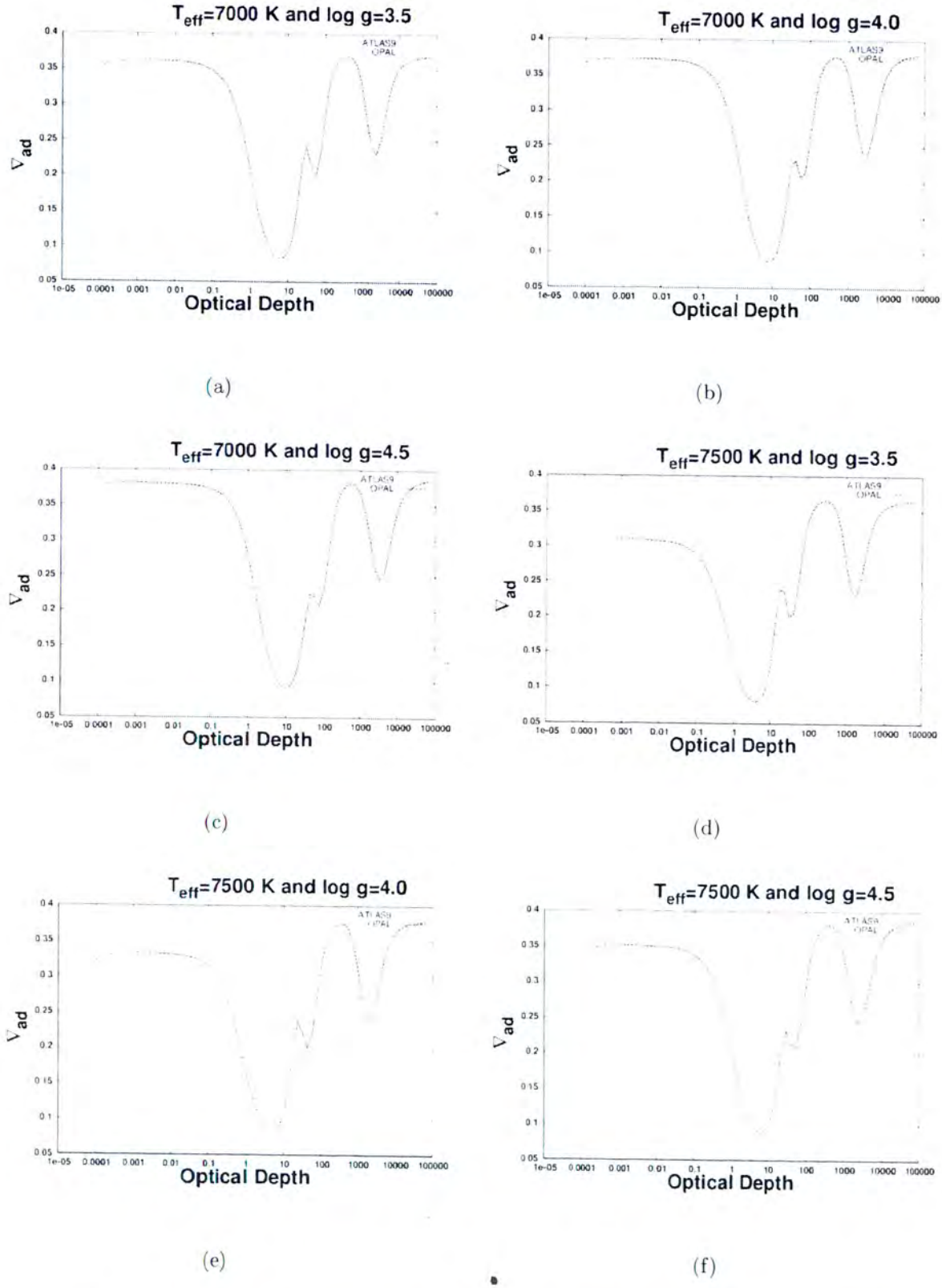

Figure 2.16: Plots of the adiabatic temperature gradient (∇_{ad}) as a function of optical depth for various effective temperatures (T_{eff}=7000 K–7500 K) and surface gravities (log g=3.5–4.5). The solid line was calculated using normal ATLAS9 EOS. The dotted line was calculated using the OPAL EOS. These are models of the atmosphere and upper layers of the envelope.

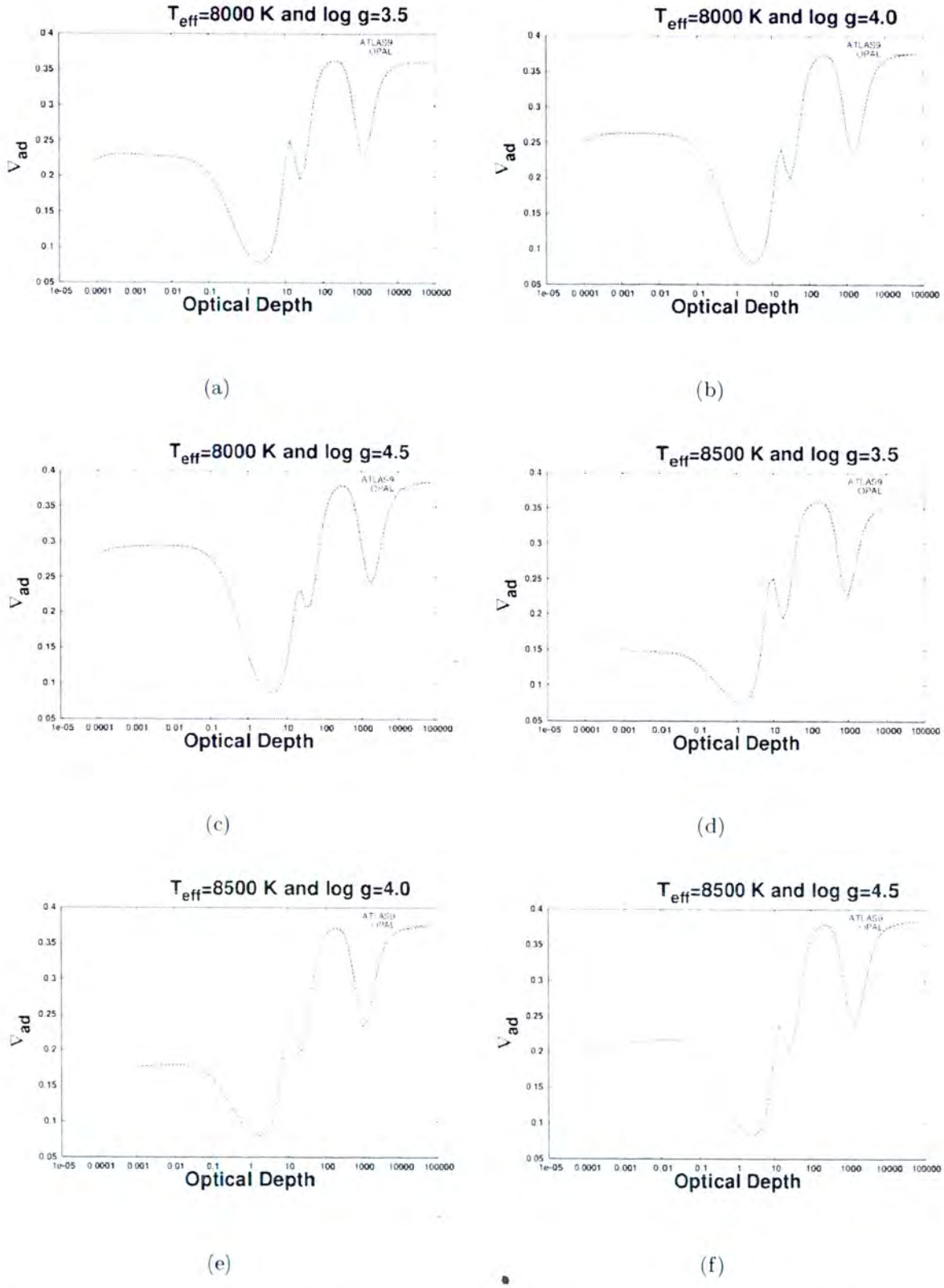

Figure 2.17: Plots of the adiabatic temperature gradient as a function of optical depth for various effective temperatures (T_{eff}=8000 K–8500 K) and surface gravities (log g=3.5–4.5). The solid line was calculated using normal ATLAS9 EOS. The dotted line was calculated with the OPAL EOS. These are models of the atmosphere and upper layers of the envelope.

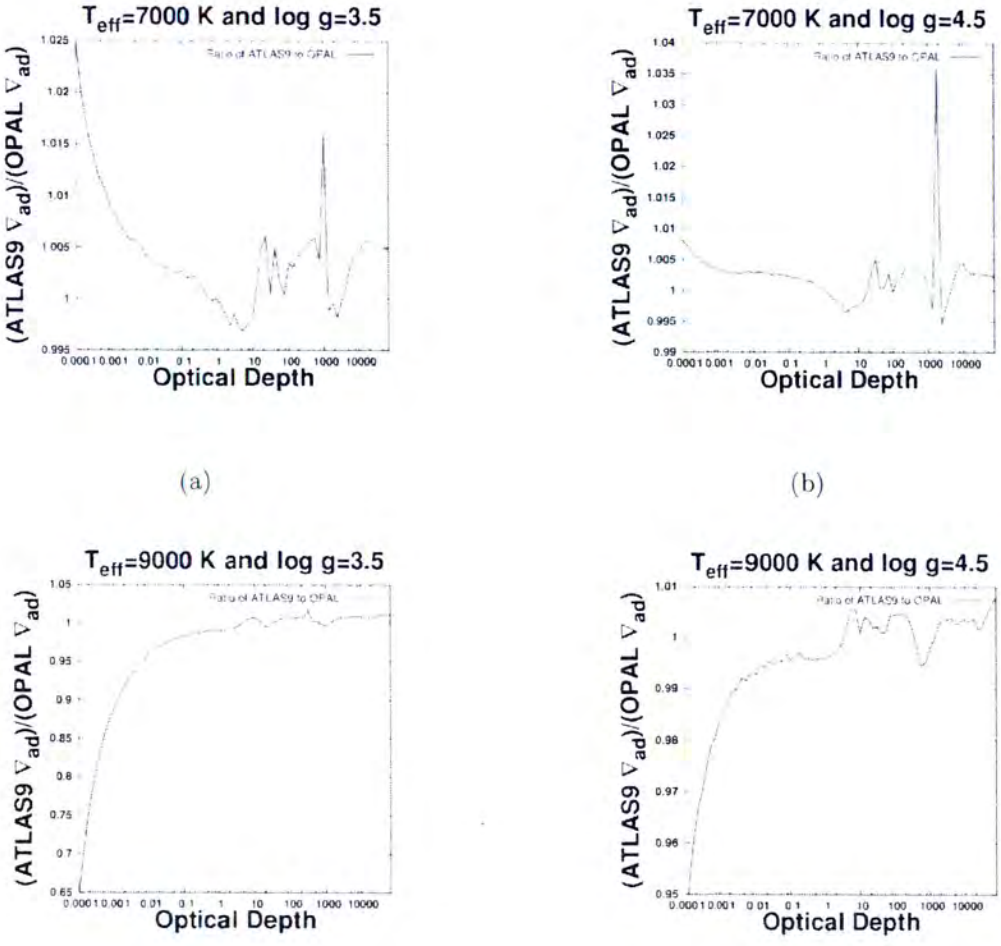

Figure 2.18: Plots of ratio of ATLAS9 $\bigtriangledown_{ad}$ to the OPAL $\bigtriangledown_{ad}$ as a function of optical depth. The ratio was taken for the atmosphere region and upper layers of the envelope region.

2.6 Specific Heat Capacity (C_p)

The specific heat capacity at constant pressure has been calculated and the results are presented in **Figures 2.19–2.21**. If one looks closely at **Figure 2.19**, we observe a relation between the specific heat and Γ_1. From the Figure the ionisation zones correspond to an increase in Specific Heat Capacity.

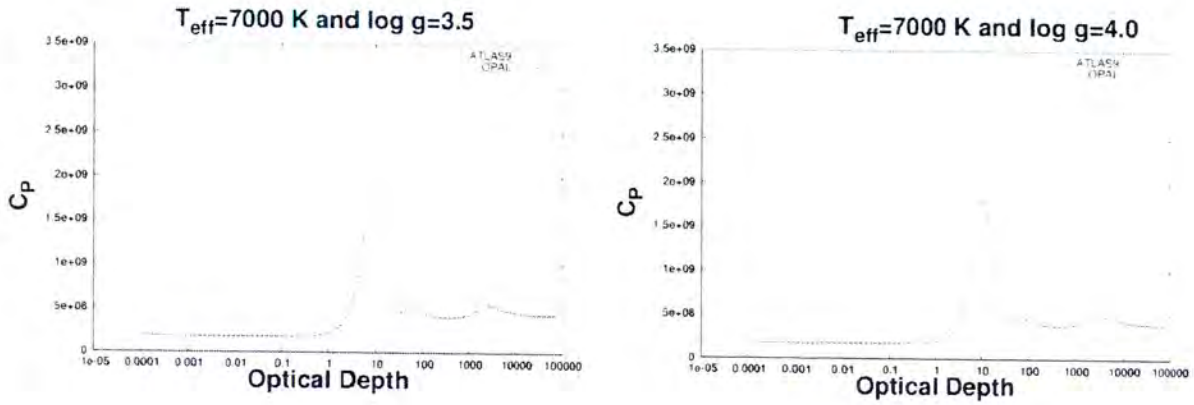

(a) (b)

Figure 2.19: Plots of the specific heat capacity as a function of optical depth for effective temperature T_{eff}=7000 K and surface gravities (log g=3.5 & log g=4.0). The solid line was calculated using normal ATLAS9 EOS. The dotted line was calculated using OPAL EOS. These are models of the atmosphere and upper layers of the envelope.

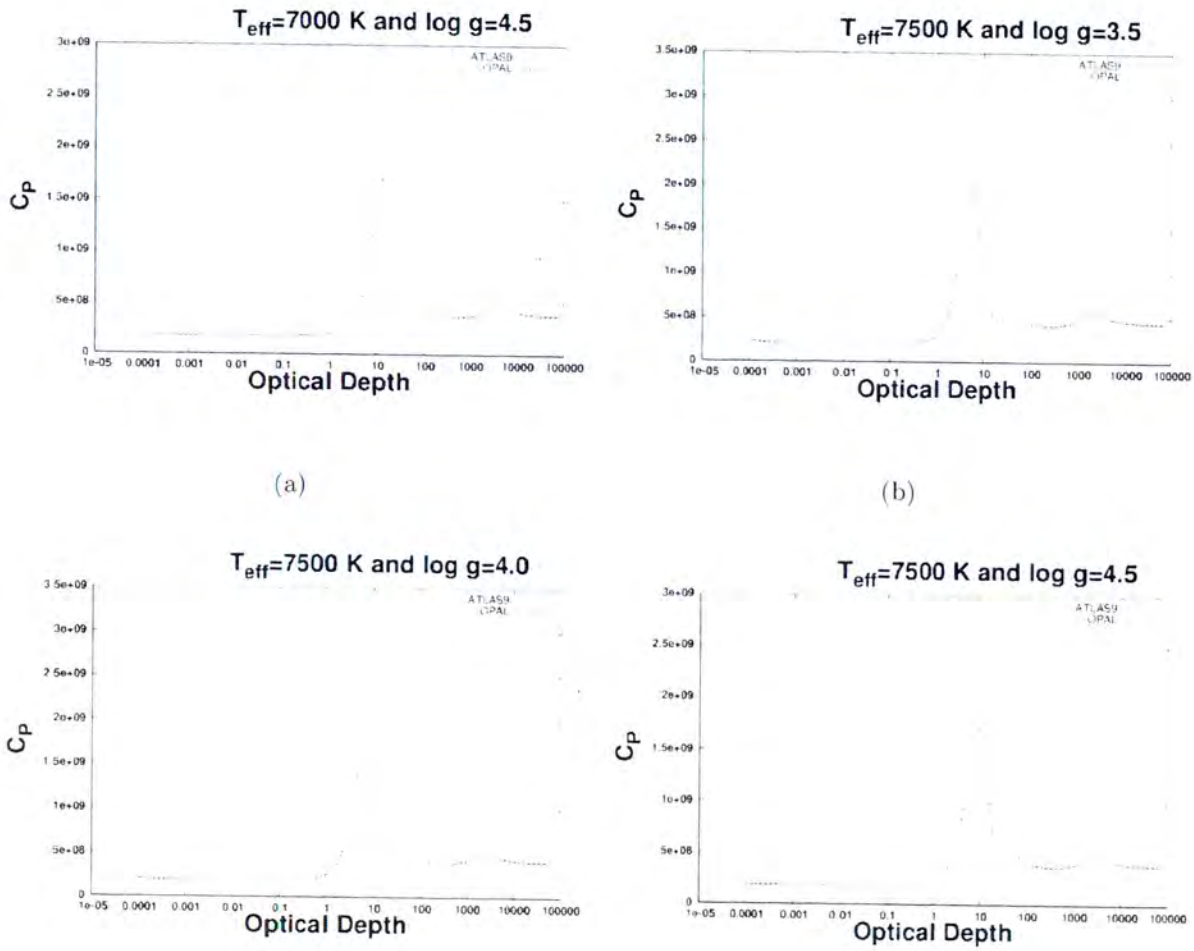

(a) (b)

(c) (d)

Figure 2.20: Plots of the specific heat capacity as a function of optical depth for various effective temperatures (T_{eff}=7000 K–7500 K) and surface gravities (log g=3.5–4.5). The solid line was calculated using normal ATLAS9 EOS. The dotted line was calculated using OPAL EOS. These are models of the atmosphere and upper layers of the envelope.

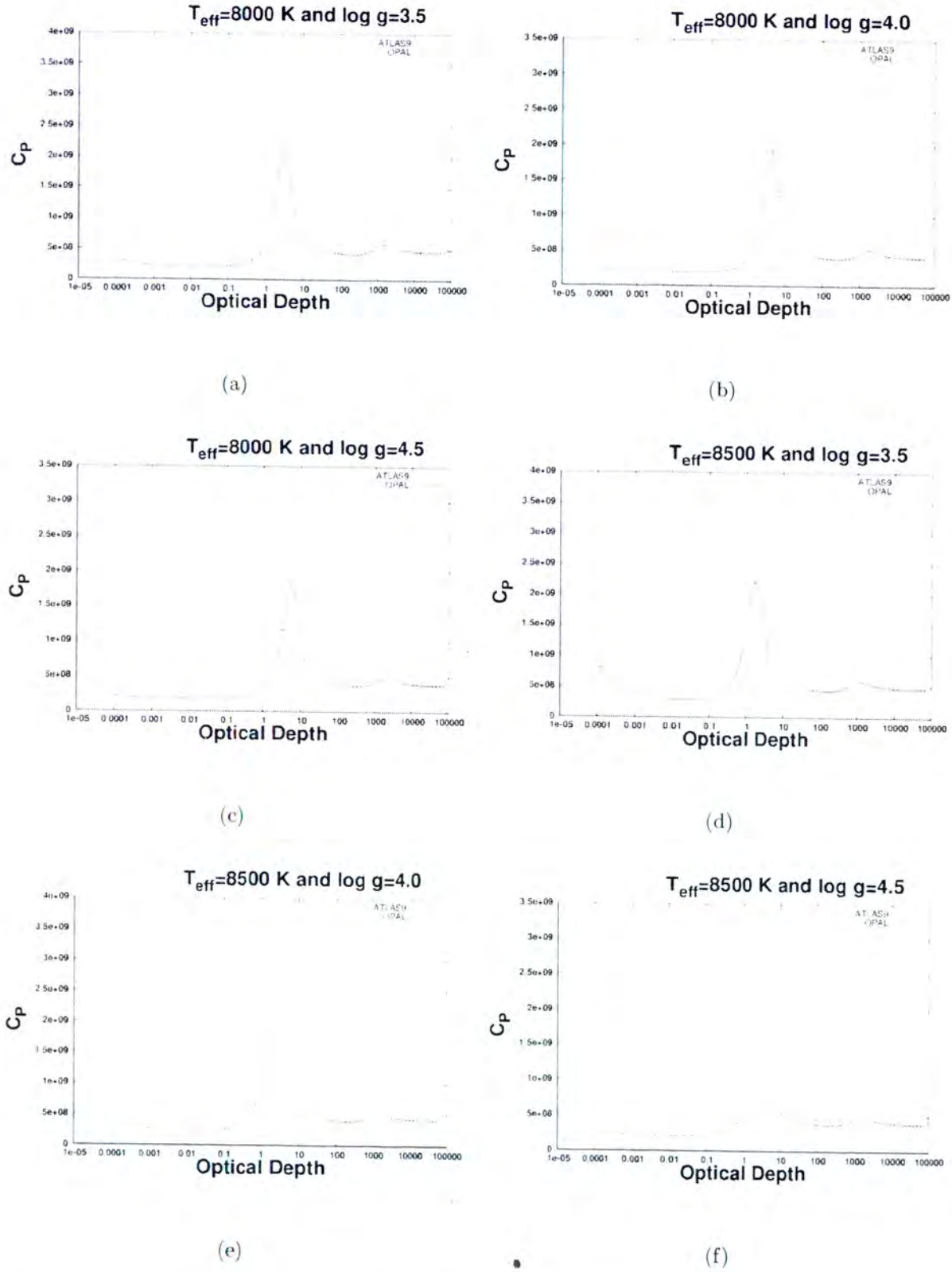

(a) (b) (c) (d) (e) (f)

Figure 2.21: Plots of the specific heat capacity (C_p) as a function of optical depth for various effective temperatures (T_{eff}=8000 K–8500 K) and surface gravities (log g=3.5–4.5). The solid line was calculated using normal ATLAS9 EOS. The dotted line was calculated using the OPAL EOS. These are models of the atmosphere and upper layers of the envelope.

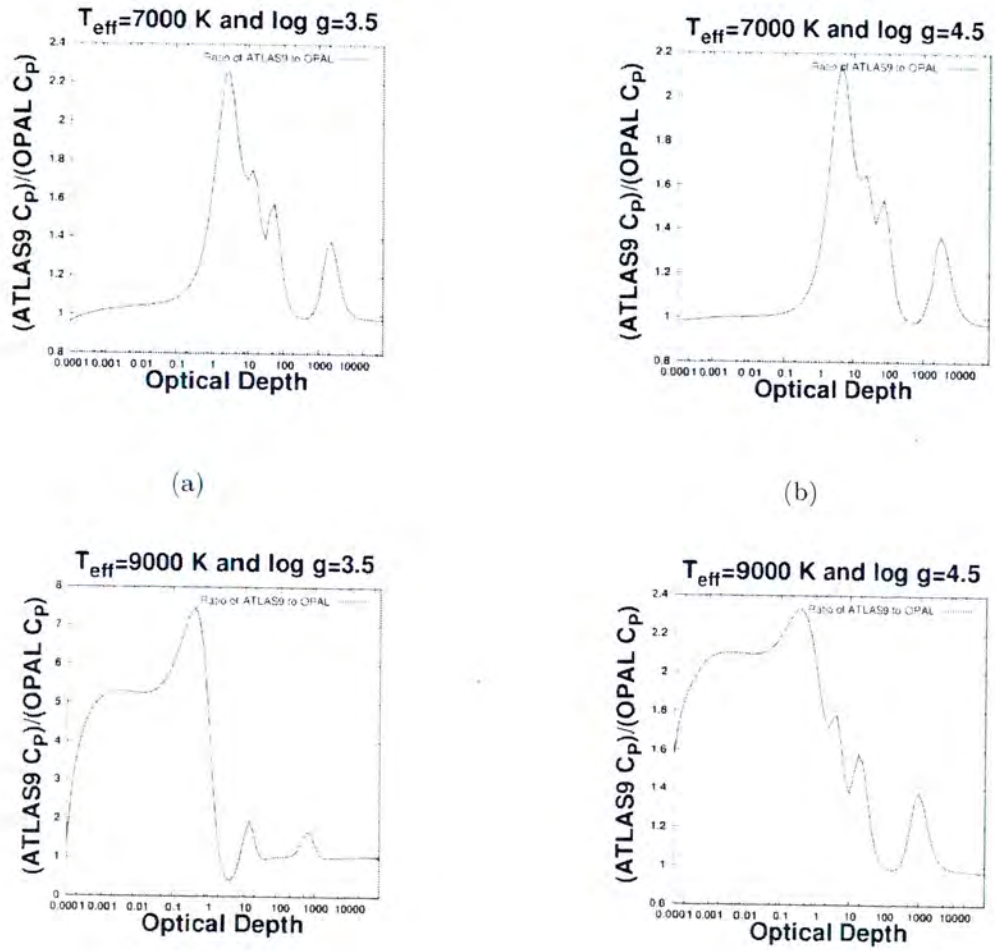

Figure 2.22: Plots of ratio of the ATLAS9 C_p to the OPAL C_p as a function of optical depth. The ratio was taken for the atmosphere region and upper layers of the envelope region.

Chapter 3

Inclusion of OPAL EOS in ATLAS9 program

3.1 Inclusion of OPAL EOS

In this chapter, we have calculated the new grids of model atmosphere by including the OPAL EOS interpolation routines in the ATLAS9 code. The importance of making such atmosphere models is that we may use these models to do spectroscopic work and consequently calculate the composition of a star. This according to Kirby (2011) is done by first making a model atmosphere from which a synthetic spectrum can be calculated. Our models have been developed with a great amount of precision and reliability using various effective temperatures (6500 K-9500 K), surface gravities (log g = 3.5-log g=4.5) and composition (X_h=0.733, Y=0.2498 and Z=0.0172). We have modified the atlas9mem−newodf.for code in our bid to include the OPAL EOS routines in the ATLAS9 program. What this implies is that there were subroutines that were modified in this code so as to include the esac.f code from OPAL. In this Chapter we discuss the results obtained when ATLAS9 program was modified. In modifying the ATLAS9 program we had to be mindful that the program was developed with certain conditions and that our models had to be computed for conditions that are found in stars. Also, according to Trampedach et al. (2006)

it is a difficult task to improve an EOS beyond the model of a mixture of an ideal gas. The significance of modifying and improving the models done before is that we have indicated the physical limits associated with the ATLAS9 program. Spectra were computed as well from the model atmosphere and these spectra were calculated for the optical region of the spectrum.

3.2 Converting ATLAS9 elemental Abundances

Prior to including the OPAL EOS in the ATLAS9 program it was key to note that ATLAS9 input specifies the number fraction of the first 99 elements of the periodic table. Main sequence stars generally have a higher fraction of hydrogen and helium nuclei. With hydrogen contributing about 92% of the nuclei and helium 7.8 % of the nuclei. This implies the number fraction in abundance of hydrogen and helium is as high as about 98 % and the remaining 2 % is the contribution by heavier elements (Fall, 2003). In ATLAS9 these heavier elements are presented in logarithmic form to simplify their minute quantities.

For uniformity in the outcome for the respective abundances of elements used in OPAL EOS and opacity tables, the number fraction used in ATLAS9 had to be converted to the mass fraction. This was accomplished by multiplying each element by its relative mass to get the total mass that the normalised abundance would accumulate. The next trivial step was that of adding the individual elements into the heavier elements (Z), Hydrogen (X_h) and Helium (Y). A program was written to implement this. Also, the significance of converting ATLAS9 elemental abundances to mass fractions is due to OPAL EOS tables working in mass fractions. Furthermore, the correct mass fractions computed have been used in the matching code to see the effect of composition when matching the envelope to the atmosphere. Abundance evaluations done previously indicate that even though a 1-D homogeneous model does not give a good explanation about spectroscopic and photometric observations, the atmosphere models have come in handy to predict thermodynamic variables such as temperature gradient. This stellar variable has been found to be closer to the radiative and matching observations better (Montalban, 2004).

Also recent studies by Trampedach et al. (2013) have attempted 3-D convection stellar models with a view of matching advance stellar observations provided by MOST, COROT and Kepler.

3.3 Density

The density plots with convection included are shown in **Figure 3.1**. This was done for the modified ATLAS9 program and the original ATLAS9 code for the optical depths ranging from $0.001 \leq \tau \leq 10000$. From the Figure we see major differences in the trends for higher optical depths and this is partly in line with the discussed opacity profile. This appears to be the case from low effective temperatures and log g =3.5. The differences are clearly seen in subfigures (e) and (f) for higher effective temperatures. We can then conclude that the higher the effective temperature and the lower the surface gravity, the greater the differences between the old ATLAS9 and the new ATLAS9.

From the profiles, we see the hydrogen ionisation zone at the point when the density starts being relatively constant and decreasing with increasing optical depth. The density decreases until the second dip at the first helium ionisation. Subsequent to this we observe a steady increase in density gradient as we move to deeper layers in a star. What we note is the increase in density with optical depth, before the hydrogen ionisation zone and the first helium ionisation zone. At significantly higher temperatures the matter density becomes fully ionised. At these high temperatures with ionisation the Thomas-Fermi treatment usually has a reasonable Equation of State (Magni & Mazitelli, 1979).

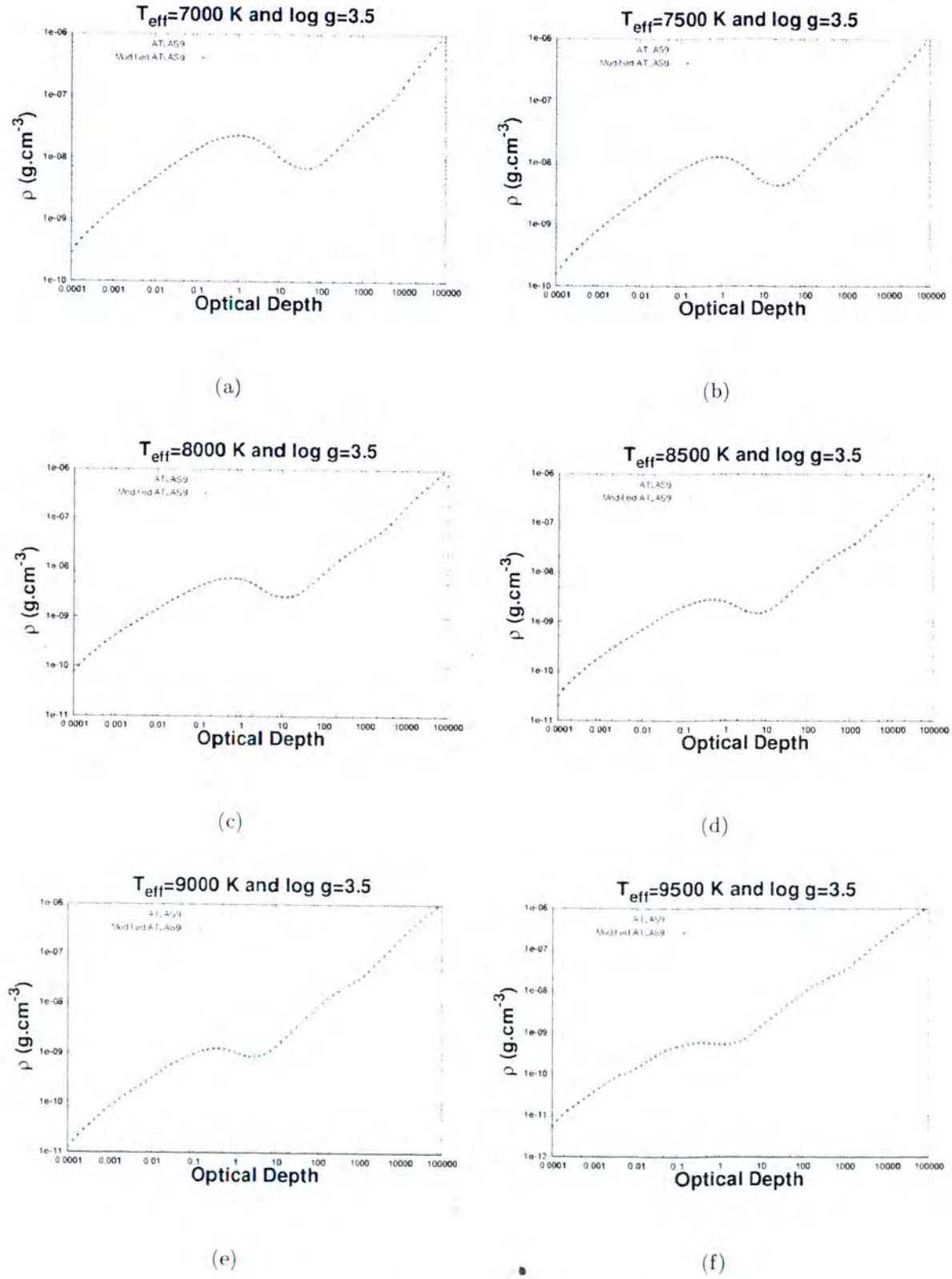

Figure 3.1: Plots of the density as a function of optical depth for various effective temperatures (T_{eff}=7000 K–9500 K) and surface gravity (log g=3.5). The solid line was calculated using normal ATLAS9 EOS. The crossed line was calculated using ATLAS9 with OPAL EOS. These are models of the atmosphere and upper layers of the envelope.

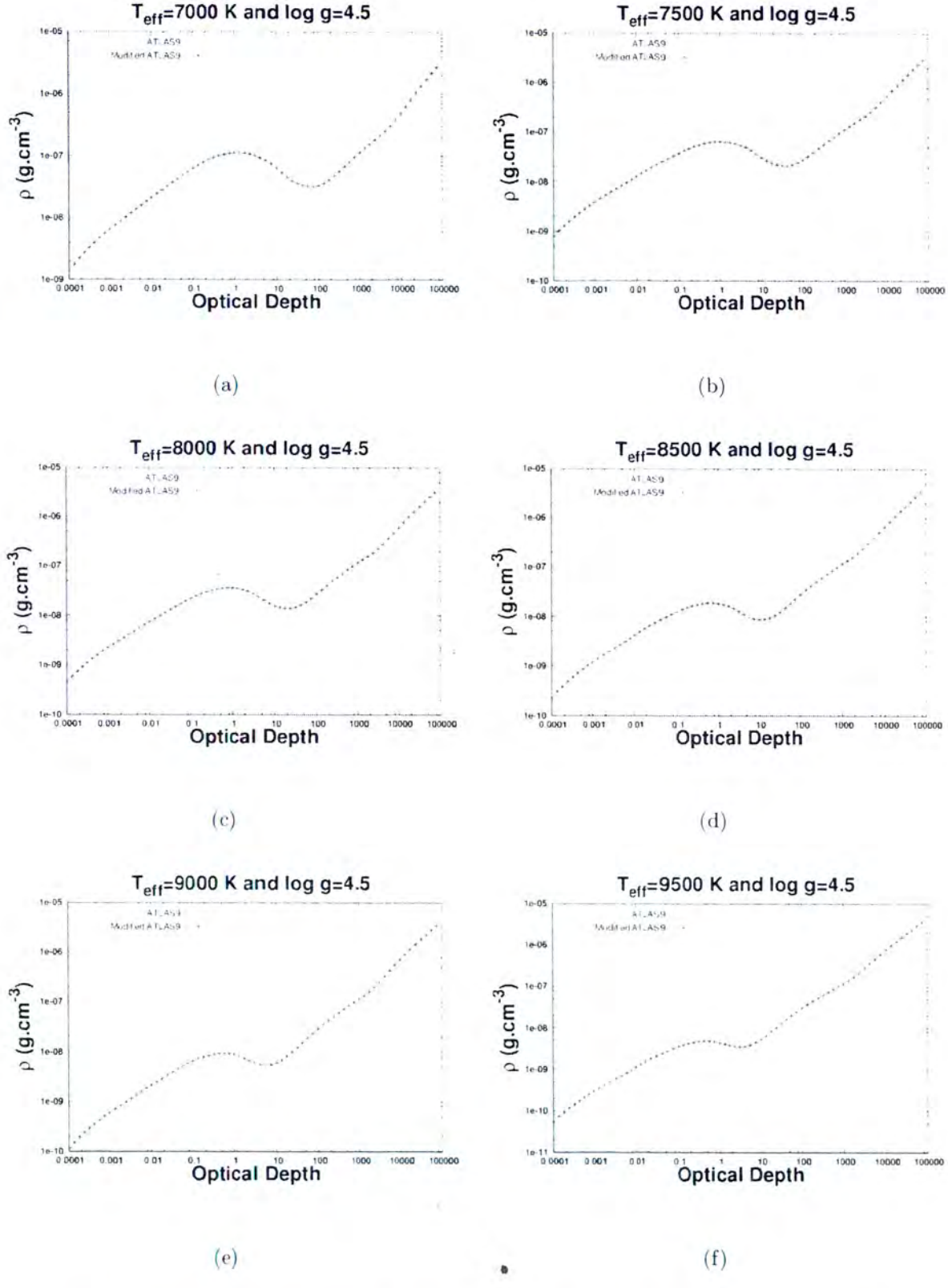

Figure 3.2: Plots of the density as a function of optical depth for various effective temperatures (T_{eff}=7000 K–9500 K) and surface gravity (log g=4.5). The solid line was calculated using normal ATLAS9 EOS. The crossed line was calculated using ATLAS9 with OPAL EOS. These are models of the atmosphere and upper layers of the envelope.

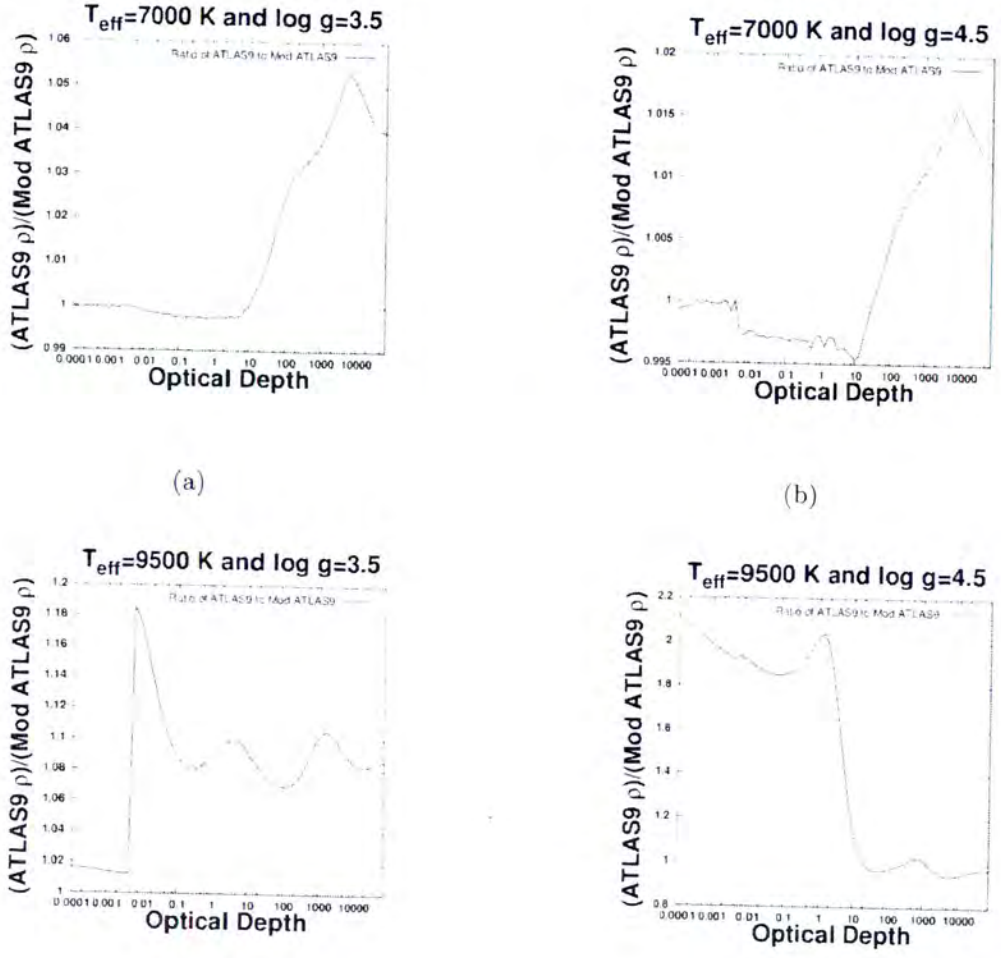

Figure 3.3: The ratio of the old ATLAS9 density to the new ATLAS9 density as a function of optical depth. The ratio was taken over the atmosphere region and the upper layers of the atmosphere.

We have zoomed in on the density plots as seen in **Figure 3.3**. From the Figure at low effective temperatures, the old ATLAS9 and the new ATLAS9 match quite well with the ratio ≈ 1. At these low effective temperatures for high surface gravity values we see an overestimation of the new ρ value to the original ATLAS9 code. The new ρ is then underestimated for high optical

depths. This was observed for **Figure 3.3** (a) & (c). For these low effective temperatures, the percentage difference between the two old ATLAS9 and the new ATLAS9 ranges from 1.5 %–5.5 %. At high effective temperatures, the matching between the old ATLAS9 and the new ATLAS9 prevails for log g=4.5 at high optical depths. For other depths at these high effective temperatures there is an underestimation to the original ρ ATLAS9 model atmosphere value. The resulting percentage difference at these high effective temperatures ranges from 2.8 %–18 %.

3.4 Temperature

We have also calculated temperature for the old ATLAS9 and the new ATLAS9 for various effective temperatures and surface gravity values. By doing our models with varied temperature, surface gravity and chemical composition we can infer the color indices as well as the metal abundances indicators. From this we can possibly do a main sequence of g vs temperature and make a comparison with the interior models. From the stellar interiors going outwards we know the temperature to be decreasing. From the plots in **Figures 3.4–3.5**, the deduction we have made is that we observe good matching between the old ATLAS9 and the new ATLAS9. This is seen in the first five (5) plots of **Figure 3.4**.

The mismatch we observe is for high effective temperatures and higher surface gravity values as seen in **Figure 3.4** (e). This is at effective temperature of T_{eff} =9500 K and log g=4.5. Based on the work done in Chapter 2, there is a great deal of expectation on the OPAL EOS to work well for the atmosphere regime. This is seen in most temperature plots by good matching of the old ATLAS9 to the new ATLAS9 model atmosphere. The temperature profile is constant from the outer layers of the atmosphere towards the hydrogen ionisation zone at ≈ 1. After the hydrogen ionisation zone, there is a steady increase in temperature towards the inner layers of the atmosphere.

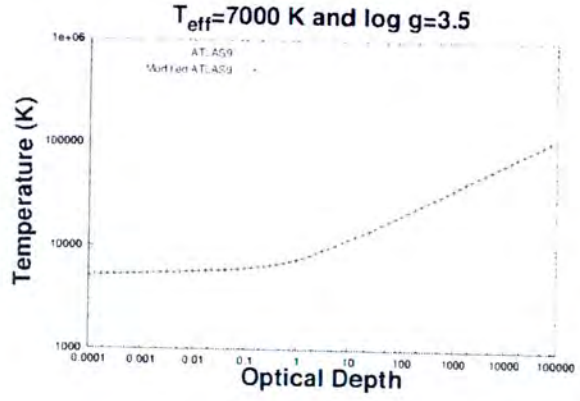

(a)

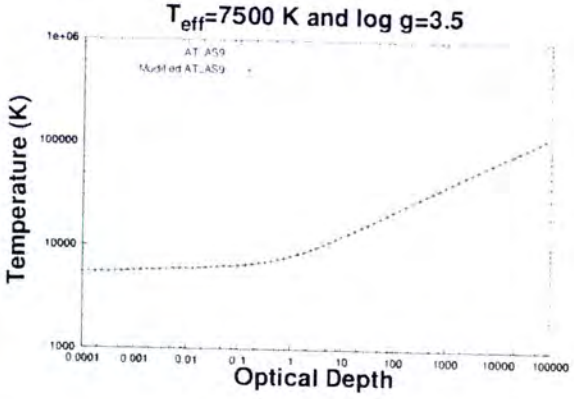

(b)

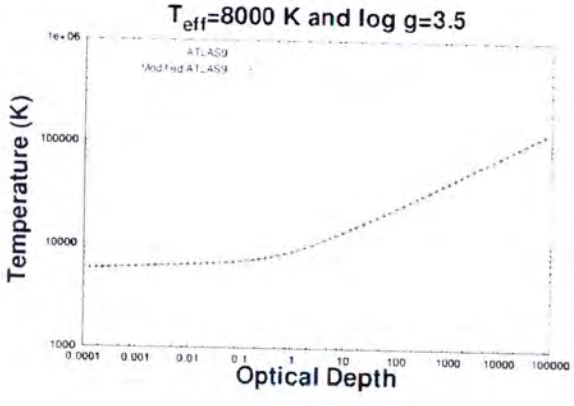

(c)

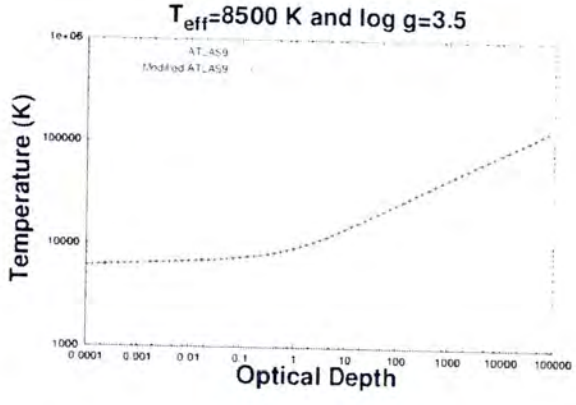

(d)

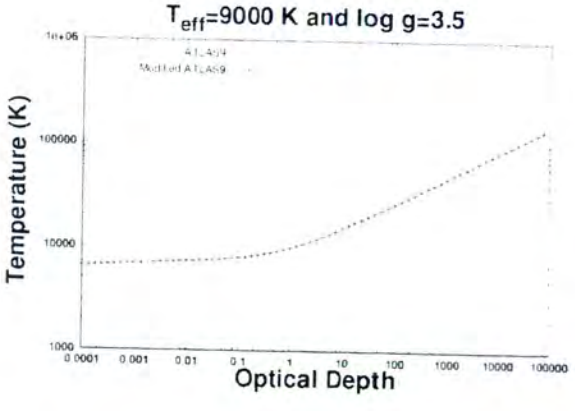

(e)

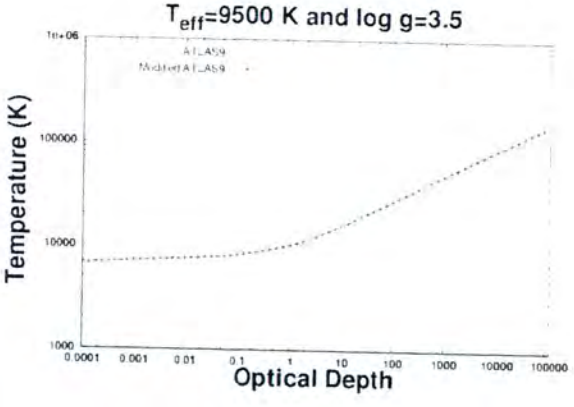

(f)

Figure 3.4: Plots of temperature as a function of optical depth for various effective temperatures (T_{eff}=7000 K–9500 K) and surface gravity (log g=3.5). The solid line was calculated using normal ATLAS9 EOS. The crossed line was calculated using ATLAS9 with OPAL EOS. These are models of the atmosphere and upper layers of the envelope.

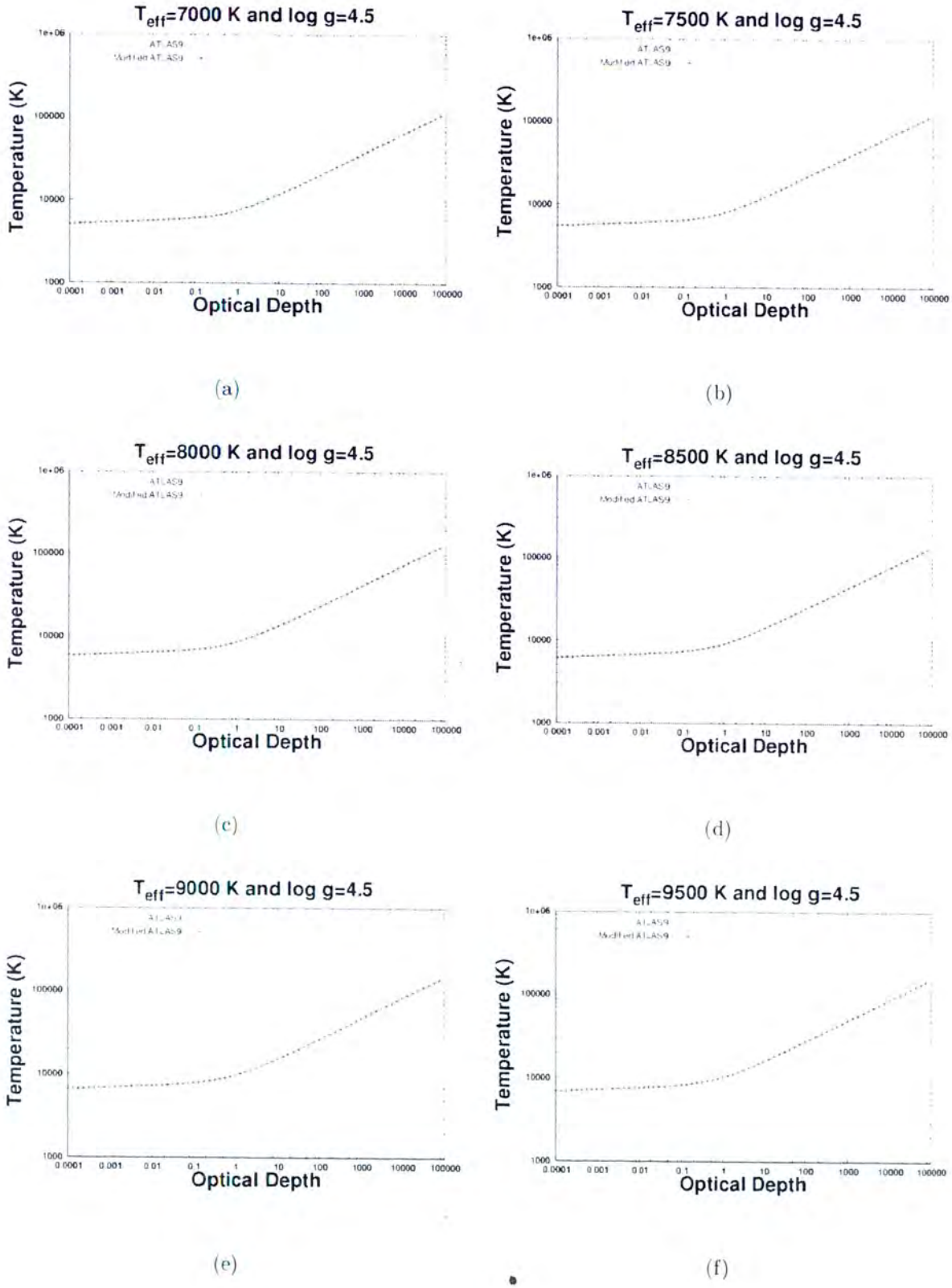

Figure 3.5: Plots of temperature as a function of optical depth for various effective temperatures (T_{eff}=7000 K–9500 K) and surface gravity (log g=4.5). The solid line was calculated using normal ATLAS9 EOS. The crossed line was calculated using ATLAS9 with OPAL EOS. These are models of the atmosphere and upper layers of the envelope.

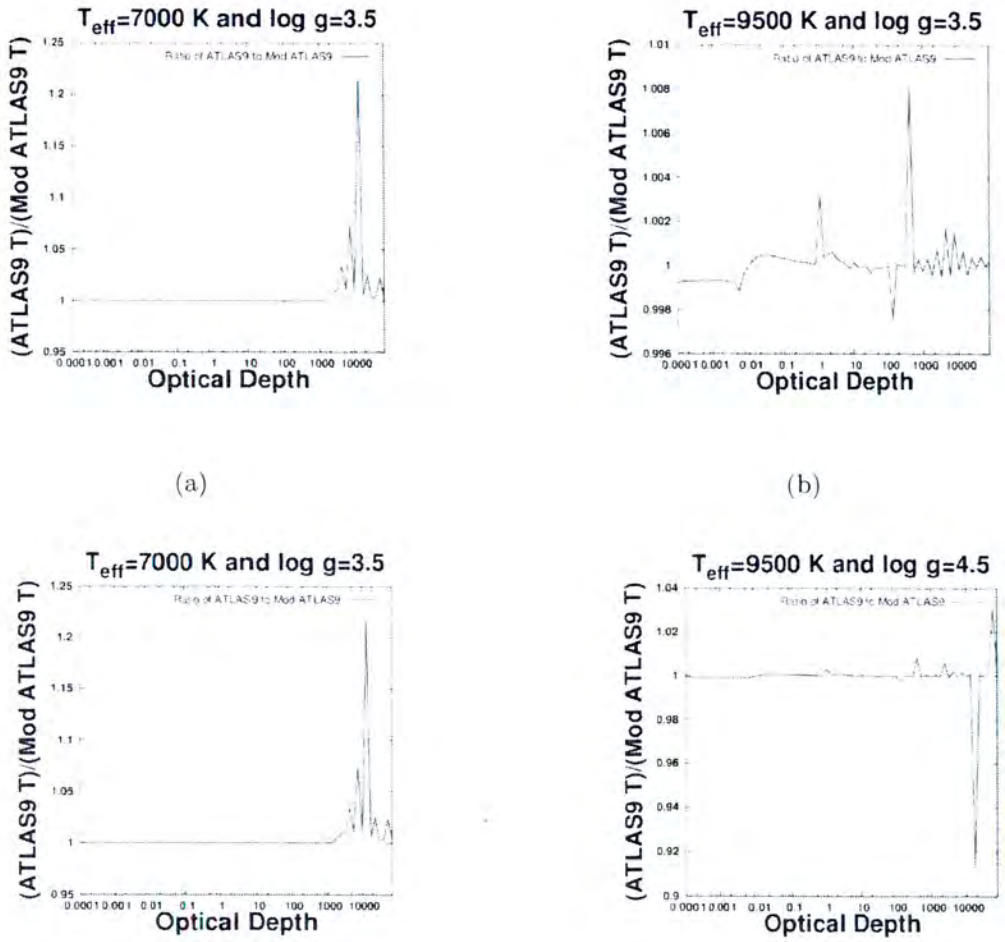

Figure 3.6: The ratio of the old ATLAS9 temperature to the new ATLAS9 temperature as a function of optical depth. The ratio was taken over the atmosphere region and the upper layers of the atmosphere.

We have also zoomed in on the plots for temperature as seen in **Figure 3.6**. At low effective temperatures for all surface gravity values, there is very good matching between the old ATLAS9 and the new ATLAS9 for $0.0001 \leq \tau \leq 1000$. The percentage difference between the two old ATLAS9 and the new ATLAS9 at these low effective temperatures ranges from 14 %–22 %. For

high effective temperatures, the percentage difference between the old ATLAS9 and the new ATLAS9 is 0.8 %.

3.5 Pressure

In **Figures 3.7–3.9**, we present plots for the pressure at the outer parts of a star and the inner parts of a star. As seen in **Figure 3.7**, the pressure has a similar trend to that of the temperature. The pressure increases with increasing optical depth in a star. The pressure and temperature are usually determined by the equations of stellar structure. We see an increase in pressure from

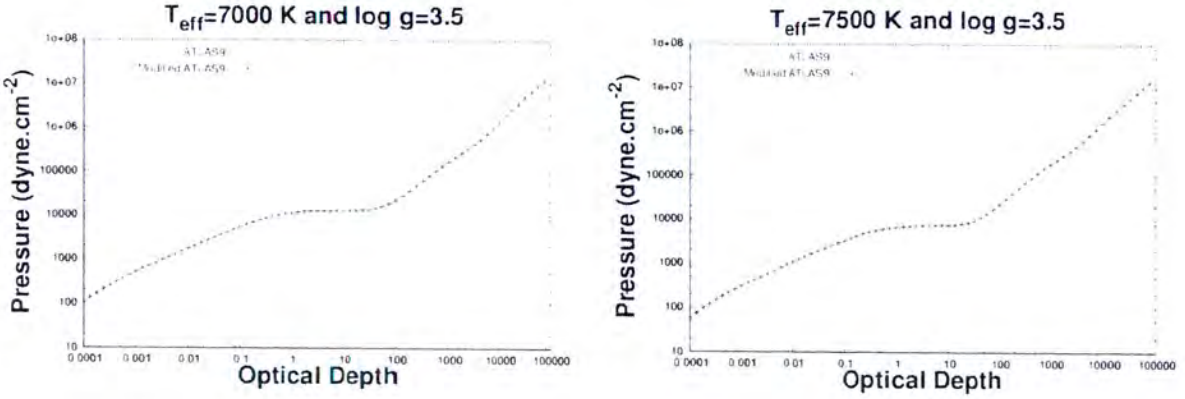

(a) (b)

Figure 3.7: Plots of pressure as a function of optical depth for various effective temperatures (T_{eff}=7000 K–7500 K) and surface gravity (log g=3.5). The solid line was calculated using normal ATLAS9 EOS. The crossed line was calculated using ATLAS9 with OPAL EOS. These are models of the atmosphere and upper layers of the envelope.

the outer layers of the atmosphere to the inner layers of the atmosphere. At the outer layers we see disagreement between the ATLAS9 and the modified ATLAS9. This mismatch is seen at the effective temperatures of T_{eff} = 9500 K and log g= 4.5. We observe good matching between the old ATLAS9 and the new ATLAS9 for outer layers of the atmosphere. We have also seen that

NWU LIBRARY

during the hydrogen ionisation zones the pressure stayed constant.

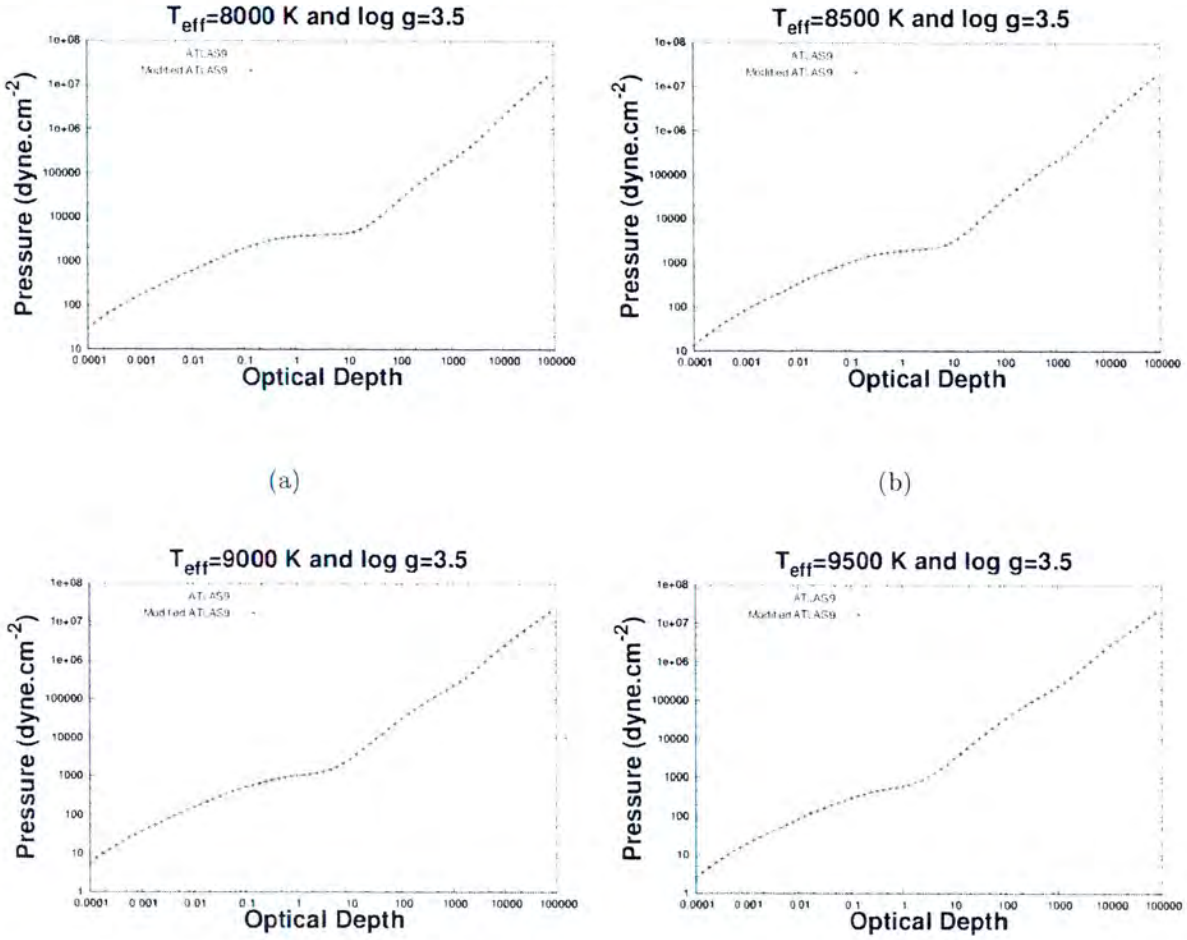

(a) (b)

(c) (d)

Figure 3.8: Plots of pressure as a function of optical depth for various effective temperatures (T_{eff}=8000 K–9500 K) and surface gravity (log g=3.5). The solid line was calculated using normal ATLAS9 EOS. The crossed line was calculated using ATLAS9 with OPAL EOS. These are models of the atmosphere and upper layers of the envelope.

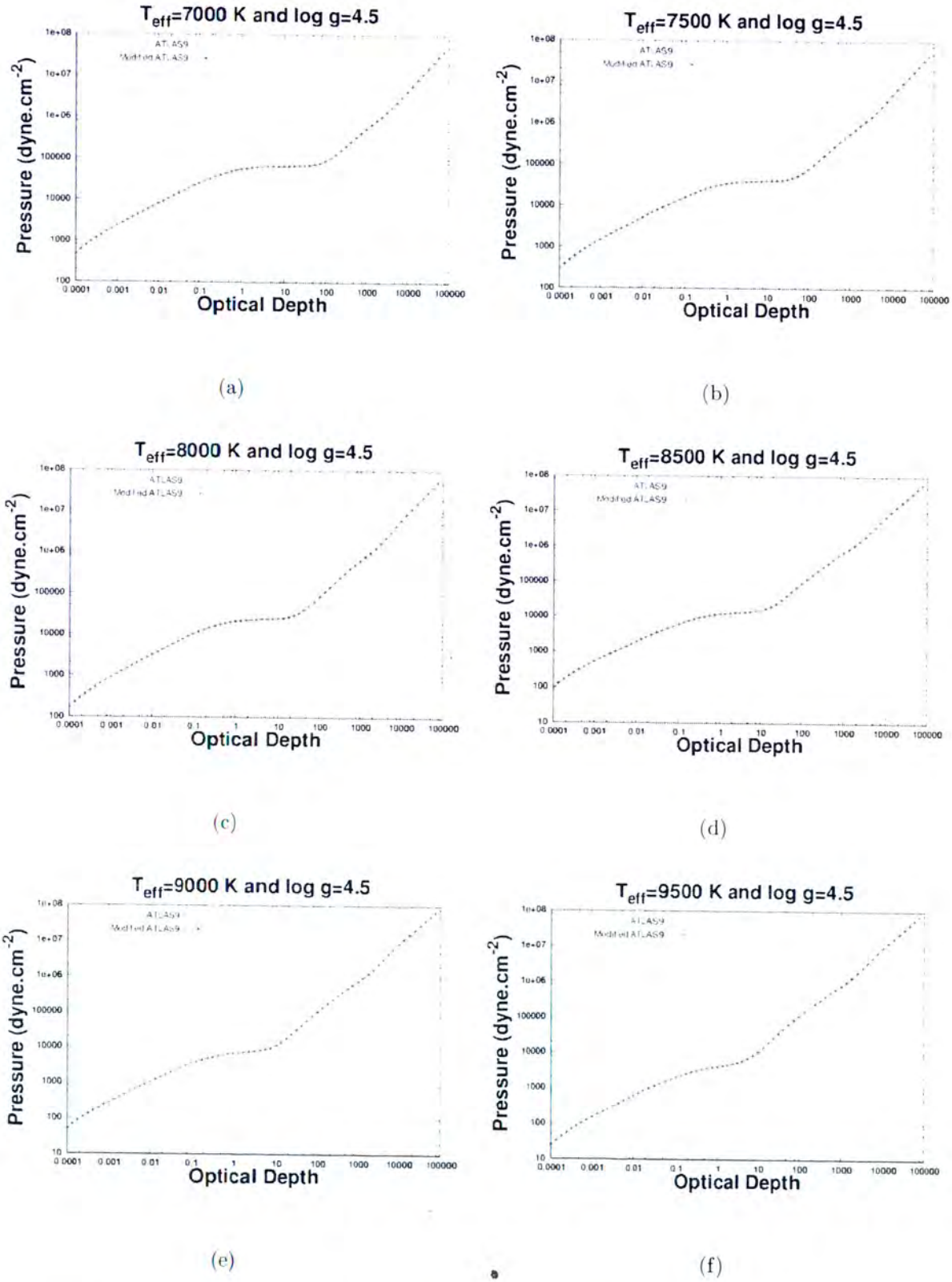

Figure 3.9: Plots of pressure as a function of optical depth for various effective temperatures (T_{eff}=7000 K–9500 K) and surface gravity (log g=4.5). The solid line was calculated using normal ATLAS9 EOS. The crossed line was calculated using ATLAS9 with OPAL EOS. These are models of the atmosphere and upper layers of the envelope.

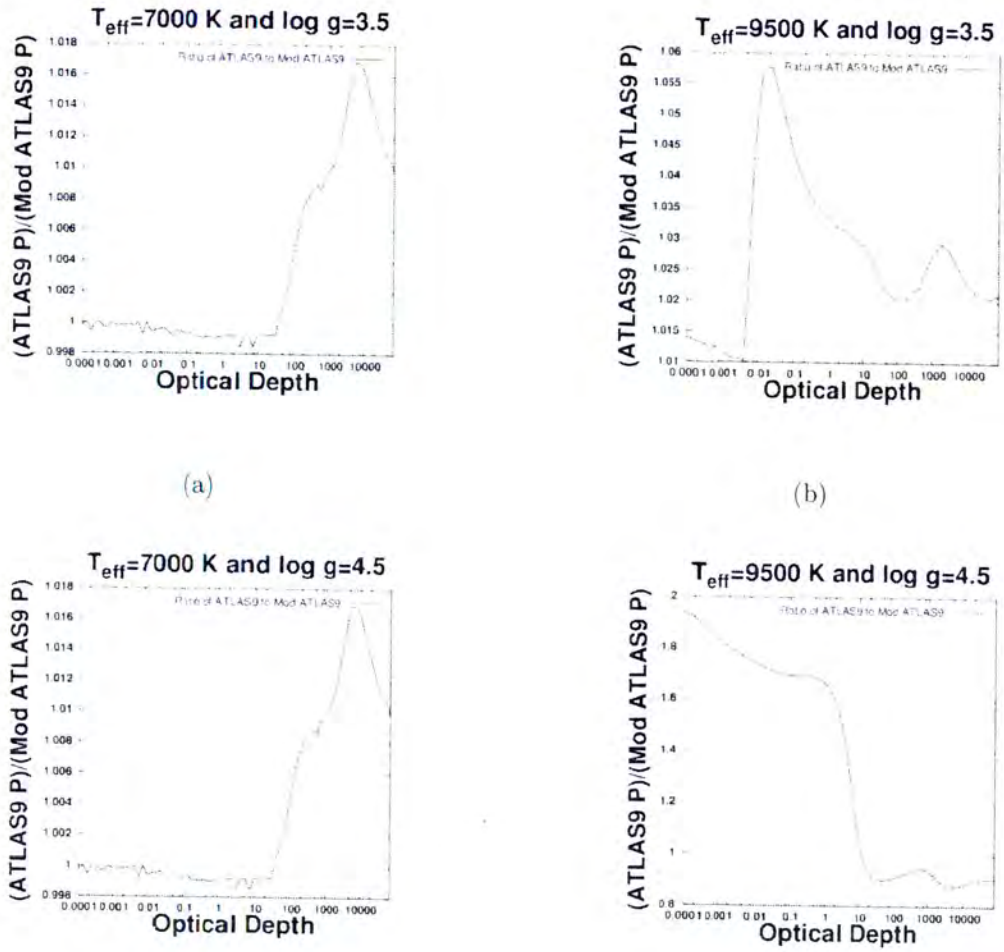

Figure 3.10: The ratio of the old ATLAS9 pressure to the new ATLAS9 pressure as a function of optical depth. The ratio was taken over the atmosphere region and the upper layers of the atmosphere.

We have also zoomed in on the pressure plot for the old ATLAS9 and the new ATLAS9. This was also done by taking the ratio between the two. As seen in **Figure 3.10** for low effective temperatures, there is very good matching with the ratio ≈ 1 between the new ATLAS9 and the old ATLAS9 at optical depths $0.0001 \leq \tau \leq 50$. At higher optical depths ($\tau > 50$) the

original ATLAS9 code has a pressure value that is bigger than that of the modified ATLAS9 code. At high effective temperatures there is a mismatch between the old ATLAS9 and the new ATLAS9 for a wide range in optical depths, with the original ATLAS9 code having a bigger value in pressure than the modified ATLAS9 code. As seen from **Figure 3.10**, we calculated the percentage difference to be ranging from 0.65 %–1.7 % for low effective temperatures. At high effective temperatures the percentage difference ranges between 0.7 %–5.5 %.

3.6 Electron Density

The electron density is the number of electrons per unit volume. We have also determined this electron density for temperature ranges of 6500 K $\leq T_{eff} \leq$ 9500 K and log g=3.5, 4.0 and 4.5. This was done for the atmosphere and much deeper layers in the atmosphere. Since the polarisation is caused by the electron scattering, decreasing of electron density causes the decrease of optical depth. This is seen in **Figure 3.11** for lower optical depths towards the surface and higher optical depths at the inner layers of the atmosphere. From **Figure 3.11**, we have observed that the ionisation zone is less prominent for higher effective temperatures as seen in **Figure 3.11** (f). The zones we see at these temperatures are located near the surface, this is when we see a slight decrease in electron density and this implies a decrease in mass for this particular region. The effect of a decrease in mass is that we will not have enough mass available in this region to drive the oscillations effectively. At lower effective temperatures we observed the ionisation zones moving closer to the surface. The inclusion of OPAL EOS in ATLAS9 results in good matching to the original ATLAS9 electron density profile. We see this good matching for lower effective temperatures and higher effective temperatures.

For OPAL EOS in the envelope, it is important to note that the ionisation zone shown in **Figure 3.11** depends on the temperature and the electron density. From this we can deduce that the opacity can be calculated using the grid of temperature and electron density. For pressure ionisation we have the star being affected by the electron degeneracy.

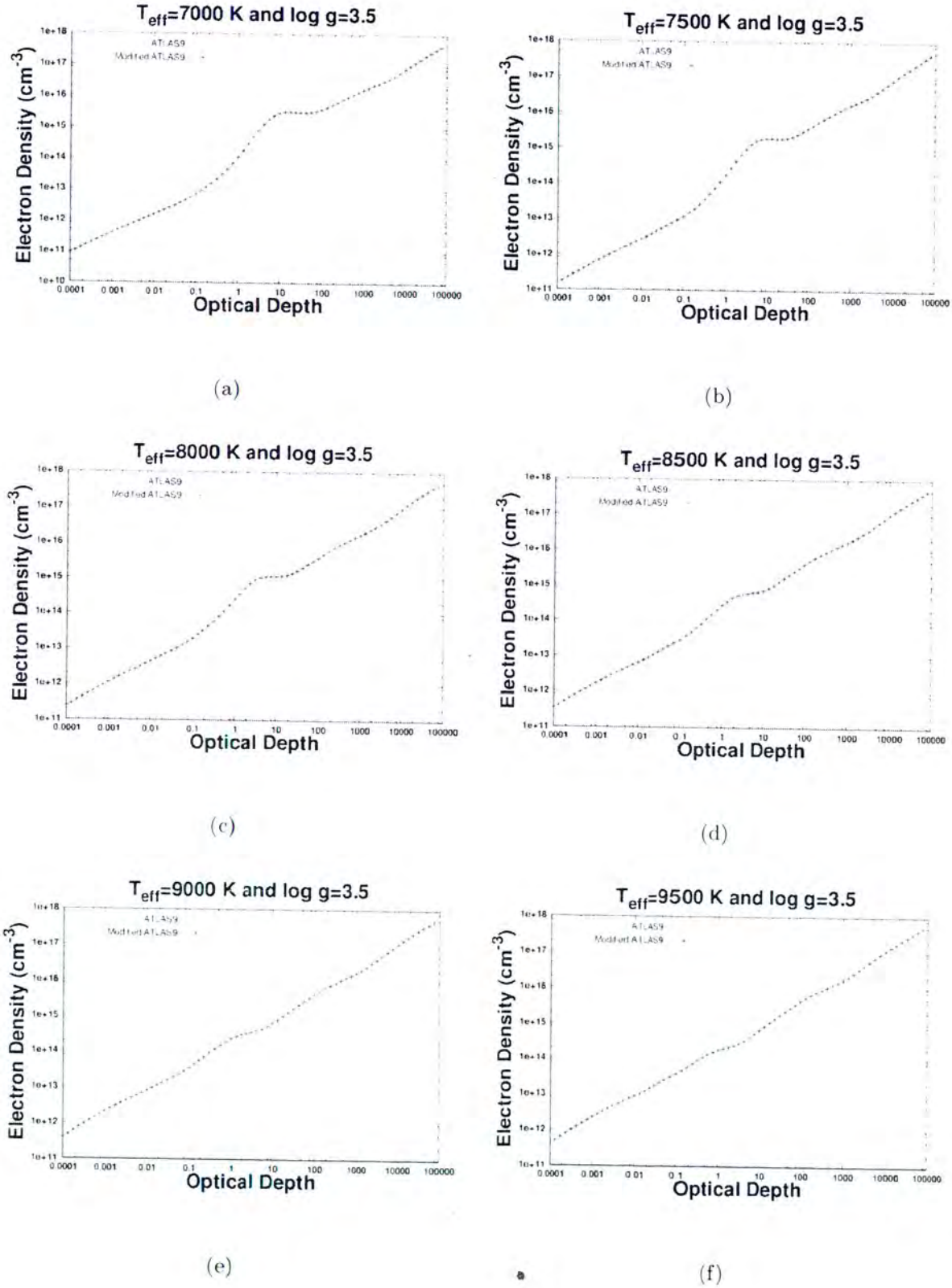

Figure 3.11: Plots of the electron density as a function of optical depth for various effective temperatures (T_{eff}=7000 K–9500 K) and surface gravity (log g=3.5). The solid line was calculated using normal ATLAS9 EOS. The crossed line was calculated using ATLAS9 with OPAL EOS. These are models of the atmosphere and upper layers of the envelope.

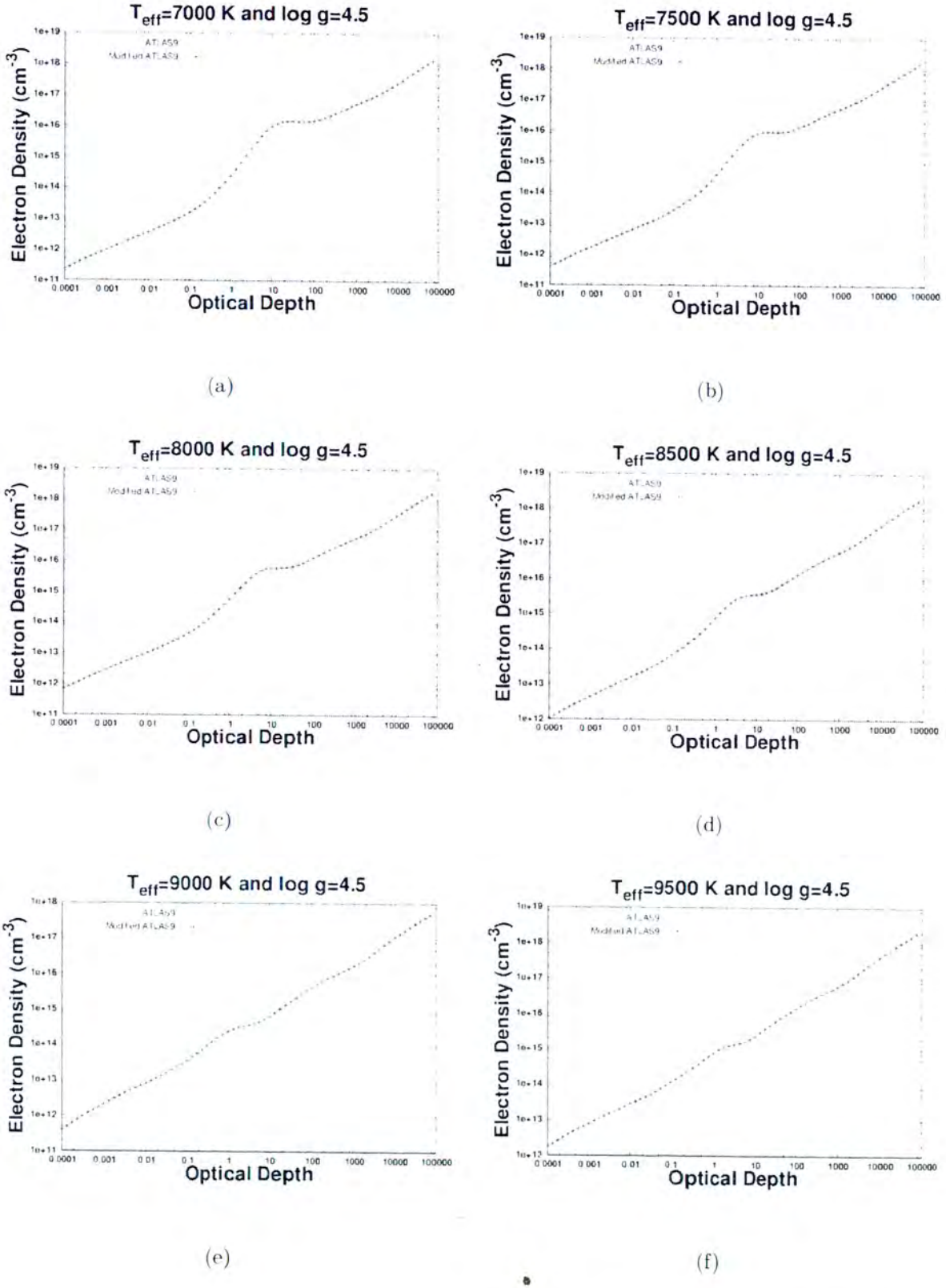

Figure 3.12: Plots of the electron density as a function of optical depth for various effective temperatures (T_{eff}=7000 K–9500 K) and surface gravity (log g=4.5). The solid line was calculated using normal ATLAS9 EOS. The crossed line was calculated using ATLAS9 with OPAL EOS. These are models of the atmosphere and upper layers of the envelope.

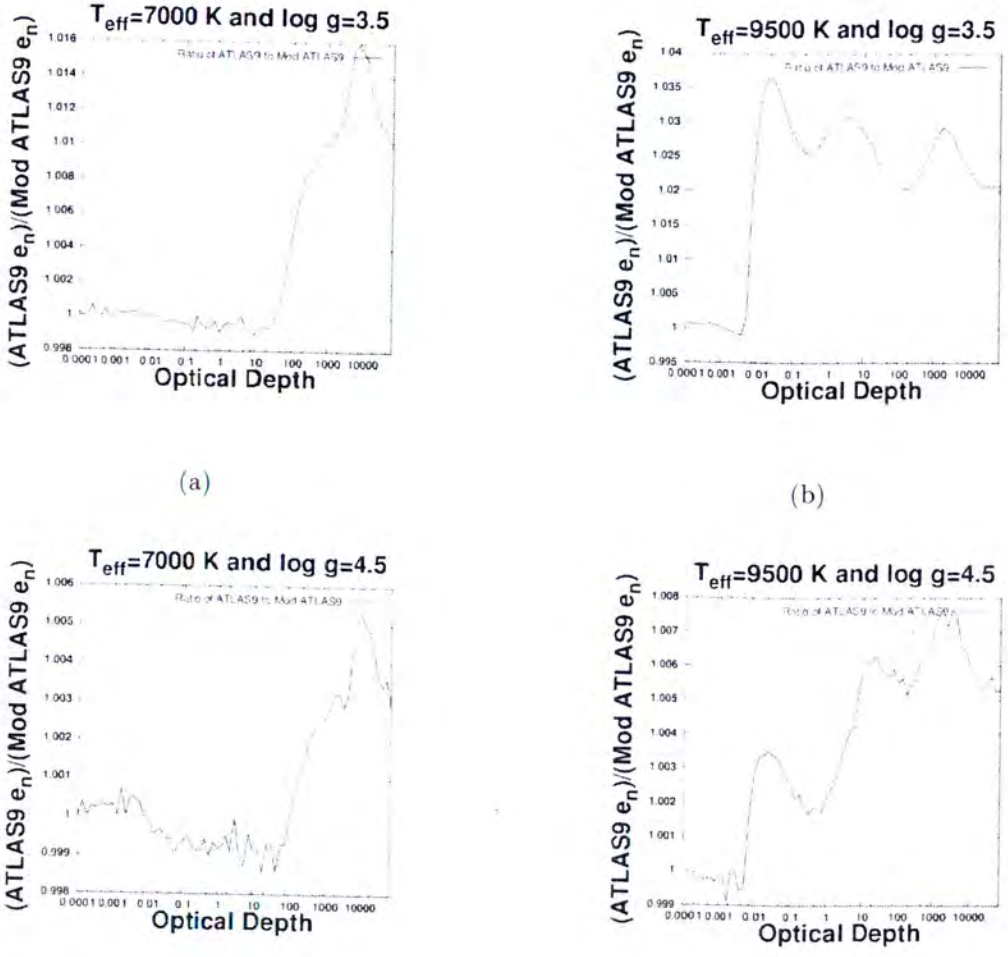

Figure 3.13: The ratio of the old ATLAS9 electron density to the new ATLAS9 electron density as a function of optical depth. The ratio was taken over the atmosphere region and the upper layers of the atmosphere.

Having zoomed in on the electron density for the old ATLAS9 and the new ATLAS9, we have observed that the ratios follow the same argument as the density, temperature and pressure plots for low and high effective temperatures. The percentage difference for low effective temperatures ranges between 0.5 %–1.6 %. For high effective temperatures the percentage differences range

between 0.75 %–3.7 %.

3.7 The Adiabatic Temperature Gradient (∇_{ad})

The adiabatic temperature gradient was also calculated and in **Figures 3.14–3.18**, we present the results thereof. The adiabatic temperature gradient is defined by equation (1.17) for the OPAL model and the ATLAS9 program calculates the adiabatic temperature gradient as

$$\nabla_{ad} = \left(\frac{\partial \ln T}{\partial \ln P}\right)_{ad} - \left(\frac{\partial \ln \rho}{\partial \ln T}\right)_{P_{tot}} \tag{3.1}$$

The plots of the old ATLAS9 and the new ATLAS9 for the temperature gradient is the same for a wide range of optical depths. At higher optical depths ($\tau \approx 60000$), we see bumps in the old ATLAS9 profile and the new ATLAS9 profile. This may be due to the numerical instabilities in the two codes. At relatively higher temperatures (T_{eff} =7000 K) and higher surface gravity we see good matching between the two models. This is in stark contrast to the low temperature values and low surface gravity, where the mismatch is prevalent for high optical depths in the inner layers of the atmosphere. Throughout our survey, we note that good matching is found for log g =4.5 and this is seen in **Figure 3.15**. For extremely higher temperatures and low surface gravity, we see major differences between the old ATLAS9 and the new ATLAS9 (see **Figure 3.15**). We have observed that in the ionisation zones in a star, the adiabatic temperature gradient becomes small because the deep interior is fully ionised.

When analysing the results for this thermodynamic variable we noted the following; at higher surface gravities (log g=4.5) and low temperatures (T_{eff}) we see good matching between the original ATLAS9 code and the modified version of ATLAS9. This is seen for **Figure 3.14** (a) and **Figure 3.15** (a). At these low temperatures there are bumps observed in deeper atmosphere layers. This is seen for **Figure 3.14** (a) & (b) and **Figure 3.15** (a). At the low effective temperatures, we have observed that good matching between the two ATLAS9 codes is seen for low optical depths at the stellar surface. The opposite happens at higher optical depths where

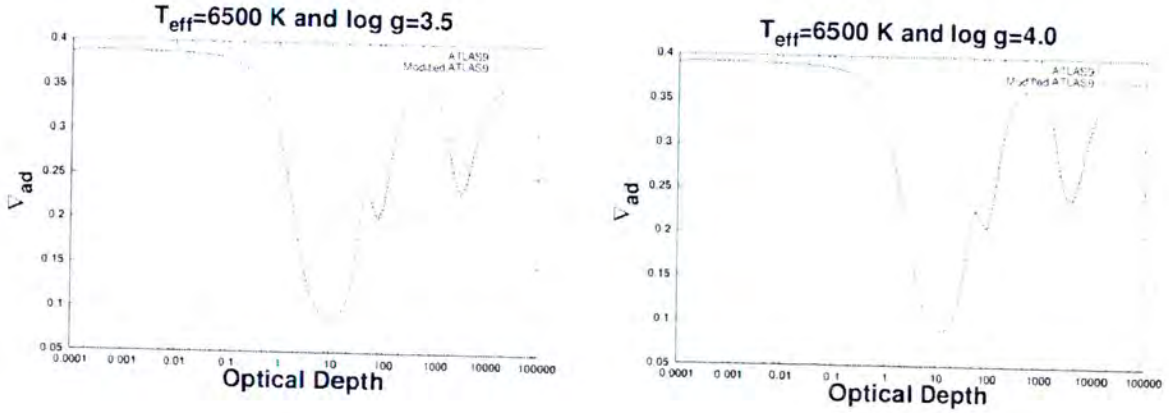

(a) (b)

Figure 3.14: Plots of the adiabatic temperature gradient (∇_{ad}) as a function of optical depth for effective temperature T_{eff}=6500 K and various surface gravities (log g=3.5 & log g=4.0). The solid line was calculated using normal ATLAS9 EOS. The dotted line was calculated using ATLAS9 with OPAL EOS. These are models of the atmosphere and upper layers of the envelope.

there is a mismatch observed.

When we move towards intermediate temperatures (7500 K $\leqslant T_{eff} \leqslant$ 8500) we observed the following; at low surface gravity there is a disagreement between the old ATLAS9 and the new ATLAS9 for ranges $40 \leqslant \tau \leqslant 10000$. This mismatch slowly narrows as we move towards higher surface gravity (log g=4.5). This was observed for **Figure 3.14** (a) & (b) and **Figure 3.15** (a). At higher effective temperatures we observed the adiabatic temperature gradient starting at a slightly lower value below 0.3. We have also observed that the high surface gravity values decreases the mismatch between the old ATLAS9 and the new ATLAS9 while for high effective temperatures we observed a great deal of mismatch between the old ATLAS9 and the new ATLAS9. This argument is seen in **Figure 3.18** and we further observed that high effective temperatures decreases the value of the adiabatic temperature gradient at the stellar surface.

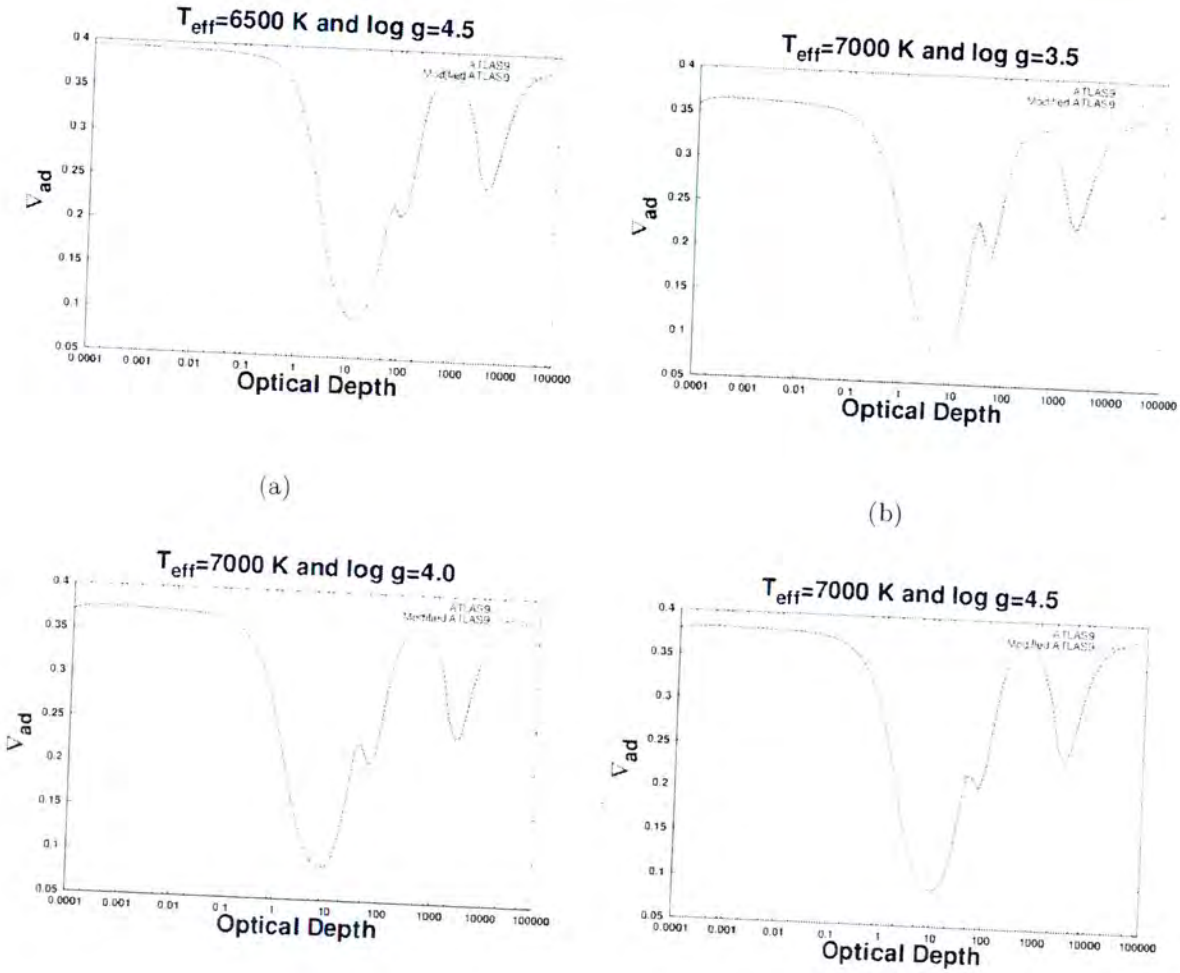

(a) (b) (c) (d)

Figure 3.15: Plots of the adiabatic temperature gradient (∇_{ad}) as a function of optical depth for various effective temperatures (T_{eff}=6500 K–7000 K) and surface gravities (log g=3.5–4.5). The solid line was calculated using normal ATLAS9 EOS. The dotted line was calculated using ATLAS9 with OPAL EOS. These are models of the atmosphere and upper layers of the envelope.

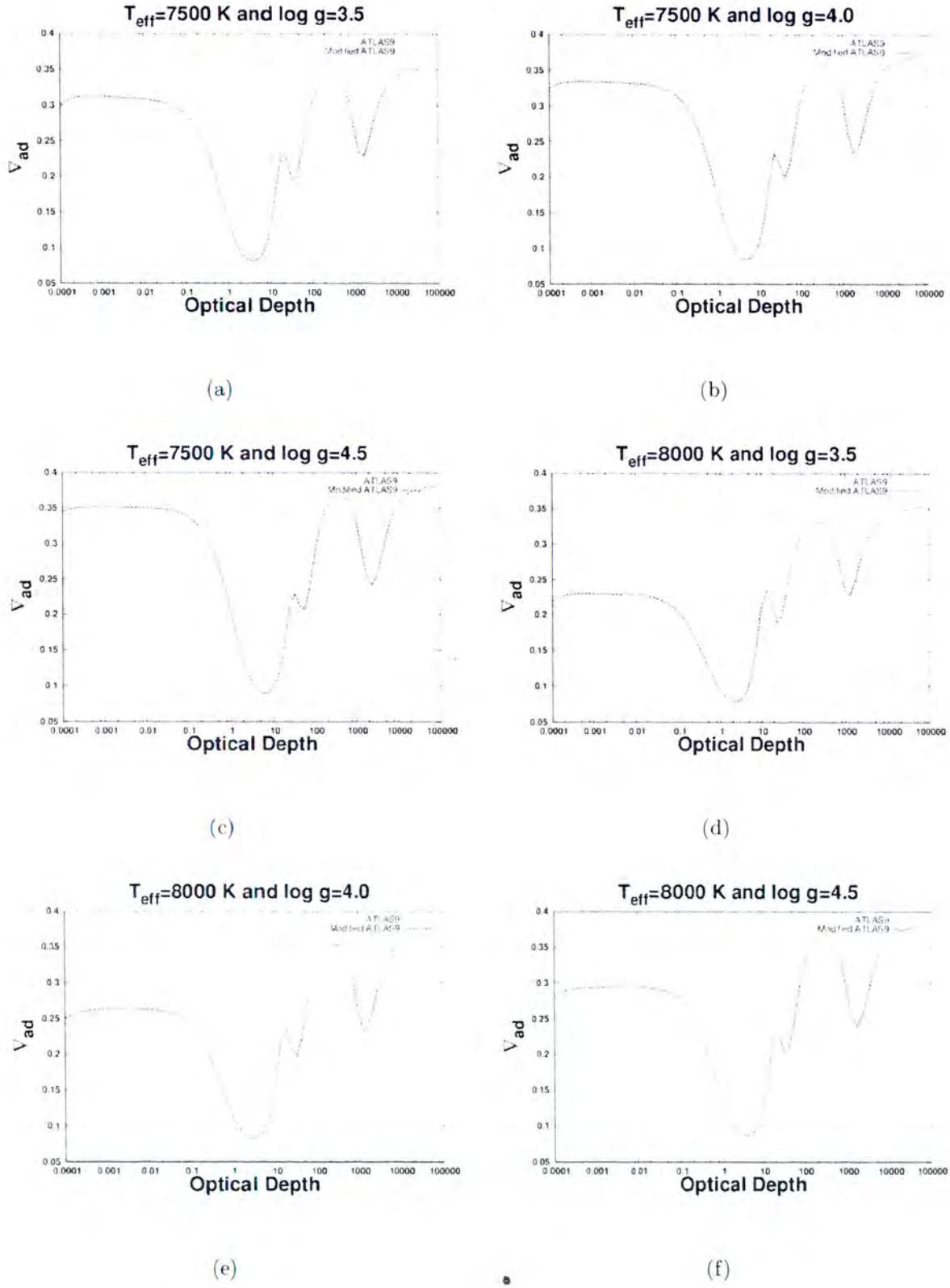

(a) (b)

(c) (d)

(e) (f)

Figure 3.16: Plots of the adiabatic temperature gradient (∇_{ad}) as a function of optical depth for various effective temperatures (T_{eff}=7500 K–8000 K) and surface gravities (log g=3.5–4.5). The solid line was calculated using normal ATLAS9 EOS. The dotted line was calculated using ATLAS9 with OPAL EOS. These are models of the atmosphere and upper layers of the envelope.

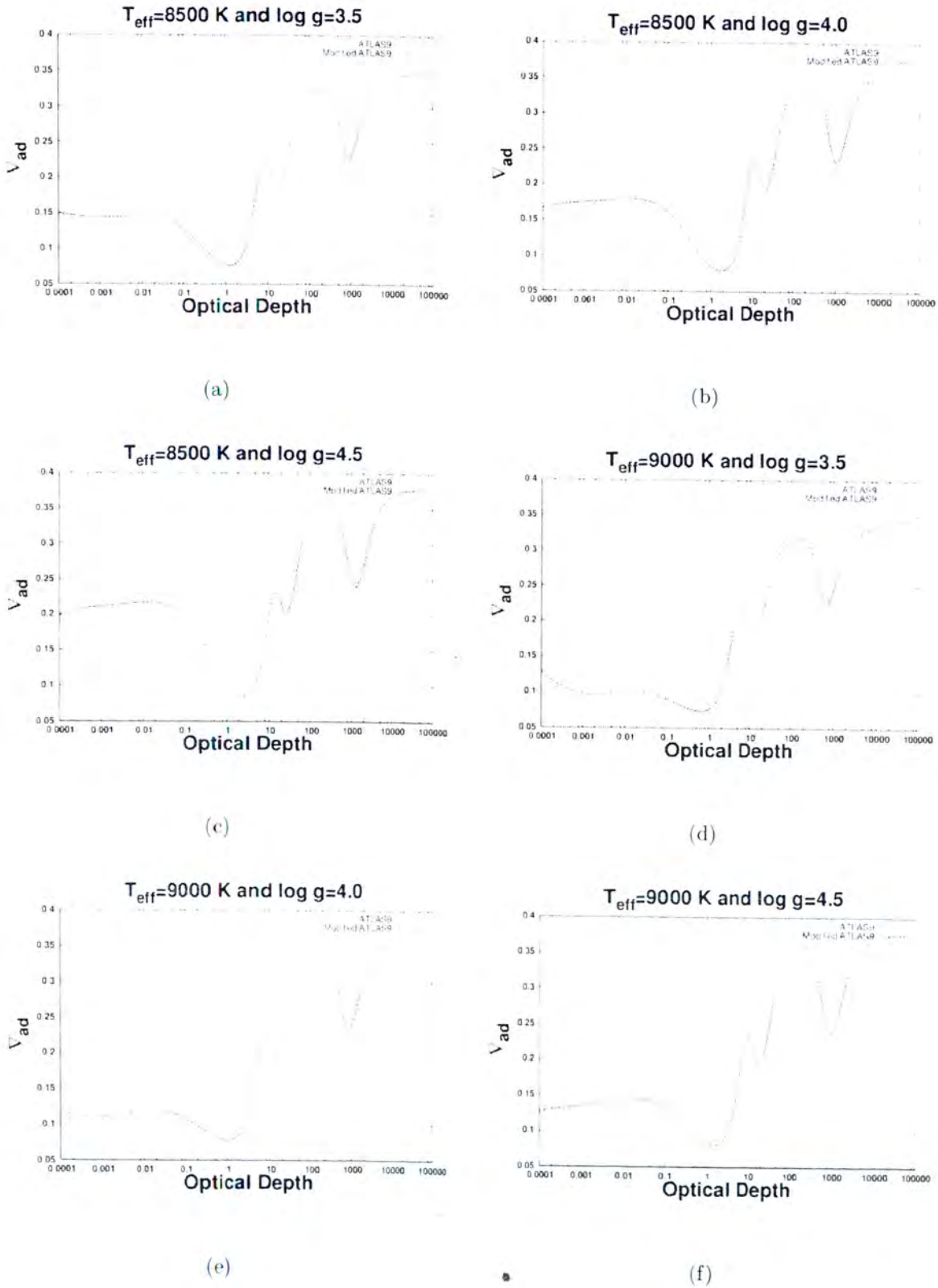

(a) (b) (c) (d) (e) (f)

Figure 3.17: Plots of the adiabatic temperature gradient (∇_{ad}) as a function of optical depth for various effective temperatures (T_{eff}=8500 K–9000 K) and surface gravities (log g=3.5–4.5). The solid line was calculated using normal ATLAS9 EOS. The dotted line was calculated using ATLAS9 with OPAL EOS. These are models of the atmosphere and upper layers of the envelope.

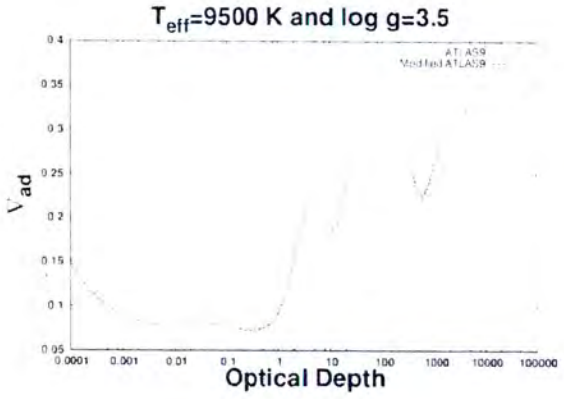

(a)

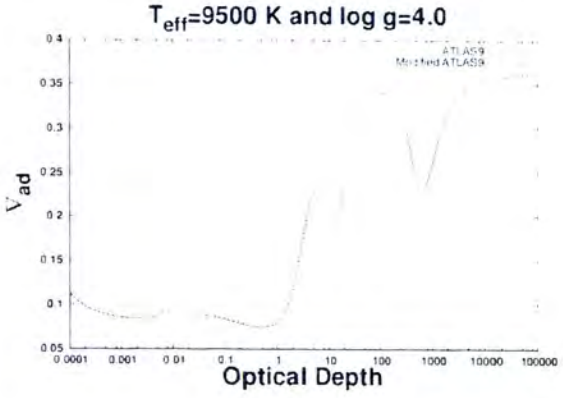

(b)

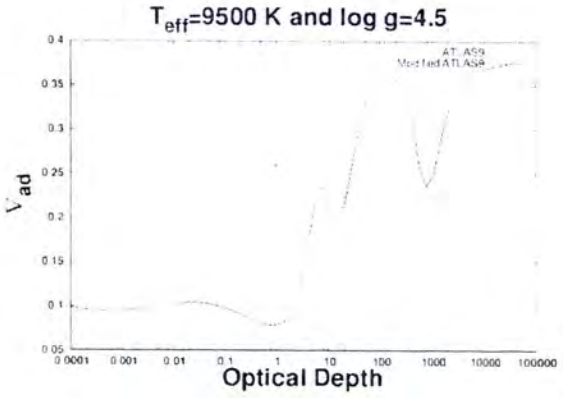

(c)

Figure 3.18: Plots of the adiabatic temperature gradient (∇_{ad}) as a function of optical depth for effective temperature T_{eff}=9500 K and surface gravities (log g=3.5–4.5). The solid line was calculated using normal ATLAS9 EOS. The dotted line was calculated using ATLAS9 with OPAL EOS. These are models of the atmosphere and upper layers of the envelope.

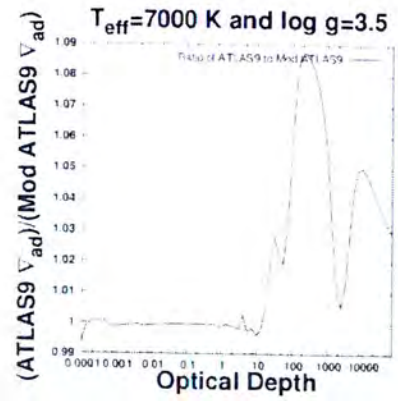

(a)

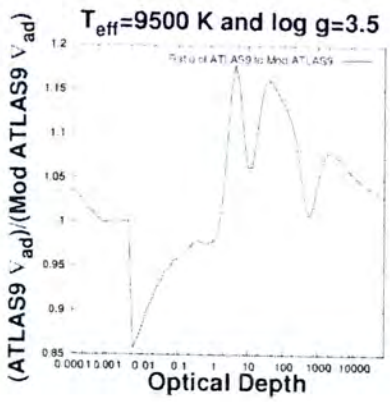

(b)

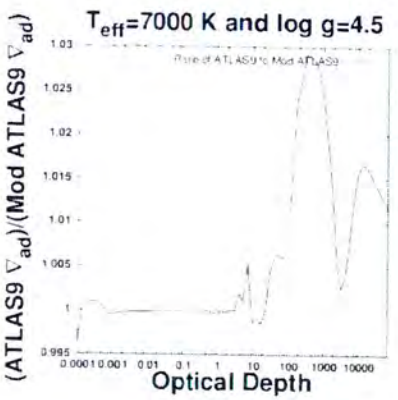

(c)

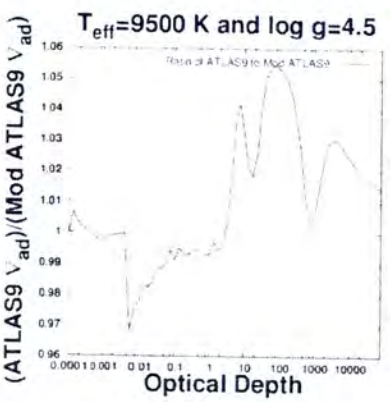

(d)

Figure 3.19: The ratio of the old ATLAS9 adiabatic temperature gradient to the new ATLAS9 adiabatic temperature gradient as a function of optical depth. The ratio was taken over the atmosphere region and the upper layers of the atmosphere.

As seen from **Figure 3.19** good matching prevails between the old ATLAS9 and the new ATLAS9 for optical depths $0.0001 \leq \tau \leq 5.0$. The new adiabatic temperature gradient from our modified ATLAS9 code is less than the original ATLAS9 code value for optical depths ≥ 5.0. This was observed for both low effective temperatures and high effective temperatures. The percentage

difference for low effective temperatures was calculated to be in ranges 2.8 %–8.5 %. For high effective temperatures the differences was calculated to be ranging between 5.4 %–18 %.

3.8 The first Adiabatic Exponent (Γ_1)

In **Figures 3.20–3.23**, we present plots for the first adiabatic exponent (Γ_1). This adiabatic exponent is defined as

$$\Gamma_1 = \frac{V_s^2 \times \rho}{P} \tag{3.2}$$

where V_s is the speed of sound, ρ is the density and P is the pressure. The Γ_1 function has the same profile as the adiabatic temperature gradient. Also the profile of our modified ATLAS9 program is the same as that of the original ATLAS9 program. The various ionisation zones are prominent as well. We have observed that for low effective temperatures the mismatch is narrowed as we gradually move towards the high surface gravity. The bumps are seen as well for much deeper layers in the atmosphere as seen in **Figure 3.20** (a),(b) and (c). The mismatch at low optical depths is seen for Γ_1 but it is not clearly seen at high surface gravities. What we have seen as well is that as the temperature increases the ionisation zones move closely towards the surface. Additionally, what we have observed is that for high surface gravities the profile flattens out at low optical depths. We have observed that at lower optical depths, the profile of the modified ATLAS9 code is much steeper than the original ATLAS9 code. However, at high temperatures there appears to be numerical instabilities in the modified ATLAS9 code. This is seen for $0.001 \leqslant \tau \leqslant 0.01$. At the hydrogen ionisation zone, we observed that at lower effective temperatures ($\leqslant$ 7500 K) the old ATLAS9 and the new ATLAS9 match fairly well. However, at intermediate effective temperatures ($7500 \leqslant T_{eff} \leqslant 8000$ K) we observed a mismatch and the original ATLAS9 code has a higher numerical value than the modified ATLAS9 code. For higher effective temperatures ($\geqslant$), we have observed that as we moved towards high surface gravities, the mismatch gradually decreases. This was observed for **Figure 3.22** (a), (b) and (c). At these higher effective temperatures, the Γ_1 is smaller and closer to one while for lower effective temperatures we observed a higher Γ_1 value towards the surface.

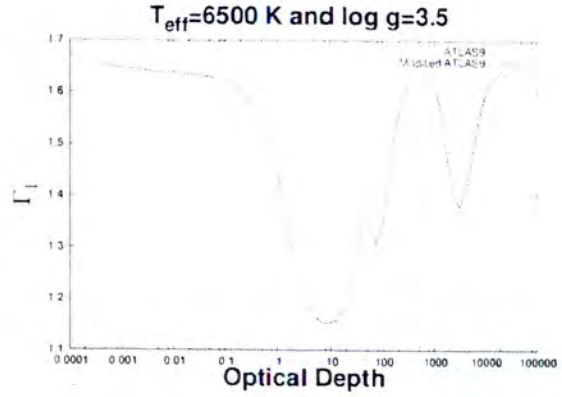

(a)

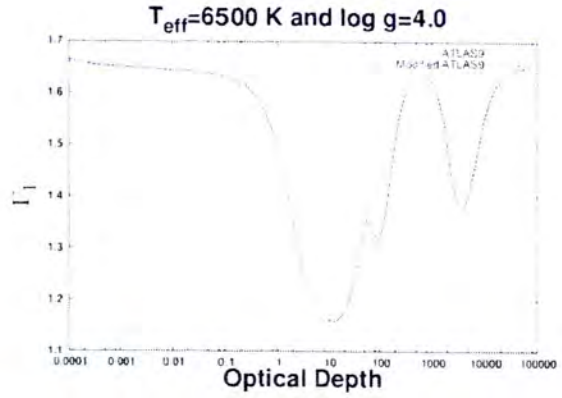

(b)

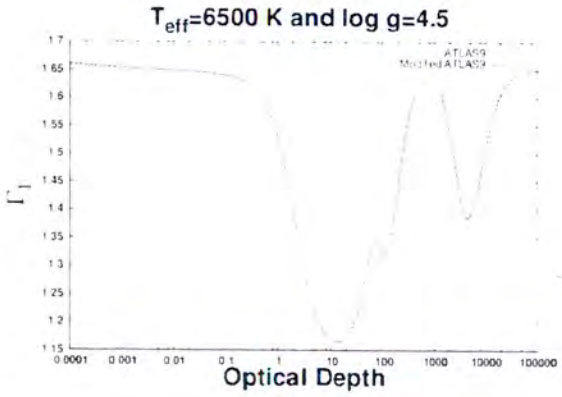

(c)

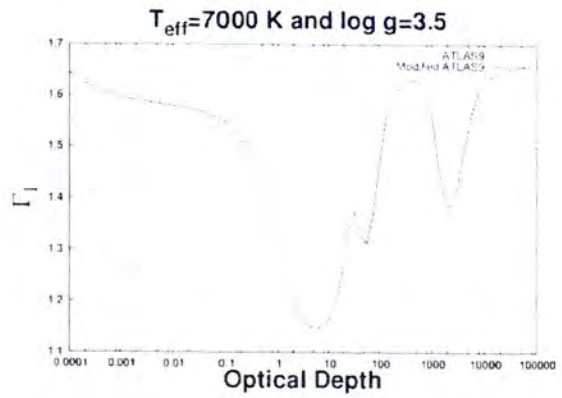

(d)

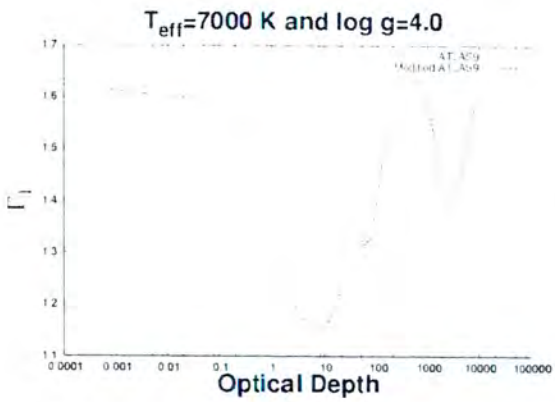

(e)

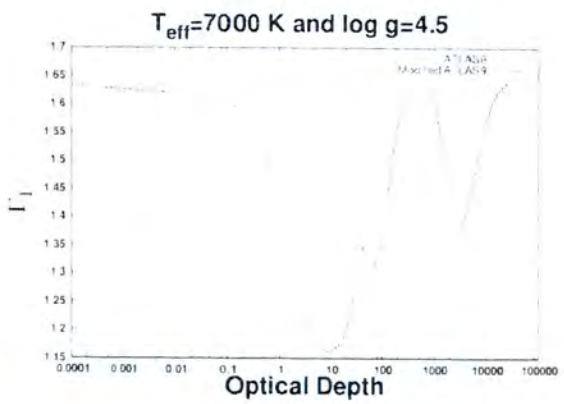

(f)

Figure 3.20: Plots of the first adiabatic exponent (Γ_1) as a function of optical depth for various effective temperatures (T_{eff}=6500 K–7000 K) and surface gravities (log g=3.5–4.5). The solid line was calculated using normal ATLAS9 EOS. The dotted line was calculated using ATLAS9 with OPAL EOS. These are models of the atmosphere and upper layers of the envelope.

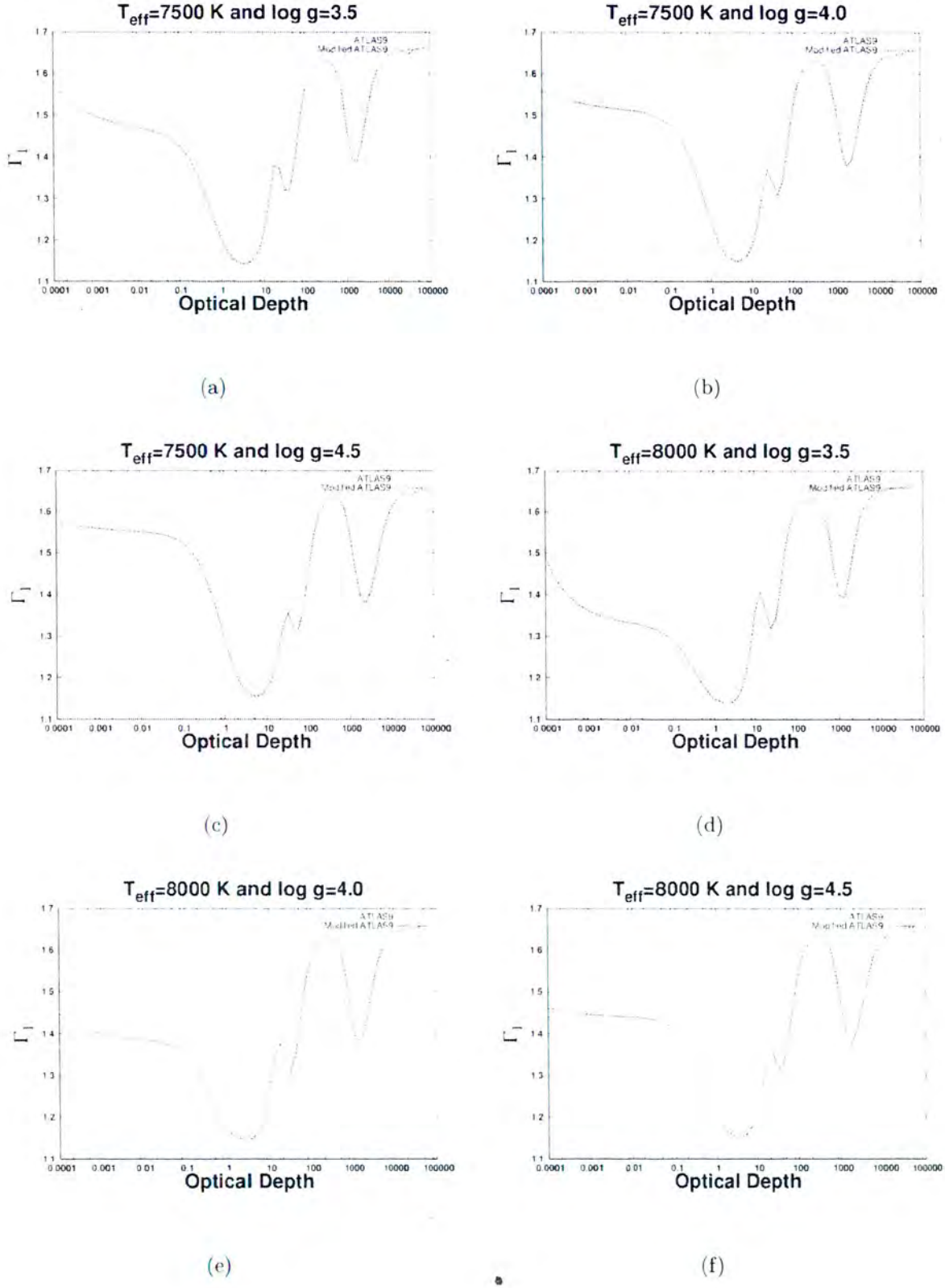

Figure 3.21: Plots of the first adiabatic exponent (Γ_1) as a function of optical depth for various effective temperatures (T_{eff}=7500 K–8000 K) and surface gravities (log g=3.5–4.5). The solid line was calculated using normal ATLAS9 EOS. The dotted line was calculated using ATLAS9 with OPAL EOS. These are models of the atmosphere and upper layers of the envelope.

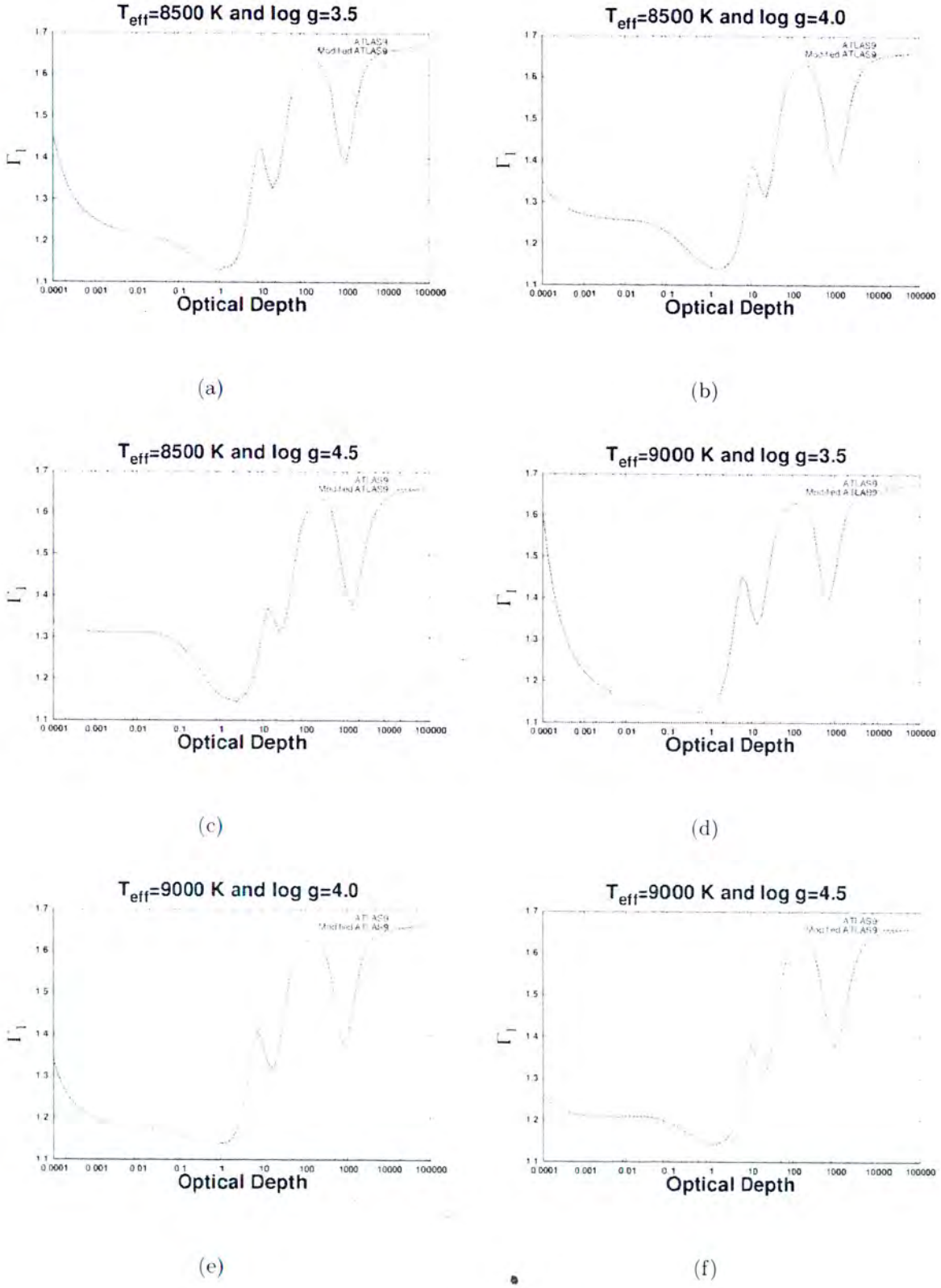

Figure 3.22: Plots of the first adiabatic exponent (Γ_1) as a function of optical depth for various effective temperatures (T_{eff}=8500 K–9000 K) and surface gravities (log g=3.5–4.5). The solid line was calculated using normal ATLAS9 EOS. The dotted line was calculated using ATLAS9 with OPAL EOS. These are models of the atmosphere and upper layers of the envelope.

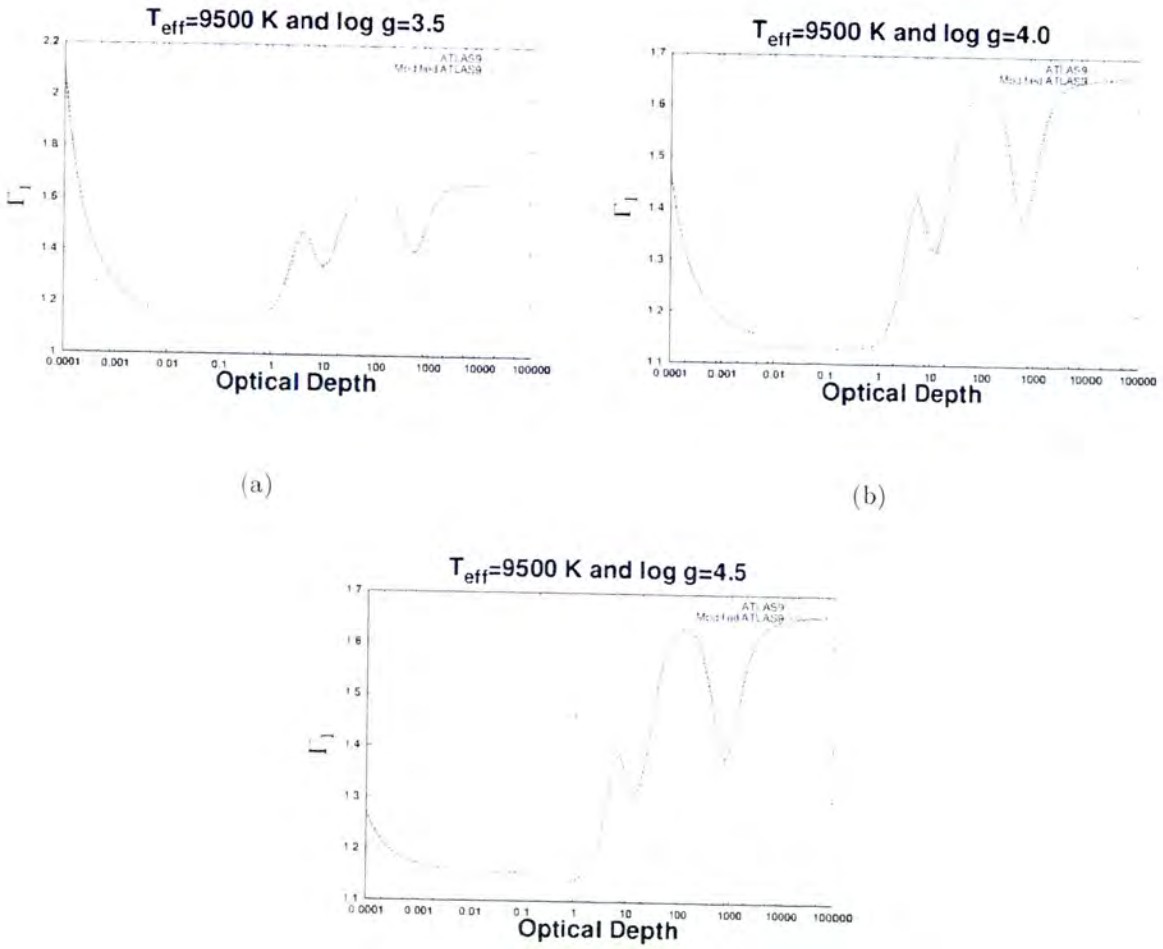

Figure 3.23: Plots of the first adiabatic exponent as a function of optical depth for effective temperature T_{eff}=9500 K and various surface gravities (log g=3.5–4.5). The solid line was calculated using normal ATLAS9 EOS. The dotted line was calculated using ATLAS9 with OPAL EOS. These are models of the atmosphere and upper layers of the envelope.

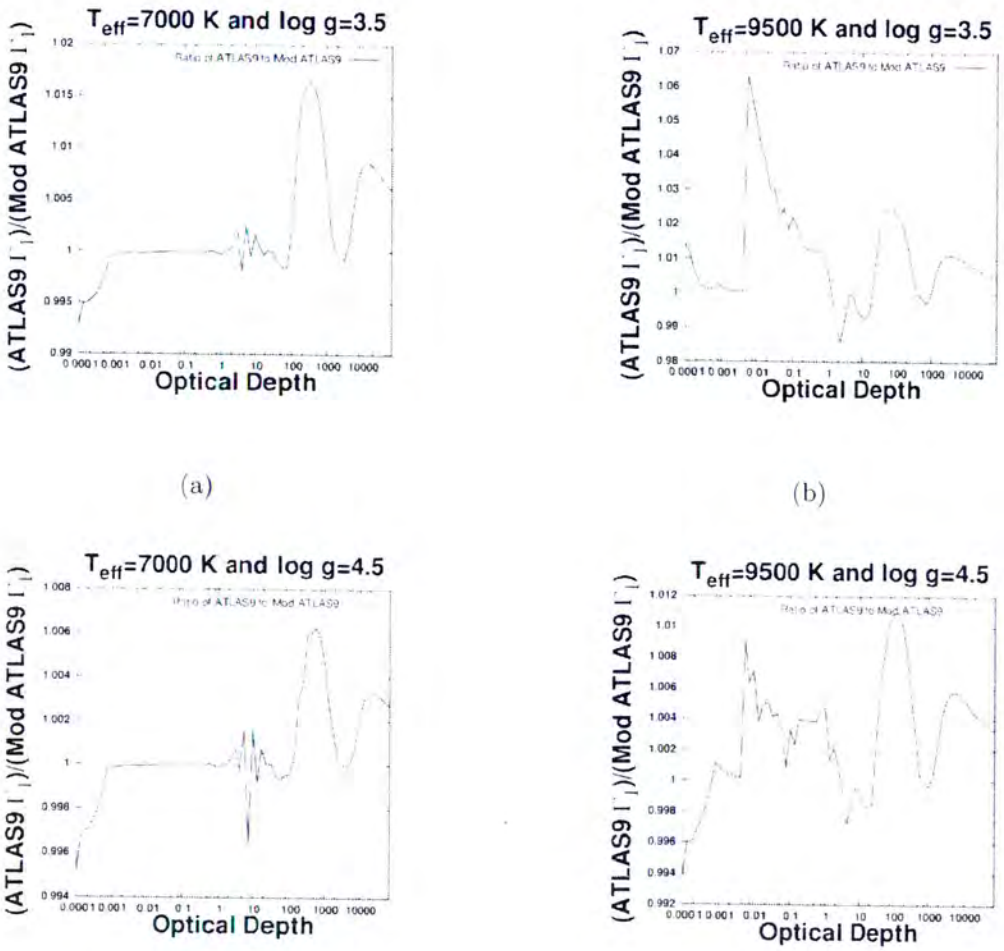

Figure 3.24: The ratio of the old ATLAS9 Γ_1 to the new ATLAS9 Γ_1 as a function of optical depth. The ratio was taken over the atmosphere region and the upper layers of the atmosphere.

As seen in **Figure 3.24**, the ratio of the old ATLAS9 to the new ATLAS9 is ≈ 1 for low optical depths and at high optical depths there is an underestimation of our new Γ_1 value to the original ATLAS9 code value. At higher effective temperatures the agreement between the old ATLAS9 and the new ATLAS9 is seen for low optical depths only. For higher effective temperatures,

the differences between the old ATLAS9 and the new ATLAS9 is seen at optical depths $\geq$ 0.01. The percentage differences between the old ATLAS9 and the new ATLAS9 at low effective temperatures ranges between 0.6 %–1.65 % and for high effective temperature the percentage difference ranges between 1.1 %–6.3 %.

3.9 The Radiative Temperature Gradient (∇_{rad})

In **Figure 3.25–3.27**, we present plots of the Radiative Temperature Gradient (∇_{rad}) defined as

$$\nabla_{rad} = \left(\frac{\partial \ln T}{\partial \ln P}\right)_R = \left(\frac{\partial T}{\partial M}\right)\frac{P_{tot}}{Tg} \tag{3.3}$$

where P_{total} is the total pressure due to the gas pressure, radiation pressure and turbulence pressure while g is the gravity. The first thing we notice are the peaks near optical depth (τ)= 10 and near τ=1000. The main peak near τ=10 is due to the hydrogen ionisation zone, the second peak is peak near τ =1000 is due to the He II ionisation zone. A comparison of ∇_{rad} calculated using ATLAS9 EOS to that calculated using OPAL EOS shows that good matching is observed throughout **Figure 3.25–3.27** except at low optical depths in the outer parts of a star, where there is a mismatch between the two models. As we move towards high effective temperatures we have observed that the other zones start appearing quite visibly as peaks. These are the helium ionisation zones observed at $\tau \approx 10\ 000$. This was observed in **Figure 3.27** for high effective temperatures ($\geqslant$ 8500 K).

In **Figure 3.27** (d), we have observed a mismatch between the two models at the hydrogen ionisation zone. We have also zoomed in on the two models to calculate the percentage difference between the two models. As seen is **Figure 3.28**, the radiative temperature gradient for the old ATLAS9 EOS and the new ATLAS9 EOS match quite well for high optical depths and this is seen with the ratio $\approx$ 1 for optical depths $\geq$ 0.001. However, there were differences between the old and the new ATLAS9 at low optical depths in the outer regions of a star. For this region the percentage difference between the old and the new ATLAS9 was calculated to be 90 %.

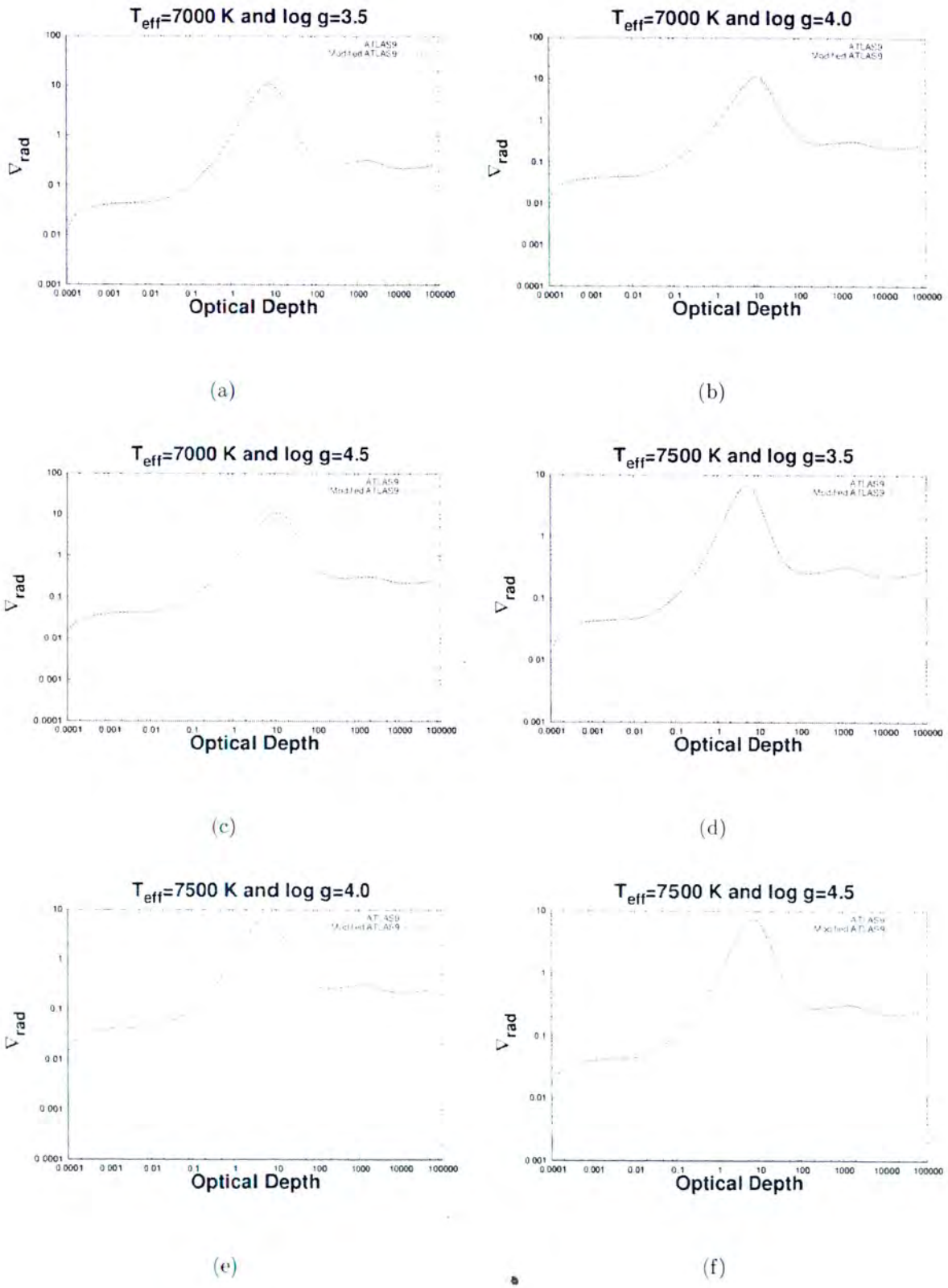

Figure 3.25: Plots of the radiative temperature gradient as a function of optical depth for various effective temperatures (T_{eff}=7000 K–7500 K) and surface gravities (log g=3.5–4.5). The solid line was calculated using normal ATLAS9 EOS. The dotted line was calculated using ATLAS9 with OPAL EOS. These are models of the atmosphere and upper layers of the envelope.

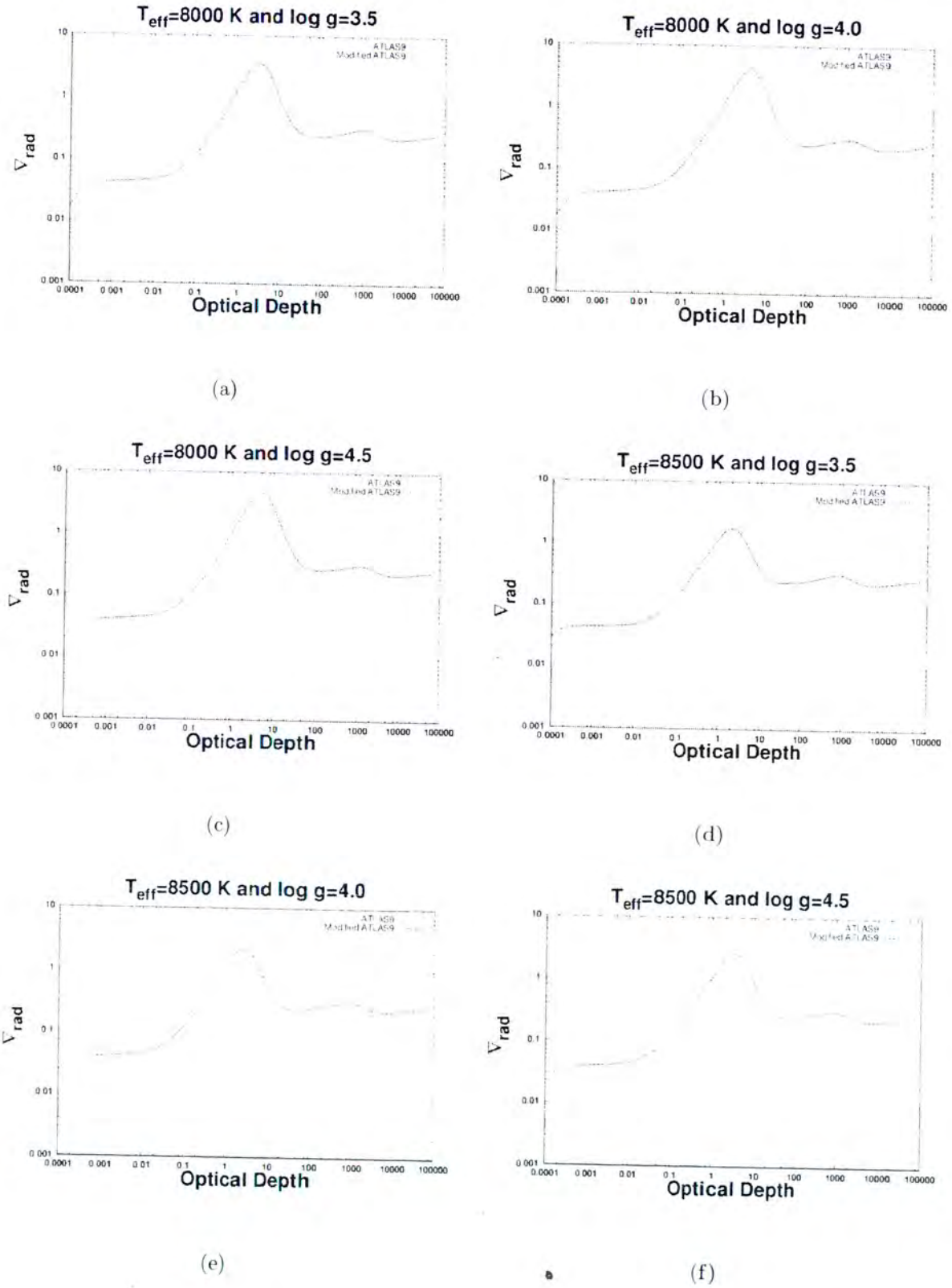

(a) (b) (c) (d) (e) (f)

Figure 3.26: Plots of the radiative temperature gradient as a function of optical depth for various effective temperatures (T_{eff}=8000 K–8500 K) and surface gravities (log g=3.5–4.5). The solid line was calculated using normal ATLAS9 EOS. The dotted line was calculated using ATLAS9 with OPAL EOS. These are models of the atmosphere and the upper layers of the envelope.

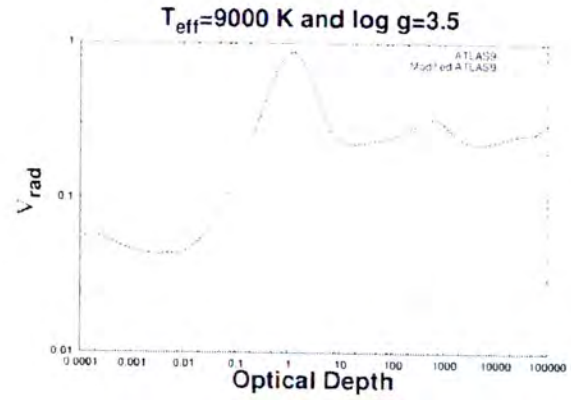

(a)

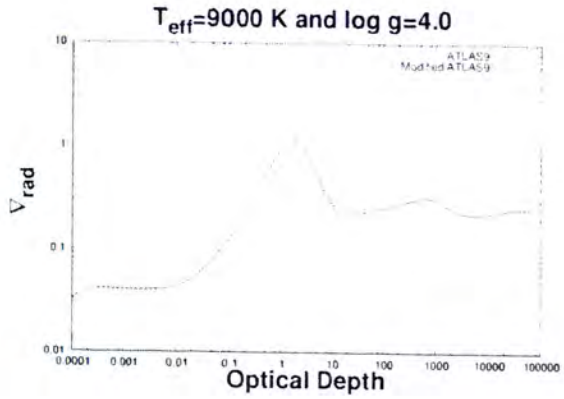

(b)

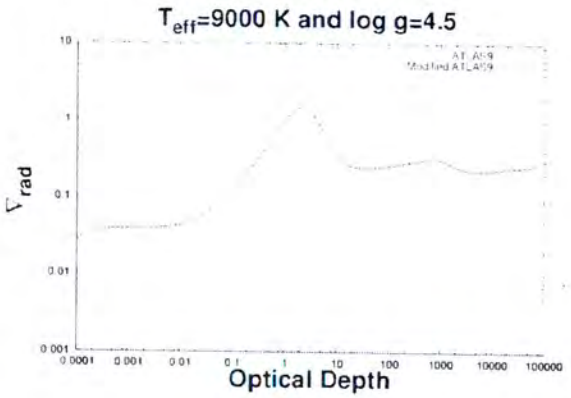

(c)

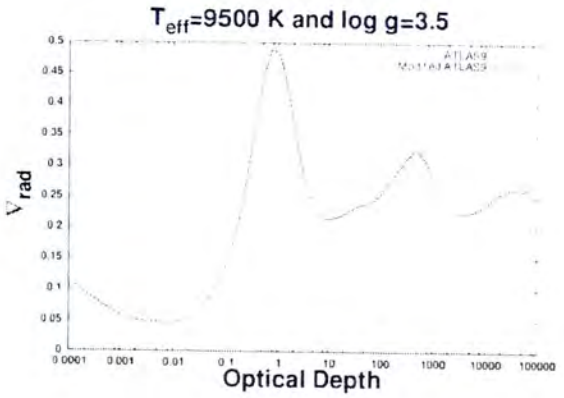

(d)

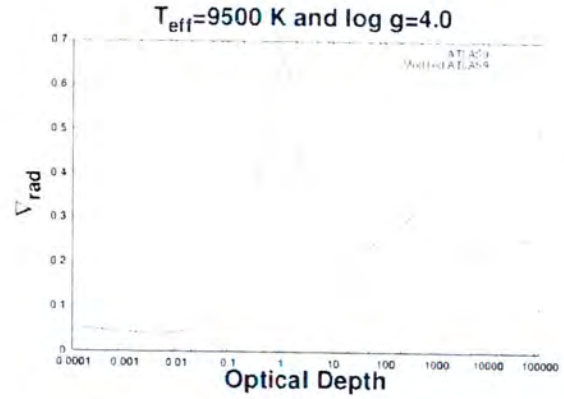

(e)

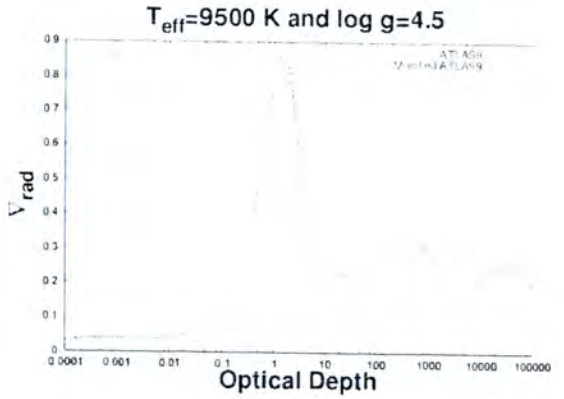

(f)

Figure 3.27: Plots of the radiative temperature gradient as a function of optical depth for various effective temperatures (T_{eff}=9000 K–9500 K) and surface gravities (log g=3.5–4.5). The solid line was calculated using normal ATLAS9 EOS. The dotted line was calculated using ATLAS9 with OPAL EOS. These are models of atmosphere and upper layers of the envelope.

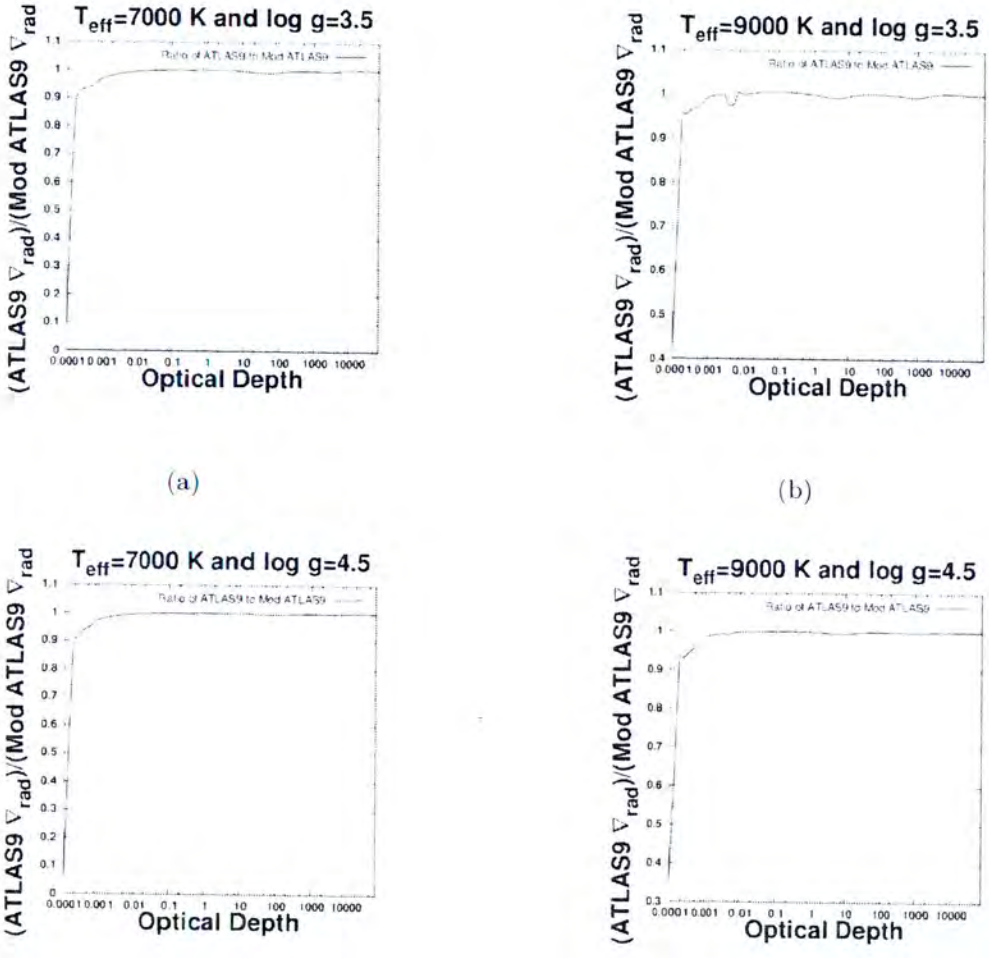

Figure 3.28: The ratio of the old ATLAS9 radiative temperature gradient to the new ATLAS9 radiative temperature gradient as a function of optical depth. The ratio was taken over the atmosphere region and the upper layers of the atmosphere.

3.10 Rosseland Mean Opacity

In **Figures 3.29–3.32**, we present plots for the stellar opacity at different effective temperatures and surface gravity. We have calculated the opacity using the old ATLAS9 code and our new ATLAS9 code. These comparisons are shown in **Figures 3.29–3.32**. The trend that we observe shows the effect of ionisation zones on the Rosseland mean opacity. The humps that are seen are caused by the ionisation zones. These humps occur at different optical depths depending on the effective temperatures. For example, for higher effective temperatures we observed the humps to appear at the photosphere. The first hump that was observed is caused by the hydrogen ionisation zone while the second one is due to the helium ionisation zone. The other humps seen, are not well defined and indicate the ionisation due to other elements. The hydrogen ionisation zone and the first helium ionisation zone are the most prominent zones we see for opacity.

Since the temperature, pressure and density are the same in the new ATLAS9 and the old ATLAS9, it is not suprising that opacity (κ) is the same. At high effective temperatures (T_{eff} = 9500 K), there appears to be a major difference in the trends as seen in **Figure 3.32** (a) and the percent difference ranges between 6.5 %–16 % as seen in **Figure 3.33**. However, the mismatch decreases as the surface gravity gradually increases for these high effective temperatures. Our visual inspection informs us of no differences in the trends for low effective temperature but a closer inspection by taking the ratio reveals that at low temperatures we observe differences between the old ATLAS9 and the new ATLAS9 for higher optical depths. As seen in **Figure 3.33**, at low effective temperatures we observed good matching for a wide range ($0.001 \leq \tau \leq 8$) of optical depths with a percentage difference of 1 % for optical depths ≥ 8. As seen in **Figure 3.29**, the opacity reaches a maximum of ≈ 200 while for higher surface gravities the maximum value reached for opacity is ≈ 500. This was also seen in **Figure 3.29**. Also, the low surface gravities decreases the value of opacity. In a nutshell, we showed that the overall structure of the model was unchanged. This good matching is due to the same ATLAS9 routines that were used to calculate opacity in the old ATLAS9 code and the new ATLAS9 code.

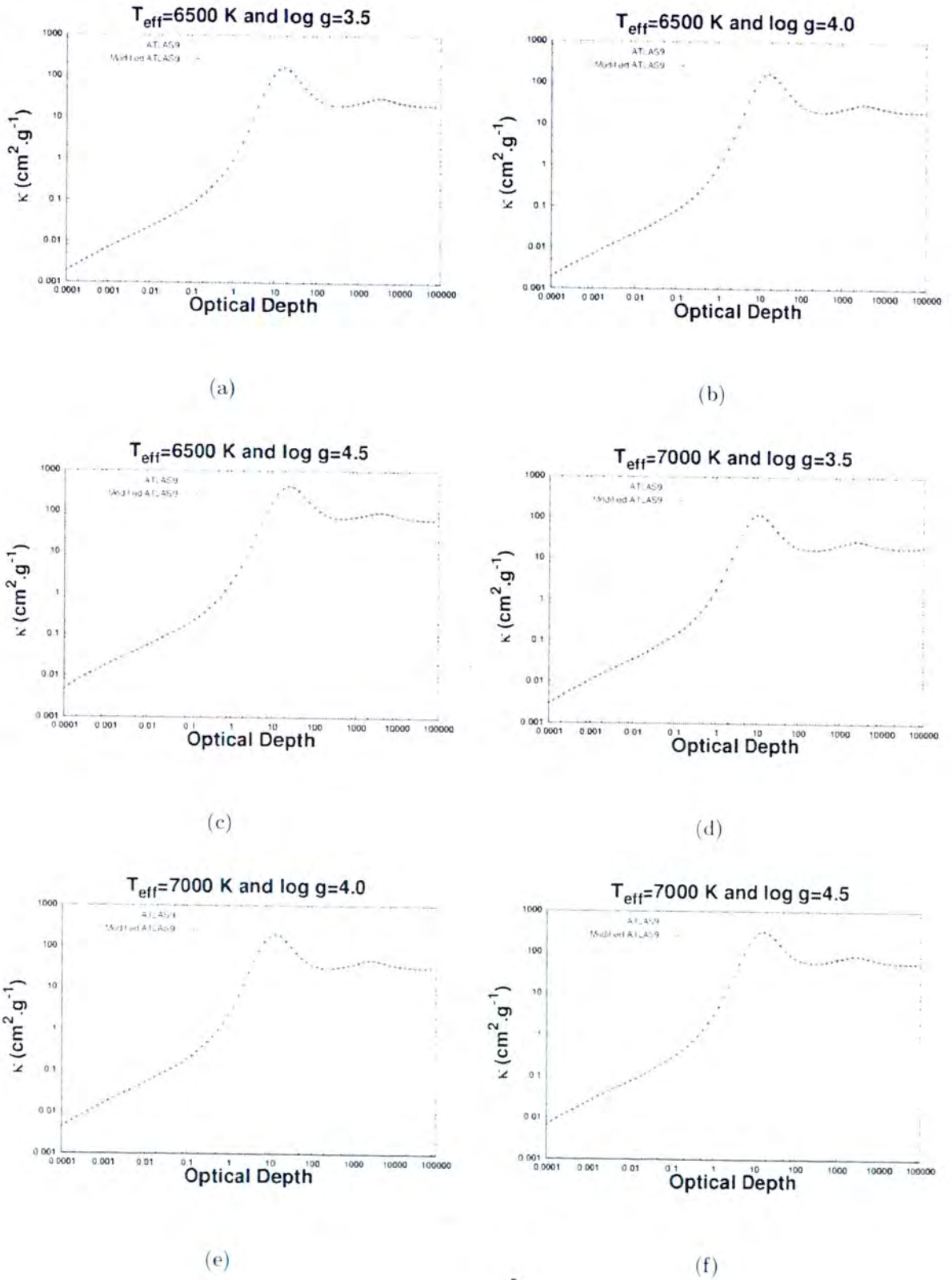

Figure 3.29: Plots of the Rosseland mean opacity as a function of optical depth for various effective temperatures (T_{eff}=6500 K–7000 K)and surface gravities (log g=3.5–4.5). The solid line was calculated using normal ATLAS9 EOS. The crossed line was calculated using ATLAS9 with OPAL EOS. These are models of atmosphere and upper layers of the envelope.

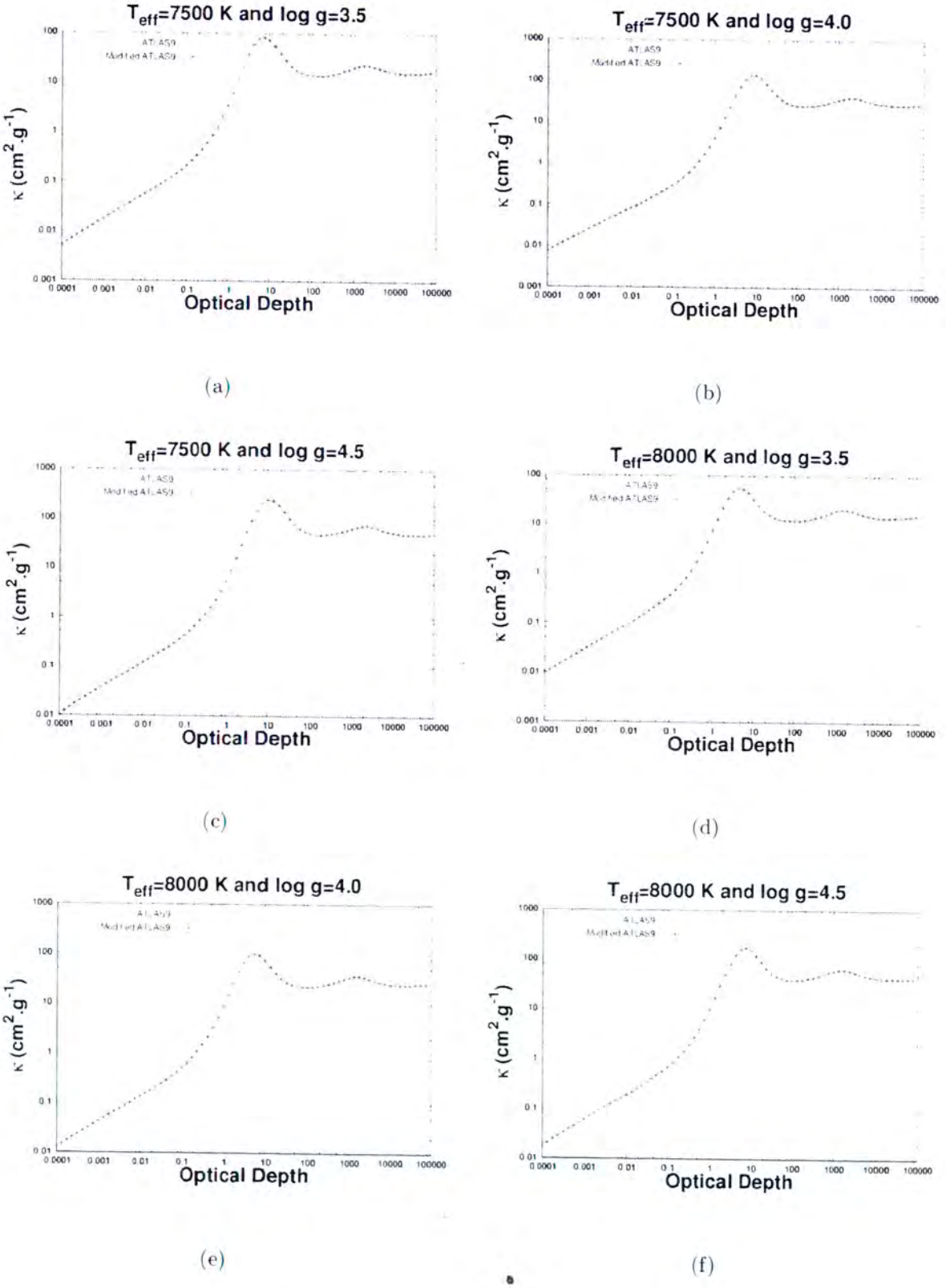

Figure 3.30: Plots of the Rosseland mean opacity as a function of optical depth for various effective temperatures (T_{eff}=7500 K–8000 K) and surface gravities (log g=3.5–4.5). The solid line was calculated using normal ATLAS9 EOS. The crossed line was calculated using ATLAS9 with OPAL EOS. These are models of atmosphere and upper layers of the envelope.

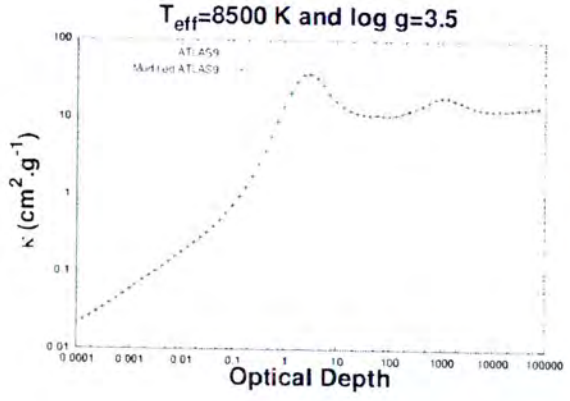

(a)

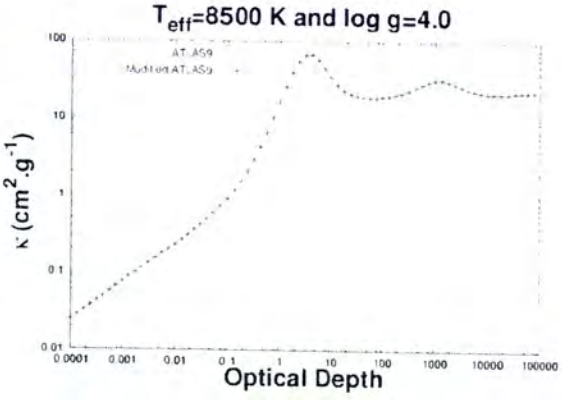

(b)

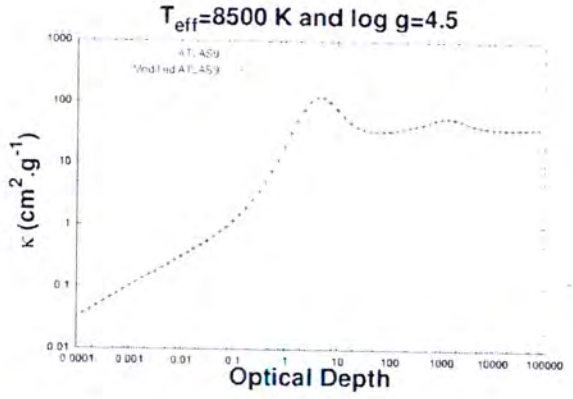

(c)

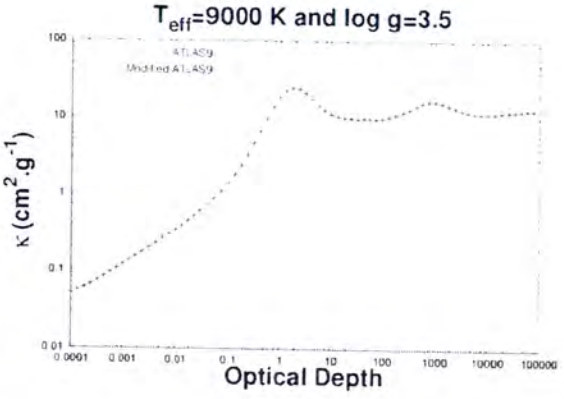

(d)

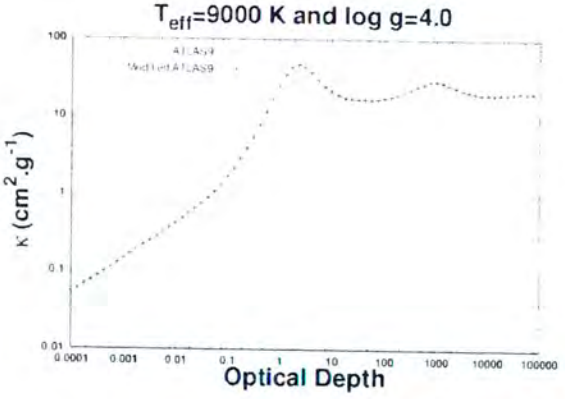

(e)

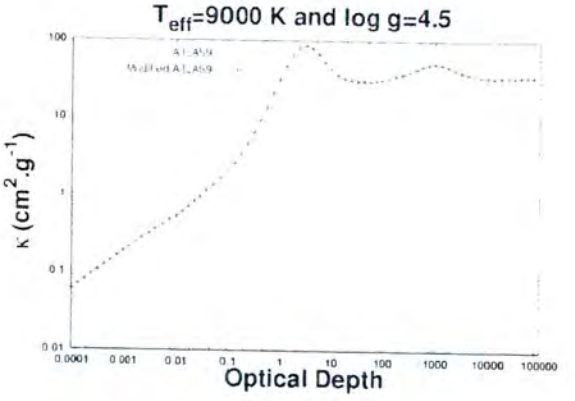

(f)

Figure 3.31: Plots of the Rosseland mean opacity as a function of optical depth for various effective temperatures (T_{eff}=8500 K–9000 K)and surface gravities (log g=3.5–4.5). The solid line was calculated using normal ATLAS9 EOS. The crossed line was calculated using ATLAS9 with OPAL EOS. These are models of atmosphere and upper layers of the envelope.

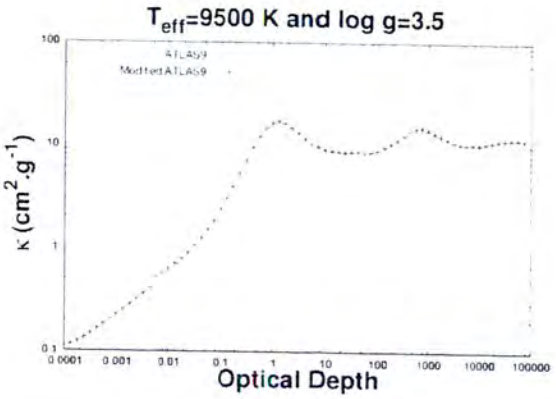

(a)

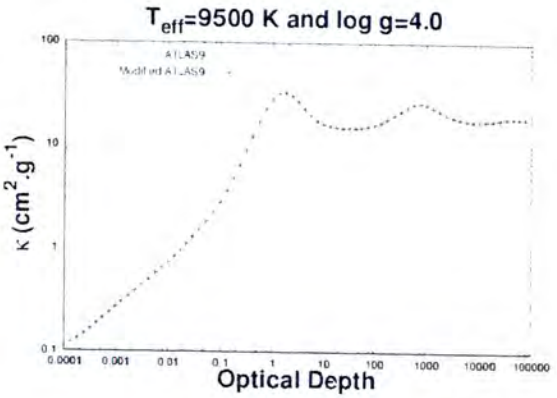

(b)

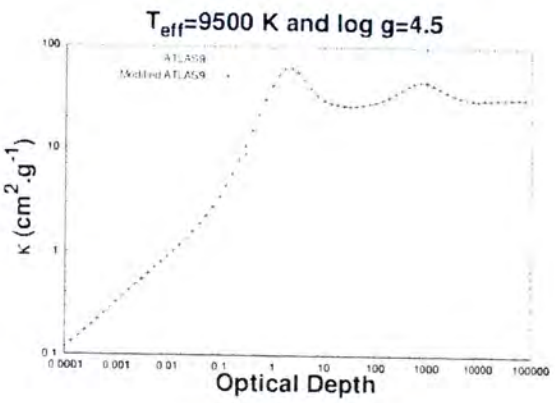

(c)

Figure 3.32: Plots of the Rosseland mean opacity as a function of optical depth for effective temperature T_{eff}=9500 K and surface gravities (log g=3.5–4.5). The solid line was calculated using normal ATLAS9 EOS. The dotted line was calculated using ATLAS9 with OPAL EOS. These are models of atmosphere and upper layers of the envelope.

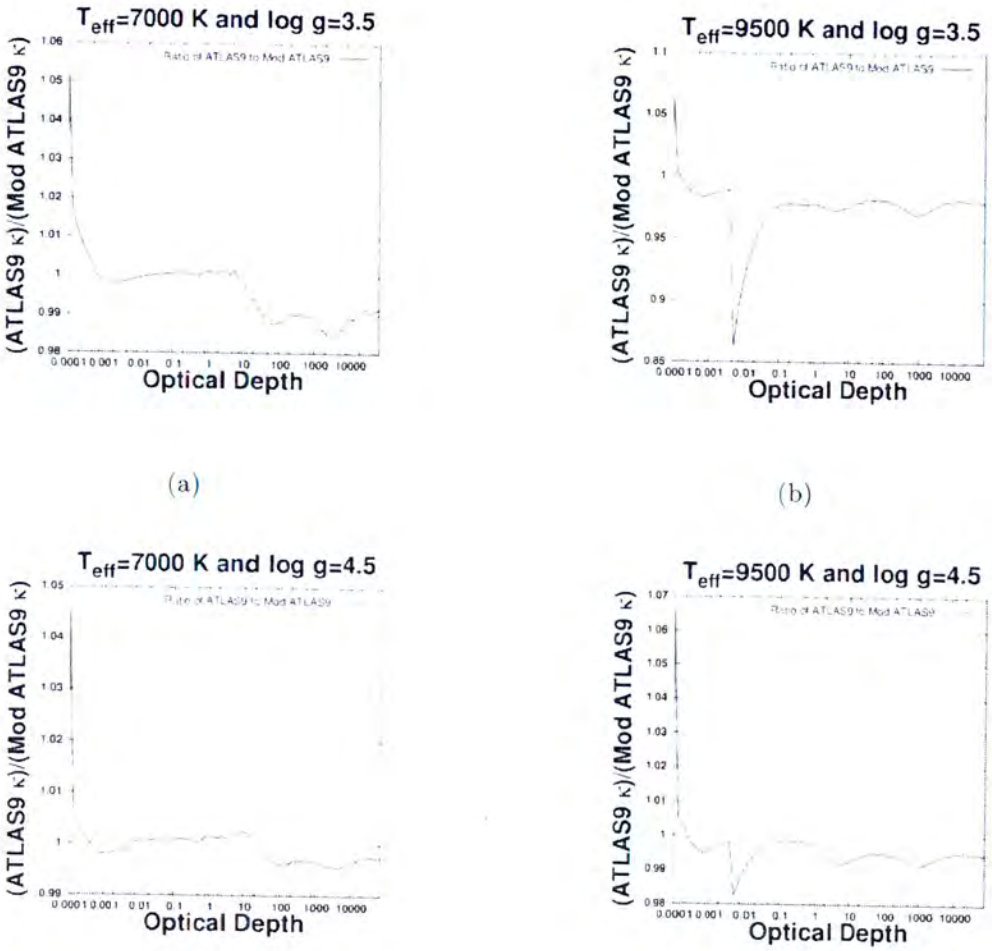

Figure 3.33: The ratio of the old ATLAS9 Rosseland mean opacity to the new ATLAS9 Rosseland mean opacity as a function of optical depth. The ratio was taken over the atmosphere region and the upper layers of the atmosphere.

3.11 The Specific Heat (C_p)

In **Figures 3.34–3.38**, we also present plots for the specific heat capacity at constant pressure (C_p) as a function of optical depth. The specific heat capacity at constant pressure, is defined as

$$C_p = \left(\frac{\partial E}{\partial T}\right)_{P_{total}} - \frac{P_{tot}}{\rho}\left(\frac{\partial \rho}{\partial T}\right) \tag{3.4}$$

As seen in **Figure 3.35**, the only significant differences between the C_p calculated using the old

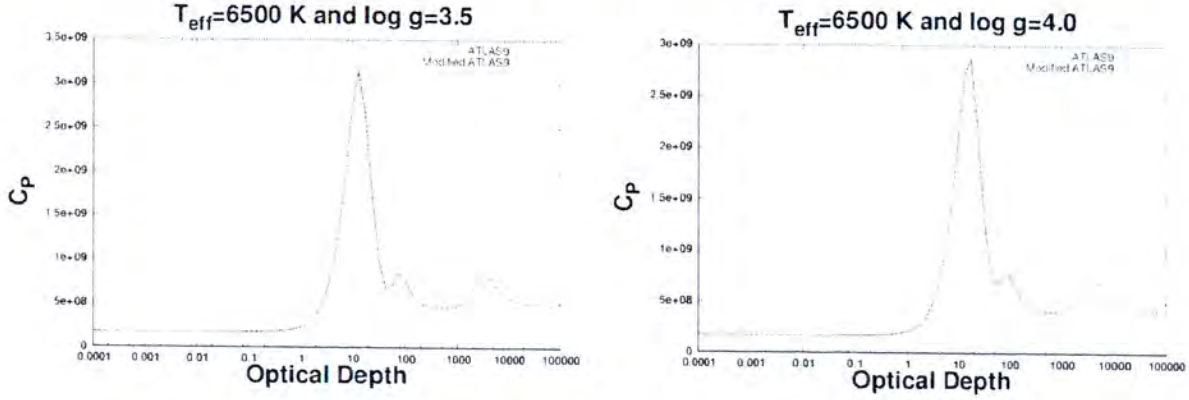

(a) (b)

Figure 3.34: Plots of specific heat capacity (C_p) as a function of optical depth for effective temperature T_{eff}=6500 K and surface gravities (log g=3.5–4.0). The solid line was calculated using normal ATLAS9 EOS. The dotted line was calculated using ATLAS9 with OPAL EOS. These are models of atmosphere and upper layers of the envelope.

ATLAS9 and the new ATLAS9 are at larger optical depths ($\tau > 50$). These differences range from 6.5 %–19 %. However, at effective temperatures higher than 8000 K, differences appear at lower optical depths. This is clearly seen in **Figure 3.38** (a)-(c) for T_{eff}=9500 K. There is a discontinuity seen in **Figure 3.38** (a). This is due to the fact that OPAL EOS could not be calculated for temperatures outside the normal (ρ, T) range. In such cases we used the ATLAS9 EOS. The various ionisation zones were also observed for the specific heat capacity and these

are seen as prominent humps. These ionisation zones correspond to the increases in the specific heat capacity.

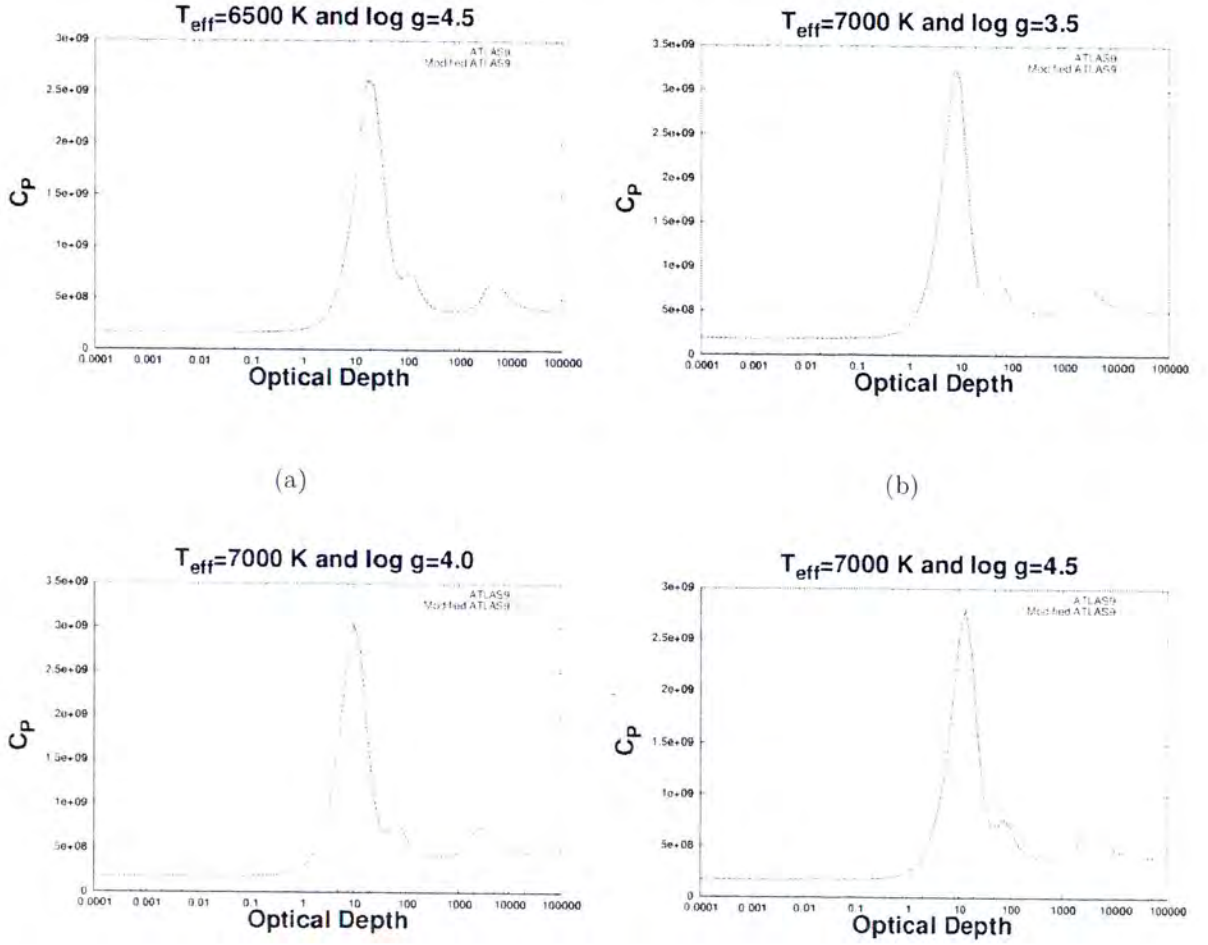

(a) (b)

(c) (d)

Figure 3.35: Plots of specific heat capacity (C_p) as a function of optical depth for various effective temperatures (T_{eff}=6500 K–7000 K) and surface gravities (log g=3.5–4.5). The solid line was calculated using normal ATLAS9 EOS. The dotted line was calculated using ATLAS9 with OPAL EOS. These are models of atmosphere and upper layers of the envelope.

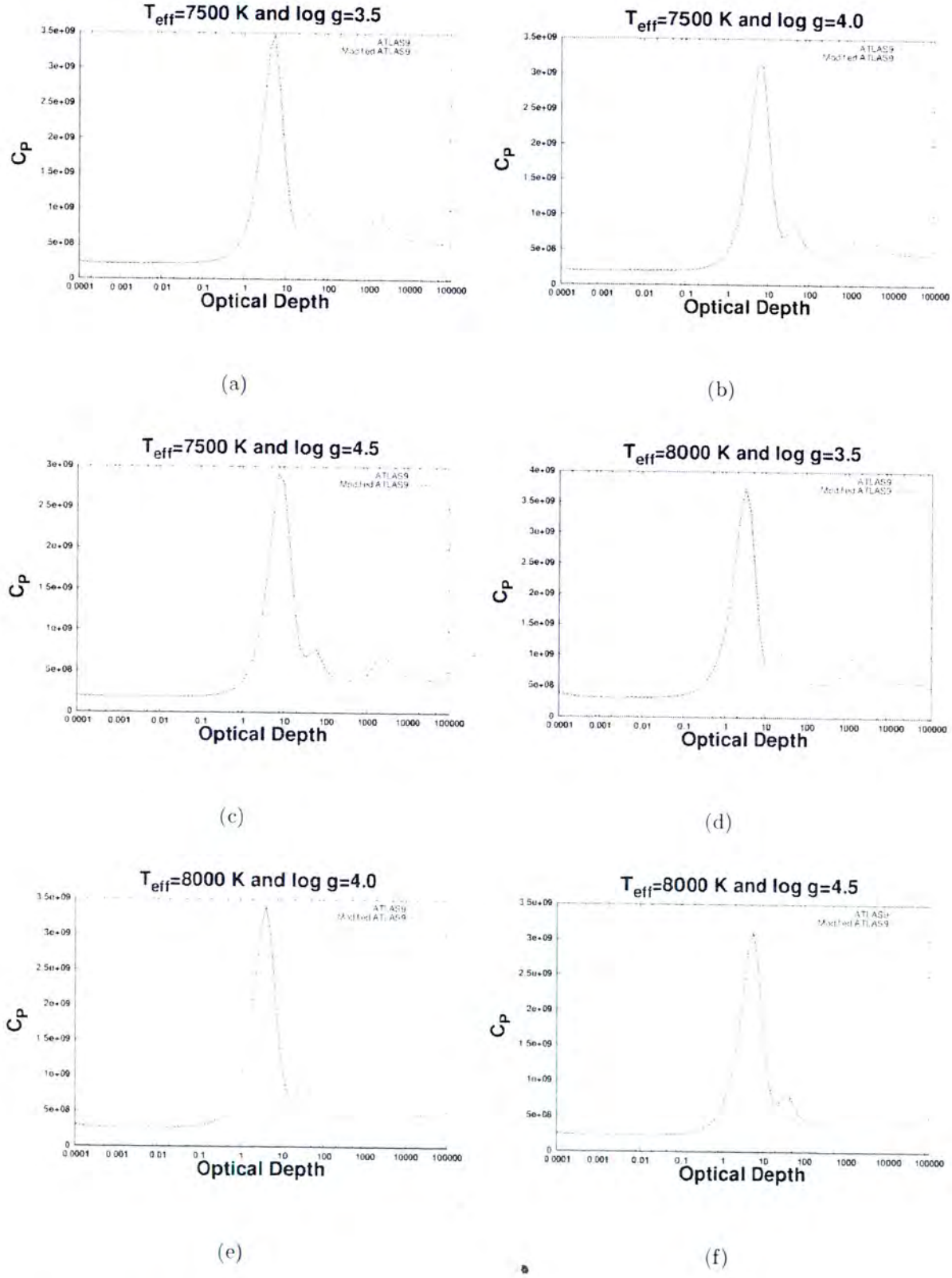

Figure 3.36: The Plots of the specific heat capacity (C_p) as a function of optical depth for various effective temperatures (T_{eff}=7500 K–8000 K) and surface gravities (log g=3.5–4.5). The solid line was calculated using normal ATLAS9 EOS. The dotted line was calculated using ATLAS9 with OPAL EOS. These are models of atmosphere and upper layers of the envelope.

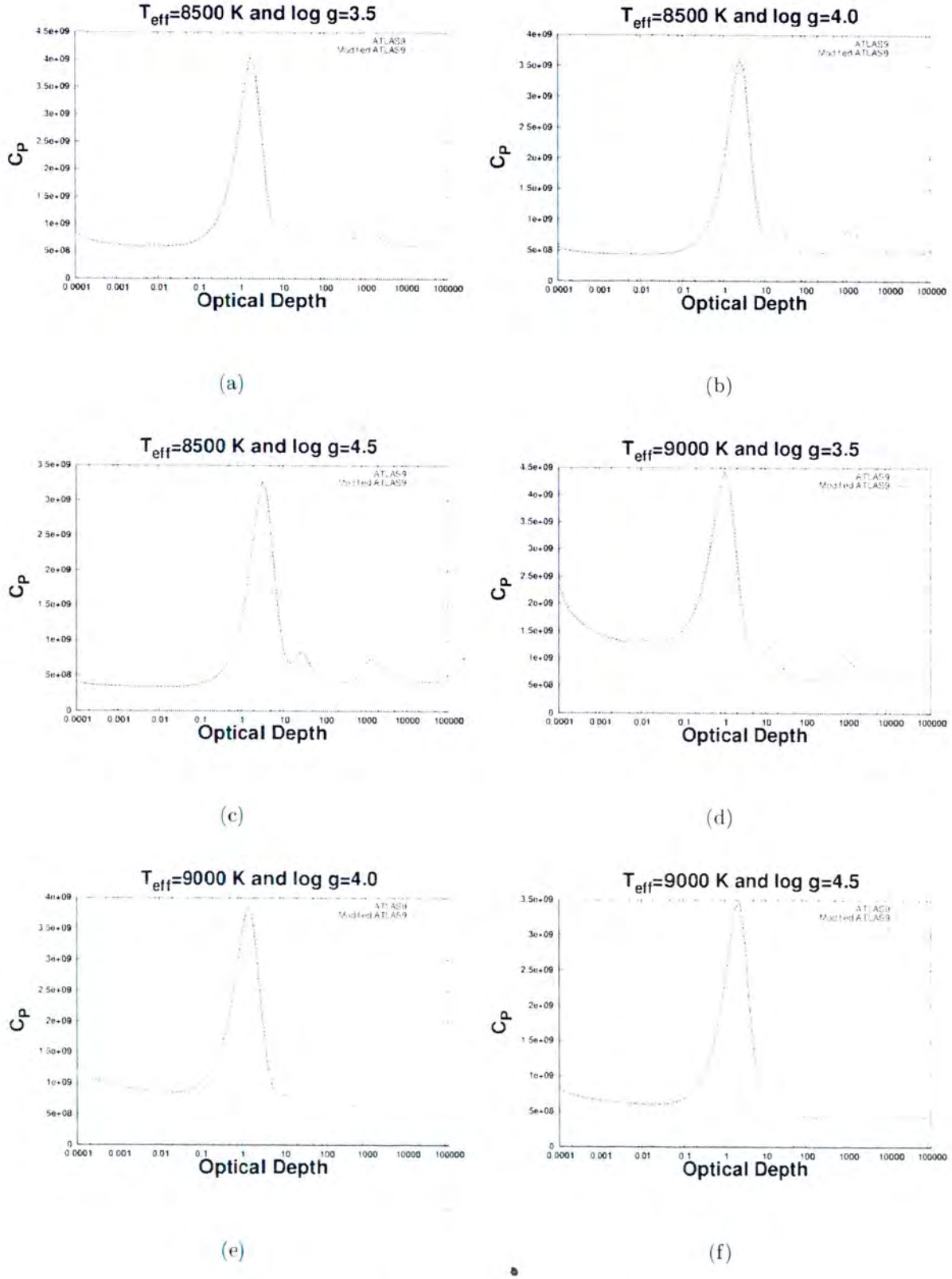

Figure 3.37: Plots of the specific heat capacity (C_p) as a function of optical depth for various effective temperatures (T_{eff}=8500 K–9000 K) and surface gravities (log g=3.5–4.5). The solid line was calculated using normal ATLAS9 EOS. The dotted line was calculated using ATLAS9 with OPAL EOS. These are models of atmosphere and upper layers of the envelope.

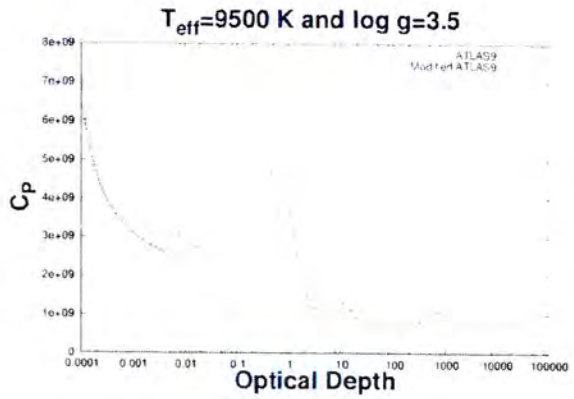

(a)

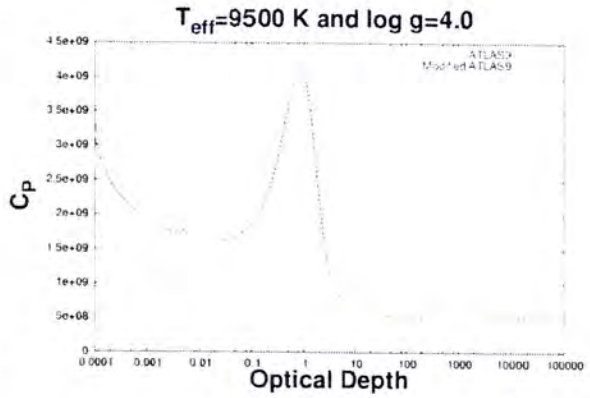

(b)

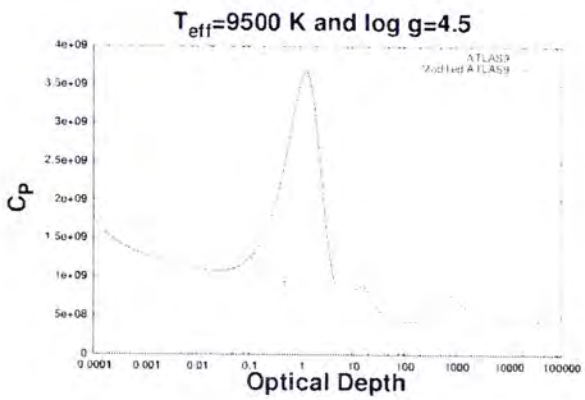

(c)

Figure 3.38: Plots of specific heat capacity (C_p) as a function of optical depth for effective temperature T_{eff}=9500 K and various surface gravities (log g=3.5–4.5). The solid line was calculated using normal ATLAS9 EOS. The dotted line was calculated using ATLAS9 with OPAL EOS. These are models of atmosphere and upper layers of the envelope. We note the discontinuity in the new ATLAS9 profile at $\tau \approx 0.01$ due to OPAL EOS not being valid at lower (T, ρ) temperature ranges.

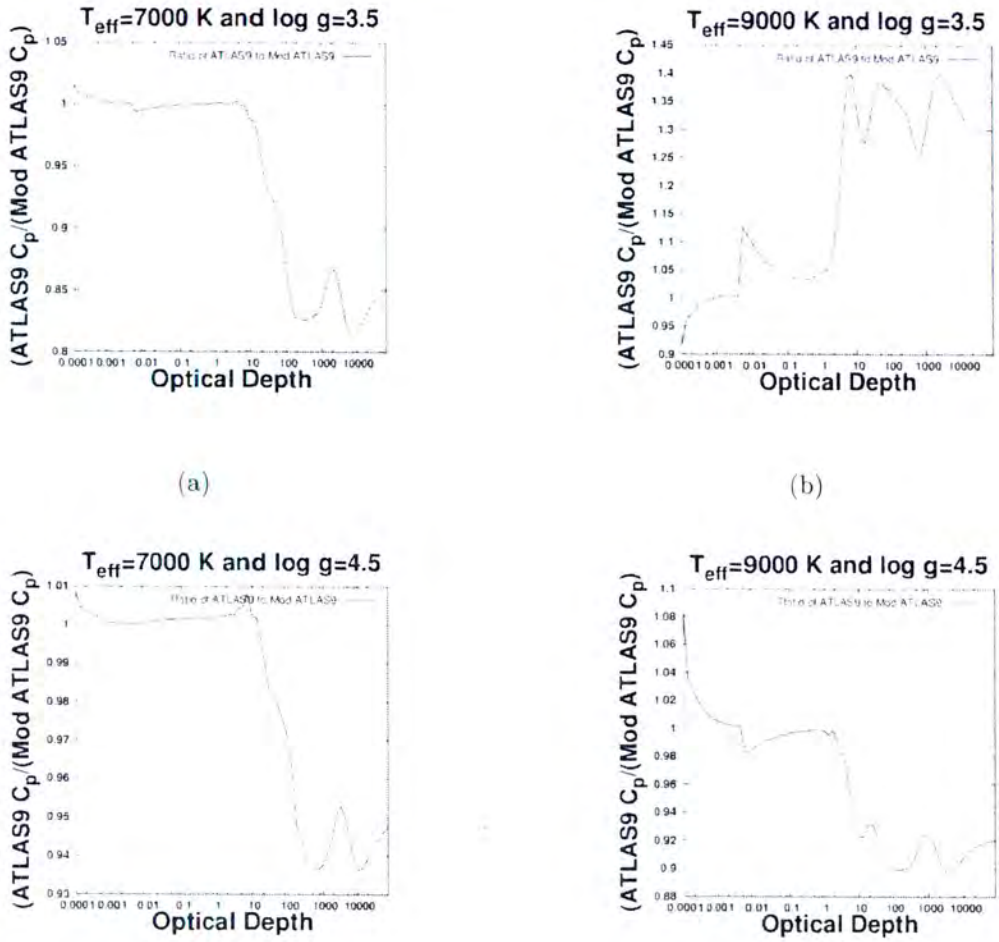

Figure 3.39: The ratio of the old ATLAS9 specific heat capacity to the new ATLAS9 specific heat capacity as a function of optical depth. The ratio was taken over the atmosphere region and the upper layers of the atmosphere.

We have also zoomed in on the plots of the specific heat capacities at constant pressure. As seen in **Figure 3.39**, there is good agreement for low effective temperatures and at other optical depths there is a percentage difference of 7 %.

3.12 The Density Derivative at constant pressure $(\frac{d\log\rho}{d\log T})|_p$

The Density Derivative is the measure of how density fluctuates with respect to the temperature and pressure. The density derivative at constant pressure is given by $(\frac{d\log\rho}{d\log T})|_p$. The plots of $(\frac{d\log\rho}{d\log T})|_p$ as a function of optical depth are presented in **Figures 3.40–3.44**. **Figures 3.40** (a)–(d) show differences between the two methods at lower and higher optical depths.

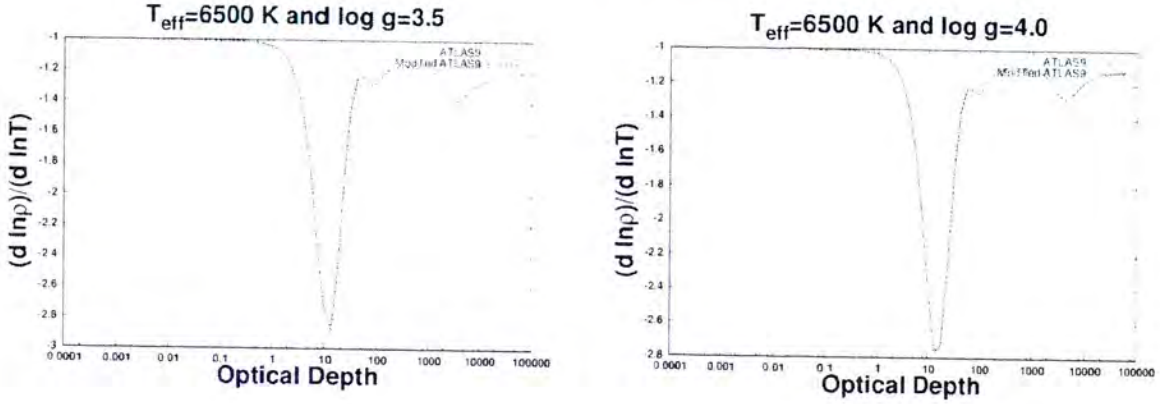

(a) (b)

Figure 3.40: Plots of the Density Derivative $(\frac{d\log\rho}{d\log T})$ at constant pressure as a function of optical depth for effective temperature T_{eff}=6500 K and various surface gravities (log g=3.5 & log g=4.5). The solid line was calculated using normal ATLAS9 EOS. The dotted line was calculated using ATLAS9 with OPAL EOS. These are models of atmosphere and upper layers of the envelope.

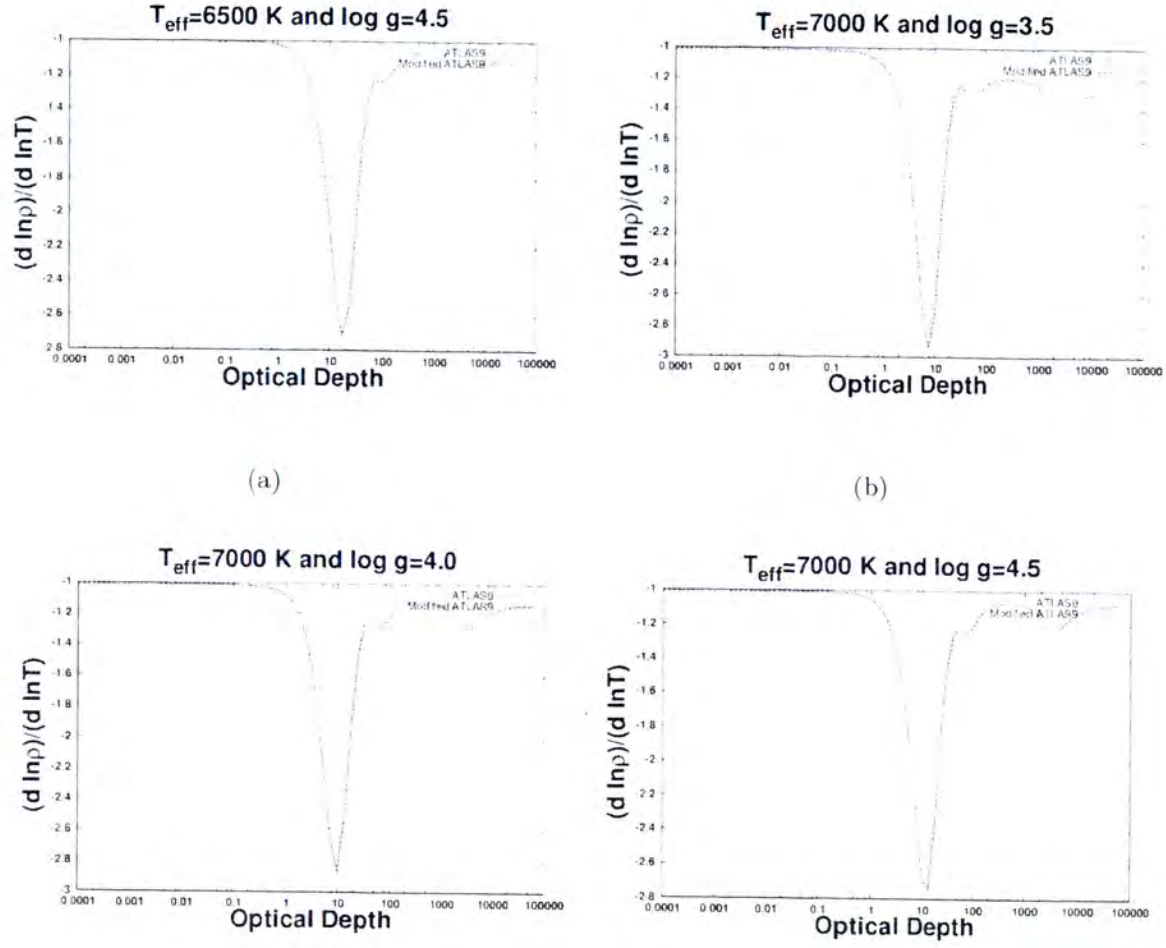

Figure 3.41: Plots of the Density Derivative ($\frac{d\log\rho}{d\log T}$) at constant pressure as a function of optical depth for various effective temperatures (T_{eff}=6500 K–7000 K) and surface gravities (log g=3.5–4.5). The solid line was calculated using normal ATLAS9 EOS. The dotted line was calculated using ATLAS9 with OPAL EOS. These are models of atmosphere and upper layers of the envelope.

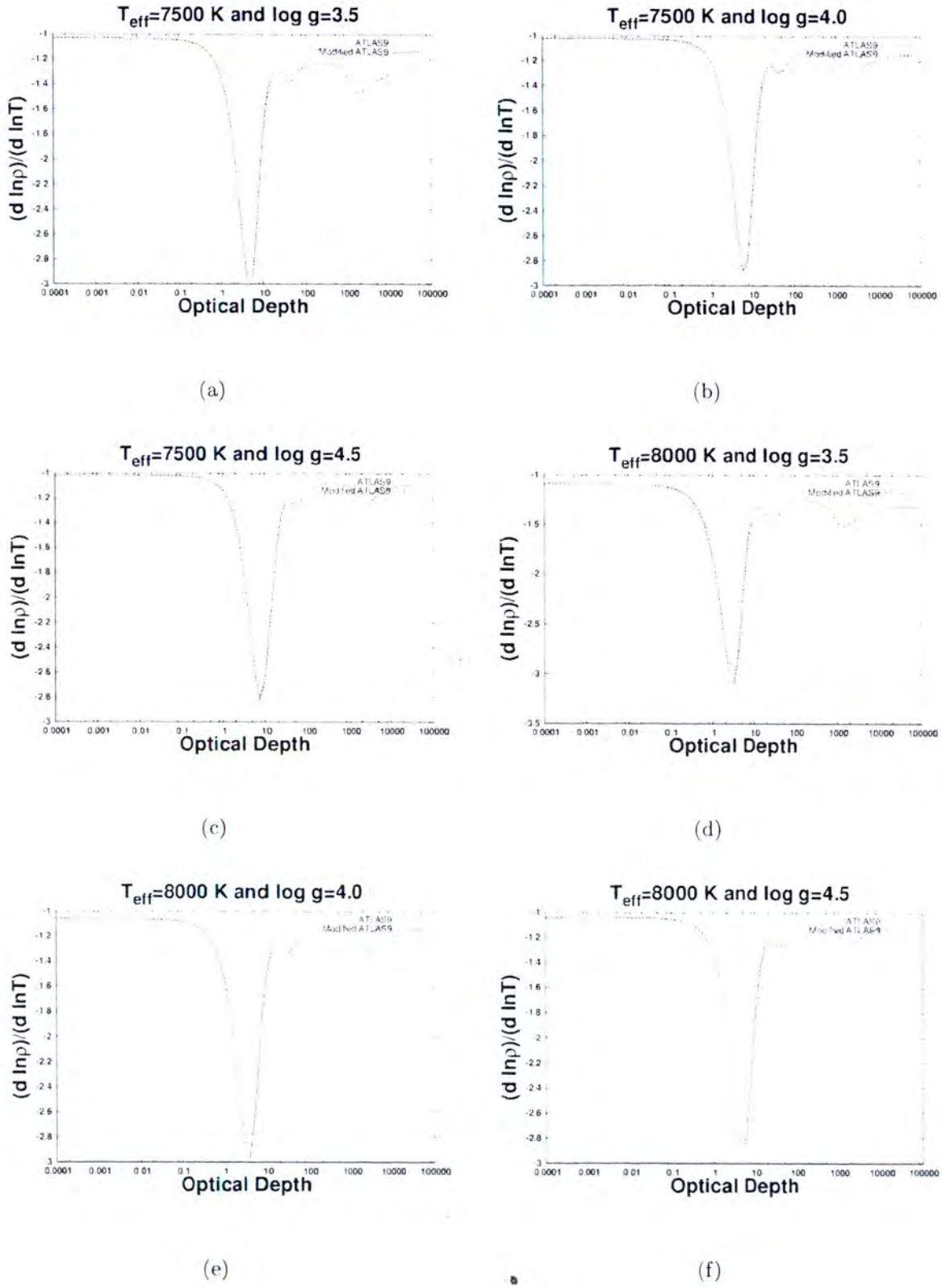

Figure 3.42: Plots of the Density Derivative ($\frac{d \log \rho}{d \log T}$) at constant pressure as a function of optical depth for various effective temperatures (T_{eff}=7500 K–8000 K) and surface gravities (log g=3.5–4.5). The solid line was calculated using normal ATLAS9 EOS. The dotted line was calculated using ATLAS9 with OPAL EOS. These are models of atmosphere and upper layers of the envelope.

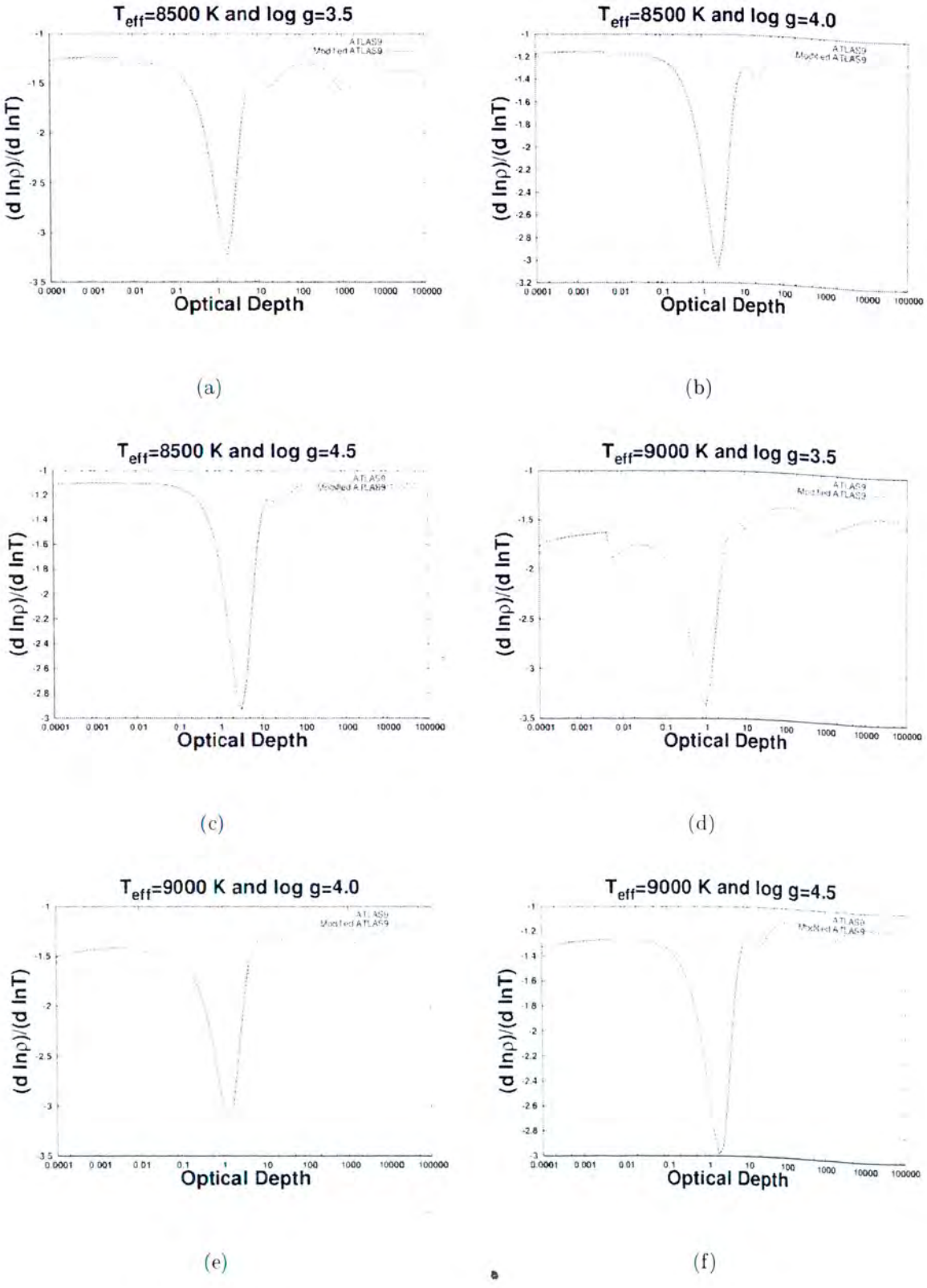

Figure 3.43: Plots of the Density Derivative ($\frac{d\log\rho}{d\log T}$) at constant pressure as a function of optical depth for various effective temperatures (T_{eff}=8500 K–9000 K) and surface gravities (log g=3.5–4.5). The solid line was calculated using normal ATLAS9 EOS. The dotted line was calculated using ATLAS9 with OPAL EOS. These are models of atmosphere and upper layers of the envelope.

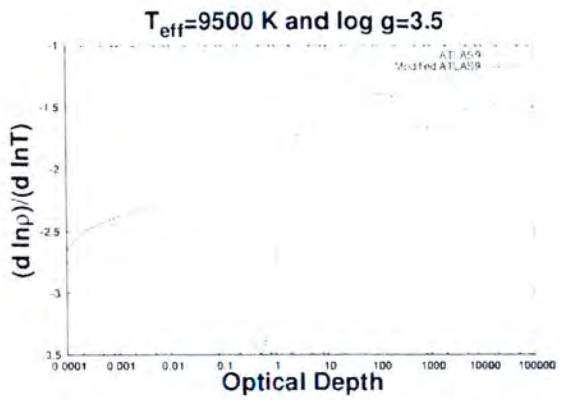

(a)

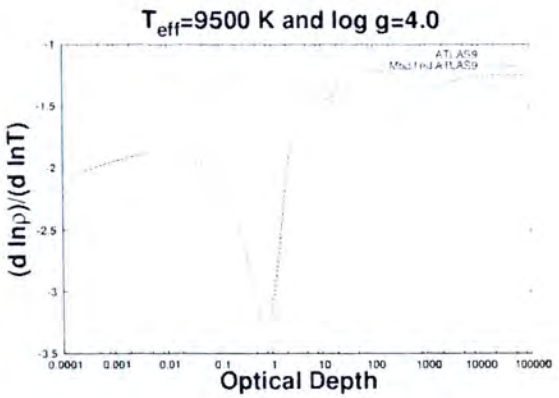

(b)

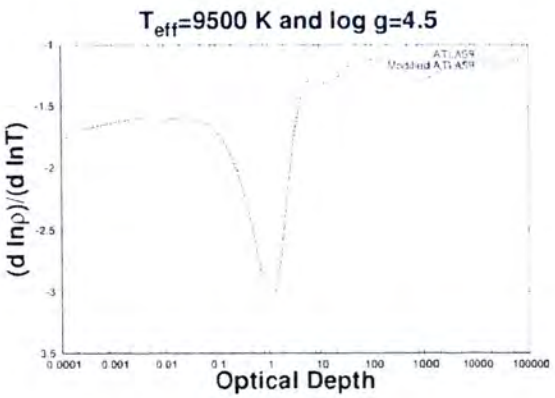

(c)

Figure 3.44: Plots of the Density Derivative ($\frac{d \log \rho}{d \log T}$) at constant pressure as a function of optical for effective temperature T_{eff}=9500 K and surface gravities (log g=3.5–4.5). The solid line was calculated using normal ATLAS9 EOS. The dotted line was calculated using ATLAS9 with OPAL EOS. These are models of atmosphere and upper layers of the envelope.

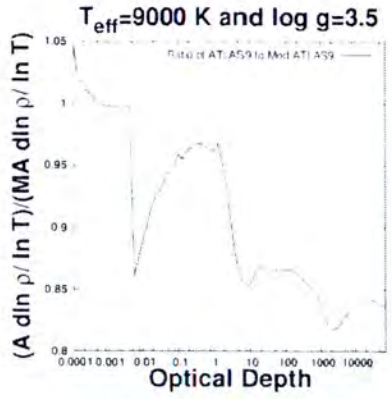

(a)

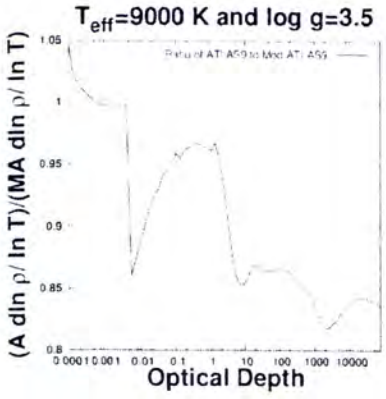

(b)

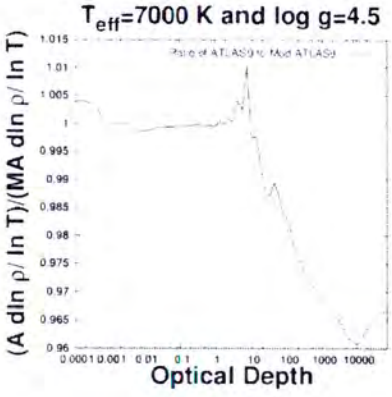

(c)

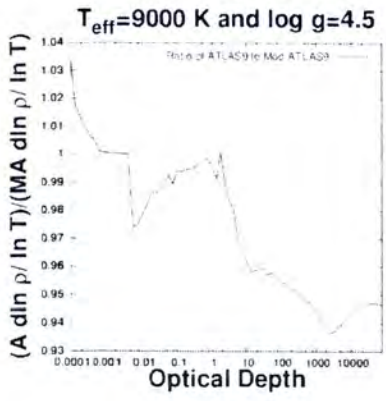

(d)

Figure 3.45: Plots of ratio of the old ATLAS9 Density Derivative at constant pressure to the new ATLAS9 density derivative at constant pressure as a function of optical depth. The ratio was taken over the atmosphere region and the upper layers of the atmosphere. **A** on the axis stands for ATLAS9 and **MA** stands for Modified ATLAS9.

The Density Derivatives at constant pressure were also closely looked at. From **Figure 3.45**, we see good agreement between the old ATLAS9 and the new ATLAS9 at optical depths of range $0.001 \leq \tau \leq 9$. The percentage difference at these low effective temperatures ($T_{eff} \approx 7000K$) is

in ranges 4 %–12 %. For high effective temperature at $T_{eff} \approx 9000$ K, the percentage difference ranges between 6.5 %–18 %.

3.13 Density Derivative $(\frac{d\log\rho}{d\log P})|_T$ at constant temperature

Figures 3.46–3.46 show comparisons of the density derivative at constant temperature. The $(\frac{d\log\rho}{d\log P})|_T$ measures the rate of change of the density with respect to pressure. The density derivative at constant temperature is given by $(\frac{d\log\rho}{d\log P})=\frac{1}{\chi_\rho}$ The peaks that we see are due to the ionisation zones. The peak that stands out is caused by the hydrogen ionisation zone. For other regions in the inner layers of the atmosphere, we have observed that the density derivative has a value ≈ 1. This is the same as the density derivative at constant temperature for an ideal gas.

For low effective temperatures, we see relatively good matching between the old ATLAS9 and the new ATLAS9 for optical depths ranging between $\leq 0.01\ \tau \leq 1$. At high optical depths, the newly calculated density derivative at constant temperature is slightly bigger than the original density derivative value. The percentage difference at these low effective temperatures range between 1.2 %–3.7 %. These percentage differences were calculated using **Figure 3.50**. Also, as seen in **Figure 3.49**, for high effective temperatures there is a prominent discontinuity for the new ATLAS9 at optical depths ($0.001 < \tau < 0.01$). This was observed for $0.01 \leqslant \tau \leqslant 1$ in **Figure 3.46** (a), (b) and (c) for low effective temperature.

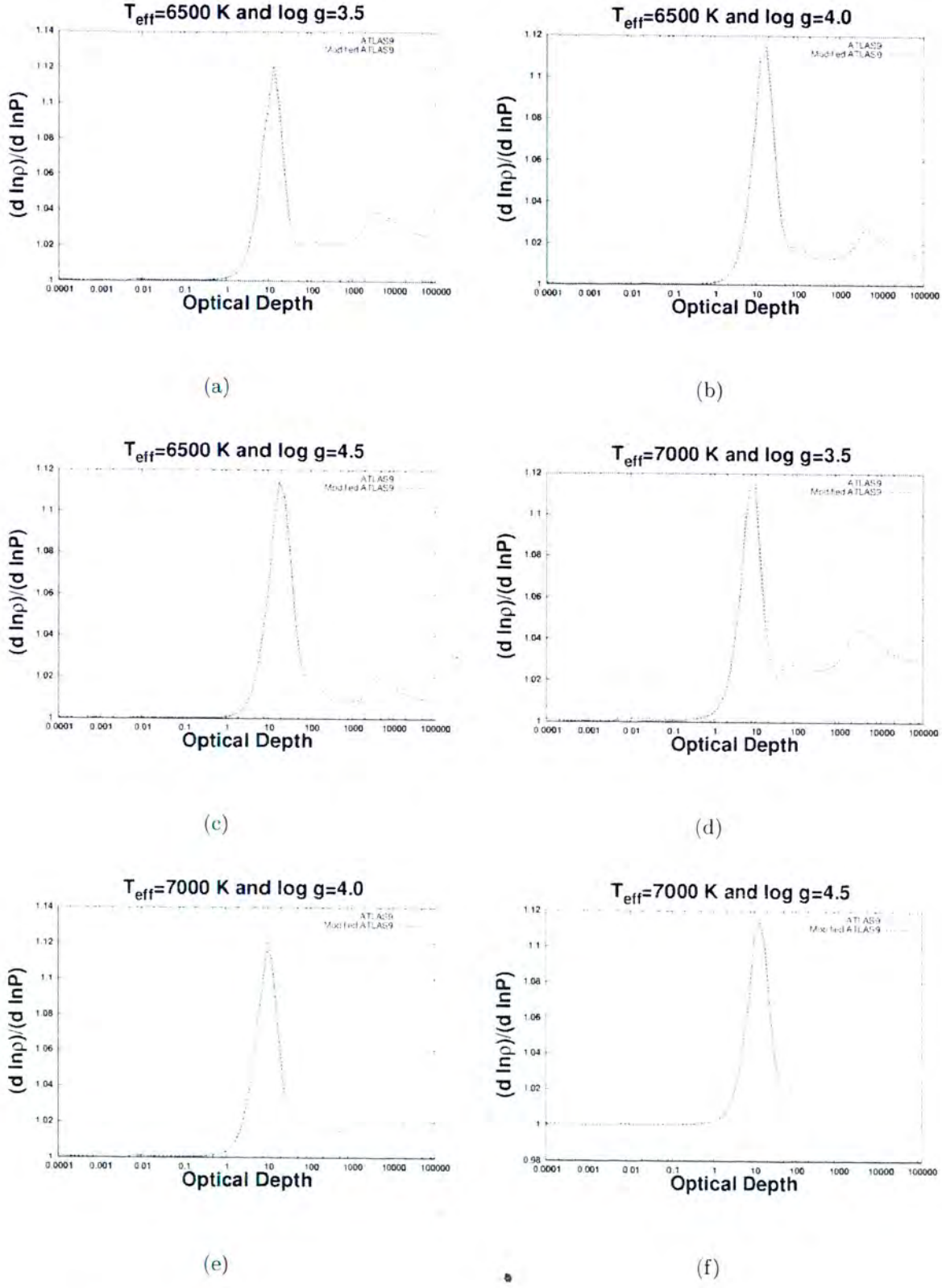

Figure 3.46: Plots of the Density Derivative ($\frac{d\log\rho}{d\log P}$) at constant temperature as a function of optical depth for various effective temperatures (T_{eff}=6500 K–7000 K) and surface gravities (log g=3.5–4.5). The solid line was calculated using normal ATLAS9 EOS. The dotted line was calculated using ATLAS9 with OPAL EOS. These are models of atmosphere and upper layers of the envelope.

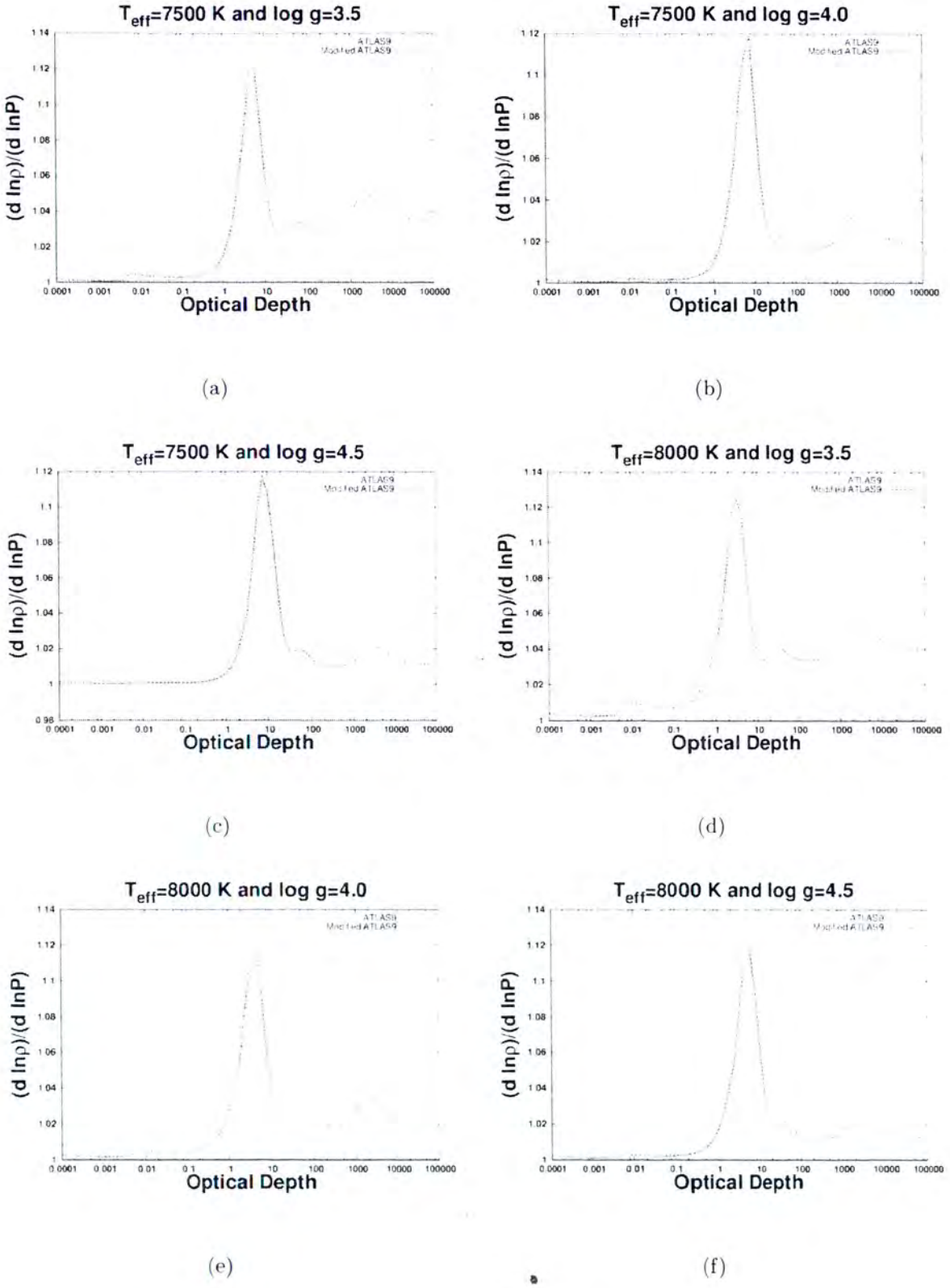

Figure 3.47: Plots of the Density Derivative ($\frac{d\log\rho}{d\log P}$) at constant temperature as a function of optical depth for various effective temperatures (T_{eff}=7500 K–8000 K) and surface gravities (log g=3.5–4.5). The solid line was calculated using normal ATLAS9 EOS. The dotted line was calculated using ATLAS9 with OPAL EOS. These are models of atmosphere and upper layers of the envelope.

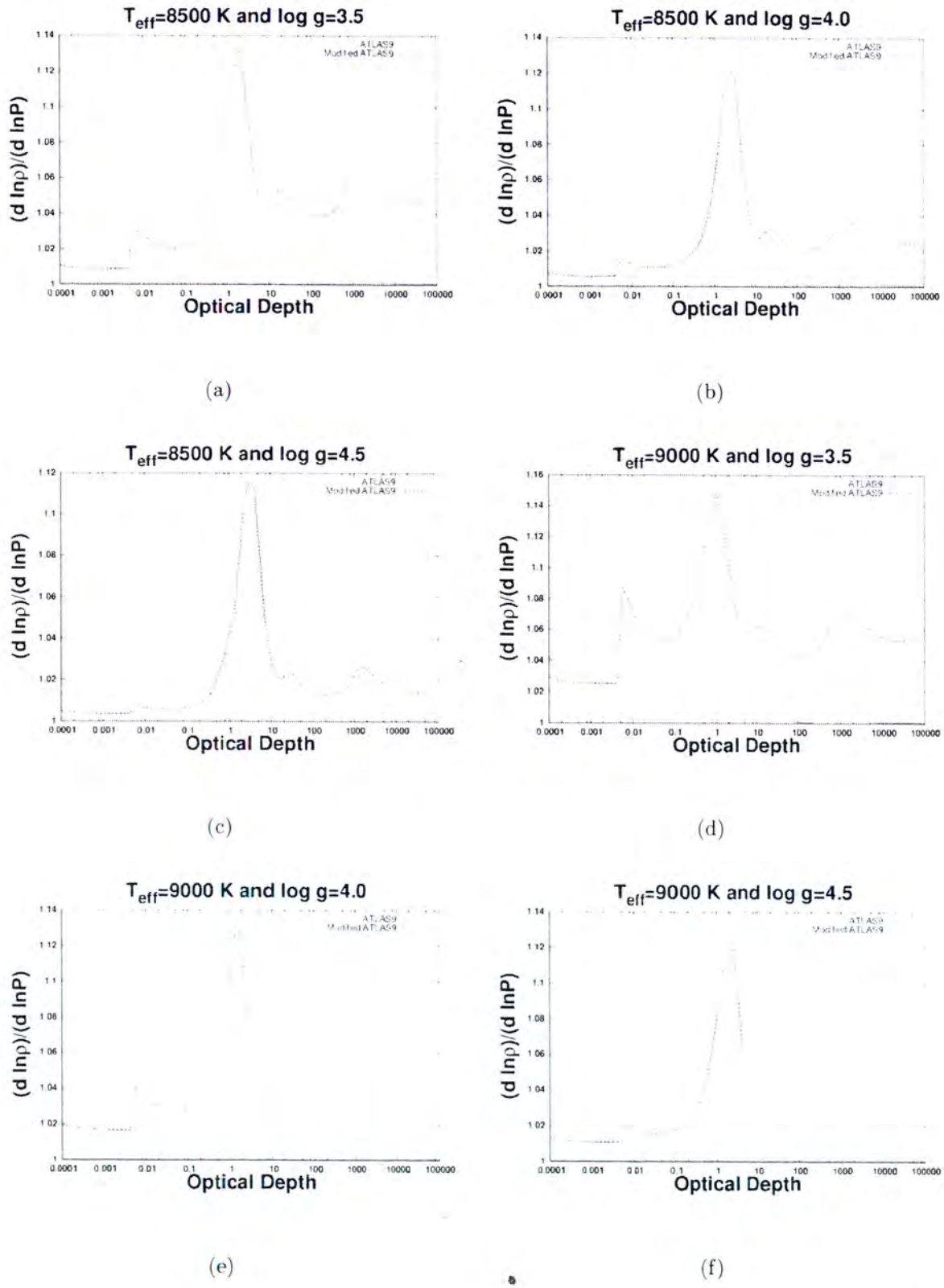

Figure 3.48: Plots of the Density Derivative $(\frac{d\log\rho}{d\log P})$ at constant temperature as a function of optical depth for various effective temperatures and surface gravities (log g=3.5–4.5). The solid line was calculated using normal ATLAS9 EOS. The dotted line was calculated using ATLAS9 with OPAL EOS. These are models of atmosphere and upper layers of the envelope.

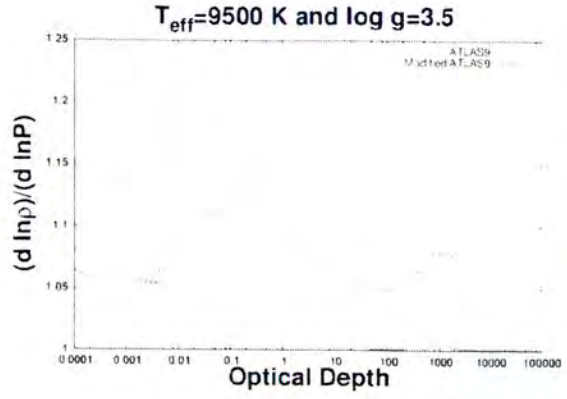

(a)

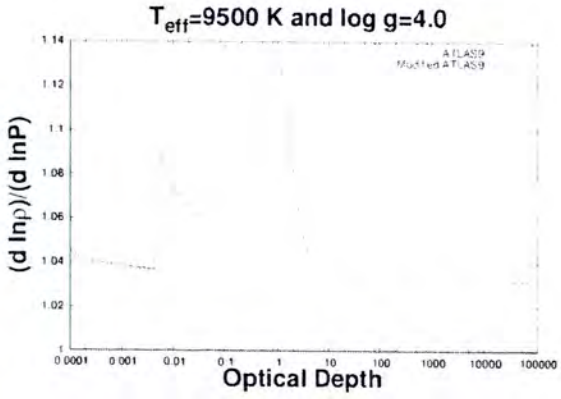

(b)

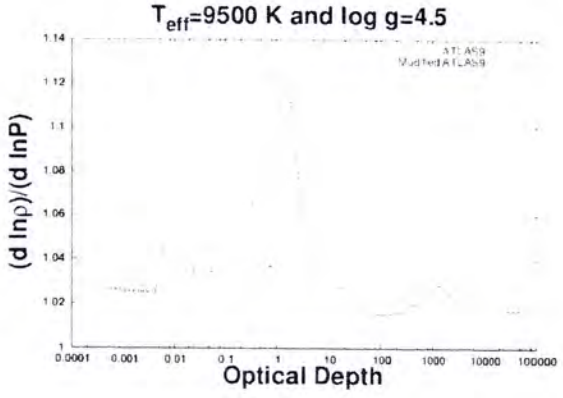

(c)

Figure 3.49: Plots of the Density Derivative ($\frac{d\log\rho}{d\log P}$) at constant temperature as a function of optical depth for effective temperature T_{eff}=9500 K and various surface gravities (log g=3.5–4.5). The solid line was calculated using normal ATLAS9 EOS. The dotted line was calculated using ATLAS9 with OPAL EOS. These are models of atmosphere and upper layers of the envelope.

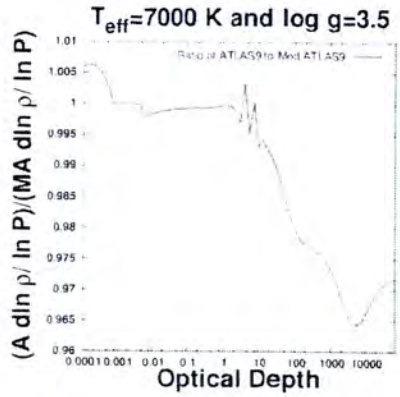

(a)

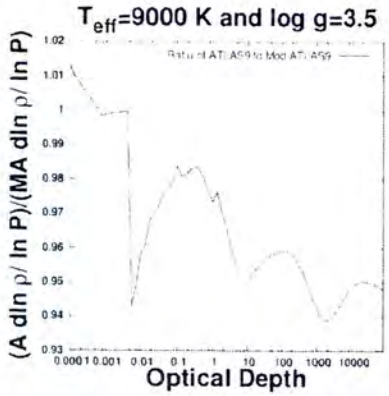

(b)

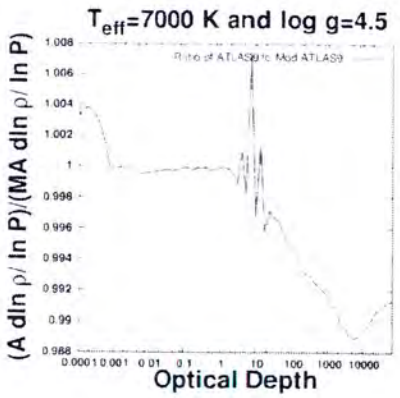

(c)

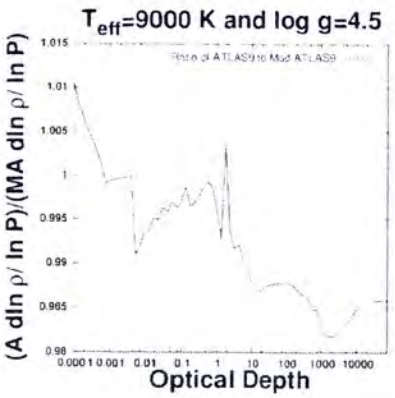

(d)

Figure 3.50: The ratio of the old ATLAS9 Density Derivative at constant temperature to the new ATLAS9 density derivative at constant temperature as a function of optical depth. The ratio was taken over the atmosphere region and the upper layers of the envelope. **A** on the axis stands for ATLAS9 and **MA** stands for Modified ATLAS9.

3.14 The effect of OPAL EOS on the Spectrum

A synthetic spectral grid for a given range of effective temperature, surface gravity and composition allows one to accurately determine certain stellar parameters for a given spectrum (Kirby, 2011). Furthermore, a model is useful in computing stellar surface fluxes, surface intensities and molecular densities. The solar oscillation spectrum has also been somewhat dependent on the Equation of State (Hummer & Mihalas, 1988). A model spectra has previously been used to determine effective temperature, surface gravity and the composition. For our purpose, we have calculated the spectra for model atmosphere using the original ATLAS9 code and the modified version of this code. The significance of calculating the spectra was to see if the OPAL EOS added to the original ATLAS9 routines changed the original synthetic spectra in any way. The abundances used to calculate the spectra were the same as those that were used to compute the model atmosphere and are solar abundances.

In **Figures 3.51–3.53**, we present plots for the spectra as a function of wavelength and the ratio of the intensities for the old ATLAS9 to the new ATLAS9, as a function of wavelength. The intensities were calculated for wavelength ranges of the optical region and this ensured that more details on the spectrum were seen. From **Figure 3.51**, we observed various absorption lines for the given wavelength ranges. At wavelengths λ= 656 nm, we see the H_α lines, at λ= 486 nm we observed the H_β lines, at λ= 434 nm we see H_γ lines and at λ= 410 nm we observed the H_δ lines. We produced plots similar to **Figure 3.51** (a), at different effective temperatures and surface gravities. We also could not find the differences between the old ATLAS9 and the new ATLAS9 when we visually inspected these plots at their respective effective temperatures and surface gravities. We thus zoomed in, by taking the ratio of the two spectra at optical wavelengths. What we have observed is that for higher effective temperatures (T_{eff} =8500 K), the differences between the old ATLAS9 and the new ATLAS9 are big (0.6 %) compared to models at lower effective temperatures (T_{eff} =6500 K) where we see slightly smaller (0.28 %) differences between the two methods. This is shown in **Figure 3.51** (b) & **Figure 3.52** (c). For effective temperatures T_{eff}=8000 K–8500 K with lower surface gravity (log g=3.5), we have

observed that the intensity of the modified ATLAS9 approach is much higher than that of the original ATLAS9 approach, this is shown in **Figure 3.52** (b) & (c). If one looks at the two methods for log g=4.5, we have observed that the original ATLAS9 is higher than the modified ATLAS9 for effective temperatures (T_{eff}=6500 K–7000 K). The percentage difference between the two methods for log g=4.5 was calculated to be in ranges (0.13 %–0.23 %). When making

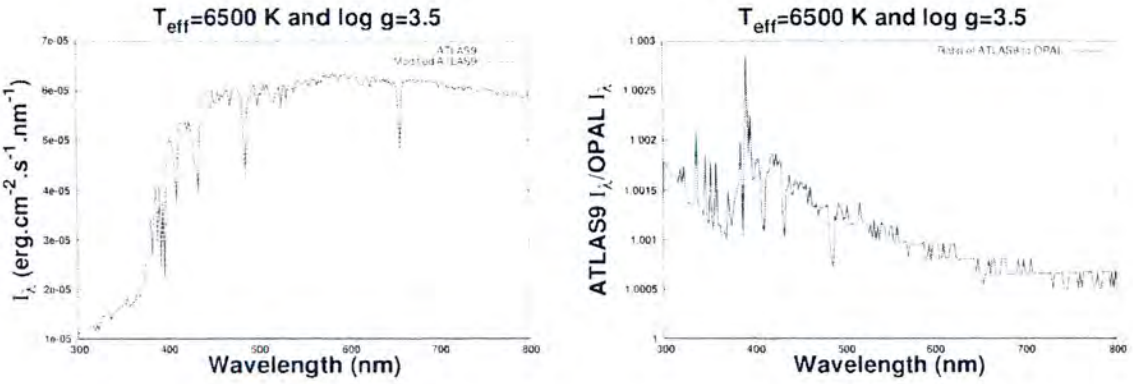

(a) (b)

Figure 3.51: A plot of intensity as a function of wavelength for effective temperature T_{eff} =6500 K and surface gravitity log g=3.5. The solid line in the first plot was calculated using normal ATLAS9 EOS and the dotted line was calculated using ATLAS9 with OPAL EOS. Also plotted on the right is the ratio of the old ATLAS9 intensity as a function of wavelength. These are models of atmosphere and upper layers of the envelope.

comparisons of spectra calculated with the two codes, we must bear in mind that the outer most layers of A-stars are so cool that the temperature and densities are outside the ranges of OPAL EOS tables. Due to time constraints, we used ATLAS9 EOS in these layers for all the models presented in this thesis. This introduces artificial discontinuities, especially in thermodynamic variables. Differences found in deeper parts of the models are more reflective of the differences between the physics of the two equation of state. Further calculations could be done as part of

a Phd thesis for instance.

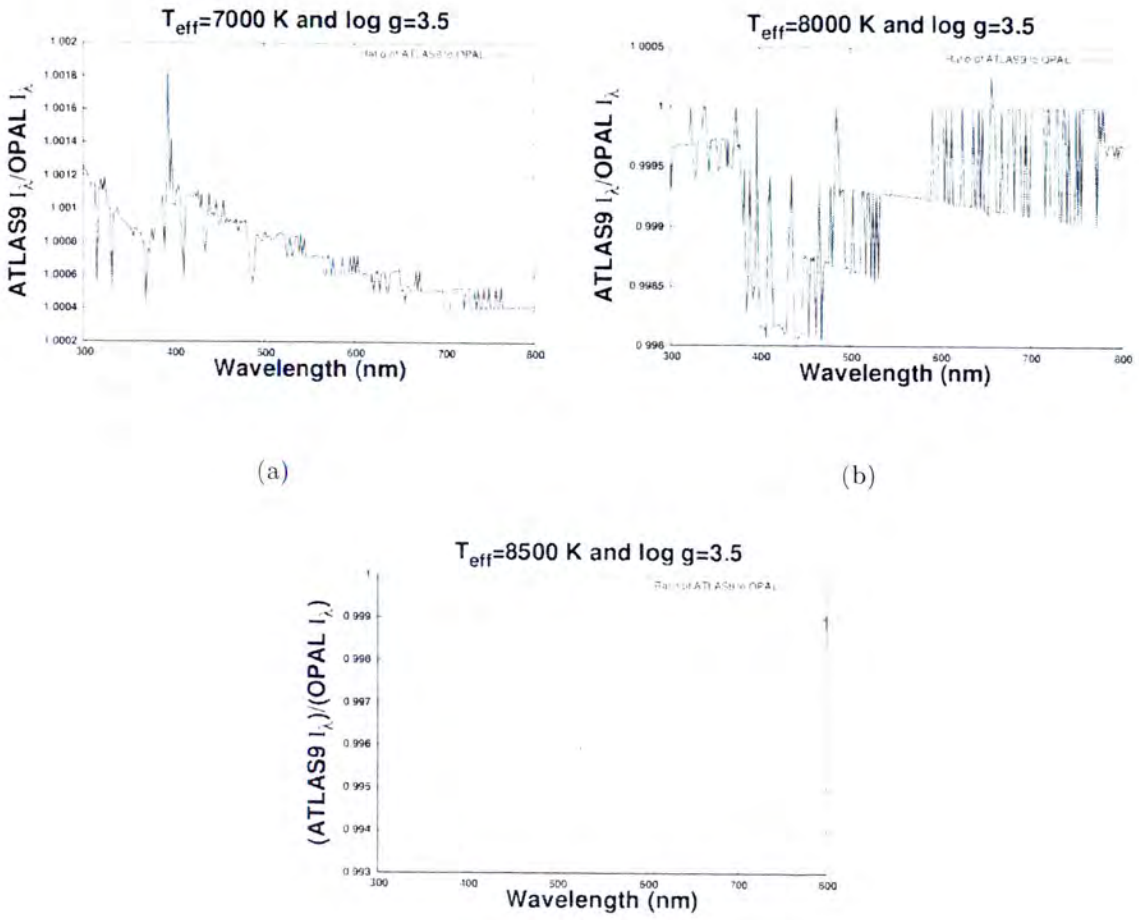

Figure 3.52: The ratio of the old ATLAS9 intensity to the new ATLAS9 intensity as a function of wavelength. These are models of atmosphere and upper layers of the envelope.

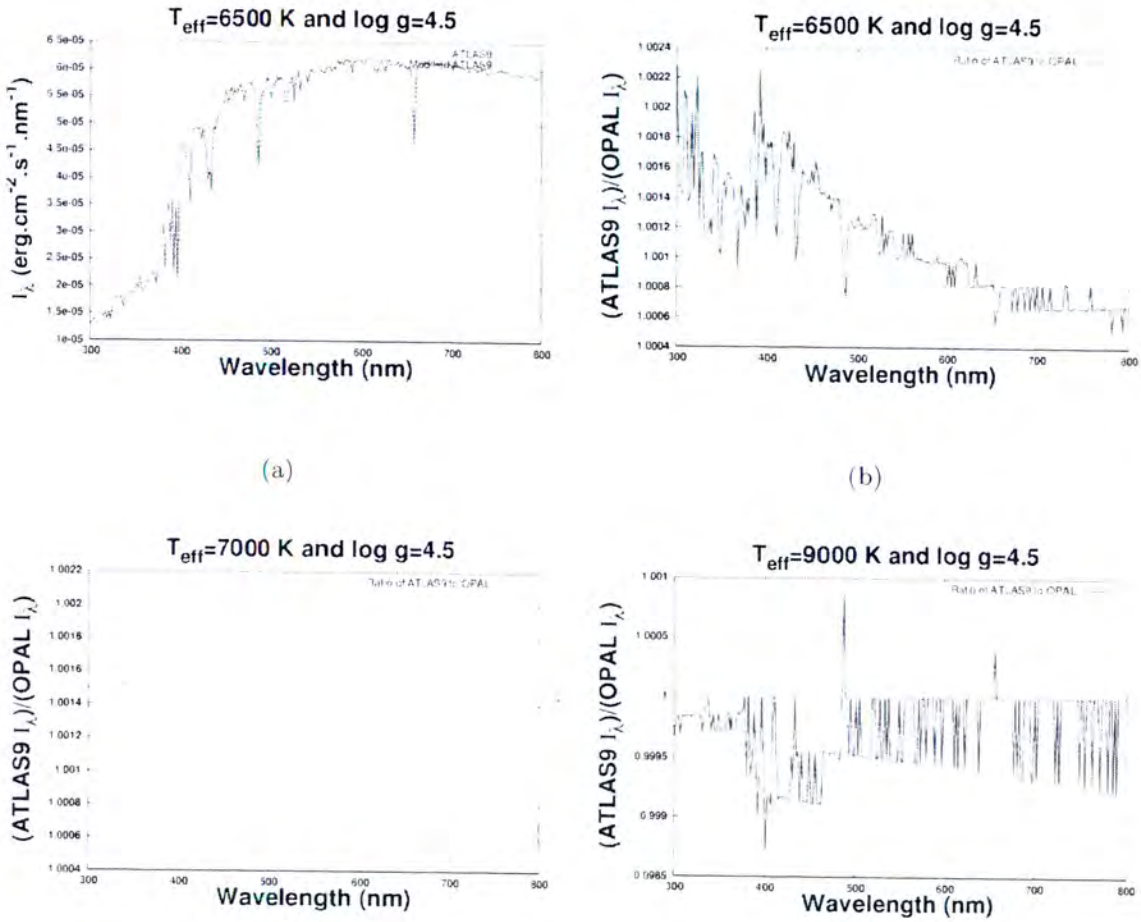

Figure 3.53: A plot of intensity as a function of wavelength for effective temperature T_{eff} =6500 K and surface gravity log g=4.5. The solid line in the first plot was calculated using normal ATLAS9 EOS and the dotted line was calculated using ATLAS9 with OPAL EOS. Also plotted is the ratio of the old ATLAS9 intensity as a function of wavelength for various effective temperatures (T_{eff}=6500 K–9000 K).

3.15 Comparing the new models to the old models

We have compared the new ATLAS9 models to the old ATLAS9 models, to see if they are consistent. The variables we have compared are density (ρ), Γ_1, the adiabatic temperature gradient ($\bigtriangledown_{ad}$) and $\Gamma_3 - 1$.

- In **Figure 3.54**, we present the density results to see if the obtained density from our new models matches with the older models calculated. As observed from this figure, the new ATLAS9 density models calculated with ATLAS9 and OPAL EOS are generally consistent with the older models calculated with ATLAS9. The consistency was observed for both the upper layers of the envelope and the outer layers of the atmosphere. The discernible differences were only observed for hotter models between the OPAL method and both the original ATLAS9 and the modified ATLAS9 (ATLAS9 + OPAL EOS). The new ATLAS9 models for density agree more with the original ATLAS9 models at the inner parts of a star.

- In **Figure 3.55**, we present figures for the first adiabatic exponent to see if the previously calculated results are consistent with the new ATLAS9 model atmosphere results. From **Figure 3.55**, we notice the following; the profiles are the same throughout. In **Figure 3.55** (e), the Γ_1 function calculated using the old and the new ATLAS9 code has a much steeper gradient at low optical depths compared to the OPAL method. For high surface gravities at log g=4.5 we note that the three models compared were virtually similar for low effective temperatures. Also at lower optical depths we see similar trends and the same numerical values for the modified ATLAS9 and the original ATLAS9. We also noted that the OPAL method is always below the two ATLAS9 methods. The differences range from 15 % to 44 % and these differences are due to the physics involved in the calculations of OPAL EOS as opposed to ATLAS9 The modified ATLAS9 is consistent with the original

ATLAS9 for Γ_3-1 and $\bigtriangledown_{ad}$ as seen in **Figures 3.56–3.57**.

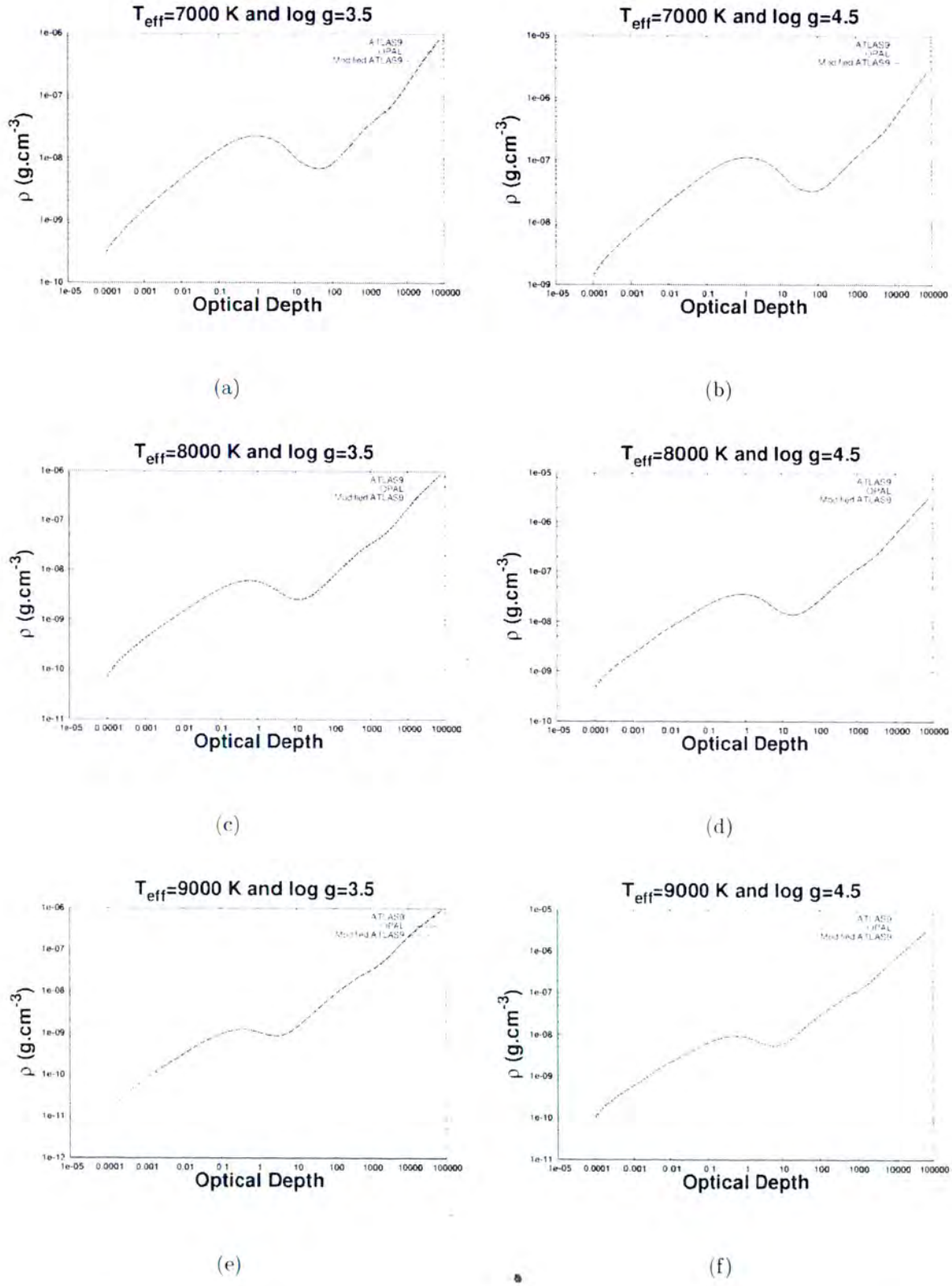

Figure 3.54: Plots of Density (ρ) as a function of optical depth for various effective temperatures and surface gravities. The solid line was calculated using normal ATLAS9 EOS. The dashed line was calculated using OPAL EOS and the double-dotted line was calculated using ATLAS9 with OPAL EOS. These are models of atmosphere and upper layers of the envelope.

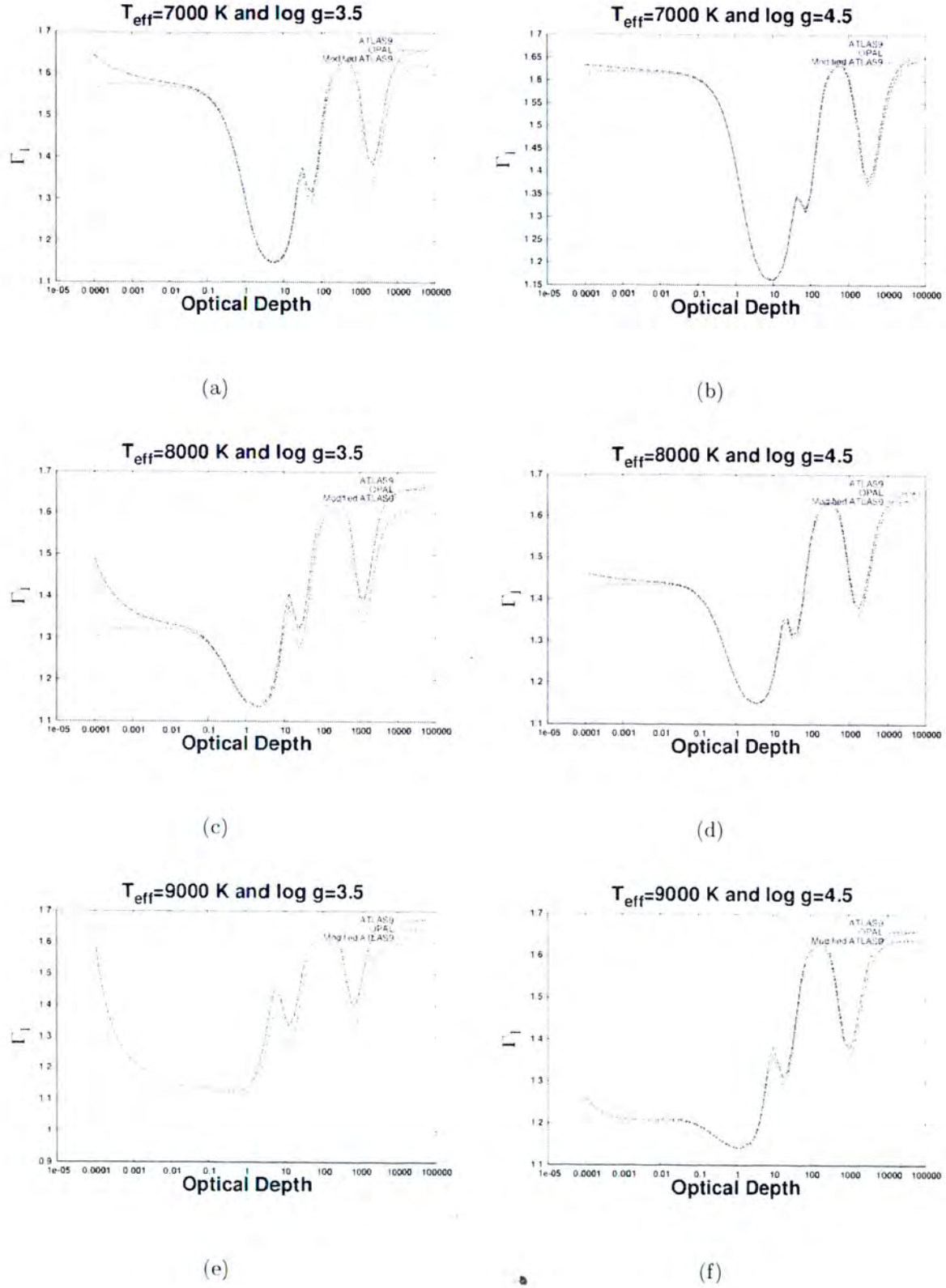

(a) (b)

(c) (d)

(e) (f)

Figure 3.55: Plots of Γ_1 as a function of optical depth for various effective temperatures and surface gravities. The solid line was calculated using normal ATLAS9 EOS. The dashed line was calculated using OPAL EOS and the double-dotted line was calculated using ATLAS9 with OPAL EOS. These are models of atmosphere and upper layers of the envelope.

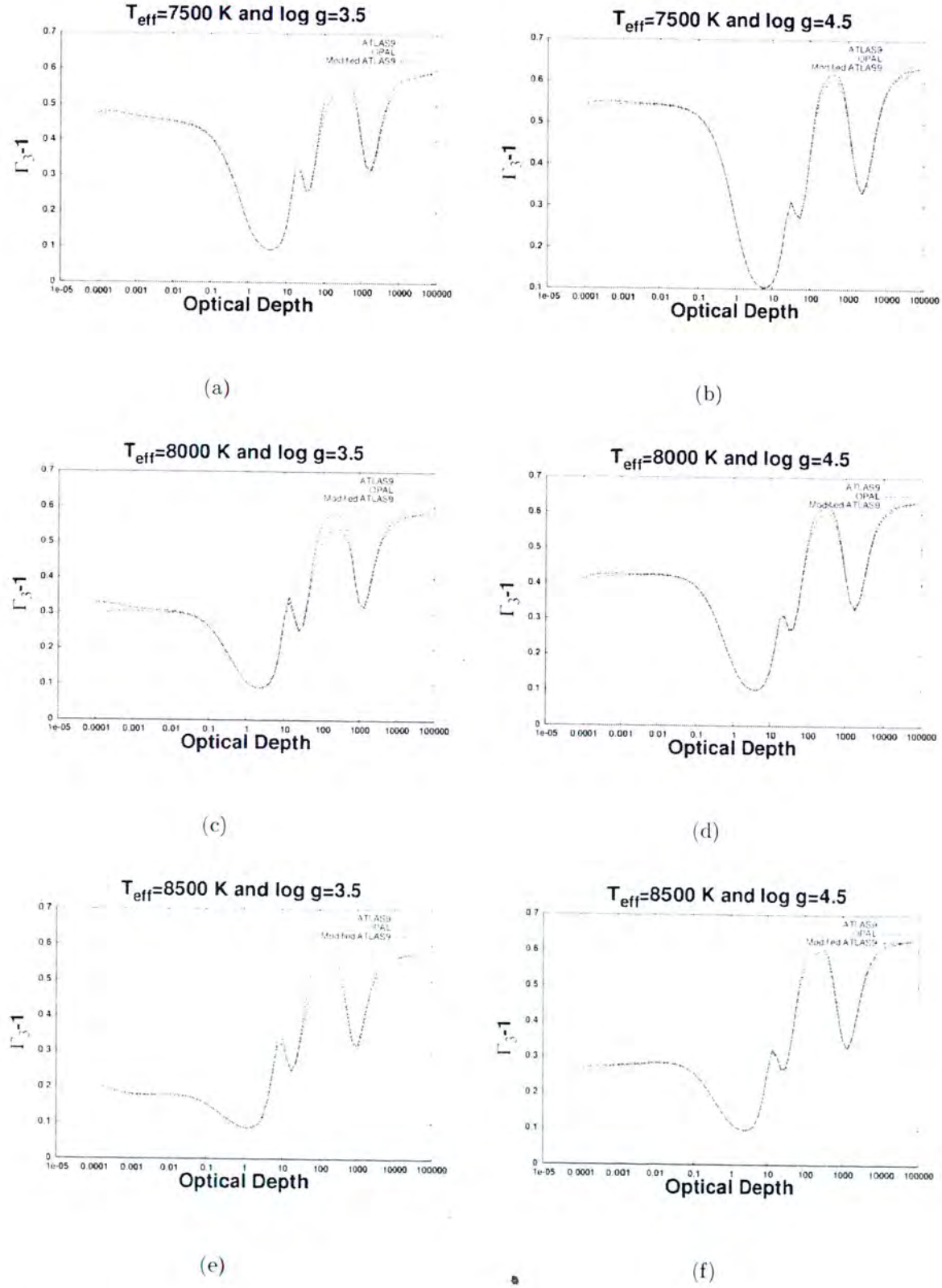

Figure 3.56: Plots of Γ_3-1 as a function of optical depth for various effective temperatures and surface gravities. The solid line was calculated using normal ATLAS9 EOS. The dashed line was calculated using OPAL EOS and the double-dotted line was calculated using ATLAS9 with OPAL EOS. These are models of atmosphere and upper layers of the envelope.

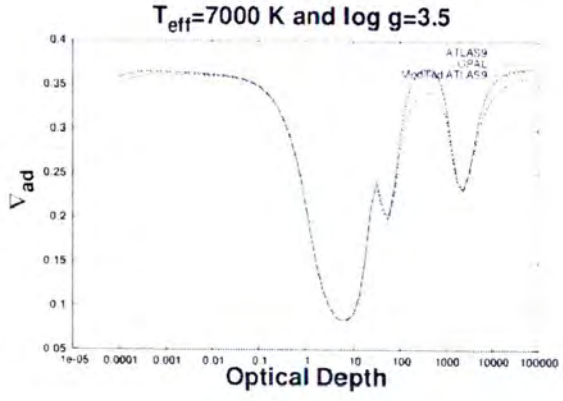

(a)

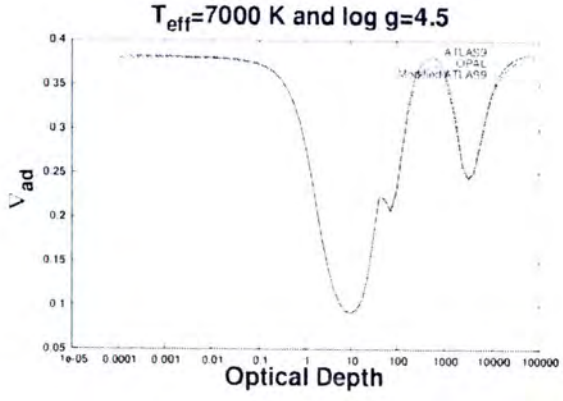

(b)

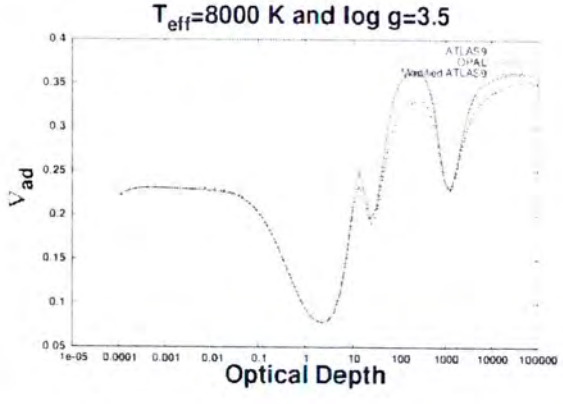

(c)

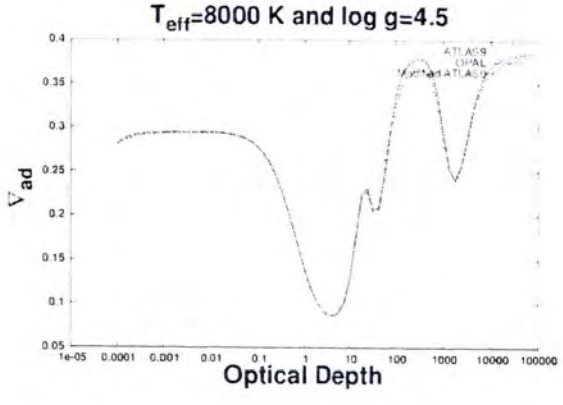

(d)

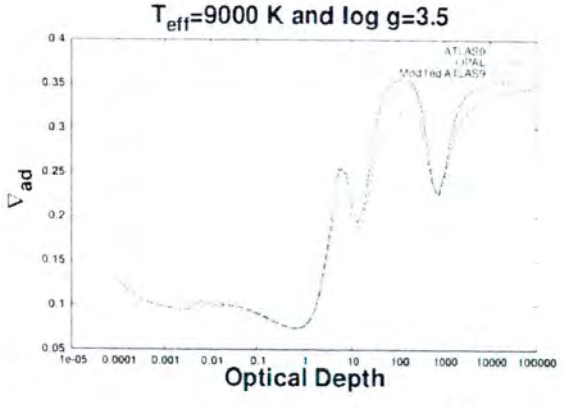

(e)

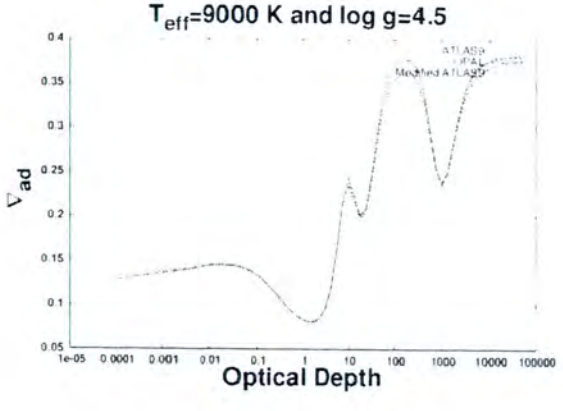

(f)

Figure 3.57: Plots of ∇_{ad} as a function of optical depth for various effective temperatures and surface gravities. The solid line was calculated using normal ATLAS9 EOS. The dashed line was calculated using OPAL EOS and the double-dotted line was calculated using ATLAS9 with OPAL EOS. These are models of atmosphere and upper layers of the envelope.

Chapter 4

Conclusions and Recommendations

The primary aim of the research project was to replace the ATLAS9 EOS with the OPAL EOS in the ATLAS9 model atmosphere code. Comparisons were done for effective temperature range of 6500 K $\leqslant$ T_{eff} $\leqslant$ 9500 K. This was done to determine the effect of replacing the OPAL EOS in the ATLAS9 calculations of model atmospheres. The findings are that the OPAL EOS gives results similar to those of the original ATLAS9 EOS for this atmosphere region. This conclusion stems from the agreement between the ATLAS9 density (ρ) profile and the OPAL EOS density profile in the atmosphere region. The discrepancy for this stellar variable was only found in the high effective temperature models. This discrepancy was mainly prominent on the stellar surface at low optical depths with the OPAL approach having a steeper gradient. For the work that was carried out in Chapter 2, we saw differences in the ATLAS9 model atmospheres and OPAL EOS for thermodynamic variables ($\Gamma_1, \nabla_{ad}, C_p$ & $\Gamma_3 - 1$). We noted that this was due to the differences in the thermodynamic states of gases between the old ATLAS9 and the new ATLAS9 program that uses OPAL EOS. For the work carried out in Chapter 3, we changed the EOS used in ATLAS9 and we observed the following: For density, pressure and temperature the differences in the slope of the profiles may be due to different elemental composition at high optical depths. Also, this may be due to ionisation zones of other metals. Furthermore, the different ways of code convergence may also account for the differences between the two methods at these high optical

depths. This same argument can be put forward for temperature. For all the thermodynamic variables, the differences that were seen were due to the different thermodynamic states of the gas.

- Furthermore, for density (ρ), the major differences between the old ATLAS9 and the new ATLAS9 were found in the upper layers of the envelope at higher optical depths. This was the case for all cooler models and hotter models. The differences in the slope for the density profiles may be due to other ionisation zones of metals at high optical depth. The percentage difference ranges between 5.5 %–18 %.

- For Temperature (T), very good matching was observed on the outer parts of a star for both hotter and cooler models. The differences between the old ATLAS9 and the new ATLAS9 were found in the upper layers of the envelope. This upper layer region of the envelope is the region where the temperature is reatively cooler. The percentage difference between the models for this region ranged from 0.32 %–22 %

- For pressure (P), we saw relatively good matching at the surface for cooler models. The major differences were observed in the upper regions of the envelope. The percentage differences for this envelope region was in ranges 1.7 %–5.5 %.

- For the electron density (e_n), we have also seen that major differences between the old ATLAS9 and the new ATLAS9 were seen in the upper regions of the envelope. The percentage difference were calculated to be in ranges 0.5 %–3.7 %.

- For the adiabatic temperature gradient (∇_{ad}), the good matching between the old ATLAS9 and the new ATLAS9 prevails for the outer parts of a star. As we moved to deeper layers, we have observed some differences between the two approaches. The percentage difference was calculated to be in ranges 2.8 %–18 %.

- For the first adiabatic exponent (Γ_1), we saw good matching at low optical depths for low effective temperatures. There were differences between the old ATLAS9 approach and

the new ATLAS9 approach in the upper region of the envelope. For this thermodynamic variable, the percentage differences between the two approaches were calculated to be in ranges 0.6 %–6.3 %. However, in all models the 'bump' due to Helium II ionisation zone is more pronounced than in Model S (Christensen-Dalsgaard et al. 1996). This suggests somehow ATLAS9 exaggerates the Helium abundance in the second Helium ionisation zone. Indeed this 'bump' gets reduced when Helium abundance is increased.

- For the Rosseland Mean Opacity (κ), we saw relatively good agreement in the upper layers of the envelope. For both cooler models and hotter, the difference between the new and the old ATLAS9 was seen in the outer parts of a star. The percentage difference were calculated to be in ranges 4.8 %–16 %.

- For the radiative temperature gradient ($\bigtriangledown_{rad}$), we observed good agreement for a wide range of optical depths. The disagreement was observed for the outer most parts of a star at τ <0.001. The percentage differences were calculated to be in ranges of up to 90 % for cooler models (T_{eff}=7000 K) and up to 75 % for hotter models (T_{eff}=9000 K).

- For the specific heat capacity (C_p), we observed that there was good agreement between the old ATLAS9 and the new ATLAS9 for the outer parts of a star. In the deeper layers, we saw differences between the two methods. The percentage difference was calculated to be in ranges up to 6.5 % for T_{eff}=7000 K & log g=4.5 and up to 40 % for T_{eff}=9000 K & log g=3.5.

- The Density Derivative at constant pressure $(\frac{d\log\rho}{d\log T})|_p$ for the two methods, was found to have agreed well in the outer layers of a star. This was for the cooler models at effective temperatures T_{eff}=7000 K. There were differences between the two methods for both high effective temperatures and low effective temperatures in the upper layers of the envelope. The percentage difference was found to be in ranges 4 %–18 %.

- For the Density Derivative at constant temperature $(\frac{d\log\rho}{d\log P})|_T$ for the two methods investigated, the findings were that good agreement was observed between the old ATLAS9 and

the new ATLAS9 for the outer parts of a star. The differences were found in the upper layers of the envelope. The percentage differences was calculated to range from 1.2 %–6 % for T_{eff}=7000 K & T_{eff}=9000 K and log g=4.5.

- For the spectrum, the differences between the two methods were quite small and ranged between 0.13 %–0.6 % for both cooler and hotter models.

Changing the EOS results in significant changes in thermodynamic variables of up to (90 % in ∇_{rad} for example) and the models changed up to 22 % while the spectra do not change much with only up to 0.6 % of a difference. From the opacity results, we see very good agreement for the opacity because the overall structure of the model was not changed significantly by inclusion of OPAL EOS in ATLAS9 model atmosphere.

One of the major challenges was that OPAL EOS does not work well for low temperature opacity. We believe that this challenge can be solved by using an EOS that is easy to access and has EOS tables that can be used for low temperature opacity. We have made tests to our models by revisiting the matching code but the mismatch between the envelope and the atmosphere prevails. Perhaps the mismatch problem lies with the matching procedure used.

Bibliography

[1] Adelman, S. J. 2004, The physical properties of normal A stars. *In: Proceedings International Astronomical Union Symposium No. 224*, eds. Zverko, J., Ziznovsky, J., Adelman, S. J., & Weiss, W. W. 8–13 July 2004: Poprad Slovakia. Cambribge UK: Cambribge University Press, 1–11.

[2] Aerts, C., Christensen-Dalsgaard, J., & Kurtz, D. W. 2010, *Asteroseismology*. Netherlands (Dordrecht): Springer-Verlag.

[3] Alexander, D. R. 1975, Low temperature Roseland opacity tables. *APS*, 29, 363–370.

[4] Alexander, D. R., & Ferguson, J. W. 1994, Low Temperature Opacity. *Ap.J*, 437, 879-891.

[5] Asplund, M., Grevesse, N., Sauval, A. J., & Scott, P. 2009, The chemical composition of the Sun. *ARA&A*, 47, 481–522.

[6] Audard, N., Kupka, F., Morel, P., Provost, J., & Weiss, W. W. 1998, Effects of atmosphere modelling on the acoustic cut-off frequency of Ap stars. *A&A*, 335, 954–958.

[7] Bahcall, J. N., Pinsonneault, M. H., & Wasserburg, G. J. 1995, Solar models with helium and heavy-element diffusion. *RMP*, 67, 781–808.

[8] Balona, L. A., Bohm, T., Foing, B. H., Ghosh, K. K., Janot-Pacheco, E., Krisciunas, K., Lagrange, A. M., Lawson, W. A., James, S. D., Baudrand, J., Catala, C., Dreux, M., Felenbok, P., & Hearson, J. B. 1996, Line profile variations in γ Doradus. *MNRAS*, 281, 1315–1325.

[9] Balona, L. A., Krisciunas, K., & Cousins, A. W. J. 1994, Hybrid γ Doradus-δ Scuti pulsators: New insights into the physics of the oscillations from Kepler observations. *MNRAS*, 270, 905–913.

[10] Basu, S., & Antia, H. M. 2008, Helioseismology and Solar abundances. *Phys. Rep*, 457, 217–283.

[11] Basu, S., & Christensen-Dalsgaard, J. 1997, Equation of State and Helioseismic inversions. *A&A*, 322, L5–L8.

[12] Basu, S., Däppen, W., & Nayfonov, A. 1999, Helioseismic Analysis of the Hydrogen partition function in the solar interior. *Ap.J.* 518, 985–992.

[13] Baturin, V. A. 2010, Smooth models of overshooting at the base of the solar convection. *AAS*, 328, 147–151.

[14] Bi, S. L., Maruo, M. P., & Christensen-Dalsgaard, J. 2000, Non-ideal effects on the Solar Equation of State. *A&A*, 364, 157–164.

[15] Breger, M. 1995, Astrophysical applications of Scuti stars. *PASP*, 83, 70–78.

[16] Carol, B. W., & Ostli, D. A. 1995, *Introduction to Modern Astrophysics*. San-Fransisco: Addison-Wesley.

[17] Castelli, F. 2005, DFSYTHE: how to use it. *Mem. Soc. Astron. Ital.*, 8, 34–39.

[18] Castelli, F., Gratton, R. G., & Kurucz, R. L. 1997, Notes on convection in the ATLAS9 model atmosphere. *A&A*, 318, 814–869.

[19] Castelli, F., & Kurucz, R. 2004, New Grids of ATLAS9 Model Atmospheres. *In: International Astronomical Union Symposium: Coronal and Stellar Mass Ejections*, eds. Piskunov, N., Weiss, W. W., & Gray, D. F. 13–17 September 2004. China: Beijing, 210, 20–26.

[20] Castelli, F. 1996, Model Atmospheres and Spectrum Synthesis. *In: ASP Conf. Ser: Model Atmosphere and Stellar Spectra*, eds. Adelman, S. J., Kupka, F., & Weiss, W. W. 1996, Vienna, 108, 85–93.

[21] Charbonnel, C., Däppen, W., Schaerer, D., Bernasconi, P. A., Maeder, A., Meynet, G., & Mowlavi, I. 1999, Grids of stellar models. *Astron.Astrophys.Suppl.Series*, 135, 405–413.

[22] Christensen-Dalsgaard, J., Däppen, W., Ajukov, S. V., Anderson, E. R., Antia, H. M., Basu, S., Baturin, V. A., Berthomieu, G., Chaboyer, B., Chitre, S. M., Cox, A. N., Demarque, P., Donatowicz, J., Dziembowski, W. A., Gabriel, M., Gough, D. O., Guenther, D. B., Guzik, J. A., Harvey, J. W., Hill, F., Houdek, G., Iglesias, C. A., Kosovichev, A. G., Leibacher, J. W., Morel, P., Proffitt, C. R., Provost, J., Reiter, J., Rhodes, E. J., Rogers, F. J., Roxburgh, I. W., Thompson, M. J., & Ulrich, R. K. 1996, The current state of Solar Modelling. *AAAS*, 272, 1286–1292.

[23] Christensen-Dalsgaard, J., Di Mauro, M .P., Schalttl, H., & Weiss, A. 2005, On Helioseismic tests of basic physics. *MNRAS*, 356, 587–595.

[24] Christensen-Dalsgaard, J. 2003, *Lecture notes on Stellar Oscillations*. Aarhus University. Available at: http://users-phys.au.dk/jcd/oscilnotes/print-chap-full.pdf [Accessed: May 2003].

[25] Christensen-Dalsgaard, J., & Frandsen, S. 1983, Radiative transfer and solar oscillations. *In: International Astronomical Union and Akademiia Nauk SSSR, 66th Colloquium on Problems of Solar and Stellar Oscillations*, 1-5 September 1981, Nauchny, Ukrainian SSR, 82, 165–204.

[26] Christensen-Dalsgaard, J., & Däppen, W. 1992, Solar Oscillations and the Equation of State. *A&A*, 4, 267–361.

[27] Christy, R. F. 1962, Energy Transport in the Hydrogen Ionisation Zone of Giant Stars. *Ap.J*, 136, 887–892.

[28] Ciancio, F., Deglinnocenti, S., & Ricci, B. 1997, Updating Standard Solar Models. *AASS*, 123, 449–454.

[29] Clayton, D. D. 1986, Solar Structure without Computers. *AJP*, 54, 354–362.

[30] Cousins, A. W. J. 1966, *MNASSA*, 25, 40–46.

[31] Cousins, A. W. J. 1992, *SAAO circulars*, 112, 53–60.

[32] Cousins, A. W. J., & Warren, R. R. 1963, Photometric Data for Stars in the Equatorial Zone. *MNASSA*, 22, 65–71.

[33] Cox, A. N., & Steward, J. N. 1970, Roseland Opacity tables for population I compositions. *Ap.JS*, 19, 243–260.

[34] Cox, P. J., & Giuli, R. T. 1968. *Stellar Structure Principles*. New York (Gordon and Breach): Science Publishers.

[35] Cugier, H. 2012, Testing Opacity and Equation of State of LTE and non LTE model atmospheres with OPAL and OP data for early type stars. *A&A*, 547, 17–23.

[36] Däppen, W., Anderson, L., & Mihalas, D. 1987, Statistical Mechanics of Partially Ionised Stellar Plasma. *Ap.J*, 319, 195–206.

[37] Däppen, W., & Guzik, J. A. 2000, Astrophysical Equation of State and Opacity. *Nato SS*, 544, 177–183.

[38] Däppen, W., Mihalas, D., & Hummer, D. G. 1988, The Equation of State for stellar envelopes III. *Ap.J*, 332, 261–270.

[39] Di Criscienzo, M., Ventura, P., & D'Antona, F. 2010, The role of the Equation of State in models of very low mass stars. *ASS*, 328, 167–189.

[40] Di Mauro, M. P. 2012, Theoretical Aspects of Astereoseismology: Small steps towards a golden future. *In:Proceedings of the SOHO 14 / GONG 2004 Workshop*, New Haven, Connecticut, USA, 12-16 July 2004., ed, Danesy, D., 559, 186–200.

[41] Dziembowski, W. A., & Pamjatnykh, A. A. 1991, A potential asteroseismological test for convective overshooting theories. A&, 248, L11-L14.

[42] Eddington, A. S. 1929, *MNRAS*, 89, 620–636

[43] Eggleton, P. P., Faulkner, J., & Flannery, B. P. 1973, An approximate Equation of State for stellar material. *A&A*, 23, 325–330.

[44] Eliezer, S., Ghatak, A., & Hora, H. 2002. *Fundamentals of Equation of State*. Singapore: World Scientific Pub Co Inc.

[45] Eyer, L., Aerts, C., Van Loon, M., Boukaert, F., & Cuypers, J. 2001, A γ Doradus star campaign. *In: ASP Conf Series: Observational aspects of pulsating B & A stars*, eds. Sterken, C., & Kurtz, D. W, 265, 203–218:

[46] Fall, A. 2003, Lecture notes in Astrophysics (ASTR 3730), retrieved from: jila.colorado.edu/-pja/astr3730/lecture16.pdf.

[47] Ferguson, J. W., Alexander, D. R., Allard, F., Barman, T., Bodnarik, J. G., Hauschildt P. H., Heffner-Wong, A., & Tamania, A. 2005, Low Temperature Opacities. *Ap.J*, 623, 585–596.

[48] Fotov, V. E., & Lomonosovo, I. V. 2010, *TOPPJ*, 3, 122–130.

[49] Gong, Z., Däppen W., & Nayfonov A. 2001, Effects of heavy elements and excited states in the Equation of State of the Solar interior. *Ap.J*, 563, 419–433.

[50] Grevesse, N., & Noels, A. 1991, Vibration rotation bands of CH in the Solar infrared spectrum and the Solar carbon abundance. *A&A*, 242, 488–495.

[51] Grevesse, N., & Sauval, A. J. 1998, Standard Solar Composition. *SSR*, 85, 161–174.

[52] Grigahcene, A., Antoci, V., Balona, L., Catanzaro, G., Daszynska-Daszkiewicz, J., Guzik, J. A., Handler, G., Houdek, G., Kurtz, D. W., Marconi, Monteiro, M. J. P. F. G., Moya, A., Ripepi, V., Suarez, J. C., Uytterhoeven, K., Borucki, W. J., Brown, T. M., Christensen-Dalsgaard, J., Gilliland, R. L., Jenkins, J. M., Kjeldsen, H., Koch, D., Bernabei, S., Bradley, P., Breger, M., Di Criscienzo, M., Dupret, M. A., Garcia, R. A., Hernandez, A., Jackiewicz, J., Kaiser, A., Lehmann, H., Marin-Ruiz, S., Mathias, P., Molenda-Zakowicz, J., Nemec, J. M., Nuspl, J., Paparo, M., Roth, M., Szabo, R., Suran, M. D., & Ventura, R. 2010, Hybrid γ Doradus-δ Scuti Pulsators: New Insights into the physics of the oscillations from Kepler Observations. *Ap.J*, 713, L192–L197.

[53] Guenther, D. B., Demarque, P., Kim, Y. M., & Pinsonneault, M. H. 1992, Standard Solar Model. *Ap.J*, 387, 372–393.

[54] Guenther, D. B., Kim, Y. C., & Demarque, C. 1996, Seismology of the Standard Solar Model. *Ap.J*, 463, 382–390.

[55] Guzik, J. A., & Swenson, F. J. 1997, Seismological comparisons of Solar models with element diffusion using the MHD, OPAL and SIREFF EOS. *Ap.J*, 491, 967–979.

[56] Haensel, P., Potenkihin, A. Y., & Yakovlev, D. G. 2007. *Neutron Stars I: Equation of State and Structure*. New York: Springer.

[57] Hummer, D. G., & Mihalas, D. 1988, The Equation of State for Stellar Envelopes I. *Ap.J*, 331, 794–814.

[58] Iglesias, C. A., & Rogers, F. J. 1996, Updated OPAL Opacities. *Ap.J*, 464, 943–953.

[59] Iglesias, C. A., Rogers, F. J., & Wilson, B. G. 1992, Spin-orbit interaction effects on the Rosseland Mean Opacity. *Ap.J*, 397, 717–728.

[60] Kaye, B. A., Handler, G., Krisciunas, K., Poreti, E., Zerb, M. F., & Filippo, M. 1999, Defining a new class of pulsating variables. *PASP*, 761, 840–844.

[61] Kippenhahn, R., & Weigert, A. 1994. *Stellar Structure and Evolution.* 3^{rd} Edition. Berlin: Springer-Verlag.

[62] Kirby, E. N. 2011, Grids of ATLAS9 model Atmospheres and MOOG synthetic spectra. *PASP*, 903, 531–535.

[63] Kjeldsen, H., & Bedding, T. R. 2011, Amplitudes of Solar-like Oscillations: A New Scaling Relation. *A&A*, 529, 4 pp.

[64] Kosovichev, A. G. 2005, Sun's global property measurements: Helioseismic probing of solar variability. *Mem. S.A.It*, 76, 743–749.

[65] Kurucz, R. L. 1970, Atlas: A Computer Program for Calculating Model Stellar Atmospheres. *SAO Special Report*, 309.

[66] Kurucz, R. L. 1979, Model Atmospheres. *APJS*, 40, 1.

[67] Kurucz, R. L. 2005, Physical, Numerical and Computational limits for Kurucz codes. *mem.S.A.Lt*, 8, 73–77.

[68] Kurtz, D. W. 1982, Rapidly oscillating AP stars. *MNRAS*, 200, 807–859.

[69] Kurtz, D. W. 1990, Rapidly Oscillating AP stars. *ARA&A*, 28, 607–655.

[70] Lattimer, J. M., & Prakash, M. 2001, Neutron Star Structure and the Equation of State. *Ap.J.* 550, 426–442.

[71] Leighton, R. B., Noyes, R. W., & Simon, G. W. 1962, Velocity Fields in the Solar Atmosphere. *Ap.J*, 135, 474–479.

[72] Lester, J. B., & Neilson H. R. 2008, Atlas: Spherical Versions of the Atlas Stellar Atmosphere Program. *A&A*, 491, 633–639.

[73] Lin, C. H., & Däppen, W. 2005, The Chemical Composition and Equation of State of the Sun Inferred from Seismic Models through an Inversion Procedure. *Ap.J*, 623, 556–570.

[74] Lin, C. H., & Däppen, W. 2010, Emulating the OPAL Equation of State. *ASS*, 328, 175–178.

[75] Lin, C. H., & Däppen, W. 2012, A Practical Equation of State for the Sun and Sun-like Stars. *CPP*, 52, 126–129.

[76] Lobel, A., Achmad, L., De Jager, C., & Nieuwenhuij, C. 1992, On the Insability parameters of stellar atmospheres. *A&A*, 264, 147–152.

[77] Luo, G. 1994, The Equation of State in the chemical picture: A grand-canonical approach. *A&A*, 410, 611–621.

[78] Maceroni, C., Montalban, J., Michele, E., Harmanec, P., Prsa, A., Briquet, M., Niemczura, E., Morel, T., Ladjal, D., Auvergne, M., Baglin, A., Baudin, F., Catala, C., Samadi, R., & Aerts, C. 2009, HD 174884: A strongly eccentric, short-period early type binary system discovered by CoRoT. *A&A*, 508, 1375–1389.

[79] Maeder, A. 1995, 'Population I stellar structure and evolution:facing the lingering difficulties to make a step forward', *In* ASP conf series. *Proceedings of IAU Colloquium. Vol.83*, eds. Stobie, R. S., & Whitelock, P. A. 6–10 February 1995: Cape Town, San Fransisco: Astronomical Society of the Pacific. 1–12.

[80] Magni, G., & Mazitelli, I. 1979, Thermodynamic properties and Equations of State for hydrogen and helium in stellar conditions. *A&A*, 72, 134–147.

[81] Martines, P., & Kurtz, D. 1995, Rapid Pulsations in AP Stars. *Astronomical Society of the Pacific Conference Series.*, *Proceedings of IAU Colloquium*, eds. Stobie, R. S., & Whitelock, P. A. 6–10 February 1995: Cape Town, San Fransisco: Astronomical Society of the Pacific, 58–70.

[82] Meszaros, Sz., Prieto, C. A., Edvardsson B., Castelli, F., Perez E. G., Gustafsson, B., Majewski, S. R., Plez, B., Schiavon, R., Shetrone, M., & Vicente, A. D. 2012, New ATLAS9 and MARCS Model Atmosphere Grids for the Apache Point Observatory Galactic Evolution Experiment (APOGEE). *Ap.J*, 144, 8 pp.

[83] Meszaros, Sz., & Prieto, C. A. 2013, On the interpolation of model atmosphere and high-resolution synthetic stellar spectra. *MNRAS*, 430, 3285–3291.

[84] Mguda, Z. 2010, *Matching Stellar envelope Models to ATLAS9 model atmospheres.* Thesis (M.sc). University of Cape Town.

[85] Mihalas, D., Däppen, W., & Hummer, D. G. 1988, The Equation of State for Stellar Envelopes II. *Ap.J*, 331, 815–825.

[86] Montalban, J., Antona, F. D., & Kupka, F. 2004, Convection in the atmospheres and envelopes of Pre-Main Sequence stars. *A&A*, 416, 1081–1096.

[87] Mullan, D. J. 2009. *Physics of the Sun.* Boca Raton: CRC Press.

[88] Murdin, P., ed. 2001. *Encyclopedia of Astronomy and Astrophysics.* London: IoP and Nature Publishing Group.

[89] Nayfonov, A. J., Däppen, W., Hummer, D. G., & Mihalas, D. M. 1999, The MHD Equation of State with Post-Holtsmark Microfield Distributions. *Ap.J*, 526, 451–464.

[90] Neuforge, C. 1993, Low temperature Rosseland mean opacities. *A&A*, 274, 818–820.

[91] Padmanabhan, T., & Narlikar, J. V., ed. 2006. *An invitation to Astrophysics.* 8^{th} Edition. Singapore: World Scientific Publishing Co.Ltd.

[92] Pols, O. R., Tout, C. A., Eggleton, P. P., & Han, Z. 1995, Approximate input physics for stellar modelling. *MNRAS*, 274, 964–974.

[93] Preston, G. W. 1974, The chemically peculiar stars of the upper main sequence. *ARA*, 12, 257–277.

[94] Rogers, F. J. 1981, Equation of state of dense, partially degenerate, reacting plasmas. *Phys. Rev*, 24, 1531–1543.

[95] Rogers, F. J. 1994, Equation of State of stellar plasma, *In* International Astronomical Union. *147th Proceedings of the IAU Colloquium*, eds. Chabrier, G., & Schatzman, E. 14–18 June 1993: Saint Malo, Cambribge: Cambribge University Press, 16 pp.

[96] Rogers, F. J., & Iglesias, C. A. 1992, Equation of State of Partially-Ionised Plasmas in the Physical Picture. *RMAA*, 23, 133–139.

[97] Rogers, F. J., & Nayfonov, A. 2002, Updated and Expanded OPAL Equation of State tables: Implications for Helioseismology. *Ap.J*, 576, 1064–1074.

[98] Rozelot, J. P., & Neiner, C., eds. 2011. *Pulsations of the Sun and other Stars*. Berlin: Springer.

[99] Saha, M. 1920, *Philos.mag*, 40, 472–479.

[100] Samadi, R., Nordlund, A., Stein, R. F., Goupil, M. J., & Roxburgh, I. 2003, Stochatic Excitation of acoustic modes in stars. *A&A*, 404, 1129–1133.

[101] Saumon, D. 1994, A comparative study of hydrogen Equations of State, *In* International Astronomical Union. *147th Proceedings of the IAU Colloquium*, eds. Chabrier, G., & Schatzman, E. 14–18 June 1993: Saint Malo, Cambribge: Cambribge University Press, 147, 306-312.

[102] Saumon, D., Chabrier, G., Wagner, D. J., & Xie, X. 1999, Modelling Pressure-Ionisation of Hydrogen in the context of Astrophysics. *HPR*, 16, 331–343.

[103] Seaton, M. J., & Badnel, N. R. 2004, A comparison of Roseland Mean Opacities from OP and OPAL. *MNRAS*, 354, 457–465.

[104] Seaton, M. J., Yan, Yu., Mihalas, D., & Pradhan, A. K. 1994, Opacities for Stellar Envelopes. *MNRAS*, 266, 805–828.

[105] Semenov, D., Henning, T. H., Helling, C. H., Ilgner, M., & Sedlmayr, E. 2003, Roseland and Planck mean opacities for protoplanetary discs. *A&A*, 410, 611–621.

[106] Shulyak, D., Tsymbal, V., Ryabchikova, T., Stutz, C. H., & Weiss, W. W. 2004, Line-by-line opacity stellar model atmosphere. *A&A*, 428, 993–1000.

[107] Soriano, M., & Vauclair, S. 2010, New seismic analysis of the exoplanet host μ Arae. *A&A*, 513, 8 pp.

[108] Stoltmann, W., & Blocker, T. 2000, Thermodynamical Properties of Stellar Matter. *A&A*, 361, 1152–1168.

[109] Strom, S. E., Kurucz., & R. L. 1966, A statistical procedure for computing line-blanketed model stellar atmospheres with applications to the F5IV star procyon. *JQSRT*, 6, 591–607.

[110] Stutz, C. H. 2005, Stellar models and opacity: The LL MODELS approach. *mem S.A.it Suppl*, 8, 165–169.

[111] Swenson, F. J., & Rogers, F. J. 1992, An Improved EFF Equation of State: Comparison with the OPAL Equation of State. *AAS*, 24, 1176–1181

[112] Trampedach, R., Asplund M., Collet, R., Nordlund, A., & Stein, R. F. 2013, A Grid of Three-dimensional Stellar Atmosphere Models of Solar Metallicity: General Properties, Granulation and Atmospheric expansion. *Ap.J*, 769:18 (15 pp).

[113] Trampedach, R., Däppen, W., & Baturin, V. A. 2006, A synoptic comparison of the Mihalas-Hummer-Däppen and OPAL Equation of State. *AAS*, 646, 560–578.

[114] Turcotte, S., Richer, J., Michaud, G., Iglesias, C. A., & Rogers, F. J. 1998, Consistent Evolution of Stars: Diffusion, Radiative Accelerations and Abundance Anomalies. *Ap.J*, 504, 539–558.

[115] Van Horn, H. M. 1992, *APJ*, 397, 674–679.

[116] Waelkens, C. 1995, Pulsation and evolution: *In* ASP conf series. *Proceedings of IAU Colloquium. Vol.83*, eds. Stobie, R. S., & Whitelock, P. A. 6–10 February 1995: Cape Town, San Fransisco: Astronomical Society of the Pacific. 23–31

[117] Wolff, S. C. 1983, The A-type stars: Problems and perspective. *NASA*, 463–469.

[118] Wood, M. 1994, *In: International Astronomical Union, 147th Proceedings of the IAU Colloquium*, eds. Chabrier, G., & Schatzman, E. 14–18 June 1993: Saint Malo, Cambribge: Cambribge University Press, 147, 612–618.

[119] Yildiz, M., & Kiziloglu, N. 1997, Solar Models: Influence of the Equation of State and Opacity. *A&A*, 326, 187–194.

In this Appendix we outline how the calculations in Chapter 2 were carried out. We do this by explaining all the algorithms that were used to get the results. The first code that we used was the OPAL routine code called **calling.f** and **esac.f**. The function of **calling.f** was to call the routine **esac.f**. Before using these two codes we had to generate data (E0S5−data) by running separately a code called ZFS−interp−EOS5.f This data was included in the **esac.f** code. The first step in our calculations was to create a stellar atmosphere model using ATLAS9. The output of this model included stellar variables such as temperature, pressure, electron density, density, rosseland mean opacity and optical depth. The models that were calculated were for various effective temperatures from 7000 K to 9500 K with varying surface gravity from log g=3.5 to 4.5 in steps of 0.5. The main generator of the model is depicted in **Figure 4.1**. We first calculated the OPAL density by using temperature and pressure as inputs. The other inputs were the stellar compositions. The code below calculates density as subroutine r =rhoofp(xh,ztab,t6,P,irad), where xh is the hydrogen composition, $ztab$ is the composition of all elements heavier than helium, $t6$ is the temperature, P is the pressure and irad is used to either make a radiative model or a non-radiative model.

```
rm -f fort.*
ln -s  kapp00.ros fort.1
ln -s  p00big2.bdf fort.9
ln -s  molecules.dat fort.2
#Starting model assignation
ln -s a00t8000g45.mod  fort.3
./atlas9mem_newodf3.exe <<EOF
READ KAPPA
READ PUNCH
MOLECULES ON
READ MOLECULES
FREQUENCIES 337 1 337 BIG
VTURB 0.0E+5
CONVECTION OVER 1.25 0
TITLE Teff=10000 model 4
ABUNDANCE SCALE   1.00000 ABUNDANCE CHANGE 1 0.91930 2 0.07824
 ABUNDANCE CHANGE  3 -10.94  4 -10.64  5  -9.49  6  -3.52  7  -4.12  8  -3.21
 ABUNDANCE CHANGE  9  -7.48 10  -3.96 11  -5.71 12  -4.46 13  -5.57 14  -4.49
 ABUNDANCE CHANGE 15  -6.59 16  -4.71 17  -6.54 18  -5.64 19  -6.92 20  -5.68
 ABUNDANCE CHANGE 21  -8.87 22  -7.02 23  -8.04 24  -6.37 25  -6.65 26  -4.54
 ABUNDANCE CHANGE 27  -7.12 28  -5.79 29  -7.83 30  -7.44 31  -9.16 32  -8.63
 ABUNDANCE CHANGE 33  -9.67 34  -8.63 35  -9.41 36  -8.73 37  -9.44 38  -9.07
 ABUNDANCE CHANGE 39  -9.80 40  -9.44 41 -10.62 42 -10.12 43 -20.00 44 -10.20
 ABUNDANCE CHANGE 45 -10.92 46 -10.35 47 -11.10 48 -10.27 49 -10.38 50 -10.04
 ABUNDANCE CHANGE 51 -11.04 52  -9.80 53 -10.53 54  -9.87 55 -10.91 56  -9.91
 ABUNDANCE CHANGE 57 -10.87 58 -10.46 59 -11.33 60 -10.54 61 -20.00 62 -11.03
 ABUNDANCE CHANGE 63 -11.53 64 -10.92 65 -11.69 66 -10.90 67 -11.78 68 -11.11
 ABUNDANCE CHANGE 69 -12.04 70 -10.96 71 -11.98 72 -11.16 73 -12.17 74 -10.93
 ABUNDANCE CHANGE 75 -11.76 76 -10.59 77 -10.69 78 -10.24 79 -11.03 80 -10.91
 ABUNDANCE CHANGE 81 -11.14 82 -10.09 83 -11.33 84 -20.00 85 -20.00 86 -20.00
 ABUNDANCE CHANGE 87 -20.00 88 -20.00 89 -20.00 90 -11.95 91 -20.00 92 -12.54
 ABUNDANCE CHANGE 93 -20.00 94 -20.00 95 -20.00 96 -20.00 97 -20.00 98 -20.00
 ABUNDANCE CHANGE 99 -20.00
CALCULATE STARTING MODEL 500 DEPTHS STARING AT -4.00 SPACING 0.125
CORRECTIONS ON
SCALE 72 -4.000 0.125 8000. 4.50
ITERATIONS 15   PRINT 1 1 0 0 0 0 0 0 0 1 1 0 0 0 1
               PUNCH 1 0 0 0 0 0 0 0 0 1 0 0 0 0 1
BEGIN
SCALE 72 -4.000 0.125 8000. 4.50
ITERATIONS 15   PRINT 1 1 0 0 0 0 0 0 0 1 1 0 0 0 1
               PUNCH 1 0 0 0 0 0 0 0 0 1 0 0 0 0 1
BEGIN
END
```

Figure 4.1: An example of an input script.

• Program written by Papi Lekwene to calculate the specific heat capacity (Cp) using the formula.

$$C_p = (\Gamma_1 \times C_v)/(\chi_p) \tag{4.1}$$

```
real E5,E6,E7,rhox2,n,rhox,t6,p,po,density,p1,p3,
x tau,p5,p6,p7,p8,CP1
integer i
open(unit=50,file="CV.dat",status="unknown") ! this is Cv, specific heat capacity with constant volume (eos(5)).
open(unit=51,file="Xt.dat",status="unknown") ! this is eos(6), Xt
open(unit=52,file="E7.dat",status="unknown") ! this is Xp
open(unit=53,file="CP.dat",status="unknown") ! where we write data for opal
open(unit=55,file="vsound4.5=7000.dat",status="unknown")
open(unit=54,file="oriGer70004.5a.dat",status="unknown")
open(unit=59,file="Ht.dat",status="unknown") ! for atlas9
i=1 10 read(50,*,end=20)E5,tau
read(51,*,end=21)E6,tau
read(52,*,end=22)E7,tau
read(54,*,end=23)num,rhox,t6,p,po,density,p1,p3,tau,p5,p6,p7,p8
read(55,*,end=30)rhox1,Ptotal,Pturb,PRDADB,DLTDLP,Velsd,
x DLRDLT,Cp,H,Vconvec,cocn
print*,p
CP1=((((p)/(density*t6))*(((E7)**(2))/(E6)))-(E5))
print*,CP1
CP1= (E6*E5)/(E7)
write(53,*)CP1,tau ! writing to opal file
```

```
write(59,*)Cp,tau ! writing to atlas9 file.
i=i+1
goto 10
20 close(50)
21 close(51)
22 close(52)
23 close(54)
close(53)
30 close(55)
end
```

In the following appendix we outline how the calculations in Chapter 3 were done.

• In the main program of atlas9v.for, the following declaration variables and common blocks were made.

```
parameter(mx=5,mv=10,nr=169)
real rhoofp,t6,pp,xh,ztab,rrhox(kw),esact,eos,xxh,zztab
common /opalv/ xh,ztab,irad
common/eeos/esact,eos(mv)
```

Variable rhoofp represents the function that OPAL calculates for the density, t6 is input temperature from ATLAS9, pp is the pressure, xh is the hydrogen fraction in mass, ztab is the fraction for all elements heavier than helium.

The following program statement defines how we called the subroutine convAB This statement was written in the main program.

```
call convAB()
print*,'xh,ztab ',xh,ztab,irad
444 format(1pe23.14,1pe23.14,1p50e23.14)
call convec
write(39,*)
write(39,*)'TAUROS TEMP PRES RHO KAPPA GRDAB CP GAMMA1 NABLA'
do j=1,NRHOX
write(39,444)tauros(j),T(j),P(j),rho(j),abross(j),grdadb(j)
x heatcp(j),velsnd(j)**rho(j)/P(j),dltdlp(j),
x dlrdlt(j),dlrdlp(j)
enddo
close(39)
SUBROUTINE convAB()
real*8 el,sum,mass,tmass,sMass,atMassu,a,d,Y,Z1
```

```
real xh,ztab
double precision Ntotal,NH,NHe,ABUND
double precision ATMASS,ELEM
common /opalv/ xh,ztab,irad ! OPAl variables in a common block
COMMON /ELEM/ABUND(99),ATMASS(99),ELEM(99)
sum=0.0
irad=1
sMass=1.989e30 !mass of the Sun
atMassu=1.66053886e-27 !atomic mass
c PRINT*,'sMass',sMass,atMassu
do j=3,99 !leave out Hydrogen and Helium
Z1=(10)**(ABUND(j)) ! the number fraction of heavy elements.
mass=ATMASS(j)
tmass=(mass*atMassu) ! atomic weights. just conversion
a=Z1*tmass
sum=sum+a !rest of the elements as one entity
c PRINT*,Z1,mass,tmass,a,sum
enddo
c d=(0.91930*atMassu)+(0.07824*4.003*atMassu)+(sum)
Ntotal=(sMass)/(d)
NH=Ntotal*0.91930
NHe=Ntotal*0.07824
xh=(NH*atMassu)/(sMass)
Y= (NHe*4.003*atMassu)/(sMass)
ztab=1.-xh-Y
print*,'HANO ',ztab,d,Ntotal,NH,NHe
c print*,Y
c print*,xh
```

```
1000 format(f2.3)
RETURN
END
```

• Program that converts the Grevesse solar composition (in number) to the atlas9 composition.

```
real Ael,Nel,NH,Nat,He,Rel
integer i
NH=0.91930
He=10.93
open(92,file="SSScomp.dat",status="unknown")
open(93,file="convert.dat",status="unknown")
i=0
10 read(92,*,end=20)de
Nat=10**(He-12)*NH !HELIUM CONVERSION
Rel=de-12 !working out the rest of the elements in log scale as in atlas9
write(93,*)Rel
i=i+1
goto 10
20 close(92)
close(93)
```

• The following program was written to compare the original ATLAS9 spectrum with the modified ATLAS9 code.

```
parameter(nmmu=20,N=5000)
real*8 wav(N),In(nmmu,N),mu(nmmu),freq,te,logg
character*10 inn
111 FORMAT(5HTEFF ,F7.0,9H GRAVITY,F8.5,1X,A4/6HTITLE ,74A1)
112 FORMAT(I3,' ANGLES',10F7.4/10X,10F7.4)
open(unit= 11,file='intensM.dat',status='unknown')
read(11,111)te,logg
```

```
c read(11,*)
read(11,112)nmu,(mu(j),j=1,17)
i=1
415 read(11,416,end=417)i,WAV(i),FREQ,(IN(j,i),j=1,NMU)
416 FORMAT(9HINTENSITY,I5,F9.2,1PE15.6/(1P8E10.3))
418 FORMAT((1P18E10.3))
write(*,418)wav(i),(IN(j,i),j=1,Nmu)
i=i+1
goto 415
417 continue
close(11)
end
```

to compare the modified ATLAS9 and the original ATLAS9 code we wrote the following code.

• In the subroutine READIN (MODE) the following changes were made.

```
parameter(mx=5,mv=10,nr=169)
real rhoofp,t6,pp,xh,ztab,rrhox(kw),esact,eos,xxh,zztab
common /opalv/ xh,ztab,irad !opal variables
common/eeos/esact,eos(mv)
parameter(nmmu=20,N=5000)
real*8 wav(N),In(nmmu,N),mu(nmmu),freq,te,logg
character*4 inn
111 FORMAT(1(5HTEFF ,F7.0,9H GRAVITY,F8.5,1X,A4/6HTITLE ,74A1))
112 FORMAT(I3,' ANGLES',10F7.4/10X,10F7.4)
open(unit= 11,file='i00t6500g35Mod.dat',status='unknown')
open(unit=12, file="OPAL650045.dat",status="unknown")
c open(unit=13, file="ATLAS9650045.dat", status="unkwown")
read(11,111)te,logg
read(11,*)
```

```
read(11,112)nmu,(mu(j),j=1,17)
i=1
415 read(11,416,end=417)i,WAV(i),FREQ,(IN(j,i),j=1,NMU)
416 FORMAT(9HINTENSITY,I5,F9.2,1PE15.6/(1P8E10.3))
418 FORMAT((1P18E10.3))
write(*,418)wav(i),(IN(j,i),j=1,Nmu)
write(12,418)wav(i),((IN(j,i))/1e-141,j=1,Nmu)
c write(13,418)wav(i),(IN(j,i),j=1,Nmu)
i=i+1
goto 415
417 continue
close(11)
close(12)
close(13)
end
```

The Computer Platform

The first set of calculations carried out in this thesis were done using an OPAL code developed at the Lawrance Livermore National Laboratory. The big directory were the code is stored has EOS data files and the interpolation codes. These calculations were carried out using the Darwin Kernel Version 12.5.0. This is an open source unix computer operating system that was released by apple Inc. The code that composed this operating system was written in the C and C++ programming language. Furthermore, Darwin operating system supports the 64-bit x 86-64 variant of the Intel x86 processors used in Macs. For our purpose, this operating system had FORTRAN 77 installed and various editting platforms such as nano for our computer scripts. The compiler that was used was the gfortran free FORTRAN 77 compiler from the Free Software Foundation (FSF). It can compile any code written in FORTRAN 77 and to compile and run such a code one needs to use the terminal command lines as follows. For our purpose, these calculations were first done using the command line gfortran -o calling.f calling esac2.f as the compilation phase. The program was consequently ran with the command ./calling. The modified FORTRAN program calling.f calls the program esac.f in order to retrieve the OPAL EOS.

The second set of calculations were done using the Ubuntu 12.04 Long Term Support (LST) server at the UCT NASSP Lab. The compiler that was invoked was the FORTRAN ifort from intel. The ifort compiler calls on intel (R) FORTRAN compiler that is created, to put together, compile and link FORTRAN programs. The compiler processes FORTRAN language source and produces object files. The user then has to decide on the input and output desired by setting various options when the compiler is executed. For our purpose, this was done by invoking the compiler ifort by the command source atlas-compile3 where atlas-compile3 contains source filenames and the compilation options. The atlas-compile3 was scripted as fort -c -save -1 -tpp7 -w -V -WB -o atlas9mem-newodf3.o atlas9memnewodf3.for, ifort -Vaxlib -static -zero -o atlas9mem-newodf3.exe, atlas9mem-newodf3.o , where the .for file is the file where all the modifications

were done. The .exe file is the output file that was ran on the atlas9 input script as shown in Figure 4.1. The atlas9 input file was ran with the command source teko4.sh where the .sh file is the input script. This ifort compiler was used for the spectra calculations using different atlas9 modified codes.